The impact of baryonic physics on galaxy clusters in cosmological hydrodynamical simulations

Alisson Pellissier

UNIVERSITÉ CÔTE D'AZUR

ÉCOLE DOCTORALE
SCIENCES FONDAMENTALES ET APPLIQUÉES

THÈSE DE DOCTORAT

L'impact de la physique baryonique sur les amas de galaxies dans les simulations cosmologiques hydrodynamiques

Alisson Pellissier

Laboratoire J.-L. Lagrange – Observatoire de la Côte d'Azur

Présentée en vue de l'obtention du grade de docteur en science de la planète et de l'Univers de l'Université Côte d'Azur

Dirigée par : Oliver Hahn
Co-encadrée par : Chiara Ferrari
Soutenue le : 30 septembre 2021

Devant le jury, composé de :

Stefano Borgani, Professeur, Université de Triestre
Frédéric Bournaud, Chercheur, CEA, Département d'Astrophysique
Florence Durret, Astronome, Institut d'astrophysique de Paris
Chiara Ferrari, Astronome, Observatoire de la Côte d'Azur
Oliver Hahn, Professeur, Université de Vienne
Lorenzo Lovisari, Docteur, Observatoire de Bologne
Sophie Maurogordato, Directeur de recherche, CNRS, UCA

European Research Council
Established by the European Commission

L'impact de la physique baryonique sur les amas de galaxies dans les simulations cosmologiques hydrodynamiques

Jury

Président du jury

Sophie Maurogordato, Directeur de recherche, *Université de la Côte d'Azur, CNRS*

Rapporteurs

Frédéric Bournaud, Chercheur, *CEA, Département d'Astrophysique*
Florence Durret, Astronome, *Institut d'astrophysique de Paris, Sorbonne Université*

Examinateurs

Stefano Borgani, Professeur, *Osservatorio Astronomico di Trieste, Università degli Studi di Trieste, INAF*
Lorenzo Lovisari, Docteur, *Osservatorio di Astrofisica e Scienza dello Spazio di Bologna, INAF*

Oliver Hahn, Professeur, *Universität Wien, Institut für Astrophysik, Fakultät für Mathematik*
Chiara Ferrari, Astronome, *Observatoire de la Côte d'Azur, CNRS*

Doctoral Thesis

The impact of baryonic physics on galaxy clusters in cosmological hydrodynamical simulations

Author:
Alisson Pellissier

Supervisor:
Oliver Hahn

Co-Supervisor:
Chiara Ferrari

A thesis submitted in fulfillment of the requirements for the degree of "Docteur en science de la planète et de l'Univers"

Université Côte d'Azur
École doctorale Sciences Fondamentales et Appliquées

Observatoire de la Côte d'Azur
Laboratoire J-L. Lagrange

⊙

L'impact de la physique baryonique sur les amas de galaxies dans les simulations cosmologiques hydrodynamiques

Résumé

Les amas de galaxies occupent une place particulière dans la hiérarchie de l'Univers : ils constituent les structures virialisées les plus massives de l'Univers et forment les nœuds de la toile cosmique. Au delà de la dizaine de mégaparsec, la gravité gouverne l'évolution de ces structures et l'abondance des amas est extrêmement sensible à la cosmologie sous-jacente. Tandis qu'au deçà du mégaparsec, la physique baryonique s'ajoute aux effets gravitationnels, ce qui complexifie la modélisation physique des amas de galaxies. En effet, suite aux processus de coalescence entre amas de masse comparable et d'accrétion de systèmes de masse inférieure, le gaz intra-amas est chauffé par compression et chocs, et atteint des températures suffisamment élevées pour émettre des rayons X. De plus, les processus énergétiques liés à la rétroaction des supernovae et des noyaux actifs de galaxie, peuvent injecter des quantités substantielles d'énergie ainsi que des particules relativistes dans le milieu intra-amas. Les amas de galaxies représentent donc un lieu privilégié où la cosmologie et l'astrophysique se rencontrent, faisant des amas des laboratoires idéaux pour l'étude de la physique de formation des galaxies et des grandes structures.

La force des amas de galaxies en tant que sondes cosmologiques est principalement limitée par notre capacité à mesurer avec précision leur masse. Une calibration précise des relations d'échelle, reliant les quantités observables et la masse totale des amas, sont des ingrédients cruciaux pour les études d'amas qui visent à contraindre les paramètres cosmologiques. Il est donc important de comprendre à la fois les processus physiques qui donnent lieu à ces relations ainsi que tout biais et dispersion. En effet lors de la formation des amas de galaxies, les propriétés du milieu intra-amas sont affectées par l'assemblage cosmique et les differents processus astrophysiques.

Les codes hydrodynamiques couplés aux algorithmes à N-corps sont les outils les plus avancés pour décrire la complexité de tels processus ainsi que leur impact sur l'histoire d'assemblage des structures cosmiques. Dans ce contexte, nous utilisons des simulations cosmologiques magnétohydrodynamiques d'amas de galaxies massifs, pour étudier l'impact des processus baryoniques à la fois sur les observables du gaz intra-amas et sur les propriétés des galaxies en leur sein.

Dans cette thèse, nous montrons tout d'abord la dépendance de la topologie du champ magnétique primordial sur l'amplification du champ magnétique intra-amas. Bien que les champs magnétiques ne soient pas une composante dominante dans la dynamique des amas, leur présence façonne le transport des particules dans le plasma intra-amas. Pour étudier cet aspect, nous examinons l'effet de la conduction thermique anisotrope sur la thermodynamique du gaz intra-amas. Nous étudions conjointement différents modèles de formation et d'évolution des trous noirs supermassifs ainsi que la rétroaction des noyaux galactiques actifs. Nous présentons une vue d'ensemble des succès et faiblesses de nos simulations dans la reproduction des propriétés physiques du plasma intra-amas ainsi que les propriétés stellaires des galaxies, à la fois de champ et au sein des amas. Enfin, nous dérivons les relations d'échelle pour les amas de galaxies massifs constituant notre échantillon. En démontrant l'impact relatif de nos différents modèles, nous montrons comment les processus astrophysiques peuvent modifier ces relations d'échelle essentielles, pour la cosmologie.

Mots clés :

Astrophysique – Simulations numériques – Cosmologie – Amas de galaxies – Milieu intra-amas

The impact of baryonic physics on galaxy clusters in cosmological hydrodynamical simulations

Abstract

Clusters of galaxies reside at a unique place in the Universe's hierarchy: they are the most massive virialised structures and form the nodes of the cosmic web. Above scales of tens of megaparsecs, gravity drives the evolution of structures in our Universe and the abundance of clusters is heavily sensitive to the underlying cosmology. While below the megaparsec scale and in addition to gravity, the physics of baryons play an important role in making the physical modelling of clusters more complex. Indeed, following sequences of mergers and the accretion of smaller systems, the intra-cluster gas is heated by compressions and shocks and reaches temperatures high enough to emit X-ray radiation. Additionally, energetic feedback processes due to supernovae and active galactic nuclei in the cluster galaxies can inject substantial amounts of energy and relativistic particles into the intra-cluster medium. Galaxy clusters therefore represent a place where cosmology and astrophysics meet each other, making clusters key laboratories to study the physics of structure and galaxy formation.

The power of galaxy clusters as cosmological probes is limited especially by our ability to accurately measure their mass. Well-calibrated scaling relations, between observable properties and the total cluster masses, are crucial ingredients for studies that aim to constrain cosmological parameters. It is therefore of great importance to understand both physical processes that give rise to these relations and understand any bias and scatter. Indeed, properties of the intra-cluster medium are affected by the cosmic assembly and astrophysical processes during cluster formation.

Hydrodynamical codes coupled to N-body techniques are the most advanced tools to describe such complex processes as well as their impact on the assembly history of cosmic structures. In this context, we use cosmological magnetohydrodynamical simulations of massive galaxy clusters to study the impact of baryonic processes on both the intra-cluster gas observables and the galaxy properties.

In this thesis, we first show the dependence of the magnetic seed field topology on the amplification of the cluster magnetic fields. Although magnetic fields are not dynamically relevant, their presence shapes the transport of particles in the intra-cluster plasma. To study this aspect, we examine the effect of the induced anisotropic thermal conduction on the thermodynamics of the intra-cluster gas. We jointly investigate different models of formation and evolution of supermassive black holes as well as feedback from active galactic nuclei. We present an overview of the achievements and shortcomings of our simulations in reproducing both the hot plasma in clusters as well as the stellar properties of cluster and field galaxies. Finally, we derive cluster scaling relations for our massive galaxy cluster sample. By demonstrating the relative impact of our different galaxy formation models, we show how astrophysical processes are expected to alter such relations used for cosmology.

Keywords :

Astrophysics – Numerical simulations – Cosmology – Galaxy clusters – Intracluster medium

Contents

Acronyms used in this thesis

Acronym	Definition
AMR	Adaptative Mesh Refinement
AGN	Active Galactic Nucleus
BCG	Brightest Cluster Galaxy
BH	Black Hole
CMB	Cosmic Microwave Background
CPU	Central Processing Unit
CC	Cool Core
CR	Cosmic Ray
CT	Constrained Transport
EMW	(X-ray) Emission-Weighted
IC	Initial Condition
ICL	Intra-Cluster Light
ICM	Intra-Cluster Medium
IGM	Intra-Galactic Medium
ISM	Interstellar Medium
GC	Galaxy Cluster
HMF	Halo Mass Function
LLA	Local Lagrangian Approximation
MHD	Magneto-Hydrodynamics
MPI	Message Passing Interface
MC	Mass-weighted+Conduction, see text
MW	Mass-Weighted
NCC	Non-Cool Core
NR	Non-Radiative
PLM	Piecewise Linear Method
PMF	Primordial Magnetic Field
PPM	Piecewise Parabolic Method
RMS	Root Mean Square
SF	Star Formation
SFR	Star Formation Rate
SL	Spectroscopic-Like
SF	Spectral Fit
SN	Supernova
SPH	Smoothed Particle Hydrodynamics
SMBH	Super Massive Black Hole
SMHM	Stellar Mass-Halo Mass (relation)
VW	Volume-Weighted

General Context

Introduction 1

In this chapter, we will introduce the reader to the subject of this thesis and develop the outline of the manuscript.

1.1 Brief history and description of galaxy clusters

The exploration of galaxy clusters began in the XVIII century when Charles Messier [1] and Friedrich Wilhelm Herschel [2] independently detected collection of nebulae in the sky.[1] At that time, 7 members of the Local group of galaxies were already known but the extragalactic nature of these systems was established in the early twenties by Edwin Hubble [4].

1: For more details, see the great historical review of Biviano [3].

In the second part of the XX century, surveys and catalogues such as Abell's, opened a new era in the scientific investigation of galaxy clusters. Abell [5] demonstrated the existence of "clusters of clusters" and de Vaucouleurs [6] found that 85% of all nearby galaxies are in groups : it was the seeds for idea of the Universe's large scale structures...

Figure 1.1: George Abell teaching in 1976. He inspected plates of the Palomar Observatory Sky Survey during his PhD to prepare the eponymous catalog of 2,712 rich clusters of galaxies still widely used today. He dedicated a great part of this time for popularising science and teaching to young people.

Galaxies aggregate into clusters of galaxies at late times, forming bound structures at locations where the initial fluctuations create the deepest potential wells. The study of these galaxy clusters has played a significant role in the development of cosmology over many years. Modern cosmology theorised the idea of a hierarchical structure formation where initial cosmological overdensities form gravitationally bound halos of increasing mass via collapse and mergers [7]. As such, galaxies aggregate into groups ($\lesssim 50$ members within a sphere of $\sim 750\,h^{-1}$kpc) and galaxy clusters at late times ($\gtrsim 50$, $\gtrsim$ kpc/h). Clusters of galaxies are therefore the most massive gravitationally bound structures of our Universe and provide unique signatures of its evolution. Moreover, they mark the transition from the linear infall regime to the non-linear relaxation stage and constitute large scale astrophysical laboratories and important probes for the study of our Universe's structures.

With typical masses of $10^{14} - 10^{15}\mathrm{M}_{\odot}$, galaxy clusters consist of multi-component objects composed of dark matter (85%), which

Figure 1.2: *Left :* Stephan's Quintet Stephan's (or Hickson Compact Group 92) is a beautiful example of a small group of galaxies. *Right :* Galaxy Cluster SDSS J1336 0331 showing its gravitational influence on background lensed galaxies. Both images were taken by the new Wide Field Camera 3 (WFC3) aboard NASA's Hubble Space Telescope

dominates the mass budget, stars, cold gas, and dust in galaxies ($\sim$ 3%), and a hot ionized intra-cluster medium (12%) reflecting the matter content of our Universe [8].
In addition of being extrema in the Universe density field, major mergers of galaxy clusters are the most energetic phenomena since the Big Bang and dissipate up to 10^{64} ergs of gravitational potential energy during one cluster crossing time ($\sim$ Gyr). This energy is primarily dissipated at shocks into heating of the intra-cluster gas to high temperatures, but also through large-scale ICM motions generating turbulence. A fraction of this energy can can be channeled into non-thermal plasma components, (i.e. relativistic particles or cosmic rays) and magnetic fields.

Galaxy clusters are therefore veritable crossroads of astrophysics and cosmology. On one hand, they probe the physics governing the dynamics of the large-scale structures in the Universe. On the other hand, they are key laboratories to study acceleration mechanisms of relativistic particles and energy dissipation processes during the hierarchical sequence of matter accretion and formation of structures.

For this reason, the study of the formation and evolution of galaxy clusters occupies a fundamental position in cosmology and astrophysics.

1.2 Why galaxy clusters?

Thanks to their multicomponent nature, clusters of galaxies offer multiple observable signals across the electromagnetic spectrum :

- At X-ray wavelengths, the intra-cluster medium shines bright thanks to thermal bremsstrahlung and line emission from ionized metals injected by feedback processes.
- The optical and near-infrared is dominated by the emission of the intra-cluster light and the stars in cluster galaxies.
- At millimeter wavelengths, clusters distort the spectrum of the cosmic microwave background.
- Synchrotron emission from cosmic ray electrons in the intra-cluster medium is visible at radio frequencies.

This variety of observed signatures provides unique physically coupled, and often observationally independent, probes of the evolution of the Universe.

Indeed, the overall growth of structures is regulated by few key parameters of our standard cosmological model such as the mean matter density, the amplitude of matter density fluctuations or the equation of state of the dark energy [9, 10].
And because galaxy clusters originate from the highest peaks in the initial cosmic density field, their spatial distribution and abundance carry the imprints of the process of structure formation and are heavily sensitive to the underlying cosmology. Therefore, counting galaxy clusters, as a function of their mass and cosmic time provides an excellent (late Universe) probe of such cosmological parameters.

However, the predictive power of galaxy clusters as cosmological probe is limited especially by our ability to accurately measure their mass. Cosmological surveys of clusters heavily rely on scaling relations to relate an easily observed quantity (such as the X-ray luminosity) to the true cluster mass. However, it is crucial to understand the physics that give rise to these relations and interpret any scatter originating from non-gravitational processes (e.g. shocks, star formation and galactic feedback).

Carried out on massive parallel supercomputers, numerical simulations represents well-suited modern tools to describe and follow the complexities of the galaxy cluster formation. Incorporating increasingly detailed galaxy formation models, numerical simulations can provide important insights for the interpretation of observational data. Therefore, it is possible to explore possible biases introduced by the used assumptions for the mass estimation

Figure 1.3: The Joliot-Curie supercomputer at the CEA's Very Large Computing Centre (TGCC) has been used for the galaxy cluster simulations presented in this thesis. The name is a tribute to Irène et Frédéric Joliot-Curie and the supercomputer has been customised by the stencils of the street artist C215. – Credits: CEA

based on exactly known cluster properties.
However, modelling the formation of realistic galaxy clusters in a cosmological context is one of the most challenging problems of galaxy formation, but it remains a crucial ingredient for calibrating cluster scaling relations used in cosmology.

1.3 Outline of this thesis

In this context, we use cosmological zoom-in simulations of massive galaxy clusters to study in this thesis the role of cosmic assembly vs. astrophysical processes at shaping the thermodynamic structure of the intra-cluster gas.
In order to understand why galaxy clusters are used as cosmological probes, we will start by giving in Chapter 2 a short introduction to the basics of cosmology and learn how (the dark component of) a cluster forms and grows.
In Chapter 3 we will discuss the observational properties of galaxy clusters and the underlying physical processes.
Numerical techniques used for astrophysical simulations will be discussed in Chapter 4 as well as common astrophysical codes and sub-resolution models.
We will especially focus in Chapter 5, on the methods employed in the adaptive-mesh refinement code Ramses. We will present the Rhapsody-G simulation suite which constitutes the basis of this work.

In a second part, we will show the main results of our study by starting with the respective impact of magnetic fields, thermal conduction and models of AGN feedback on key cluster diagnostics and scaling relations. But before we delve into such details, we will describe in Chapter 6 the simulations we ran for this work.
Then Chapter 7, we will be mostly focused on the seeding of magnetic fields as well as their amplification in clusters.
After a discussion on transport processes within clusters, we will study in Chapter 8 the role of anisotropic thermal conduction in idealised magnetohydrodynamical simulations of the intra-cluster medium.

In Chapter 9 we will detail the choice of the physical models used in our simulations and also the improvements in our black hole and AGN modelling. We will show the impact they can have on a relaxed system.
We will then extend this analysis to the full Rhapsody-G sample in Chapter 10. We will show key diagnostics such as distribution of mass in the cluster potential, the thermodynamics of the intra-cluster gas as well as the properties of the galaxy population.

In Chapter 11 we will consider the self-similar model of galaxy clusters to derive the scaling relations used for cosmology. We will present our measurements of cluster observables and show the evolution of halos of the Rhapsody-G sample along these scaling relations.

Finally, in Chapter 12 we will draw the general conclusions from our study and discuss prospects for future works.

Understanding the formation of galaxy clusters

2

This chapter will set the basic theoretical aspects of galaxy cluster formation in a cosmological framework. We will focus on the use of galaxy clusters as cosmological probes in a second part.

2.1 The homogeneous Universe

2.1.1 An expanding Universe

In order to understand how large structures, such as galaxy clusters, formed in our Universe, it is necessary to start with description of the properties the Universe and its evolution as a whole.

The observed distribution of galaxies in our Universe (shown in Figure 2.1) appears, on large scale, isotropic as no direction seems privileged. Moreover, the cosmic microwave radiation (CMB) reaching us from all directions is also isotropic except for tiny, but immensely important, fluctuations with a relative amplitude of $\sim 10^{-5}$.
We also assume that we do not live in any particular location in the cosmos. It means that our Universe is isotropic in any other places too, which therefore implying its homogeneity.
The combined assumption of isotropy and homogeneity is known as the cosmological principle.[1]

1: Of course, the assumption of homogeneity breaks down on small scales where structures like galaxies and clusters clearly appear.

2.1.2 Geometry and dynamics

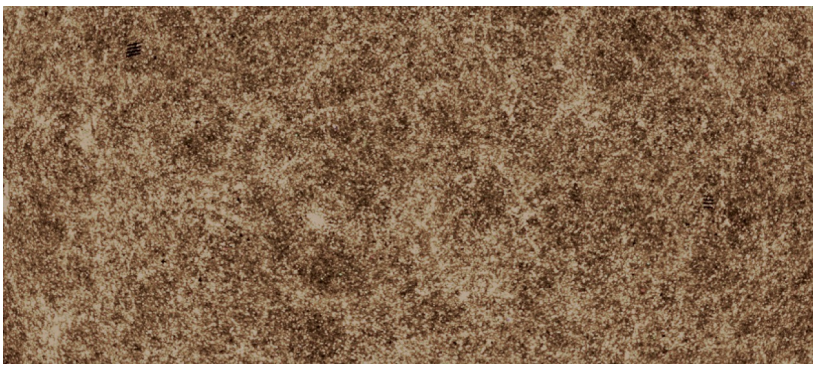

Figure 2.1: Distribution of galaxies in a fragment of the northern galactic cap of the SDSS survey. The intensity denotes the projected number of galaxies – Credits: M. Blanton & SDSS-III

Only gravity and the electromagnetic force can act over large distances, and, as cosmic matter is electrically neutral on large

scales, gravity is the driving force in cosmology. In the framework of general relativity, gravity is described by a curvature of space-time.

The causal and geometric structure of a curved space-time can be described as a four-dimensional manifold whose tensor metric $g_{\mu\nu}$ is the dynamic field. In our case, the description of an expanding, homogenous and isotropic universe is given by the so-called Friedman-Lemaître-Robertson-Walker (FLRW) metric yielding the line element :[2]

2: in spherical coordinates

$$\begin{aligned} \mathrm{d}s^2 =& g_{\mu\nu}\mathrm{d}x^\mu \mathrm{d}x^\nu, && (2.1)\\ =& -\mathrm{d}t^2 + a^2(t)\left(d\chi^2 + S_k^2(\chi)\mathrm{d}\Omega^2\right), && (2.2) \end{aligned}$$

where χ is the comoving spatial distance, $a(t)$ is the cosmological expansion or scale factor, $\mathrm{d}\Omega^2$ is the angular separation and the function S_k which depends on the constant curvature k as follows :

$$S_k(\chi) = \begin{cases} \sinh(\chi) & k = -1 \quad \text{open} \\ \chi & k = 0 \quad \text{flat} \\ \sin(\chi) & k = +1 \quad \text{closed} \end{cases} \qquad (2.3)$$

As relativistic cosmology is not transacted in space but in spacetime, it is thus convenient to include a time coordinate that allow for the expansion of the Universe. If we assume that the Universe in the past was also homogeneous, the only thing that can change is the radius of the curvature, and so we can write :

$$R(t) = a(t)R_0, \qquad (2.4)$$

were R_0 is the present day curvature[3] (i.e. when $t = t_0$) where we define $a(t = t_0) \coloneqq 1$. These are the comoving coordinates.

3: The flat space is handled by taking the limit $R_0 \to \infty$

The scale factor $a(t)$ is very important : it does not only measure the size of the past Universe but it also measures the separation of any two fundamental observers as a fraction of their separation today.

We can also define the cosmological redshift, z, which is directly linked to the scale factor and commonly used by astronomers.

Indeed, a direct consequence of the FLRW metric is the reddening of waves[4] as they propagates.

4: electromagnetic or gravitational

For instance, a photon of wavelength λ_{emit} emitted at a time $t = t_{\text{emit}}$ in an expanding Universe will be observed at a larger wavelength $\lambda_{\text{obs}} = \lambda_{\text{emit}}\, a(t_{\text{obs}})/a(t_{\text{emit}})$, as we have $a(t_{\text{obs}}) > a(t_{\text{emit}})$.

As the result, remote galaxies appear redder than close-by ones. The redshift is defined to be the relative difference between the observed wavelength today λ_0 and the emitted wavelength. It is immediately related to the scale factor as :

$$1 + z \coloneqq \frac{\lambda_0}{\lambda_{\text{emit}}} = \frac{1}{a(t_{\text{emit}})}, \qquad (2.5)$$

The dynamics of the metric are governed by Einstein's field equations which couple $g_{\mu\nu}$ to the matter-energy content of space-time :

$$G_{\mu\nu} + g_{\mu\nu}\Lambda = \frac{8\pi G}{c^4} T_{\mu\nu}, \tag{2.6}$$

with G, the gravitational constant, and Λ, the cosmological constant, firstly introduced by Einstein to allow static cosmological models, accounts in fact for the accelerated expanding space-time.

Equation 2.6, also have $G_{\mu\nu}$, the Einstein tensor and $T_{\mu\nu}$ the stress-energy tensor, being respectively measures of the Universe's curvature and energy-momentum. On sufficiently large scales, we assume the Universe as an ideal fluid being completely characterised by a pressure p and a (energy) density ρ[5] . Therefore, we can write the stress-energy tensor of this cosmic fluid as :

5: which can only be a function of time because of the assumed homogeneity

$$T_{\mu\nu} = \left(p + \frac{\rho}{c^2}\right) U_\mu U_\nu + p g_{\mu\nu}, \tag{2.7}$$

with U the 4-velocity of the fluid.
Solving Einstein's equations with the FLRW metric yield two ordinary differential equations for the scale factor. They are called the Friedmann's-Lemaître equations :

$$\left(\frac{\dot{a}}{a}\right)^2 = \frac{8\pi G}{3}\rho - \frac{kc^2}{a^2} + \frac{\Lambda}{3} := H^2, \tag{2.8}$$

$$\frac{\ddot{a}}{a} = -\frac{4\pi G}{3}\left(\rho + \frac{3p}{c^2}\right) + \frac{\Lambda}{3}, \tag{2.9}$$

where we introduced the Hubble parameter $H := \dot{a}/a$, which takes at the present day to the value H_0 called the Hubble constant. We can combine the two above equations to yield the adiabatic equation :

$$\frac{d}{dt}\left(a^3 \rho c^2\right) + p\frac{d}{dt}a^3 = 0. \tag{2.10}$$

Intuitively, the equation above states the energy conservation, with the left hand side being the change in internal energy, and pressure work being on the right hand side. We recognize the first law of thermodynamics in the absence of heat flow[6] .

6: which would violate isotropy otherwise

2.1.3 Forms of matter

We can broadly distinguish two forms of matter : relativistic and non-relativistic often called radiation and dust respectively[7] . We can solve the adiabatic Equation 2.10 to infer the density evolution of each variety :

7: Radiation refers to electromagnetic radiation or particles moving close to the speed of light.
Dust refers to cold (non-relativistic) and collisionless matter such as cold dark matter, stars, galaxies, ...

- for relativistic matter with the pressure $p = \rho c^2/3$, we have :

$$\rho_r(t) = \rho_{r,0}\, a^{-4}, \tag{2.11}$$

- and non-relativistic matter can be approximated as pressure-free (as the rest-mass energy is much greater than the pressure), which yields :

$$\rho_m(t) = \rho_{m,0}\, a^{-3}, \tag{2.12}$$

where $\rho_{m/r,0}$ is the radiation/matter density at the present day.
We see that non-relativistic matter is diluted as space is expanding. Radiation is dropping by one power faster because particles also loose energy as they are redshifted.
Replacing $\rho = \rho_r + \rho_m$ in Friedmann's-Lemaître's Equation 2.8 results in :[8]

8: with $\Omega_r + \Omega_m + \Omega_\Lambda + \Omega_k = 1$

$$H^2(a) = H_0^2 \left(\Omega_{\mathrm{r},0} a^{-4} + \Omega_{\mathrm{m},0} a^{-3} + \Omega_{\Lambda,0} + \Omega_k a^{-2}\right), \tag{2.13}$$
$$:= H_0^2\, E^2(a), \tag{2.14}$$

which makes use of the present day density parameters :

$$\Omega_{\mathrm{r},0} := \frac{\rho_r(t)}{\rho_c(t)}, \tag{2.15}$$
$$\Omega_{\mathrm{m},0} := \frac{\rho_m(t)}{\rho_c(t)}, \tag{2.16}$$
$$\Omega_{\Lambda,0} := \frac{\Lambda}{3H^2(t)}, \tag{2.17}$$
$$\Omega_k := \frac{-k\mathrm{c}^2}{H_0^2}, \tag{2.18}$$
$$\tag{2.19}$$

where we defined the expansion function $E(a)$ and the critical density $\rho_c(t) = \frac{3H^2(t)}{2\pi \mathrm{G}}$.[9]

9: we can rewrite the critical density in the form of :

$$\frac{4}{3}\pi \frac{\rho_c a^3 \mathrm{G}}{a} = \frac{1}{2}\dot{a}^2,$$

to illustrate that the gravitational potential is exactly balanced in a sphere filled with matter of critical density.

2.1.4 Age and dynamics of the Universe

The age of the Universe at a given scale factor a follows from the first Friedmann's-Lemaître Equation 2.8 with $\mathrm{d}t = \mathrm{d}a\,(\mathrm{d}a/\mathrm{d}t)^{-1} = \mathrm{d}a/(aH)$. This relation can be integrated :

$$t(a) = \frac{1}{H_0}\int_0^a \mathrm{d}a' \left[a'^{-2}\Omega_{\mathrm{r},0} + a'^{-1}\Omega_{\mathrm{m},0} + (1 - \Omega_{\mathrm{m},0} - \Omega_{\Lambda,0}) + a'^{2}\Omega_{\Lambda,0}\right]^{-1/2}, \tag{2.20}$$

where we assume that time start running when $a = 0$. While this integral cannot be solved analytically, limiting cases are interesting to study.

In the early universe, i.e. $a \to 0$, radiation dominates as its contribution scales with a^{-4}. In this limit, Equation 2.13 becomes :

$$\frac{\dot{a}}{a} = H_0\sqrt{\Omega_{\mathrm{r},0}a^{-4}} \quad \Longrightarrow \; a(t) = \left(2\sqrt{\Omega_{\mathrm{r},0}}H_0 t\right)^{1/2}, \tag{2.21}$$

Hence, at early times the expansion of the Universe scales like $a \propto \sqrt{t}$ until the radiation density drops near the density of non-relativistic matter. This transition from the radiation dominated area to the matter dominated area occurs roughly when :

$$\Omega_{\mathrm{r},0}a_{\mathrm{eq}}^{-4} = \Omega_{\mathrm{m},0}a_{\mathrm{eq}}^{-3} \implies a_{\mathrm{eq}} = \frac{\Omega_{\mathrm{r},0}}{\Omega_{\mathrm{m},0}}, \tag{2.22}$$

This is time time of equivalence when radiation and matter have the same energy density. Recent Planck observations find $z_{\mathrm{eq}} = 3402 \pm 26$ corresponding to $a_{\mathrm{eq}} \sim 3 \times 10^{-4}$ [11].

Then, the Universe enters the matter dominated area also known as an Einstein-de Sitter (EdS) universe. The dynamics of the expansion factor is governed by :

$$\frac{\dot{a}}{a} = H_0\sqrt{\Omega_{\mathrm{m},0}a^{-3}} \quad \Longrightarrow \; a(t) = \left(\frac{3}{2}\sqrt{\Omega_{\mathrm{m},0}}H_0 t\right)^{3/2}, \tag{2.23}$$

At later times, the expansion will transition to a vacuum dominated state. The second time of equivalence, when the matter density equals the vacuum energy, is given by :

$$\Omega_{\mathrm{m},0}a_{\mathrm{eq},2}^{-3} = \Omega_{\Lambda,0} \implies a_{\mathrm{eq},2} = \left(\frac{\Omega_{\mathrm{m},0}}{\Omega_{\Lambda,0}}\right)^{1/3}, \tag{2.24}$$

which corresponds to $a_{\mathrm{eq},2} \sim 0.772$, i.e $z_{\mathrm{eq},2} \sim 0.295$ [11].

The vacuum dominated very late Universe, so called de Sitter Universe, grows exponentially as :[10]

$$H_0 t = \frac{\ln a}{\sqrt{\Omega_{\Lambda,0}}} \quad \Longrightarrow \quad a(t) \propto \mathrm{e}^{\sqrt{\Omega_{\Lambda,0}}H_0 t}. \tag{2.25}$$

10: We consider a flat Universe with $\Omega_{\Lambda,0} = 1$. We also ignore the lower limit integration limit because the approximaation of a dominating cosmological constant is only valid after a finite time.

2.2 How cosmic structure grew

In this section we will present an overview of how the observed Universe large-scale homogeneity comes to be broken on smaller scales by the formation of cosmic structures.

2.2.1 Gravitational instabilities

In relativistic cosmology, the expansion of the Universe is slowed down by gravity and its evolution rate, $\dot{a}/a$, is described by Equation 2.8. We see that regions having slightly greater than average local mass density will grow at a faster rate than underdense regions. In each case, the absolute value of the density contrast, $|\delta|$, increases.[11] This may eventually stop the expansion in overdense regions where matter settles into gravitationally bound objects.

In a nutshell, our relativistic expanding Universe was gravitationally unstable to the growth of inhomogeneities in the mass distribution.[12]

The primordial density fluctuations are thought to originate from quantum fluctuations in the very early universe[13] . During a period of inflation, these fluctuations were later stretched giving rise to the observed anisotropies in the CMB. Analyses of the CMB in that the overdensities were indeed quite small with $|\delta| \ll 1$ at $z \sim 1000$.

2.2.2 Evolution of density fluctuations

To comply with the fundamental cosmological assumption and observations of the CMB, the overdensity field is a homogeneous and isotropic Gaussian random field being fully described by its power spectrum $P(k)$[14] . We should expect that galaxy clusters of mass M emerged from the collapse of initial density fluctuations of a sphere filled with the mean cosmic matter density of size :

$$R(M) = \left(\frac{3M}{4\pi \Omega_m(a) \rho_c(a)} \right)^{1/3}, \tag{2.27}$$

Because we aim at halos of mass M, we should filter out the overdensity field on this specific scale, $R(M)$. To this end, we use a window function W_R[15] such as :

$$\delta_R(\mathbf{r}, t) = \delta_M(\mathbf{r}, t) = \int \delta(\mathbf{r}') W_R\left(|\mathbf{r} - \mathbf{r}'|\right) \mathrm{d}\mathbf{r}'. \tag{2.28}$$

To perform such filtering, it is convenient to work in Fourier space where the variance of the filtered density contrast is given by :

$$\sigma_R^2 = \sigma_M^2 = 4\pi \int \frac{1}{(2\pi)^2} k^2 P(k) \hat{W}_R^2(k) \, \mathrm{d}k, \tag{2.29}$$

where $\hat{W}_R$ is the Fourier transform of the chosen window function.

11: We define the relative density constrast (or overdensity) field:

$$\delta(\mathbf{r}, t) := \frac{\rho(\mathbf{r}, t) - \bar{\rho}(t)}{\bar{\rho}(t)}, \tag{2.26}$$

with $\bar{\rho}$, the mean matter cosmic density.

12: provided that the $\bar{\rho}$ is not too small, the radiation pressure and Λ are note too large

13: Related to the uncertainty principle of Heisenberg.

14: which only depend on the modulus of the wavevector $\mathbf{k}$, but not its direction

15: The idea of a window function W_R is to approch a finite value within R and drop to zero outside. Common choices for the window function are a Gaussian filter or a top hat function

The variance on a scale of $R = 8\,h^{-1}$Mpc, σ_8, is commonly used to characterise the power spectrum amplitude[16] .

On such length-scales, substantially smaller than the Hubble radius, the growth of structures can be described in the framework of Newtonian gravity.[17] Futhermore, we describe the matter in our Universe as a non-relativistic collisionless cosmic fluid. Indeed, in our current cosmological model, cold dark matter is the dominant component driving structure formation.

The equations of motion of a self-gravitating fluid are given by the continuity equation (which formulates the conservation of mass), Euler's equation (for conservation of momentum), Poisson's equation (to relate matter to the gravitational potential), and for closure, an equation of state linking pressure to density fluctuations. We have respectively, in physical coordinates :

$$\frac{\partial \rho}{\partial t} + \nabla \cdot (\rho \mathbf{v}) = 0, \tag{2.30}$$

$$\frac{\partial \mathbf{v}}{\partial t} + (\mathbf{v} \cdot \nabla)\,\mathbf{v} = -\frac{\nabla p}{\rho} + \nabla \Phi, \tag{2.31}$$

$$\nabla^2 \Phi = 4\pi \mathrm{G} \rho, \tag{2.32}$$

$$\delta p = c_\mathrm{s}^2 \delta \rho, \tag{2.33}$$

where we have : c_s the adiabatic sound velocity of a fluid, Φ the gravitational potential. We work the above equations in the limit of pressure-free perturbations around the constant-density, pure Hubble-flow solution i.e. :

$$\rho = \bar{\rho}\,(1+\delta)\,, \qquad \boldsymbol{v} = H\boldsymbol{r} + \delta \boldsymbol{v}, \qquad \Phi = \bar{\Phi} + \delta\Phi, \tag{2.34}$$

leaving out non-linear terms, and performing derivatives in Fourier space.

We derive at the fundamental equation for the growth of structure in Newtonian theory, which illustrates the competition between infall by gravitational attraction and pressure support :

$$\ddot{\delta} + 2H\dot{\delta} + \left(k^2 \frac{c_s^2}{a^2} - 4\pi \mathrm{G}\bar{\rho}\right)\delta = 0. \tag{2.35}$$

The second order linear and homogeneous differential Equation 2.35 has two independant solutions which can be combined to a general solution [12] :[18]

$$\delta(\mathbf{x}, t) = D_+(t)\delta(\mathbf{x}, 0) + D_-(t)\delta(\mathbf{x}, 0), \tag{2.36}$$

where we have, in the Einstein-de Sitter cosmology, the growing mode $D_+(t) \propto t^{2/3} \propto a$ (also known as the growth factor) and the

16: Historically, this convention originates from the observed distribution of galaxies for which $\sigma_{\mathrm{gal}} = b\sigma(R = 8\,h^{-1}\mathrm{Mpc}) \sim 1$, with b the bias parameter describing the different clustering amplitude of galaxies as tracers of the dark matter distribution [12]

17: The effects General relativity and space-time curvature need to be accounted for scales comparable or above the Hubble radius

18: using the time derivative of $H^2 + \dot{H} = \ddot{a}/a$ and Equation 2.9

decaying mode $D_-(t) \propto t^{-1} \propto a^{-3/2}$.
Consequently, in a matter dominated Universe, the perturbations grow at the same rate as the scale factor, while the decaying mode falls rapidly and can be safely ignored at late times.

We notice that Equation 2.35 is an equation of a damped oscillator, provided that the sign of the term in brackets is positive, giving rise to acoustic oscillations in the fluid. Otherwise, the system is unstable and undergoes gravitational collapse.

This is the Jeans' stability criterion. The critical wave number separating these two regimes is k_J which is in real space the (comoving) Jeans length λ_J:

$$k_J = \sqrt{\frac{4\pi G\bar{\rho}}{c_s^2 a^2}}, \tag{2.37}$$

$$\lambda_J = \frac{2\pi a}{k_J} = \sqrt{\frac{\pi c_s^2}{G\bar{\rho}}}. \tag{2.38}$$

But how to describe quantitatively such an inhomogeneous Universe. In other words, how can we quantify the structures it contains ?

We see that a particular Universe cannot be described by $\delta(\mathbf{x}, t)$. We cannot describe in detail the matter distribution in the vicinity of a particular galaxy or the exact position of its closest galaxy. Such specific features highly depend on the early Universe matter distribution. We can only statistically predict properties of our Universe such as the average number density of galaxy clusters above a given mass for instance or the probability to find a galaxy at a given distance from another.

Indeed full non-linear gravitational dynamics are too complicated to be solved analytically and only limiting cases of structure formation can be described (e.g. linear perturbation theory or the spherical collapse model - see below). So, we rely on numerical simulations which are able to follow the non-linear regime of structure formation. On the other hand, they cannot predict exactly our Universe, but, can reproduce the a mass distribution that share the same statistical properties of it. We will describe in Chapter 4 the principles of such simulations.

It is interesting to study some limiting cases which allow to characterise the non-linear evolution of the Universe mass distribution.

2.2.3 From overdensities to virialised halos

Let us start with the spherical collapse model of Gunn & Gott [13]. It allows to derive analytically the evolution of isolated spherical density perturbations in the matter dominated regime.
We will consider an expanding flat matter-dominated universe ($\Omega = \Omega_m = 1 \implies H = H_0 a^{-3/2}$) embedding a spherical overdense region of radius R whose density ρ is homogeneous.[19] This spherical region is expanding with the background universe, but, due to the enhanced gravitational force, the sphere will expand at a slightly slower rate if it is overdense and faster if it is underdense. As a result, the sphere density contrast increases with respect to the background, decelerating even more its expansion. If the density is large enough, the expansion will come to a halt before collapsing. Therefore the sphere reaches a maximum size $R_{\rm ta}$ at turn-around before its collapse.

19: We also assume a spherical symetry outside the sphere, such as no gravitational force is exerted onto it.

In the case of a perfect homogeneity, the sphere will collapse to a single point if its particles move along perfectly radial orbits. Of course, in a more realistic case there are small scales density inhomogeneities within the sphere, which generates, via Poisson's equation, corresponding gravitational fluctuations. These, will scatter infalling particles, amplifying even further density inhomogeneities until the system settles in a bound equilibrium state. The resulting virialised object is called a dark matter halo.[20]

20: Indeed, since baryons contribute only to $\sim 15\%$ of the total mass, they will not appreciably change the dark matter collapse

While realistic density perturbations are not really spherical, the assumption above will nonetheless provide an insightful basis for understanding the non-linear collapse of more realistic cases.

For convenience, we introduce some dimensionless parameters with respect to the turn-around point :

$$x \coloneqq \frac{a}{a_{\rm ta}}, \tag{2.39}$$

$$y \coloneqq \frac{R}{R_{\rm ta}}, \tag{2.40}$$

$$\tau \coloneqq H_{\rm ta} t = H_0 a_{\rm ta}^{-3/2} t. \tag{2.41}$$

We also define the density at the turn-around, $\rho_{\rm ta}$, by the critical density and the overdensity ξ such as :

$$\rho_{\rm ta} = \frac{3H_{\rm ta}^2}{8\pi G}\xi. \tag{2.42}$$

From Friedmann's-Lemaître's Equation 2.8, the sphere expansion can be expressed as :

$$x' \coloneqq \frac{\mathrm{d}x}{\mathrm{d}\tau} = \frac{1}{H_{\mathrm{ta}}}\frac{\dot{a}}{a_{\mathrm{ta}}} = x^{-1/2}. \tag{2.43}$$

Where the Newtonian equation of motion for the sphere boundary is :

$$\ddot{R} = -\frac{GM}{R^2} = -\frac{G}{R^2}\frac{4}{3}\pi\rho_{\mathrm{ta}}R_{\mathrm{ta}}^3, \tag{2.44}$$

$$\iff y'' = -\frac{\xi}{2y^2}. \tag{2.45}$$

Integrating Equation 2.43 yields :

$$\tau = \frac{2}{3}x^{3/2} \tag{2.46}$$

Using the obvious boundary conditions and $y|_{x=0} = 0$, where the halo start at $a = 0$ with a zero radius gives the equation for the (reduced) boundary velocity : $y' = \pm\left[\xi\left(y^{-1}-1\right)\right]^{1/2}$ where the positive sign solution applies prior to the turn-around, and the negative after.
Because at time of turn-over, i.e. $a = a_{\mathrm{ta}}$, we have $y'|_{x=1} = 0$, this second boundary condition allows to write :

$$\tau = \frac{1}{\sqrt{\xi}}\left[\frac{1}{2}\arcsin\left(2y-1\right) - \sqrt{y-y^2} + \frac{\pi}{4}\right], \tag{2.47}$$

At turn-around, we have $x = y = 1$ for which $\tau = 2/3$. Hence, we are able to infer the overdensity ξ threshold for which a halo can collapse :

$$\xi = 1 + \delta = \left(\frac{3\pi}{4}\right)^2 \sim 5.55. \tag{2.48}$$

At early times, we can expand Equation 2.47 to lower order of y :

$$\tau = \frac{8}{9\pi}y^{3/2}\left(1 + \frac{3y}{10}\right), \tag{2.49}$$

in order to obtain, δ_L, the linear density contrast of the overdense sphere :

$$\delta_L = \left(\frac{\rho}{\bar{\rho}}\right)^3 \xi - 1 = \left(\frac{x}{y}\right)^3 \sim \frac{3y}{5}, \tag{2.50}$$

where we use the scalings of the background density and the halo mean density being respectively $\bar{\rho} \propto (a_{\mathrm{ta}}/a)^3 = 1/x^3$ and $\rho \propto (R_{\mathrm{ta}}/R)^3 = 1/y^3$.
We can now linearly extrapolate the density contrast δ_L to the time

of turn-around :

$$\delta_{L,\mathrm{ta}} = \frac{a_{\mathrm{ta}}}{a}\delta_L = \frac{\delta}{x} = \frac{3y}{5x} \tag{2.51}$$

By equating Equation 2.46 and 2.50, we are able to compute the ratio y/x which allows to derive :

$$\delta_{L,\mathrm{ta}} = \frac{3}{5}\left(\frac{3\pi}{4}\right)^{2/3} \sim 1.06 \tag{2.52}$$

Due to the symmetry of the equations of motions, theoretically, the final collapse is expected to happen at twice the time for turn-around, i.e. when $\tau_c = 4/3$ which correspond to $x_c = 4^{1/3} = 2^{2/3}$. In this case, the linear density contrast inside the sphere would be :

$$\delta_c = 2^{2/3}\delta_{T,ta} = \frac{3}{5}\left(\frac{3\pi}{2}\right)^{2/3} \sim 1.686 \tag{2.53}$$

However, as we discussed earlier, this sphere will not uniformly collapse to a point of infinite density. But due to the presence of small fluctuations in the density field, infalling particles will be scattered and virialise in a process called “violent relaxation” [14]. The dark matter halo will be in dynamical equilibrium that obeys Virial’s theorem, for which the final halo potential energy is twice that at the turn-around where the (reduced) radius drops to $y_{\mathrm{vir}} = 1/2$. Thus, we obtain the expected overdensity Δ_{vir} of a virialised halo :

$$\Delta_{\mathrm{vir}} = \frac{\rho_{\mathrm{vir}}}{\bar{\rho}(a_{\mathrm{vir}})} = \left(\frac{2^{2/3}}{1/2}\right)^3 \xi = 18\pi^2 \sim 177.7. \tag{2.54}$$

This is why the choice of $\Delta = 200$ is used to describe dark matter haloes. We note however that for studies of galaxy clusters, $\Delta = 500$ is preferred. Indeed, a majority of cluster observations (mainly X-ray) probe regions up enclosing more or less 500 times the critical density.

Thanks to its simplicity, the model of spherical collapse allows to characterise the non-linear evolution of a density perturbation in the Universe. Depsite its crude assumptions, it represents the fundamental principles of gravitationnal collapse and gives approximate relations such as the mean density inside a virialized region and the time for collapse.

From this model, we will be able to compute approximatively the number density of dark matter halos as a function of their mass and redshift.

2.2.4 The abundance of halos

Now that we have derived the conditions for the formation of dark matter halos and their characteristics, an important piece of information remains to be assessed : how many dark matter halos of a given mass do we expect at a given time ?
This information is provided by the so-called halo mass function (HMF) which gives the number density of halos at redshift z in the mass range $[M, M + \mathrm{d}M]$.

In a simplified view : a density perturbation of a given radius R in the primordial Gaussian random field is able to gravitationally collapse into a virialised halo of mass M if its density contrast δ_M exceeds the threshold density contrast δ_c defined in Equation 2.53.

Such density perturbations can be targetted by coarse-graining the density field ρ on the scale R. As we already stated in Section 2.2.2, the variance σ_M of such filtered density field is given by Equation 2.29.

Motivated by the spherical collapse model, Press & Schechter [15] suggested that the number of halos of mass M at a redshift z (or equivalently an expansion factor a) is determined by the probability that a linearly extrapolated density perturbation on scale M exceeds the linear threshold for virialisation δ_c (previously derived in Equation 2.53).
It means that for our coarse-grained random density field δ, this probability is :[21]

$$p\left(\delta > \delta_c(a) \,|\, M\right) = \int_{\delta_c(a)}^{\infty} p(\delta, \sigma_M)\, \mathrm{d}\delta\,, \tag{2.55}$$

$$= \int_{\delta_c(a)}^{\infty} \frac{1}{\sqrt{2\pi\sigma_M^2}} \exp\left(-\frac{\delta}{2\sigma_M^2}\right) \mathrm{d}\delta, \tag{2.56}$$

$$= \frac{1}{2}\mathrm{erfc}\left(\frac{\delta_c(a)}{\sqrt{2}\sigma_M}\right), \tag{2.57}$$

where $\mathrm{erfc}(x)$ is the complement error function. This equation provides the number density per unit volume of halos of mass M at a given time, a. Therefore, we derive the total volume fraction of halos with mass in the range $[M, M + \mathrm{d}M]$:

$$\mathrm{d}p\left(\delta > \delta_c(a) \,|\, M\right) = \left|\frac{\partial p\left(\delta > \delta_c(a) \,|\, M\right)}{\partial M}\right| \mathrm{d}M, \tag{2.58}$$

where the absolute value is required to ensure the positivity of the Press & Schechter (PS) mass function.

21: where we noted that the density contrast for virialisation δ_c will depend on the scale factor as $\delta_c(a) = \delta_c / D_+(a)$ with $D_+(a)$ the linear growth factor defined in Equation 2.36

However, the normalisation of the mass function is wrong as $\int_0^\infty \mathrm{d}p\,(\delta > \delta_c(a)\,|\,M) = 1/2$. It implies that the PS mass function only accounts for half of the total available mass.
A more rigorous derivation known as the extended Press-Schechter formalism correctly accounts for the missing factor of 2. We will just briefly comment on the fact that it is based on the excursion-set formalism of Bond *et al.* [16] and sees halo formation as a random walk (for more details, see e.g. [12]).

Nevertheless accounting for an ad-hoc missing factor or 2 in the PS formalism, still provides an useful insight into hierarchical structure formation. Indeed, after dividing Equation 2.58 by the volume occupied by each halo, $V_M = M/\bar{\rho}$, the mass function reads :

$$\frac{\mathrm{d}n(M,a)}{\mathrm{d}M} = \sqrt{\frac{2}{\pi}}\frac{\bar{\rho}}{M^2}\frac{\delta_c}{\sigma_M D_+(a)}\left|\frac{\mathrm{d}\log\sigma_M}{\mathrm{d}\log M}\right|\exp\left(-\frac{\delta_c^2}{2\sigma_M^2 D_+^2(a)}\right). \tag{2.59}$$

This expression of the PS mass function has turned out to describe remarkably well the distribution of dark matter halos in simulations and a large variety of fitting formulas calibrated from numerical simulations are available such as Jenkins *et al.* [17] or Tinker *et al.* [18].

The amplitude of fluctuations of the smoothed field is characterised by the dispersion σ_M. For larger smoothing scales, or higher halo mass ($R \propto M^{1/3}$), we have smaller relative fluctuations of the smooth field, hence fewer peaks. As a result, σ_M is a decreasing function of the mass M.
We see that the HMF in Equation 2.59 is a steeply decreasing function of the peak height $\nu = \frac{\delta_c}{\sigma_M D_+(a)}$ due to its exponential cutoff. Therefore, it is increasingly rare to find massive halos at high redshifts.
As a result, the PS model also describes the hierarchical structure formation (or bottom-up scenario) in CDM models, where low mass halos forms at early times whereas larger halos form latter by mergers.

We can see that the halo mass function is a powerful probe of cosmological models. Indeed, cosmological parameters enters in Equation 2.59 through the mass variance σ_M (which depend on the power spectrum), the linear growth factor D_+ and finally through the critical density contrast δ_c (to a lesser degree).
By taking the limit of massive objects such as galaxy clusters, the exponential tail dominates the shape of the HMF. Therefore,

towards high halo masses, the HMF is exponentially sensitive to the choice of the cosmological parameters .

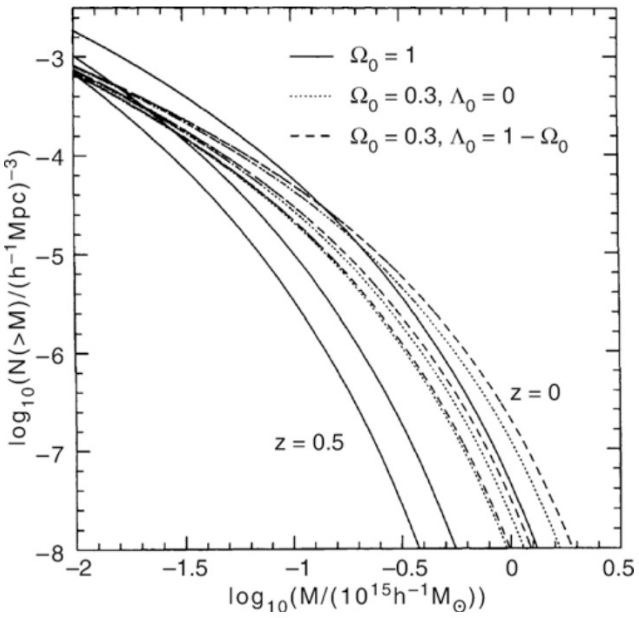

Figure 2.2: Illustration of the sensitivity of the HMF to cosmological models. The comoving number density of clusters per $\left(h^{-1}\mathrm{Mpc}\right)^3$ volume with masses larger than M shown as a function of M, for three different redshifts : $z = 0$ (upper curves), $z = 0.33$ and $z = 0.5$ (lower curves). The normalisation of the density fluctuation field has been chosen such that the halo number density at $z = 0$ reproduce the observed local number density of galaxy clusters ($M > 10^{14}\, h^{-1}\mathrm{M}_\odot$). Three cosmological models are studied : an Einstein-de Sitter model (solid curve), a low-density open model with $\Omega_{\mathrm{m},0} = 0.3$ and $\Omega_{\Lambda,0} = 0$ (dotted curves) and low-density flat model with $\Omega_{\mathrm{m},0} = 0.3$ and $\Omega_{\Lambda,0} = 0.7$ (dashed curves). – Credits : Eke *et al.* [19]

This is why counting clusters as a function of mass and at different redshifts is a powerful probe to constrain cosmological parameters [10]. As an example, we show in Figure 2.2 the predicted evolution of the cluster mass function by the PS model in different cosmological models. We can see that the shape of the halo mass function is sensitive to the cosmological model. Especially, we can see the dramatic evolution with redshift of the Einstein-de Sitter model where the abundance of clusters declines precipitously with redshift.

Therefore, galaxy clusters counts can provide strong constraints on the shape of the IMF hence our cosmology ! As long as clusters masses are accurately measured...

2.3 Galaxy clusters as Cosmological probes

Being the most massive and largest gravitationally bound objects in our Universe, galaxy clusters are of special value for cosmology. They have been and are still widely used to constrain our cosmology and are key laboratories to understand the co-evolution of dark matter and baryons.
In this section we will review cosmological results and contributions to fundamental physics that can be obtained from the observations of galaxy clusters (see Allen *et al.* [10] for a more

extensive review).

Historically, the use of galaxy clusters to study cosmology dates back to Zwicky's discovery of dark matter in the Coma cluster [20]. Brightest cluster galaxies (BCGs) were later used by Hoessel *et al.* [21] as standard candles to study the local Universe expansion. They derived a negative deceleration parameter implying an accelerated expansion consistent with present findings.
In the following decade, clusters were fond to be more spatially clustered than galaxies. The enhanced spatial clustering of galaxy clusters supported the model of Gaussian random initial conditions, expected from inflations [22].
In the early 1990s, a cosmological model with critical matter density was ruled out by the observed discrepancy of the local baryon fraction measurements of galaxy clusters with the primordial nucleosynthesis expectations [23–25].

As seen previously, counting galaxy clusters is a powerful way to constrain the normalisation of the initial power spectrum and also density parameters. They are especially useful at constraining σ_8 and Ω_m but also $D_+(a)$ and the equation of state for dark energy w_{DE}. Especially, X-ray studies in the following millennium studied the amplitude of the matter power spectrum and found a lower values than had been accepted previously [26–30]. This finding was later confirmed by CMB and cosmic shear measurements.

However, these studies draw attention to the importance of understanding the systematic effects associated with the use of quantities directly observable as mass proxies [31].

Besides cosmological constrains, galaxy cluster have been used to test fundamental physics such as the properties of dark matter, the neutrino mass, investigating dark energy and modified gravity models (see review of Allen *et al.* [10] for more details.).

For instance, observations of Markevitch *et al.* [32] of the merging Bullet cluster (or 1E 0657-558, shown in Figure 2.3) at $z = 0.29$ revealed the offsets between the dark matter component and the X-ray emission that allowed to put constraints on dark matter. Indeed, as clusters merge under the pull of gravity, their dark matter halos and respective X-ray-emitting gas can become separated temporarily. While the gas experiences ram pressure and is slowed, the dark matter halos pass through each other unperturbed by the impact (because it does not interact directly with itself or the gas except through gravity). Therefore, the dark separates from the

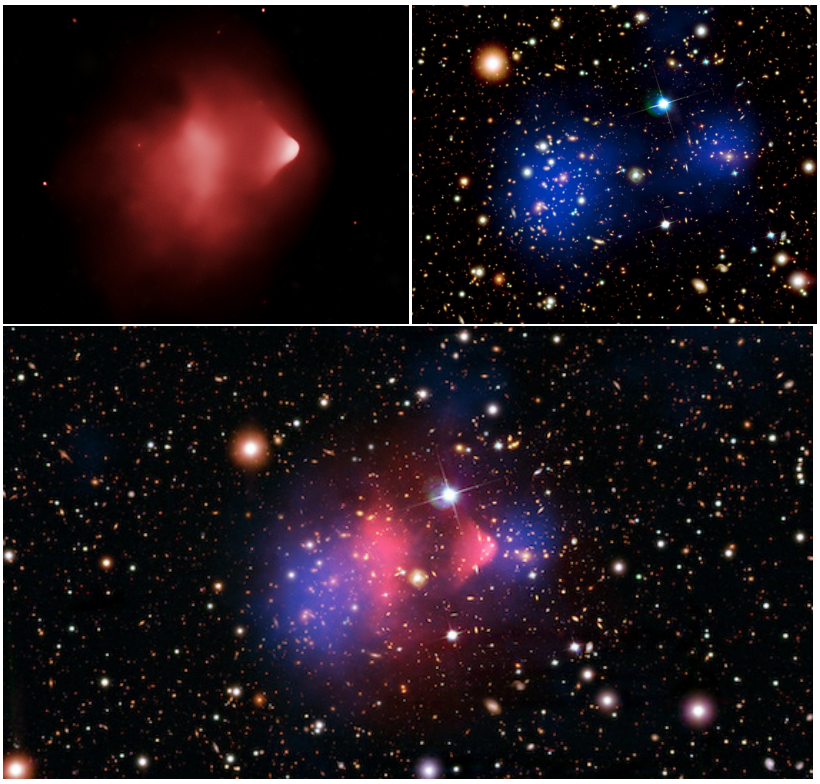

Figure 2.3: Under the pull of gravity, two clusters of galaxies have merged and the bullet-shaped clump on the right is the hot gas from one cluster, which passed through the hot gas from the other larger cluster during the collision. Most of the clusters' mass (which is mainly dark matter) is shown in blue and was determined using the weak lensing effect. Energetic X-rays (pink) are emitted by hot normal matter that has piled up where the two clusters of galaxies have collided. We can see that dark matter (blue) has mysteriously passed through the crash undisturbed – Credits : X-ray: NASA/CXC/CfA/M.Markevitch et al.; Optical: NASA/STScI; Magellan/U.Arizona/D.Clowe et al.; Lensing Map: NASA/STScI; ESO WFI; Magellan/U.Arizona/D.Clowe et al

normal matter.
The multi-wavelength observations of the Buller cluster allowed to derive limits on the velocity-independent dark matter self-interaction cross-section per unit mass of $\sigma/M < 5\,\mathrm{cm}^{-2}\,\mathrm{g}^{-1}$, which was later refined by Randall *et al.* [33] to $\sigma/M < 1.5\,\mathrm{cm}^{-2}\,\mathrm{g}^{-1}$. More similar merging clusters were later found which allows to study in a robust, statistical manner, the properties of dark matter in merging clusters.

2.4 Tensions

The Bullet cluster is well known for having a very high infall relative velocity [32]. In addition, another extreme cluster named El Gordo (or ACT-CL J0102-4915, at $z = 0.87$) is the most massive distant galaxy cluster [34]. Both of them are galaxy cluster encounters and their observations suggested that the formation of large structures took place earlier than expected in ΛCDM model.

On even larger scales of tens of Mpc, galaxy clusters are often part of a supercluster and their existence at high redshift also seems to pose problems for the ΛCDM model [35, 36]. In particular, Cucciati *et al.* [35] identified a proto-supercluster of mass $4.8 \times 10^{15}\mathrm{M}_{\odot}$ in formation at $z = 2.45$, which is consistent with a predicted mass function at $z = 1$.

If structure formation is enhanced compared to ΛCDM expectations, underdensities should also be more pronounced than expected. Actually, Keenan *et al.* [37] showed a strong evidence for a large local underdensity extending out to ∼ 300 Mpc in 6.04σ tension with ΛCDM [38][22] while El Gordo is at 6.16σ.

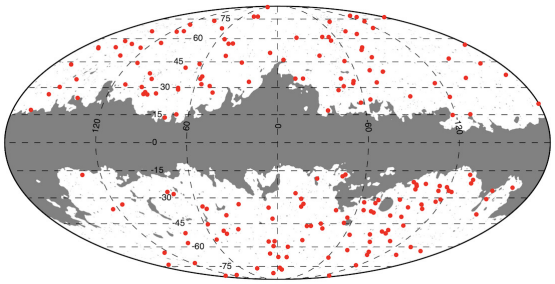

Figure 2.4: Distribution on the sky of the Planck sub-sample of galaxy clusters observed through the Sunyaev-Zel'dovich effect – Credits : Planck Collaboration *et al.* [41]

In 2013, the Planck team published its first catalogue and used a subsample of 189 clusters to probe the standard cosmological model [41, 42].
They showed that the preferred matter content, Ω_m and the amplitude density fluctuation of the power spectrum, σ_8, are different in the analyses of the CMB and SZ clusters (see the SZ cluster distribution in Figure 2.4) at more than 2 sigmas. As we can see on Figure 2.5, the predicted number counts expected from CMB measurement (shown by the dot-dashed green line) is higher than the counts of Planck SZ clusters shown in Figure 2.4. To fully reconcile the CMB model with SZ clusters, the mass of the SZ galaxy clusters derived from hydrostatic equilibrium should be 40% lower than the true cluster mass.
However, numerical simulations (e.g. [43–46]) and weak lensing measurements (e.g. [47, 48]) agree for a mass bias of 10-20%[23] .
Moreover, accounting for a different optical depth of reionisation, Salvati *et al.* [51] could only reduce the Planck tension to 1.5σ.

Investigations are still going on in order to explain such disagreements on the mass bias. Furthermore, such bias value of 38% to reconcile Planck CMB and SZ probes leads to a baryon fraction in clusters at odd with the universal value Eckert *et al.* [50].

This tension between high redshift and low redshift probes might be a sign for physics beyond ΛCDM. Nonetheless, accurate mass measurements in complete cosmological samples are crucial to use galaxy clusters as cosmological probes.
Disentangling the effects of cluster mismodelling from potential failure of the concordance cosmological model requires an in depth understanding of cluster physics.

22: The authors showed this large and deep void would cause the local expansion rate of the Universe to exceed the average by ∼ 11% which would nicely resolve the Hubble tension.
The Hubble tension emerged by the difficulty in reconciling the observed CMB anisotropies ([17, 39]) with multiple independent determinations of the local expansion rate ([40], and references therein)

23: see also Ettori *et al.* [49] and Eckert *et al.* [50] studies of the X-COP galaxy cluster sample using X-ray and SZ measurements which yielded a hydrostatic mass bias of 15%.

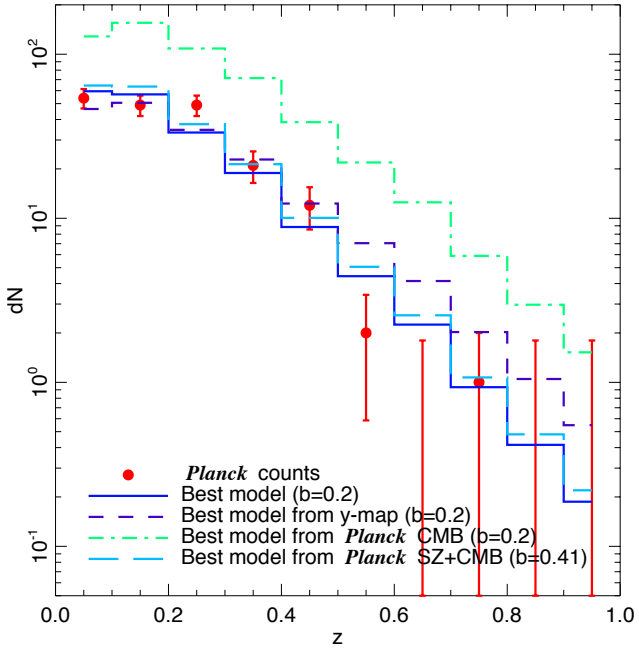

Figure 2.5: Distribution in redshift for the Planck cosmological sample of 189 clusters. The red dots shows the observed number counts compared to the Planck Collaboration *et al.* [41] best-fit model prediction shown by the solid dark blue line. The dashed purple and dot-dashed green histograms are the best-fit models from the Planck SZ power spectrum and Planck CMB power spectrum fits, respectively. The light blue long dashed histogram is the best fit CMB and SZ when an hydrostatic mass bias is left free to vary. – Credits : Planck Collaboration *et al.* [41]

Therefore, the combination of high-sensitivity multi-wavelength observations of clusters with high resolution numerical simulations including sophisticated physical models, should help to unveil the nature of the physical processes driving the evolution of galaxy clusters.

The physics of galaxy clusters and observed properties

3

We review, in this chapter, the multi-wavelength observational properties of galaxy clusters as well as the regularity of the cluster populations.

3.1 Observed properties of galaxy clusters

Clusters of galaxies are mainly composed of 85% of dark matter (not directly observable) while the remaining 15% is baryonic matter which manifests itself through different emission mechanisms from radio to X-ray wavelengths. In this chapter we will review the signatures of the different cluster components, their physical properties and respective origins.

Clusters of galaxies were first discovered as observed spatial concentrations of galaxies that determined its global appearance at optical wavelengths. But advances in X-ray astronomy lead to galaxy clusters being found to be very bright sources of X-ray radiation emitted by the hot intra cluster medium. This gas also leave imprints of the cosmic microwave background (CMB) spectrum as we will see later. Actually this filling gas contains ~ 5 times more baryons than stars seen in the galaxies [8]. But not all the stars are bound to individual galaxies, they are also distributed throughout the cluster forming an additional stellar component : the intra cluster light (ICL). The ICL can contribute up to 20% of the overall budget of stars [52]. In what follows, we focus on the wavelengths at which the signal from the galaxy clusters is used for assessing their masses.

3.1.1 Optical

In the optical window, the signal we get from galaxy clusters comes from the stars in cluster galaxies but also from the intra-cluster light to a lesser extend.

In rich galaxy clusters, we can find hundreds up to thousands of galaxies that have velocity dispersions about $\sigma_v \sim 700-1000\,\mathrm{km\,s^{-1}}$ [53, 54]. We can estimate the time that a galaxy needs to cross such cluster once with a typical size of $D \sim 1.5\,h^{-1}\mathrm{Mpc}$:

$$t_{\mathrm{cross}} \sim \frac{D}{\sigma_v} \sim 1.5\,h^{-1}\mathrm{Gyr}, \tag{3.1}$$

We see that such dynamical timescale is much shorter than the age of our universe, concluding that galaxy clusters are bound by gravity. If not, they would be dissolved on such timescales. As the result, the viral theorem can apply in such a closed system and allows to derive an estimate of the cluster dynamical mass :

$$M_{\rm dyn} = \frac{R_{\rm G}\langle v^2\rangle}{\rm G}, \tag{3.2}$$

where $\langle v^2\rangle$ is the cluster (mass-weighted) velocity dispersion and $R_{\rm G}$, the gravitational radius.[1] We obtain a characteristic mass of $\sim 10^{15}\mathrm{M}_\odot$ for rich clusters. This yields an average galaxy mass of $\sim 10^{13}\mathrm{M}_\odot$, which is very high compared to the total luminosity of cluster galaxies $L_{\rm tot} \sim 10^{12} - 10^{13}\,\mathrm{L}_\odot$. Indeed we get a mass-to-light ratio greater than 10 times the ratio of early type galaxies ![2]

1: computed from the member galaxies :

$$\langle v^2\rangle = \frac{1}{M}\sum_i m_i v_i^2,$$

$$R_{\rm G} = 2M^2\left[\sum_{i\neq j}\frac{m_i m_j}{r_{ij}}\right]^{-1}$$

2: Early type galaxies have a mass-to-light ratio of $M/L \leqslant 10$ [55]

In 1933, Fritz Zwicky concluded from such analyses of velocities of Coma cluster galaxies, that there is a large amount of unobserved *dunkle materie*[3] .

3: dark matter

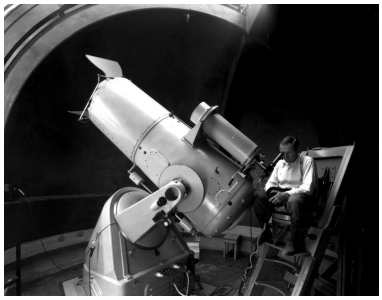

Figure 3.1: Fritz Zwicky at the Schmidt telescope at Palomar Observatory (∼1930s) – Credit: Palomar Observatory/Caltech

A few decades later, two independant groups discovered giant luminous arcs in 1986 [56, 57] (such as in the right panel of Figure 1.2) were later understood to originate from higher redshift galaxies [58]. Actually, these distorted and magnified images are produced by the differential light deflection caused by the cluster's deep potential well. An illustration of the gravitational lens effect is shown in Figure 3.2.

The simplest mass model for a galaxy cluster is the single isothermal sphere (SIS) lens model. This model allow to characterise a radius on which such distortion can occur called the Einstein radius, $\theta_{\rm E}$:

$$\theta_{\rm E} = 4\pi\frac{\sigma_v^2}{c^2}\frac{D_{ls}}{D_s}, \tag{3.3}$$

$$\sim 30''\left(\frac{M}{10^{14}\mathrm{M}_\odot}\right)^{1/2}\left(\frac{D}{1\,\mathrm{Gpc}}\right)^{-1/2}, \tag{3.4}$$

where D_s is the distance between the observer and the background source, D_l the distance between the observer and lens and D_{ls} is the distance separating the source and the lens. Finally, $D = D_l\,D_s/D_{ls}$ is the lensing efficiency distance.
The latter formula gives a typical size of cluster lensing corresponding to angular scales of the observed arcs. This size typically corresponds to the cluster cores.
We differentiate different lensing regimes from which the mass distribution encompassed within such radius can be reconstructed :[4]

4: There is also a third regime, called *microlensing*, well-known for the detection of exoplanets but less relevant for our work.

- *Strong lensing* : In this regime, pronounced arcs and multiple images of galaxies are visible. The lensing region is typically the core of a galaxy cluster as one can see on Figure 1.2.
- *Weak lensing* : Less spectacular, but more common, is the case of a subtle lensed signal of many more background galaxies, typically observed at larger angular separations from the cluster centre. While, it is possible to recover the lens mass out to large radii, it can only be measured statistically as the distortion is too weak to be identified from an individual galaxy image.

In the case of strong lensing, we can derive the projected mas within $\theta_{\rm E}$ as :[5]

$$M_{\rm SL} = \pi D_l^2 \theta_{\rm E}^2 \Sigma_{\rm cr}, \tag{3.6}$$

but the estimated mass only concerns the cluster central region.[6] This is why, the weak lensing effect can be effective to derive precise total mass measurements. In particular, with the advances of wide field-of-view cameras (e.g. Suprime-Cam and Hyper Suprime-Cam on the Subaru telescopes, MagaCam on the Canada-France-Hawaii Telescope), weak lensing analyses allowed to infer cluster masses out to the virial radius and to $z \sim 1$ in short observing times. Many projects has successfully measured accurately individual weak lensing masses of hundreds of galaxy clusters in the LoCuSS[7] , CCCP[8] , CLASH[9] and WtG[10] samples.

First examinations of the lensing signal, yielded masses which roughly agree with the dynamical mass derived using galaxy velocity dispersions. It confirmed that the total mass of clusters significantly exceeds the visible stellar mass of galaxies and of the intra cluster light.

3.1.2 X-rays

X-ray radiation from massive clusters of galaxies was first observed with the UHURU X-ray satellite launched in 1970 [64, 65]. Later, Einstein and ROSAT X-ray satellite detected X-ray emission for lower mass cluster and groups (see e.g. the review of Sarazin [66]).

Indeed, besides active galactic nuclei (AGNs), galaxy clusters are the brightest extra-galactic source of X-ray radiation.[11] Opposite to the AGN compact structure, cluster X-ray emission is extended on a megaparsec scale region with characteristic luminosity of $L_{\rm X} \sim 10^{43} - 10^{44}\,{\rm erg\,s^{-1}}$.

The observed spectral energy distribution is typical of thermal Bremsstrahlung (free-free) radiation from a collisionally ionised

5: with the critical surface mass density :

$$\Sigma_{\rm cr} = \frac{c^2}{4\pi G} \frac{D_s}{D_l\, D_{ls}}, \tag{3.5}$$

6: More detailed derivations can be found in the lecture notes of Narayan & Bartelmann [59]

7: Local Cluster Substructure Survey, [60]

8: Canadian Cluster Comparison Project [61]

9: Cluster Lensing and Supernova survey with Hubble [62]

10: Weighting the Giants [63]

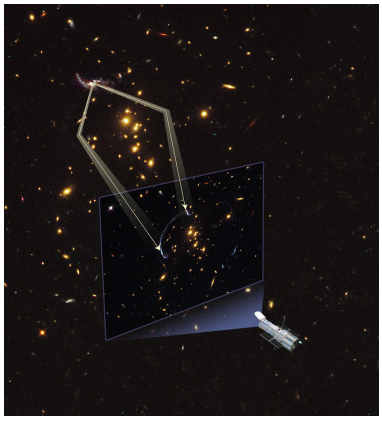

Figure 3.2: Illustration showing how a galaxy cluster distorts the light coming from a background galaxy. The grational influence of the cluster acts as a lens and we observe magnified wrapped images of the source in the plane of the sky. – Credit: NASA, ESA, A. Feild (STScI)

11: Away from the galactic dik, 85% of the detected X-ray sources are AGNs and the remaining 15% are galaxy clusters.

Figure 3.3: The "Cheshire Cat" group of galaxies (also known as SDSS J103842.59+484917.7). *Left :* The circular face and smile, seen in optical, arises from the gravitationally lensing of four faraway galaxies. The light is being distorted by the mass of galaxies forming the the two giant "eyes" and "nose". *Middle :* Chandra X-ray view of the left image. We see the X-ray emission of the hot filling gas between galaxies. *Right:* On the optical and X-ray composite image, we can see an AGN activity in the X-ray bright left "eye" galaxy. We see that each "eye" galaxy is the brightest member of its own group. These two galaxy groups are racing toward one another at over 134 km s^{-1} – Credits: X-ray: NASA/CXC/UA/Irwin *et al.* [67]; Optical: NASA/STScI

hot gas. Figure 3.4 shows such spectrum with a typical exponential decline around ~ 2 keV.

Due to the high ICM temperature ($\sim 10^7 - 10^8$ K or $1 - 10$ keV, as we usually talk in terms of particle energies), the presence of ionised metals in the ICM imprints characteristic emission lines in the spectrum.
This continuum emission is produced by deflection of the electron paths by protons and atomic nuclei of the ionised intra cluster gas. Resulting accelerated electrons will emit photons characteristic of their kinetic energy.

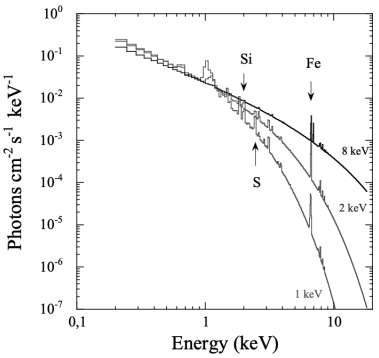

Figure 3.4: Simulated X-ray emission from a thin plasma with a solar abundance of 0.35 at different temperatures (1, 2 and 8 keV) – Credits : Adapted from Arnaud [68]

This Bremsstrahlung emissivity is given by :

$$\epsilon_\nu^{\mathrm{ff}} = g_{\mathrm{ff}}(T,\nu)\frac{32\pi Z^2 e^6 n_{\mathrm{e}} n_{\mathrm{i}}}{3\mathrm{m_e c}^3}\sqrt{\frac{2\pi}{3\mathrm{k_B}\,T\mathrm{m_e}}}\mathrm{e}^{-\mathrm{h}\nu/\mathrm{k_B}\,T}, \qquad (3.7)$$

where h is Planck's constant, n_{e} and n_{i} are respectively the number density of electrons an ions, $\mathrm{m_e}$ is the electron mass, e is the elementary charge and Ze the ion charge [69]. We also have the Gaunt factor $g_{\mathrm{ff}}(T,\nu)$, a quantum mechanical correction factor (of the order of 1).[12] We now see that the emitted spectrum is flat for $\mathrm{h}\nu \ll \mathrm{k_B}\,T$ and followed by an exponential decrease at $\mathrm{h} \geqslant \mathrm{k_B}\,T$. The number of photons emitted per unit of time in the energy range $[E, E + \mathrm{d}E]$ will be given by :

$$\mathrm{d}N = n_{\mathrm{e}}^2 \epsilon\, \mathrm{d}E\mathrm{d}V, \qquad (3.9)$$

with ϵ, the energy density. It is important to note that the intensity depends quadratically on the density since both Bremsstrahlung and the collisional excitation responsible for the metal line emissions results from two-body processes.

12: More precisely :

$$g_{\mathrm{ff}}(T,\nu) \sim \frac{3}{\sqrt{\pi}}\ln\left(\frac{9\mathrm{k_B}\,T}{4\mathrm{h}\nu}\right), \qquad (3.8)$$

One of the most prominent lines in massive galaxy cluster spectra is the Iron K line complex[13] around 6.7 keV. Other lines are observed such as the K lines of other elements ($Z > 8$, H and He-like ionisation states), as well as the L-shell complex of lower ionisation states of Iron. The line intensity rapidly decreases with increasing temperature, except for the cool clusters[14] .
From Equation 3.9, we can see that ICM spectra are steep. As the gas density rapidly decrease (but also the gas temperature), less and less photons are collected by X-ray telescopes at large distances from the custer centre. R_{500}[15] typically defines such a boundary of cluster X-ray observations. This is the reason why cluster observables are mostly defined within this radius.
We see that the position of the exponential cut-off of observed ICM spectra will provide a strong constrain on the ICM temperature.

13: iron nucleus with only a single electron

14: $\mathrm{k_B}\,T \leqslant 4\,\mathrm{keV}$

15: The mass within R_{500} enclosing 500 times the critical densty i.e. $M_{500} = 4/3\pi 500\rho_{\mathrm{c},z}R_{500}^3$

Actually, the ICM temperature in observations, is derived by fitting an observed spectrum by a single temperature thermal emission

model convolved with an instrument response (e.g. [70, 71]). However, the ICM is not strictly speaking isothermal and the inferred ICM temperature is the mean value along the line of sight in the considered region.

From X-ray observations, we can also infer the mean gas density. Indeed, at low energies ($k_B T \leqslant 2\,\mathrm{keV}$) the emissivity is not particularly sensitive to the temperature, but the flux normalisation is set by the n_e^2 dependance in Equation 3.9.
We can use X-ray images or azimuthally averaged surface brightness profiles extracted in this soft X-ray energy band[16] to reconstruct density and temperature radial profiles. As an exemple, we show in Figure 3.5 a radial profiles of the temperature for a galaxy cluster observed with XMM. However, care must be taken with X-ray images, projection effects and the presence of substructures may bias measurements of the ICM.

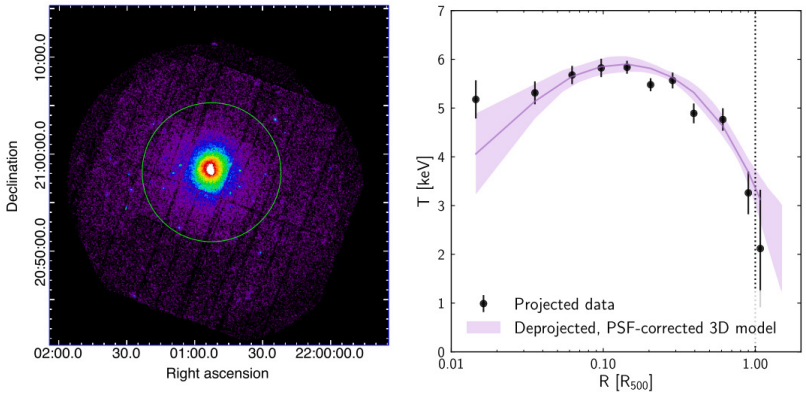

Figure 3.5: XMM-Newton image (*left*) and temperature radial profiles (*right*)of the newly-observed cluster PSZ2 G077.90-26.63, detected at a signal-to-noise ratio ∼ 178 in the $[0.2, 2]$ keV band in the $[0.15, 1]\,R_{500}$ region. The green circle indicates the R_{500} region in the left panel. In the right panel, black points show the raw temperature profile with best-fitting deconvolved, deprojected 3D model in purple and corresponding 1σ uncertainties – Credits : The CHEX-MATE Collaboration *et al.* [72]

16: Typically 0.5 – 2.0 keV or 0.1 – 2.4 keV energy bands

The launch of ESA's XMM-Newton and NASA's Chandra observatories both in 1999 enabled precise spatially resolved X-ray spectroscopy. The measurement of both the gas density and temperature profiles were possible by extracting spectra in concentric rings around the cluster center [73, 74].[17] But also, temperatures maps of the ICM [76, 77] as well as peculiar features in the X-ray emission (shocks, cold fronts , ...) [78–80].

17: Cluster centre is usually defined in X-ray studies as the X-ray emissivity peak in a given band, but there are other definitions (e.g. position of the brightest cluster galaxy). See the study of Yan *et al.* [75] for a detailed analysis of the different definitions and the bias induced by miscentering.

3.1.3 Sub-millimeter

Our Universe is permeated by the 2.75 K photons of the cosmic microwave background. Such a "cold" CMB photon interacts with electrons of the hot intra cluster gas through Compton scattering. This implies a mean energy transfer from the hot ICM electron to the CMB photon.[18] Thus, on average, the photon has an higher frequency after having traversed the ICM.
Sunyaev & Zeldovich [82–84] have formalised this inverse Compton

18: This is actually why it is called an inverse Compton scatering

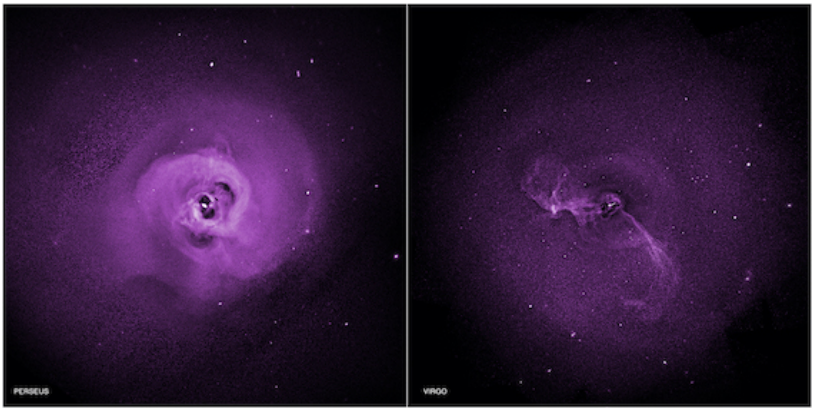

Figure 3.6: X-ray emission of Perseus cluster (*left*) and Virgo cluster (*right*). We can see the AGN activity pumping energy into the ICM driving turbulence in the gas. The ripple-like structures in Perseus show evidence for turbulence that could support ICM heating. We also note the presence of X-ray cavities created by the jets in the hot gas – Credits : NASA/CXC/Stanford/Zhuravleva *et al.* [81]

process.

As the result, compared to the Planck CMB spectrum, there is a reduced number of low energy photons which are shifted to higher energies. We can see from the spectrum in Figure 3.7 a global shift to higher frequencies which, on the other hand, leaves the intensity at 217 GHz unchanged. We can see clearly in Figure 3.8 the frequency dependance of the Sunyaev-Zel'dovich (SZ) effect : Below 217 GHz we can see a decrement in the CMB intensity, while after this frequency the intensity is higher than of the CMB.

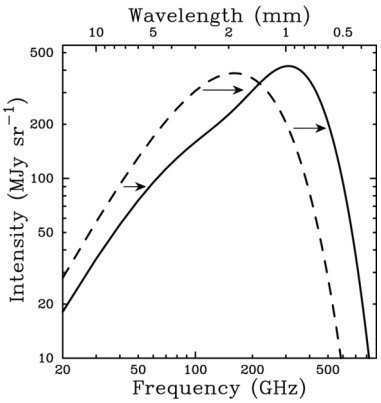

Figure 3.7: The spectral distortion of the CMB spectrum caused the SZ effect. The dashed line show the unperturbed CMB spectrum while the solid line show the spectrum distorted after the radiation has passed through a the ICM of fictional cluster 1000 times more massive than a typical massive galaxy cluster (The magnitude has been exaggerated for clarity) – Credits: Carlstrom *et al.* [85]

Therefore, galaxy clusters appears as holes in the CMB sky at frequency lower than ~ 220 Ghz. The main asset of the SZ effect is its redshift independence. Indeed, CMB photons are continuously redshifted from the last-scattering surface as our Universe expands. And irrespective of when the inverse Compton scatter event happened, the CMB photon is still undergoing continuous redshifting. Thus, the SZ signal is only limited by the angular resolution and the sensitivity of observations. Thus, it constitutes a unique probe to the high redshift Universe.

The specific intensity variation, with respect to the CMB specific intensity I_0, induced by the ICM is :[19]

$$\frac{\Delta I_{SZ}^{RJ}}{I_0^{RJ}} = -2y, \tag{3.10}$$

where we have the Compton-y parameter :

$$y = \int \frac{\sigma_T}{m_e c^2} n_e k_B T_e dl \propto \int P_e dl, \tag{3.11}$$

with the Thomson cross section $\sigma_T = \frac{8\pi}{3}\left(\frac{e^2}{m_e c^2}\right)^2$.

19: we use the fact that in the Rayleigh-Jeans limit ($\nu \leqslant 200$ GHz) the frequency dependance of the SZ effect tends to -2 [85]

We see that the Compton-y parameter is directly proportional to the ICM pressure integrated along the line of sight through the cluster.

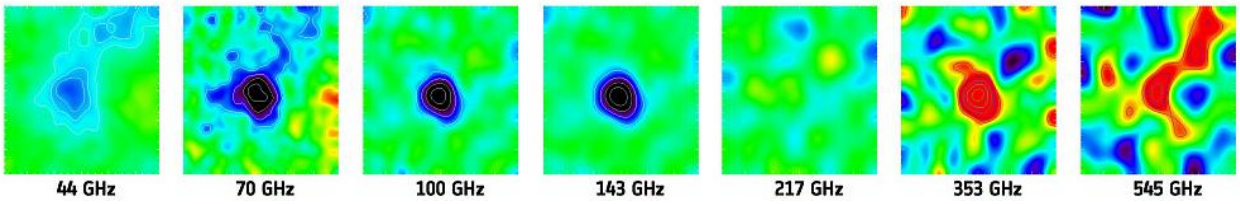

Figure 3.8: Series of 2 degree images showing Abell 2319 galaxy cluster in seven different frequency channels of the Planck telescope. We see the characteristic frequency dependance of the SZ effect : a negative signal (blue) of the order of ~ 1 mK below 217 GHz and a positive signal (red) – Credits: ESA/ LFI & HFI Consortia

It is important to notice that SZ and X-ray observations both probe the thermal pressure of the ICM along the line of sight, but with a different sensitivity on the ICM. The X-ray luminosity depends quadratically on the density while the SZ decrement only linearly. Thus, they offer very complementary probes of the intra-cluster gas. From the comparison of X-ray and SZ observations, we can infer thus informations on the gas clumpiness and the ICM inner structure. Indeed, if the ICM is completely smooth we should have $\langle n_e^2 \rangle = \langle n_e \rangle^2$.

The total SZ signal integration of y across the cluster solid angle, $d\Omega = dr^2/D_A$, gives the integrated SZ-parameter Y_{SZ} :

$$\int y d\Omega = \frac{1}{D_A^2} \int y \, dr^2 \propto \frac{1}{D_A^2} \int n_e T_e dV = \frac{Y_{SZ}}{D_A^2} \tag{3.12}$$

being the temperature-weighted mass divided by the square of the angular diameter distance D_A. The product of the gas mass and temperature can also be determined from X-ray observations so that independent measures of Y can be determined : $Y_X = M_{gas,X} T_{gas,X}$ and $Y_{SZ} = M_{gas,SZ} T_{gas,SZ}$.

In addition to this thermal SZ (tSZ) effect, another kinetic SZ (kSZ) effect arise [86]. While not being studied in this work, we just note that there is an additional distortion of the CMB spectrum caused by the Doppler effect of the cluster bulk velocity on the scattered CMB photons. As we can see on Figure 3.10, the distortion on the CMB spectrum induced by the tSZ is much larger than the kSZ. It was detected for the first time by Hand *et al.* [87] using microwave sky maps made by the Atacama Cosmology Telescope to measure the relative velocity between two galaxy clusters.

At high redshifts, the angular diameter distance is fairly flat. Moreover, as the universal matter density increases as $(1 + z)$, a cluster of a given mass will be denser at high redshifts, hence hotter. Therefore, with little dependance on redshift, SZ surveys expect to detect all clusters above some mass. Such SZ surveys are called "mass-limited".

On the other hand, X-ray surveys suffer from strong flux dimming proportional to the distance squared. X-ray observations will therefore pick mainly X-ray bright clusters. Hence, X-ray survey are "flux-limited".

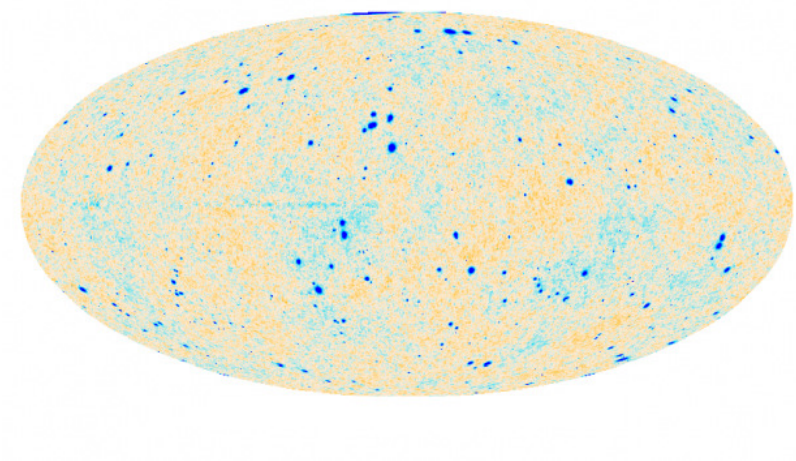

Figure 3.9: Thanks to the Sunyaev-Zel'dovich effect, galaxy clusters appear as holes in the CMB sky. From this Planck Full-sky map, we can see the SZ galaxy clusters superimposed to the CMB map. – Credits : M. Douspis & N. Aghanim

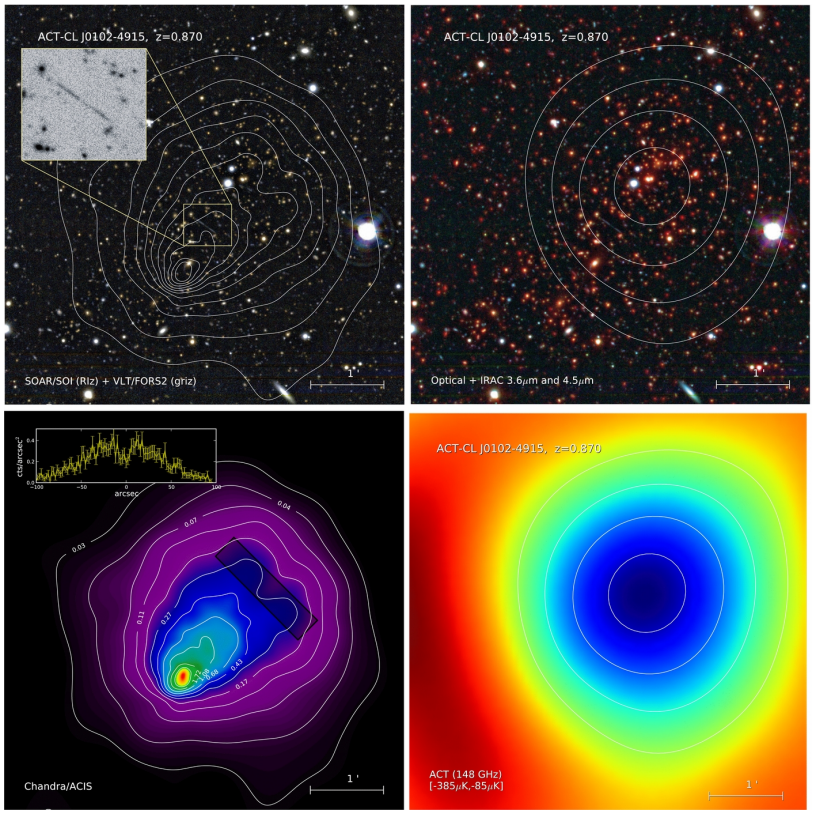

Figure 3.11: An example of multi-wavelength data set for El Gordo cluster discussed in Section 2.4, with all panels showing the same sky region. *Upper left* : Composite optical image with X-ray surface brightness contours overplotted in white. *Upper right* : Composite optical and infra-red imaging with contours correspond to the SZ signal overplotted in white. *Bottom left* : False color image of the X-ray emission with the same set of log-spaced contours as in the panel above. *Bottom right* : SZ intensity map. – Credits : Menanteau *et al.* [34]

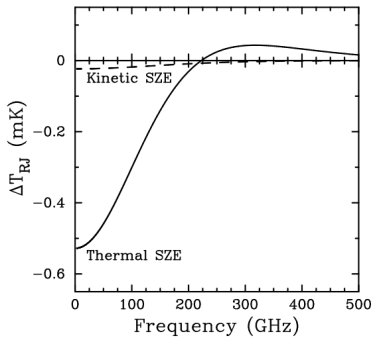

Figure 3.10: The Rayleigh-Jeans brightness temperature changes as a function of the CMB frequencies for the thermal and kinetic SZ effects respectively shown by the thick and dashed lines. – Credits : Carlstrom *et al.* [85]

3.1.4 Radio

Galaxy clusters are often found to host AGNs emitting radio synchrotron radiation (radio galaxies). Deep radio observations also revealed extended regions of radio emission with sizes ranging from few kpc up to ~ 1 Mpc as we can see in the Abell 2744 cluster shown in Figure 3.12. On this figure, we can easily spot some radio galaxies such as one in the east with its two prominent radio lobes as well as in the south-west. Actually, various radio emission of different sizes and shapes cannot be directly linked to any cluster

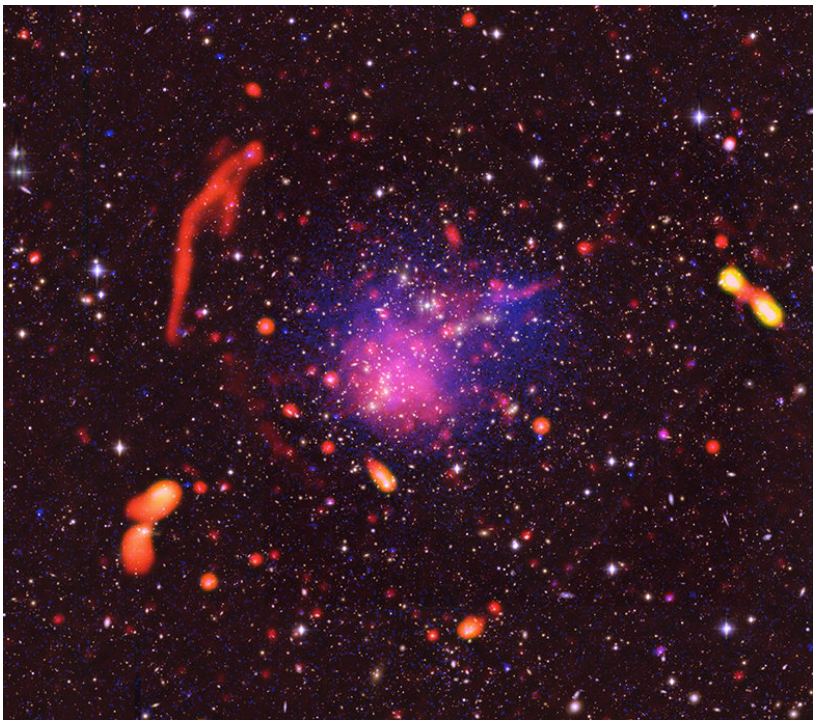

Figure 3.12: A composite image of the galaxy cluster Abell 2744. Cluster galaxies observe in optical by the SUBARU telescope. The X-ray emission of the hot ICM observed by Chandra glows in blue. In red, we see the radio emission observed by the Very Large Array (VLA). We see a multitude of radio emission with different morphologies and sizes that extend on very large distances from the center centre. This radio emission, tracing magnetic fields and cosmic rays, indicates for non thermal energetic processes in the ICM able to accelerate such particles. – Credits : Pearce *et al.* [89]

member, but rather to the synchrotron radiation of intra-cluster relativistic GeV cosmic ray (CR) electrons (Lorentz factor $\gamma > 10^3$) in weak magnetic fields ($0.1 - 10\,\mu$G) [88].

Besides playing an important role in the acceleration of particles, the ICM magnetic fields inhibit transport processes such as thermal conduction, gas mixing and the CR diffusion (see observational reviews of Ferrari *et al.* [88], Feretti *et al.* [90], van Weeren *et al.* [91], and Brunetti & Jones [92] for a more theoretical aspects).
Diffuse radio emission indicates the presence of non-thermal astrophysical processes that affect the cluster dynamical state and its evolution.

CRs in the ICM can be accelerated via different mechanisms [92] :

- *First order Fermi acceleration* (Fermi-I)[20] : Due to the presence of magnetic inhomogeneities, particles scatter in the shock down and upstream regions and gain energy at each crossing.

- *Second order Fermi acceleration* (Fermi-II): Particles randomly scatter in magnetic inhomogeneities such as in MHD turbulence. This process is rather inefficient due to its stochastic nature.

- *Adiabatic compression*: A population of (old) CRs can regain energy from a shock induced adiabatic compression.

20: this process is also known as diffuse shock acceleration (DSA)

- *Secondary models* : CR can also be produced as secondary particles. For instance, the collision of CR protons with thermal ions of the ICM will produce CR electrons.[21]

21: Due to the mass difference, CR protons have a very long lifetime compared to CR electrons. Hence once they are accelerated at shocks (Fermi-I), AGN or stellar feedback, protons will accumulate in the ICM.

The population of cosmic rays in the ICM is commonly assumed to follow a power law energy distribution :

$$n(E)\,\mathrm{d}E \propto E^{-(1-2\alpha)}\mathrm{d}E \tag{3.13}$$

where α is the spectral index[22] . The study of the radio spectral shape allows to constrain acceleration mechanisms and energy losses in the ICM. Indeed, the more efficient the acceleration mechanism is, the more relativistic particles are produced, the flatter the spectrum is at high energies. In contrast, as the CR population declines due to energy losses the spectrum will steepen beyond a break frequency.

22: as thhe radio spectrum is $F_\nu \propto \nu^\alpha$

Therefore studying the distribution of the spectral index in radio emission allows to pinpoint sources of CR acceleration in the ICM, shedding light on non-thermal processes in the ICM.

Radio sources come in all shapes and sizes but can be classified in three broad classes [88] :

- *Radio halos* (including *giant radio halos* and *mini-halos*) are not localised but rather diffuse sources that roughly trace the baryonic mass distribution in the ICM. This "global" emission is not identified with a specific event (e.g. shocks or AGN) but should rather trace MHD turbulence (Fermi-II) or a population of secondary electrons.

- *Cluster radio shocks* (or *radio relics*[23]) are, in opposition to the first class, localised in a cluster region were a shock wave is present or recently passed (Fermi-I). Hence, the majority of these sources are found at the cluster periphery and are expected to show a high degree of polarization.

- *Radio phoenix*, *revived AGN fossil plasma source*, and *Gently re-energized tails*[24] (GReETs) define a third class of re-energized AGN radio emission. The nature of this sources is not the radio galaxy itself but intra cluster processes not clearly identified yet.

Figure 3.13: The bent-jet radio galaxy NGC 1265 infalling the Perseus cluster. The radio galaxy also appears in the top right of Figure 3.14 – Credits: M. Gendron-Marsolais et al.; S. Dagnello, NRAO/AUI/NSF; Sloan Digital Sky Survey

23: as well as large radio relics, Gischt, and double relics

24: Re-energized tails of radio galaxies

Properties of the magnetic fields inhibiting this radio emission can be estimated thanks to the Faraday rotation analysis of radio galaxies located either in the cluster or in the background. Indeed,

the measured polarisation angle of the radio source is altered from its intrinsic polarisation angle χ_0 by the presence of magnetic fields along the line of sight. The observed polarisation angle at a wavelength λ is :[25]

25: Ferrari *et al.* [88]

$$\chi(\lambda) = \chi_0 + \lambda^2 \times RM, \tag{3.14}$$

where the rotation measure (RM) is related to the electron number density and the magnetic fields along the line of sight ($B_{\parallel}$) :

$$RM = \frac{e^3}{2\pi m_e c^4} \int_0^L n_e \, B_{\parallel} dl. \tag{3.15}$$

Multi-wavelength radio observations of background or cluster radio galaxies can therefore allow to measure $B_{\parallel}$, if the electron number density n_e is known from e.g. X-ray observations.
Analyses of the rotation measure of individual radio sources in several clusters yield typical values of $1-10$ μG for the intra-cluster magnetic fields [93]. We will discuss in more details possible origins and amplification mechanisms of these intra-cluster fields in Chapter 7.
We also note a more sophisticated technique, called Faraday tomography, which allows to reconstruct the distribution of magnetic fields in 3D by mapping the polarised intensity at different wavelengths [94, 95].
To conclude, radio observations allow to put stringent constrains

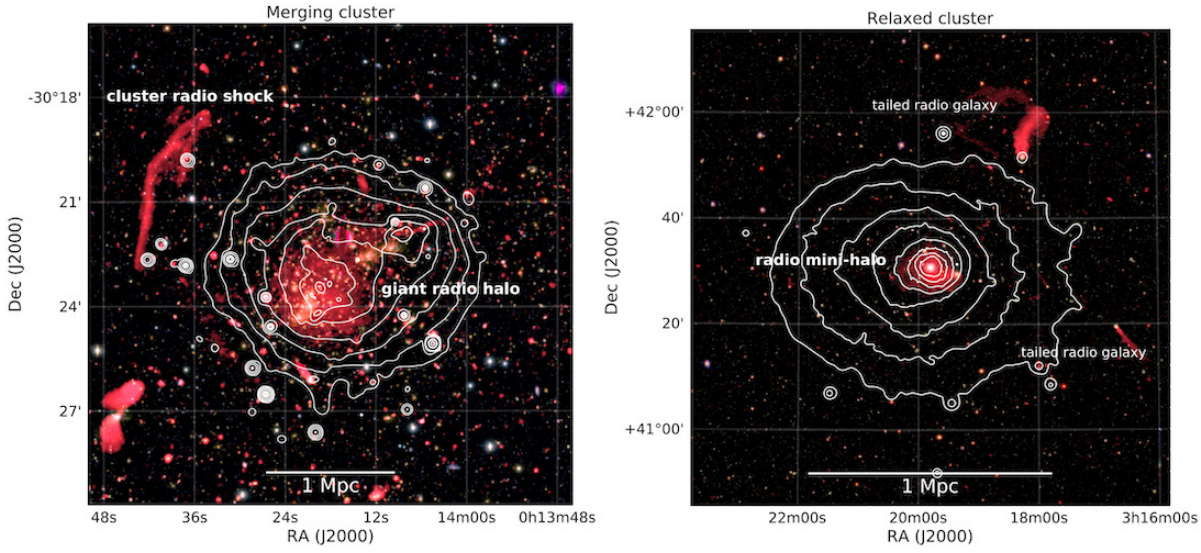

Figure 3.14: Radio sources shown in red of Abell 2744 (*left*, see also Figure 3.12) and Perseus (*right*) galaxy clusters. X-ray contours are shown in white. We see a giant halo in the centre of ther merging cluster Abell 2744 as well as a cluster radio shock on the upper left. On the other hand, the relaxed cool-core of Perseus host a mini halo with two tailed radio galaxies on the right– Credits: van Weeren *et al.* [91]

on the evolution of magnetic fields and astrophysical acceleration mechanisms in large scale structures.

3.2 Regularity vs Complexity

From the morphology of their X-ray emission, we observe regular and irregular clusters. Regular clusters will show a smooth X-ray surface brightness distribution that usually shares the same center (defined as the peak of the X-ray emission) as in optical (usually definied as the brightest cluster galaxy (BCG)). In contrast, several X-ray maxima can coexist in irregular clusters, centered on different galaxy subgroup (such as the Bullet cluster shown in Figure 3.15).

Figure 3.15: Panels of colliding galaxy clusters such as the Bullet cluster shown in Figure 2.3. The pink light shows the X-ray emission and the mass distribution is shown in blue – Credits : X-ray: NASA/CXC/EPFL/D.Harvey & NASA/CXC/Durham Univ/R.Massey; Optical and Lensing Map: NASA/ESA/D. Harvey and R. Massey

Overall, the intra-cluster medium of galaxy clusters show a high degree of similarity in a large range of size and mass (e.g. [96–98]). For instance, a good illustration of this regularity is provided by the ICM pressure profiles. We show in Figure 3.16 the study of Arnaud *et al.* [74] of the REXCESS cluster sample (with clusters mass $10^{14} < M_{500} \,/\, \mathrm{M}_{\odot} < 10^{15}$). The ICM pressure profiles, once rescaled to the values of radius and pressure at R_{500}, show a regular behaviour close to self-similarity. Indeed, a perfect self similar behaviour would correspond to a single line in the left panel plot of Figure 3.16 for all cluster masses.
We will review in Chapter 11, the self-similar model for galaxy clusters, but for now, we can state that galaxy clusters are expected to be self-similar as they are mainly driven by gravity[26] . They were able to derive an universal pressure profile that is confirmed by both observations and simulations (e.g. [70, 99]).

However, we can see that in the core region (i.e. $< 0.1 - 0.2\, R_{500}$) the pressures profiles in the left panel of Figure 3.16 shows the largest scatter from the universal profile shown in green. Indeed, clusters have a variety of behaviors in central regions, depending on the presence of non-gravitational processes such as an AGN activity, merger-induced residual gas motions, or the presence and prominence of a cool core.
Steep pressure profiles (i.e. above the green line) corresponds to cool-core clusters while flatter profiles are observed for disturbed clusters.

Cool-cores appear in the center of many relaxed clusters.
Indeed, the gas is observed to have a very short radiative cooling time, much shorted than the Hubble time. As the result, a cooling flow can develop in the absence of heating source, leading to the formation of a very cool core [100–103]. X-ray observations showed that temperatures drop in some cool cores but with much less gas than what would be expected from their radiative cooling time

26: Since gravity has no preferred scale, the properties of galaxy clusters are expected to vary in a self-similar way. A small galaxy cluster ought to resemble a scaled-down version of a large cluster, like cosmic nesting dolls.

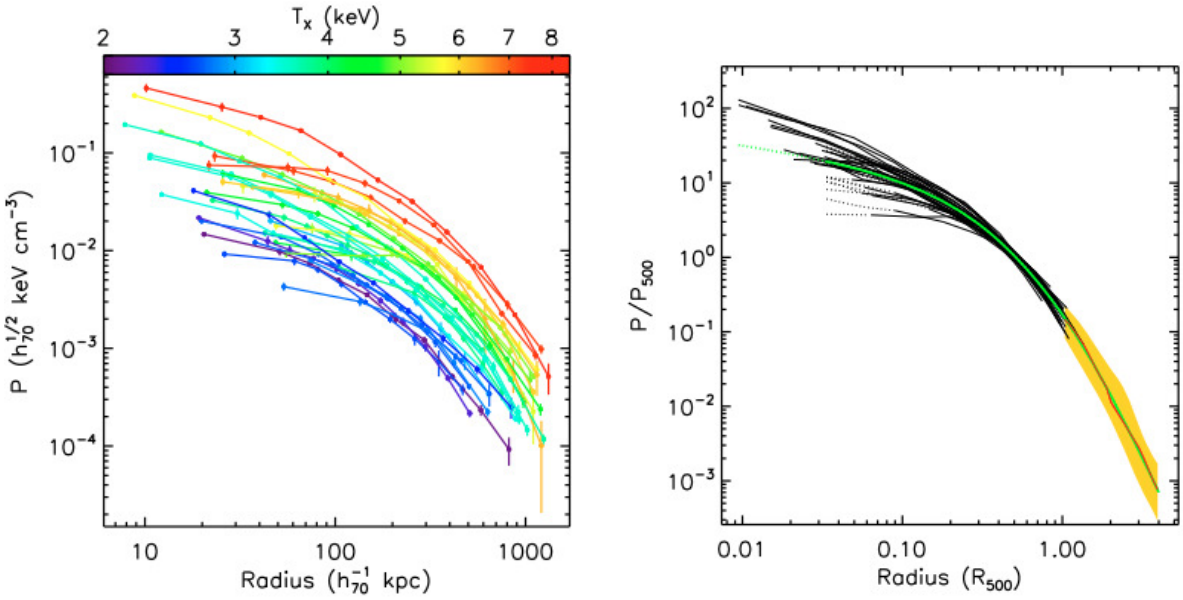

Figure 3.16: *Left* : The pressure profiles of the REXCESS galaxy cluster sample color coded according to the cluster spectroscopic temperature. *Right* : The same profiles rescaled by the pressure and radius at R_{500} are shown in black (the dotted lines shows the extrapolated pressure - see details in [74]). The universal pressure profile of Arnaud *et al.* [74] is shown by the green line, fitted from the radial REXCESS profile in the $[0.03, 1]R_{500}$ range and ,above R_{500}, with average simulation profiles shown in red (the dispersion around this average simulation profile is shown in yellow). We can see regularity above $0.2R_{500}$.

[104–106]. Thus, there must be some heating source to balances the cooling losses...

The main sources of energy input into the ICM was identified to be the radio galaxies in BCGs. Indeed numerous observations showed that X-ray cavities such as in Figure 3.17 coincided with the radio lobes of the central AGN. Actually, the radio plasma has displaced the denser X-ray emitting gas. These low density bubbles buoyantly rise in the ICM and expand to redistribute energy in their path.

The buoyantly rising bubbles inject non-thermal energy in the ICM. Moreover, merger events can also inject non-thermal energy in the ICM by the induced sloshing as illustrated in Figure 3.18.

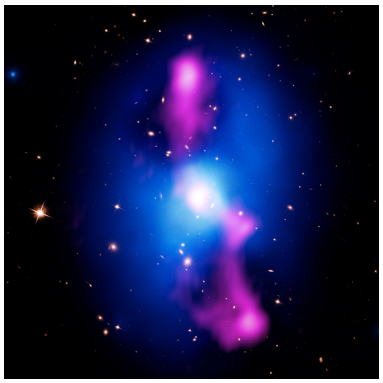

Figure 3.17: Composite image of the galaxy cluster MS 0735.6 +7421. The bright BCG and the cluster galaxies are visible in optical. The X-ray emission of the hot ICM is shown in blue while the radio jets, tracing cosmic rays and magnetic fields are shown in red. We clearly see that cavities in the X-ray emission beautifully coincide with the radio jets injecting kinetic energy to the ICM – Credits : X-ray: NASA/CXC/Univ. Waterloo/B.McNamara; Optical: NASA/ESA/STScI/Univ. Waterloo/B.McNamara; Radio: NRAO/Ohio Univ./L.Birzan et al.

To sum-up, we can distinct roughly three different radial regimes in the intra-cluster medium [107] :

- $R/R_{500} \lesssim 0.2$: Clusters cores, where large deviations from self similar scaling are observed. The scatter in cluster cores is mainly driven by the processes related to merger activity, or radiative gas cooling and AGN feedback for instance.

- $0.2 \gtrsim R/R_{500} \gtrsim 1$: Intermediate radii, which show least scatter and a with scaling with mass close to the expected self-similar scaling. Actually, this is why we can define integrated quantities over this radial range because it is not very sensitive to astrophysical processes. However, the observed

small scatter at intermediate radii is a non-trivial fact given that clusters of the same mass can be at a different stages of their dynamical evolution and can have very different assembly histories.

- $R > R_{500}$: Cluster outskirts, where the scatter increases with radius. Indeed, at these radii, clusters are dynamically younger and characterised by recent mergers with a clumpier ICM. Moreover, the offsets can also attributed to the presence of non-thermal sources such as CR pressure for instance. However, observing the outskirt region requires high sensitivity SZ and X-ray observations.

Figure 3.18: The sloshing hot gas in the galaxy cluster Abell 2052. An off-center collision produced the large spiral structure and sets the sloshing in motion when a small cluster smashed into the larger central one. The X-ray emission is shown in blue on top of the optical imaging.
Such gas sloshing can push the cold dense gas in the centre farther away to prevent further gas cooling in the core. – Credits : X-ray: NASA/CXC/BU/E.Blanton; Optical: ESO/VLT

Sophisticated numerical simulations can be used to follow the formation and evolution of galaxy clusters. They can be used to probe potential biases and the origin of scatter in observed ICM profiles and integrated quantities.
However, while there has been much recent progress on the realism of statistical samples of galaxies in cosmological simulations [108–110], reproducing a realistic structure of the intra-cluster medium especially the entropy profiles or distinct cool-core and non-cool core clusters is somewhat challenging (e.g. [111–113]).
AGN feedback have been argued to provide enough heating to balanced the gas overcooling in simulations. However, recent studies do not support this picture indicating for improvement of AGN modelling in simulation and/or the addition of more physical processes (thermal conduction, cosmic rays, ..) [114]
With the use of numerical simulations, understanding the interplay of astrophysical processes and their impact on the properties of galaxy clusters (at variance with cosmological formation histories) is what motivates this work.

Hence, before delving into the details of our simulation results, we will introduce in the next two chapters the technicals aspects of numerical simulations needed for a better understanding of what will follow.

Numerical methods 4

In this chapter, we will set the basis for understanding numerical methods used in cosmological simulations. We will review the various models that such simulations employ for galaxy formation processes. We will discuss the limitations as well as key results of galaxy formation simulations.

4.1 Cosmological framework

4.1.1 Cosmological model

Our universe is found to be spatially flat where dark matter and dark energy make up 95% of its energy budget. The former constitutes the backbone of formation of cosmic structures whereas the latter is responsible for the accelerated expansion of our Universe (represented by a constant Λ in Einstein's field equations). Dark matter is assumed to be cold, collisionless with negligible random motions when decoupled from other matter. The remaining 5% is the ordinary matter, which is commonly referred to baryons (gas and stars).
This picture of our Universe is captured in a general framework provided by the so-called Λ Cold Dark Matter (ΛCDM) model.

This simple cosmological model provides a reasonably good account for the observed properties of our Universe (e.g. CMB, distribution of galaxies and the large scale structures, the accelerated expansion). It can be parametrized by 6 independent parameters and the specific set of six parameters used to define the cosmological model is open to choice. Among, many other choice we can have the following set :

- The scalar spectral index, n_s
- The power spectrum fluctuation amplitude at 8 h^{-1}Mpc, σ_8
- The Hubble constant, H_0
- The dark energy density parameter, Ω_Λ
- The matter density parameter, Ω_m
- The baryon density parameter, Ω_c

These parameters are constrained by measurements of the CMB combined with the abundance of clusters (as discussed in Section 2.3), galaxy clustering and the distance-redshift relation from type

Ia supernovae for instance.

This ΛCDM model defines the framework in which our cosmological simulations of galaxy formation will be carried out.

4.1.2 Initial conditions

A key point in any numerical effort is to have justified and robust initial conditions. Supported by observations of the CMB, the large scale galaxy distribution but also predicted by many models of inflation and a Gaussian random field of initial density fluctuations appears as a good choice for cosmological initial conditions (ICs). Such a field is totally described by its matter power spectrum $P(k)$ which depends on the cosmological parameters and nature of dark matter.
This field has to be specified at an initial time and the starting redshift of the simulation needs to be high enough such that the perturbations are in the linear regime (i.e. $\delta \ll 1$) and in the matter dominated area. [1]
The Gaussian random field of density fluctuation can be generated in Fourrier space, such as :

1: Typically at $z \sim 100$, but see also Michaux *et al.* [115].

$$\hat{\delta}(\mathbf{k}) = A\, k^{n_s/2}\, T(k)\, \hat{G}(\mathbf{k}), \tag{4.1}$$

where A is a constant that sets the overall normalisation, $T(k)$ is the transfer function and $\hat{G}(\mathbf{k})$ is an uncorrelated ("white") Gaussian field.
The transfer function can be obtained either with numerical codes such as Camb [116] or Class [117], or by fitting formulae such as the the BBKS [118] or the Eisenstein & Hu [119]

Then particles obeying constrains of such initial density field have to be sampled in the simulation box. We can use the Lagrangian perturbation theory to compute the particle displacements and velocities from an initial cartesian lattice (where initial unperturbed positions are called the Lagrangian coordinates) to get the particle (Eulerian) positions ($\mathbf{x}$) and velocities ($\dot{\mathbf{x}}$) at the starting redshift z. In short, we have the initial positions and velocities :

$$\mathbf{x} = \mathbf{q} + D_+(t)\mathbf{\Psi}(\mathbf{q}), \tag{4.2}$$

$$a(t)\,\dot{\mathbf{x}} = a(t)\frac{\mathrm{d}D_+(t)}{\mathrm{d}t}\,\mathbf{\Psi}(\mathbf{q}), \tag{4.3}$$

Where $D_+(t)$ is the linear growth factor, a the scale factor related to the the starting redshift z as $z = 1/a - 1$ and $\mathbf{\Psi}$ is the curl-free displacement field computed by solving $\boldsymbol{\nabla} \cdot \mathbf{\Psi} = -\delta/D(t)$. This procedure of evolving particles can be extended to higher order in

Lagrangian perturbation theory.

Dark matter particles and baryons can be set in this way. In addition, baryon temperatures is often roughly initialised to the redshift-dependant CMB temperature.

There are two main type of initialisation : either a uniform and periodic sampling or zoom ICs.
Zoom ICs are especially suited for galaxy cluster simulation, as large-scale tidal forces are considered while studying an individual object at low computational cost. It consists of a high resolution region of interest consistently embedded in a low resolution background realization of the density field. This technique can be also applied on several levels of refinements to improve even further the dynamical range.
In this thesis we use such technique with the Music code from Hahn & Abel [120][2] . It allows us to initialise our simulation on many resolution levels as illustrated in Figure 4.1

2: Music is publicly available here

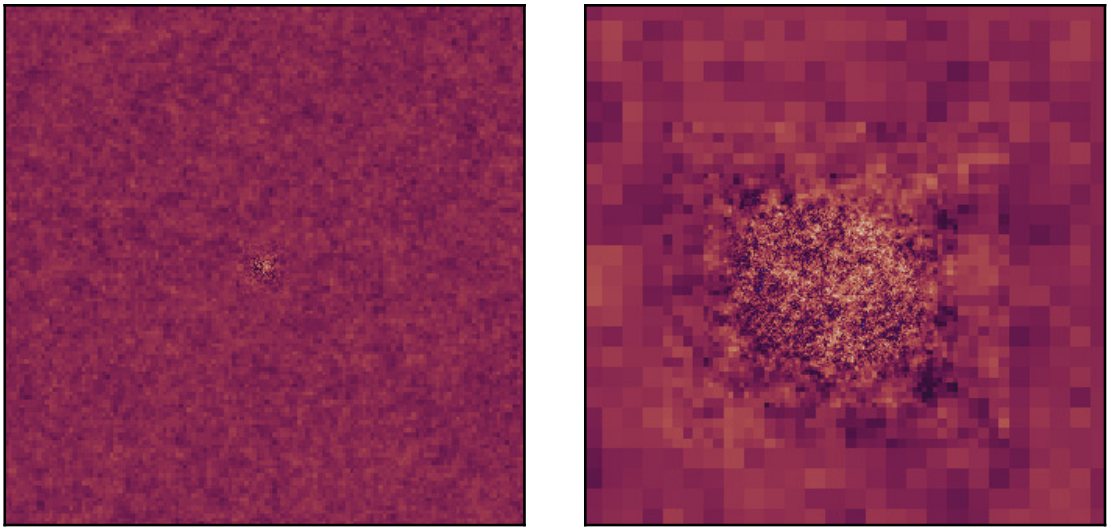

Figure 4.1: Slices of the initial density field of a simulation using the zoom technique we realised for the work presented in this thesis. *Left* panel shows a slice through the full box of size 1 h^{-1}Gpc comoving at $z = 39$ and the *right* panel shows only the central region with a size of 100 h^{-1}Mpc.

4.2 Modelling dark matter

Dark matter can be described by a collisionless fluid which is characterised by its distribution function $f(\mathbf{r}, \mathbf{v}, t)$. Its dynamical evolution is given by the collisionless Boltzmann equation that states the conservation of the local phase-space density[3] :

3: This is Liouville's theorem.

$$\frac{\mathrm{d}f}{\mathrm{d}t} = \frac{\partial f}{\partial t} + \mathbf{v}\frac{\partial f}{\partial \mathbf{r}} - \frac{\partial \mathbf{\Phi}}{\partial \mathbf{r}}\frac{\partial f}{\partial \mathbf{v}} = 0, \tag{4.4}$$

under the influence of the gravitational potential $\mathbf{\Phi}$ given by the Poisson equation :

$$\nabla^2 \mathbf{\Phi} = 4\pi \mathrm{G} \int f \mathrm{d}\mathbf{v}. \tag{4.5}$$

This pair of equations has to be solved in an expanding universe describe by Friedmann's Equation 2.8 and Equation 2.9. Due to its high dimensionality, solving the collisionless Boltzmann equation is an arduous task. Numerical techniques have been developed over the last decades to efficiently solve this issue.

The most common method is the N-body method that discretises the phase space density in N phase-space points $(\mathbf{r_i}, \mathbf{r_j})$ of mass m_i with $i = 1, ..., N$ and solves the collisionless Boltzmann equation by the method of characteristics. It can be interpreted as a Monte Carlo sampling where the distribution function is "coarse-grained" in a set of N particles. Then, it is easier to compute the force between particles at each time step.
However, this sampling is sensitive to Poisson noise and a large number of particles is preferable to infer robust estimates.
Also, gravitational interactions need to be softened at some scale to avoid unphysical two body scattering between two nearby particles i and j. Such softening scale ϵ[4] is introduced in the force calculation :

$$\mathbf{F}_{ij} = -\sum_{i \neq j} \frac{\mathrm{G}\, m_i m_j \left(\mathbf{x_i} - \mathbf{x_j}\right)}{\left(|\mathbf{x_i} - \mathbf{x_j}|^2 + \epsilon^2\right)^{3/2}} \tag{4.6}$$

4: Often, this scale is the mean inter-particle separation

Once forces have been calculated, particles are updated in phase space using symplectic integrator such as the most common Leapfrog integration scheme.

Cosmological simulations need to cover a great range of dynamical timescales : high density regions require orders of magnitude smaller timesteps than in low density regions. This is why schemes with adaptative timestep are generally used.

Different approaches exist to accelerate the above direct summation. They can roughly be divided into two groups : through approximation or mesh based method. Respectively, they aim for efficient numerical solution of the integral or differential form of the Poisson equation.

The integral form of the Poisson equation reads :

$$\phi(\mathbf{r}) = -G \int d\mathbf{r}' \frac{\rho(\mathbf{r}')}{|\mathbf{r} - \mathbf{r}'|}, \tag{4.7}$$

where the density can be translated to a discrete summation with a complexity of $\mathcal{O}(N^2)$. This method was actually behind the earliest simulations and is called the particle-particle scheme.
To accelerate this summation, particles can be grouped according to their distance from the particle at which the force is being calculated. The computational domain is hierarchically divided into a tree structure. The most common method is the oct-tree where each cubic cell is split into up to 8 child cells resulting in a tree-like hierarchy of cubic nodes with, at the basis, the cube node that contains all particles in the simulation. Such structure is illustrated in Figure 4.2. Contributions from distant groups to the

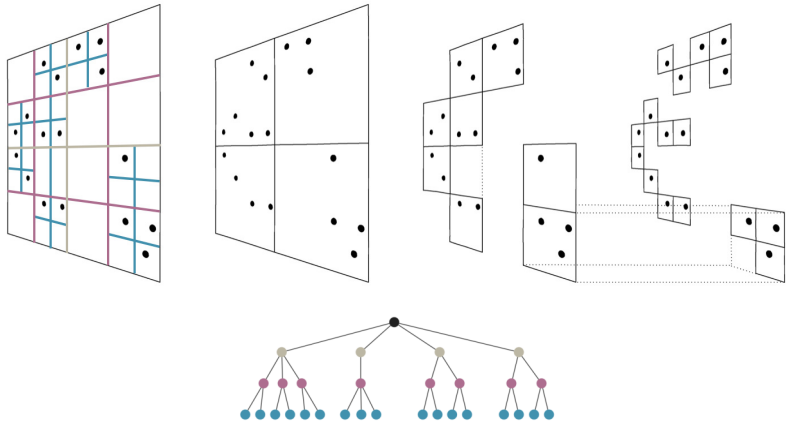

Figure 4.2: 2D schematic illustration of the Barnes & Hut [121] oct-tree (i.e. quad-tree). The particles are first enclosed in a square (root). This square is iteratively subdivided in four squares of half the size, until exactly one particle is left in each final square (leaves of the tree). The black dot at the bottom sketch represents the cubic node while the blue dots are the leaves. The colors match the division of the 2D area in the top left figure - Adapted from Springel *et al.* [122]

gravitational potential are approximated by the lowest order of the multipole expansion of the mass distribution at the coarsest level. At the result, it reduces the complexity of the system to $\mathcal{O}(N \ln N)$. This is the tree approach.

The differential form of the Poisson equation,

$$\nabla^2 \mathbf{\Phi} = 4\pi G \rho(\mathbf{r}), \tag{4.8}$$

can be solved using mesh-based methods. This equation can be solved by using fast Fourier transform to yield the equation $k^2 \hat{\mathbf{\Phi}} = -4\pi G \hat{\rho}(\mathbf{k})$ leading to the so called particle-mesh (PM) method. The calculation of the force, obtained by differentiating the potential using finite-difference approximation, has only a complexity of $\mathcal{O}(N \ln N)$[5] .

In addition, when the particle-mesh method is combined with sets of nested grids of increasing resolution, it provides an efficient

5: N is now the number of mesh cells.

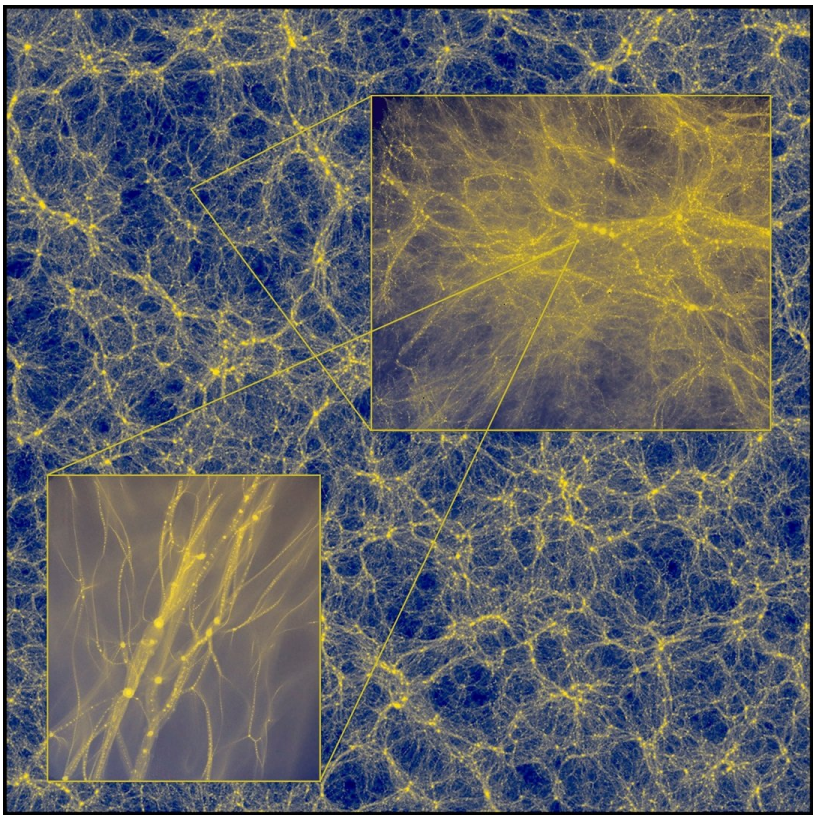

Figure 4.3: The cosmic-web structure of a Universe in a DM only simulation with Gadget-4 [123]. The simulation has a full dynamic range of 30 orders of magnitude where halo density profiles are found to be universal over the entire mass range. The bottom left insert shows the highest level of magnification and reveals Earth-mass dark matter haloes as they would appear in the universe today – Credits : J. Wang, S. Bose/CfA

solver. This is the adaptative mesh refinement method (AMR) which is adopted by Ramses.

There also exist a variety of hybrid schemes such as particle-particle particle-mesh (P^3M) or the tree particle mesh (tree-PM) methods.

N-body dark matter only simulations have provided decisive findings on the large scale distribution of dark matter and the internal structure of halos.
Cold dark matter simulations predict a web-like structure of DM, as illustrated in Figure 4.3 with voids separated by walls which intersect in filaments and nodes being at their crossing. This distribution can be quantified with the halo mass function[6] . Its predicted shape from simulations differs from the spherical Press & Schechter [15] model, but agrees better with an ellipsoidal collapse model [124]. The mass distribution in DM halos is predicted to be nearly universal over a wide mass range (e.g. Wang *et al.* [123]). From DM numerical simulations, universal spherically averaged density profiles emerged such as the well known Navarro, Frenk & White profile [125, 126],

$$\rho_{\rm DM}(r) = \frac{\rho_s}{\frac{r}{r_s}\left(1+\frac{r}{r_s}\right)^2}, \tag{4.9}$$

6: see Section 2.2.4

with a characteristic density ρ_s and a transition radius r_s for instance. The shape of DM halos was also investigated and tends to be more prolate and more massive halos tend to be less spherical than the lower mass ones .
This is particularly relevant for this thesis as we are studying the high mass end of the halo mass function. Therefore, galaxy clusters should form within DM haloes that should show the strongest departure from ellipticity.[7]
More debated, the central slope of DM halos [127] (cusp/core) that, in addition, should be affected by baryonic physics which require hydrodynamical simulations.

7: However, we will see that the assumption of spherical symmmetry of galaxy clusters is central in the theory of self-simlar evolution of galaxy clusters in Section 11.1.

4.3 Modelling baryons

The visible component of our Universe requires the modelling of gas physics even though, dark matter and dark energy dominate our Universe energy budget. Actually, modelling baryons is crucial for predicting the visible Universe.

The Universe's dominant baryonic component is a gas mostly constituted of hydrogen and helium which, during the process of structure formation, will be eventually turned into stars.
Therefore the modelling of the visible component of our Universe requires gas physics, i.e. modelling an inviscid ideal gas whose evolution is govern by Euler's equations (conservation of mass, momentum and energy) typically closed by assuming a non-relativistic ideal gas equation of state (relating gas pressure to internal energy). However, hydrodynamical cosmological simulations extremely increase the complexity compared to N-body techniques, which only solve gravity.

A variety of techniques exists to solve the set of hydrodynamical equations which mainly falls in three classes : The Eulerian method discretises the fluid into static grid cells, while the Lagrangian method follows fluid parcels individually. There also exists arbitrary Lagrangian-Eulerian methods that use an unstructured mesh where grid cells have a velocity which can be chosen freely.

The most popular Lagrangian method is smoothed particle hydrodynamics (SPH). In brief, it uses sampling particles that carry the information about the fluid. For any field $X(\mathbf{r})$, a smooth interpolated version $X_s(\mathbf{r})$ is obtained via a kernel-weighted sum over the

j neighboring particles closer than a smoothing length h :

$$X_s(\mathbf{r_i}) = \sum_j \frac{m_j}{\rho_j} X_j \, W\left(\mathbf{r_i} - \mathbf{r_j}, h_i, h_j\right), \tag{4.10}$$

where m and ρ are the particles' mass and density and W is the kernel which can be a gaussian but more commonly, a cubic spline. The Lagrangian formulation of the Euler's equation in the comoving form are given by :

$$\frac{\mathrm{D}\rho}{\mathrm{D}t} + \boldsymbol{\nabla} \cdot (\rho \mathbf{v}) = 0, \tag{4.11}$$

$$\frac{\mathrm{D}\rho\mathbf{v}}{\mathrm{D}t} + \boldsymbol{\nabla} P = 0, \tag{4.12}$$

$$\frac{\mathrm{D}\rho e}{\mathrm{D}t} + \boldsymbol{\nabla} \cdot P\mathbf{v} = 0, \tag{4.13}$$

Where $\mathrm{D}/\mathrm{D}t = \partial/\partial t + \mathbf{v} \cdot \boldsymbol{\nabla}$ is the convective (or Lagrangian) derivative and $e = u + \mathbf{v}^2/2$, the total energy per unit mass with u, the internal energy.
These equations are closed though the non-relativistic ideal gas equation of state :

$$P = (\gamma - 1)\, \rho u \tag{4.14}$$

where the γ is the adiabatic index.

Compared to the Langrangian approach which formulate the solution to Euler's equation in the fluid frame, the Eulerian approach rather use a fixed frame. Therefore, the Eulerian formulation is :

$$\frac{\partial \rho}{\partial t} + \boldsymbol{\nabla} \cdot (\rho \mathbf{v}) = 0, \tag{4.15}$$

$$\frac{\partial \rho\mathbf{v}}{\partial t} + \boldsymbol{\nabla} \cdot (\rho \mathbf{v} \otimes \mathbf{v} + P\mathbb{1}) = 0, \tag{4.16}$$

$$\frac{\partial \rho e}{\partial t} + \boldsymbol{\nabla} \cdot (\rho e + P)\, \mathbf{v} = 0, \tag{4.17}$$

with the same closure Equation 4.14 given by the gas equation of state.

The most common methods include finite volume, finite difference, finite element, spectral or wavelet methods. Most current cosmological Eulerian codes use Godunov finite volume schemes to solve the Riemann problem[8] across cell faces which yield fluxes at each cell face. Then the fluid and its properties are advected across the cell face.
A first order Godunov solver assumes uniform properties in cells. Higher orders solvers employ parabolic interpolation known as the piecewise parabolic method (PPM). For instance Ramses uses

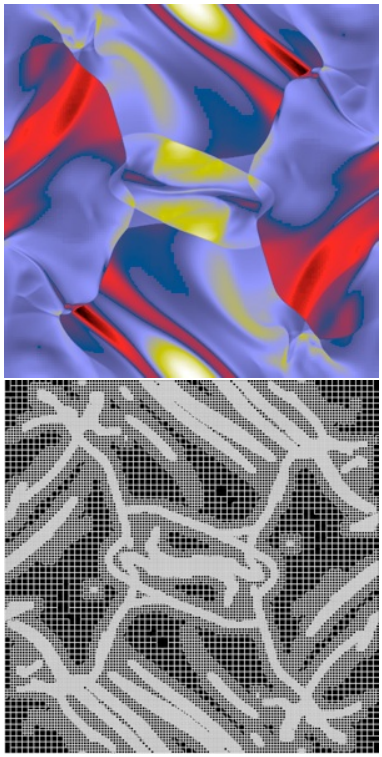

Figure 4.4: The Orszag Tang Vortex, a well-known model problem for testing the transition to supersonic 2D MHD turbulence. Mass density (*top*) at time $t = 0.5$ with 5 levels of refinement and the correspoding AMR grid (*bottom*) – Credits : Romain Teyssier/Ramses test suite webpage

8: The Riemann problem is composed of a conservation equation together with piecewise constant initial data which has a single discontinuity in the domain of interest

the second order piecewise linear method (PLM) which adopts the MUSCL scheme.
In cosmological simulations, the great dynamic range to resolve requires adaptative meshes to reduce the mesh size based on local criteria (typically based on the cell's enclosed mass). Hence, some simulation cells will be split into subcells to improve the resolution in regions of interest (see Figure 4.4). This is the adaptive mesh refinement (AMR) scheme.
Discontinuous Galerkin schemes combine features of the finite element and the finite volume framework to discretize hyperbolic problems at any order of spatial accuracy.

Arbitrary Lagrangian-Eulerian methods use the advantages of PPM in handling shocks and contact discontinuities with SPH's natural adaptivity. One approach is a deformable mesh which is allowed to freely follow the fluid. The formulation of Euler's equations is now :

$$\frac{\mathrm{d}}{\mathrm{d}t}\int_V \rho \mathrm{d}V + \int_S \rho\left(\mathbf{v}-\mathbf{w}\right)\cdot\mathbf{n}\mathrm{d}S = 0, \tag{4.18}$$

$$\frac{\mathrm{d}}{\mathrm{d}t}\int_V \rho\mathbf{v}\mathrm{d}V + \int_S \rho\mathbf{v}\left(\mathbf{v}-\mathbf{w}\right)\cdot\mathbf{n}\mathrm{d}S + \int_S P\mathbf{n}\mathrm{d}S = 0, \tag{4.19}$$

$$\frac{\mathrm{d}}{\mathrm{d}t}\int_V \rho e\mathrm{d}V + \int_S \rho e\left(\mathbf{v}-\mathbf{w}\right)\cdot\mathbf{n}\mathrm{d}S + \int_S P\mathbf{v}\cdot\mathbf{n}\mathrm{d}S = 0, \tag{4.20}$$

where $\mathbf{n}$ is the normal vector on the surface S and the grid moves with a velocity $\mathbf{w}$ and the cell volumes evolve as $\mathrm{d}V/\mathrm{d}t = \int_V \boldsymbol{\nabla}\cdot\mathbf{w}\,\mathrm{d}V$.

We will briefly now discuss the advantages and disadvantages of each approach. As we just said, Eulerian methods handle better strong shocks and surface instabilities, whereas Lagrangian methods benefit from better adaptivity and a greater dynamic range at a given computational expense.
In SPH methods, movement of mass is directly tracked. Therefore it is easier to follow where the mass ends up when galaxies assemble or outflows occur. Nonetheless, tracer particles can be used in mesh codes to benefit from this advantage.
Adaptative meshes can be refined to arbitrary high resolution whereas particle-based methods are limited by the mass resolution of the simulation.
Therefore, each astrophysical code has it own strong points. Thanks to the available variety of codes, problems can be tackled with different angles.

Generally these different methods provides similar answers in basic tests. We will discussed in Section 4.8, some code comparison

in galaxy cluster simulation project.

4.4 Thermal evolution

Baryons, opposed to DM, dissipate their potential energy via cooling processes such as collisional excitation, collisional ionisation, inverse Compton and free-free emission. These processes are fundamental ingredients for galaxy formation. They are coupled to the energy equation using cooling functions $\Lambda(\rho, T)$ either tabulated or extracted from chemical reaction networks. The first law of thermodynamics in Equation 4.17 become :

$$\frac{\partial \rho e}{\partial t} + \boldsymbol{\nabla} \cdot (\rho e + P)\,\mathbf{v} + \Lambda(e, \rho) = 0 \tag{4.21}$$

Additional, to the cooling of primordial gas (H+He), cooling due to heavy elements (metals) is also important for temperatures $10^5 \leqslant T \leqslant 10^7$ K as we can see in Figure 4.5. Recently, galaxy formation models also account for the photoionization of metals by the metagalactic radiation field [128]. Simulations that are able to resolve the cold phase of the interstellar medium also include fine structure and molecular cooling for the gas below 10^4 K.
Yet, a high numerical resolution is required to resolve the multi-

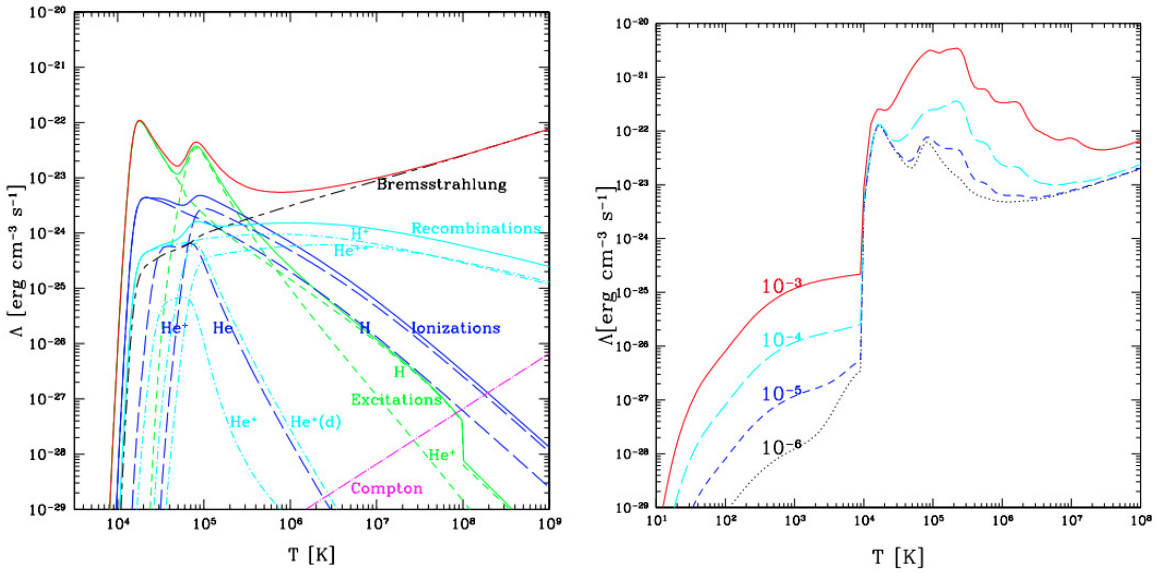

Figure 4.5: *Left* : Total cooling curve (solid line) for a primordial mixture of H and He and its composition from different processes. *Right* : Change of the total cooling curve as a function of different metallicity indicated in the plot (in absolute values). The part below 10^4K takes into account cooling by molecules (e.g. HD and H2) and metal lines – Credits : Taken from Dolag *et al.* [129], adapted from Maio *et al.* [130]

phase gas and follow all these different cooling processes.
Gas cooling is a direct physical process that is not implemented through a sub-resolution model (if the gas distribution is simply

assumed to correspond to the cell averaged values).

4.5 Sub-grid baryonic models

The physics of galaxy formation and evolution cannot be implemented in astrophysical codes from first principles. Despite the always increasing computational power that allows for better resolution, there will always be a limit to the scales of which numerical simulation can resolve. This is why models which account for the unresolved physics need to be implemented in cosmological codes in an effective way. We will give an overview of the commonly used sub-grid models in this section. However, we will give a more detailed description in Chapter 5 of the subgrid models used for this PhD implemented in the Ramses code.

4.5.1 Star formation

First, we must account for the cold and dense gas that will be eventually turned into stars. Simulations have to transform gas into a collisionless stellar particle that actually represents a stellar population following an underlying initial stellar mass function[9] with a single metallicity. The star formation (SF) efficiency at which gas is turned into stars is found to be almost universal where 1% of the dense, cold, molecular phase of the ISM is converted to stars per free-fall time [131].
A Kennicutt-Schmidt [132, 133] type relation ($\mathrm{d}M_*/\mathrm{d}t = \varepsilon M_{\mathrm{gas}}/t_{\mathrm{ff}}$)[10] is usually used to compute the SF rate (usually in the range $0.01-1$) and gas can be converted to stars by typically using a probabilistic scheme [134]. Other schemes allow for the growth of star particle by accretion of the surrounding interstellar medium (ISM).
However, SF can be restricted and criteria such as a gas density threshold, Jeans-length based criteria or converging flows need to be satisfied to trigger the formation of a star particle.

9: It describes the mass distribution of formed stars

10: where ε is the SF efficiency, M_{gas} is the gas cell or particle mass (depending on the sampling method used) and t_{ff} is the gravitational free-fall time.

4.5.2 Stellar feedback

Modern galaxy formation models also follow the evolution of these star particles as well as their mass return leading to metal enrichment of the gas [135]. Indeed, by assuming that all stars with masses above e.g. $10^8 \mathrm{M}_\odot$ will end as type-II supernovae, the total amount of stellar feedback energy released to the surrounding gas can be calculated.
This injection of momentum and energy that interacts with the ISM lead to a feedback loop that is able to regulate star formation

(mostly in low mass halos).
Essentially the stellar feedback energy can be deposited thermally or kinetically. While the radiative cooling of dense gas is physically expected, excessive radiative gas cooling occurs in cosmological simulations due to their limited resolution that prevents from a accurate modelling. Therefore, the excessive loss of energy through radiation leads to greatly reduced supernova (SN) feedback [136, 137]. Some schemes are implemented to disable the cooling of the gas for a prescribed amount of time [138, 139]. Other feedback channels have also been implemented which take into account stellar winds, photoionisation and radiation pressure from young and massive stars.
Thanks to all these processes, star formation in simulations can be regulated to the observed efficiency of 1% per free-fall time [131, 140]. In order to explain the low baryon retention fraction in galaxies, the stellar feedback has to be able to launch galactic scales outflows to eject gas from galaxies. Some simulations directly prescribe the mass loading factor[11] of these outflows.

11: The ratio of material flowing out of the galaxy to the star formation rate

4.5.3 Super-massive black holes

First black hole (BH) seeds may have been left behind after pop-III stars[12] explosions in the early Universe and are expected to have masses of $\sim 100\,\mathrm{M}_\odot$. However, these Pop-III BHs cannot power the observed quasars at $z \sim 6-7$ if their growth is Eddington limited. Different mechanisms have been proposed for creating more massive BH seeds with masses of $10^4 - 10^6 \mathrm{M}_\odot$ (see review of Volonteri [141] for more details). However, the formation of supermassive black holes (SMBHs) found in massive, dwarf and bulge-less disc galaxies, remains a mystery. Numerically, BHs are seeded typically in halos with masses $\geqslant 10^{10} - 10^{11}\mathrm{M}_\odot$ and often accrete at an Eddington-capped Bondi-Hoyle-like accretion rate[13] [108, 142, 143] :

$$\dot{M}_{\mathrm{BH}} = \frac{4\pi \mathrm{G} M_{\mathrm{BH}}^2 \rho_{\mathrm{gas}}}{\left(c_{s,\mathrm{gas}}^2 + v_{\mathrm{rel}}^2\right)^{3/2}} \tag{4.22}$$

with M_{BH} the BH mass, ρ_{gas} and $c_{s,\mathrm{gas}}$ the gas density and sound speed, v_{rel} is the relative velocity between the BH and the gas. To account for unresolved density and temperature fluctuations at scales lower than the simulation resolution, this accretion is often boosted and possibly in a density-dependant fashion [135, 144].
Another mechanism for BH growth is by mergers. Due to the resolution limitation, the relativistic effects of such process are not accounted for and usually BHs merge instantly in simulations when they come close enough, with possible more sophisticated criteria on their relative velocity for instance.

12: The very first massive stars of our Universe formed out of the primordial gas

13: However, the Bondi model implicitly assumes negligible angular momentum of the accreting gas, which is unlikely to be a good assumption in general

4.5.4 Active galactic nuclei feedback

Active galactic nuclei (AGNs), associated with accreting SMBH, manifest by electromagnetic radiation, relativistic jets and less collimated non-relativistic outflows. The AGN energy output, coupled to the surrounding gas, allows to regulate SF and BH growth in massive halo with masses typically larger the the Milky Way ($10^{12}M_{\odot}$). AGN feedback can be divided in two modes that are differently implemented in astrophysical codes. First the quasar mode feedback, associated with the BH growth radiation, is often implemented through injection of energy or momentum in the surrounding gas with a luminosity proportional to the accretion rate. And, secondly, the radio mode feedback, associated with highly collimated jets of relativistic particles, is often implemented as a second sub-resolution feedback channel once the accretion rate is below a threshold value.
The AGN feedback models have to bridge a wide range of scales from the accretion region, of few Schwarzschild radii, to tens of kiloparsec. Therefore, AGN models, while producing useful results, can have an arbitrary physical implementation as they have to bridge a very large gap of scales which cannot be resolved.

4.6 Limitations

Dark matter only simulations are only limited by the efficiency of the chosen N-body methods and the parallelisation techniques.
On the other hand, hydrodynamical simulations are more challenging as they rely on sub-resolution models and different hydrodynamical schemes.
The sub-grid models depend on various adjustable parameters which can be chosen based on physical arguments or which have to be found through a calibration procedure. Typically, it consists of a parameter-space exploration in a large number of simulations. Then, simulation outputs are compared to key observables of the galaxy populations such as the stellar-to-halo mass relation, galaxy stellar mass function or the star formation rate density as a function of time.

A calibration procedure can be performed at a coarser resolution for lower computational costs. However, the resolution adds an energy scale $\sim GM_{\mathrm{gas}}/\Delta x$, on which the sub-grid models will depend. Therefore, one has to be careful as simulation properties might be unstable against resolution change.
As an example, the Illustris TNG300[14] was run at a lower spatial resolution than TNG100 simulation, and for the latter simulation, galaxy formation physics choices and parameters were not changed as a function of mass and spatial resolution (see appendix A of

14: See the presentations papers of the IllustrisTNG simulations [110, 145–148]

Pillepich *et al.* [148]). Therefore, recalibration techniques should be applied in order to use the halo properties and their derivatives for total halo masses below $\sim 10^{12}\mathrm{M}_{\odot}$ [149].[15] .

15: see also discussion in Schaye *et al.* [150] and Pillepich *et al.* [148] about "weak" and "strong" resolution convergence.

4.7 Key simulations results

While hydrodynamical simulations have suffered a long time from unrealistic star formation histories or galaxy masses, sizes and morphology, simulations have now significantly improved in the last decade.
By the construction of detailed mock observation, simulation data can be compared to robust observed scaling relations or observables.

With the use of large volume simulations such as illustrated in Figure 4.6 global properties of galaxies can be ideally studied thanks to the large statistics. The most fundamental properties of the galaxy population is the galaxy stellar mass function[16] .

16: The galaxy stellar mass function quantifyies the number density of galaxies as a function of galaxy stellar mass

Typically, as we described above, one adjusts the key parameters in the sub-resolution models to match observations of galaxy mass functions. SN feedback typically suppresses star formation in the low halo mass end ($M \leqslant 10^{12}\mathrm{M}_{\odot}$) while feedback from AGN regulates the high-mass end. Hydrodynamical simulations show galaxy stellar mass functions consistent with observational data as shown in Figure 4.7. Simulation predictions also compare to empirical constraints derived on various galaxy-halo mapping techniques (e.g abundance matching) such as the stellar mass halo mass relation, which will be investigated in Chapter 9.

More challenging is to reproduce the multiphase gas around galaxies such as the circumgalactic medium which shows an rich multiphase structure on spatial scales of $10 - 100\,\mathrm{pc}$ (typically below the resolution limit of large volume cosmological simulations). But also, reproducing the galaxy cluster entropy profiles and the cool-core/non-cool-core dichotomy remain challenging [111, 113, 153]. Actually, this is the central goal of this PhD.

Many scaling relations of various global galaxy observables are also important tests for the galaxy formation models used in simulations. Many large-volume hydrodynamical simulations are able to reproduce e.g. the mass-size, SMBH mass-stellar velocity dispersion and the mass-metallicity relations.
However, there remain point of tension in the detailed shape of these relations, their scatter and the dependance on additional

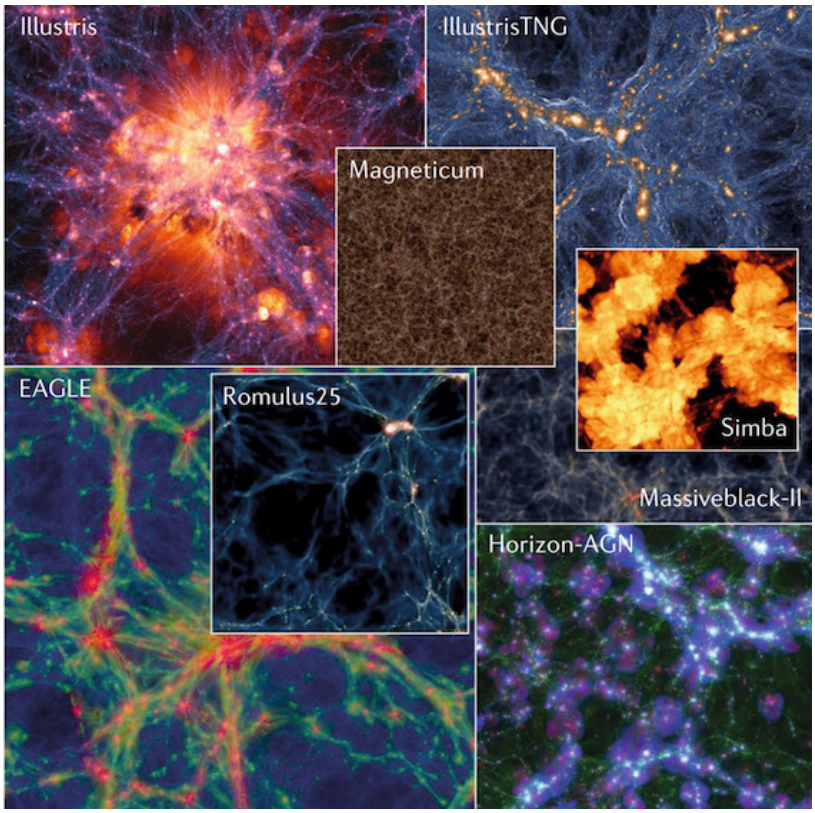

Figure 4.6: Visual representation of large volume hydrodynamical simulations which reproduce galaxy populations that agree remarkably well with observational data. However, many detailed predictions of these simulations are still sensitive to the underlying implementation of baryonic physics – Credits : Vogelsberger *et al.* [151] and references therein.

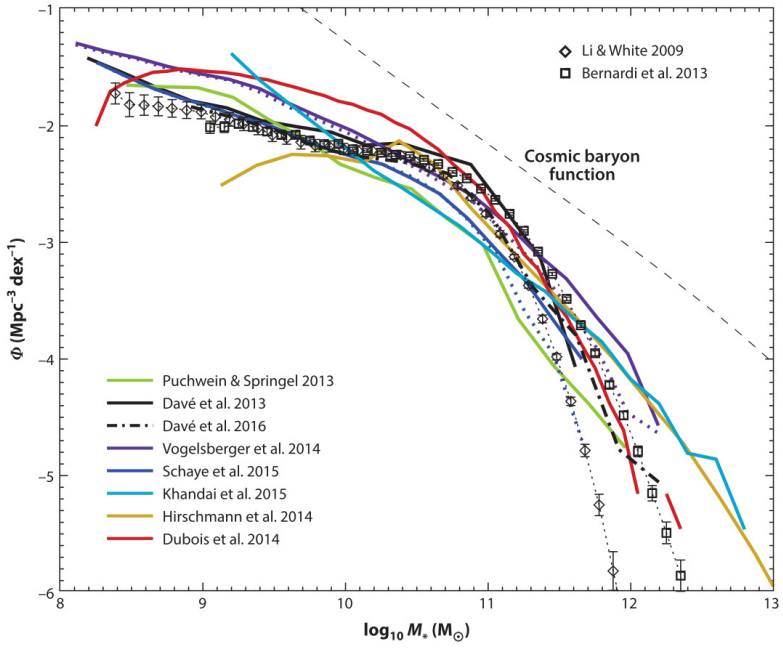

Figure 4.7: Comparison of galaxy stellar mass functions from recent large-scale cosmological simulations which include stellar and AGN feedback (with the exception of Davé et al. (2013))– Credits : Naab & Ostriker [152]

galaxy properties.

Going is a more detail, early simulation works produced galaxies dominated by a stellar spheroidal component, where the disc is only subdominant. Thanks to improved feedback schemes, modern numerical simulations successfully reproduce the disc galaxies as shown in Figure 4.8.

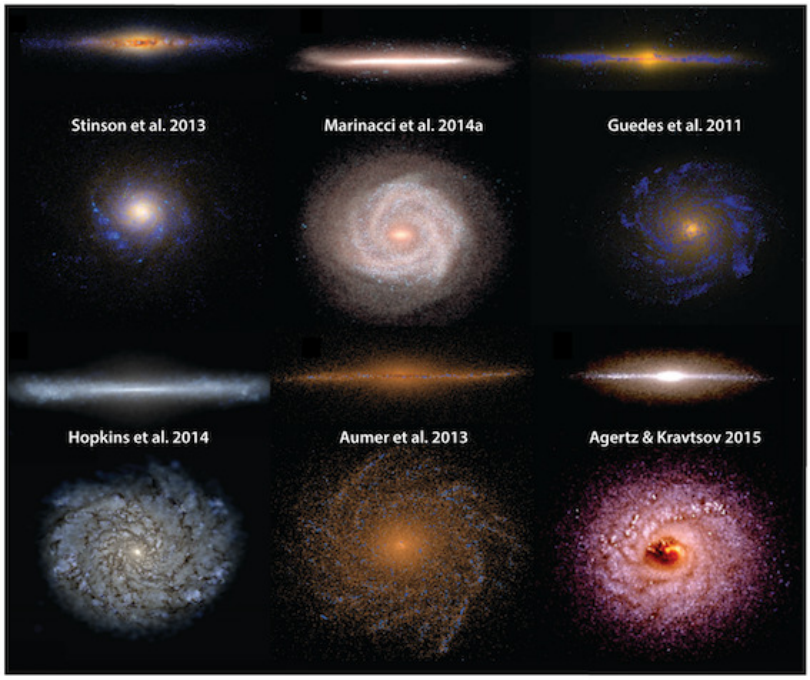

Figure 4.8: Mock images of the stellar light in recent cosmological zoom simulations with spiral-like morphologies – Credits : Naab & Ostriker [152] and references therein.

For elliptical galaxies, simulations have also been successful in reproducing system that match formation histories, scaling relations and the distribution of metals. Hydrodynamical simulations have played a major role, to explain the diversity in morphology and kinematics of spheroid-dominated galaxies.

4.8 Astrophysical codes

In this section we will sum-up some of the major galaxy formation codes in Table 4.1 as well as related recent galaxy formation simulations in Table 4.2, inspired by the review of Vogelsberger *et al.* [151].
In this work, we will compare our simulations to whose reported in the following tables. Therefore, it is convenient to be able to compare the method each simulation uses as well as the resolution they reach.

Name	Gravity	Hydrodynamics	References
RAMSES	PM/ML	AMR	Teyssier [154]
Enzo	PM/MG	AMR	Bryan *et al.* [155]
GADGET-2/3	TreePM	SPH	Springel [156]
Arepo	TreePM	MMFV	Springel [157]
ChaNGa	Tree/FMM	SPH	Menon *et al.* [158]

Table 4.1: Major galaxy formation simulation codes. We use the following acronyms : Particle-Mesh (PM); tree + PM (TreePM), Multilevel (ML), Multigrid (MG), Fast Multipole Method (FMM), Smoothed Particle Hydrodynamics (SPH), Adaptive Mesh Refinement (AMR), Moving-Mesh Finite Volume (MMFV).

Being aware of the characteristics of a simulation code and its associated galaxy formation models is fundamental before exploiting their outputs.

Table 4.2: Recent galaxy formation simulations with the lower part of the table focusing on galaxy cluster simulations. $m_{\rm DM}$ and $m_{\rm gas}$ are dark matter and (average) gas particle masses, respectively. For particle based codes we report the minimum softening length while for mesh codes we quote the minimum cell size.

Name	Code	Volume [Mpc^3]	Spatial resolution [kpc]	$m_{\rm DM}$ [$\mathrm{M}_\odot$]	$m_{\rm gas}$ [$\mathrm{M}_\odot$]	References
Horizon-AGN	Ramses	142^3	1.0	8.0×10^7	1.0×10^7	Dubois *et al.* [108]
Illustris	Arepo	107^3	1.5	6.7×10^6	1.3×10^6	Vogelsberger *et al.* [159]
IllustrisTNG300	Arepo	303^3	1.5	7.9×10^7	7.4×10^6	[110, 145–148]
IllustrisTNG100	Arepo	111^3	0.75	5.1×10^6	9.4×10^5	[110, 145–148]
IllustrisTNG50	Arepo	52^3	0.3	4.4×10^5	8.5×10^4	[160, 161]
Eagle	p-Gadget3	100^3	0.7	9.6×10^6	1.8×10^6	Schaye *et al.* [150]
Cosmo-OWLS	Gadget-3	571^3	5.9	5.7×10^9	1.0×10^9	Le Brun *et al.* [162]
BAHAMAS	Gadget3	571^3	0.25	5.7×10^9	1.0×10^9	McCarthy *et al.* [163]
Rhapsody-G 4K	Ramses	Zoom	5.5	1.2×10^9	2.6×10^8	Wu *et al.* [164]
Rhapsody-G 8K	Ramses	Zoom	2.8	1.4×10^8	3.3×10^7	Wu *et al.* [164]
FABLE	Arepo	Zoom	0.7	8.1×10^7	1.5×10^7	Henden *et al.* [165]
Cluster-Eagle	Gadget-3	Zoom	0.7	9.6×10^6	1.8×10^6	Barnes *et al.* [112]
MACSIS	Gadget-3	Zoom	5.9	5.7×10^9	1.0×10^9	Barnes *et al.* [99]
Three Hundred	Gadget-3-Music/X	Zoom	9.6	1.9×10^9	3.5×10^8	Cui *et al.* [166]
RomulusC	ChaNGa	Zoom	0.25	3.4×10^5	2.1×10^5	Tremmel *et al.* [167]

The study of galaxy formation and evolution in cluster environments occupies a fundamental position in numerical astrophysics. Indeed, because of their large sizes, galaxy clusters encompass a large range of scales. Therefore, they constitute a testbed for the study of the galaxy formation processes and their complex interplay in cosmological numerical simulations.

Following the classic Santa Barbara Cluster Comparison Project of Frenk *et al.* [168], the nIFTy simulations [169–172] aim to assess the reliability of cosmological hydrodynamical simulations in recovering the properties of galaxy clusters. They simulated the formation of a galaxy cluster ($M_{200} \sim 1.1\times10^{15}\mathrm{M}_\odot$) using 13 different codes[17] modelling gravity with radiative hydrodynamics or not.

17: Ramses, ART, Arepo, Hydra and nine incarnations of Gadget

We will briefly discuss the major differences between the codes, but we refer the reader to the nIFTy simulations papers for more details.

While the dark matter distribution of the galaxy cluster aligns very accurately for all the codes, significant scatter is observed for the gas. As an example, we can see in Figure 4.9 the comparison for the various codes of the radial entropy profiles of non-radiative simulations. We see that the mesh-based codes Ramses, ART, Arepo as well as latest SPH schemes tend to form extended entropy cores in the gas with rising central gas temperatures. SPH schemes on the other hand, show falling entropy profiles all the way into the

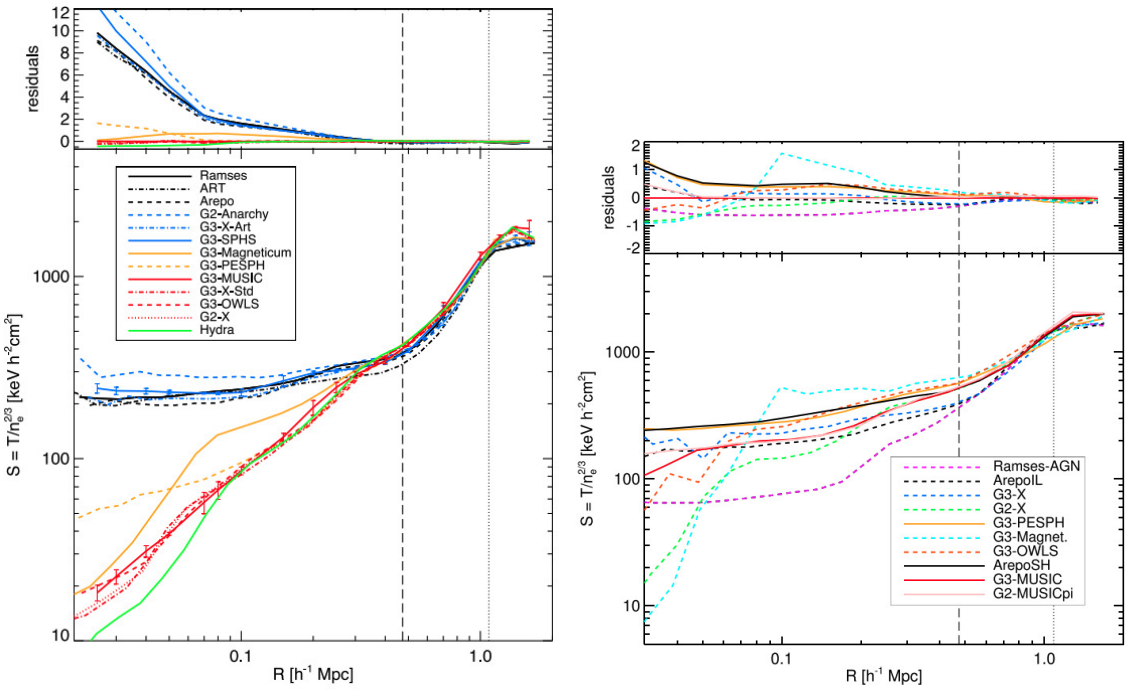

Figure 4.9: *Left* : Radial entropy profile at $z = 0$ (bottom panel) for each non-radiative simulation and difference between each simulation and the reference G3-MUSIC simulation (top panel). *Right* : Radial entropy profile for radiative physics simulations with the top panel showing again the difference between each simulation and the reference G3-MUSIC simulation . The dashed line corresponds to R_{2500} and the dotted line to R_{500} of the reference G3-MUSIC values.– Credits : Sembolini *et al.* [169, 170]

very centre. Modern SPH codes schemes that allow entropy mixing span the range between these two extremes [169].

However, when radiative physics are included the marked code-based differences seems to BE washed away [170]. Nonetheless, the simulations presented in this comparison study only reproduce a non-cool-core cluster.

While no significant impact of radiative physics is observed on the ICM, the properties of cluster galaxies show code-to-code scatter of ~ 0.5 dex in stellar mass (with systematic differences with some codes producing galaxies 70 per cent smaller than others) [171].

We will not discuss further details here but we refer the reader to the papers of the nIFTy galaxy cluster simulation comparison project.
However, we can already see that each code and sub-grid models can impact differently the cluster gas thermodynamics and the properties of the galaxy population.

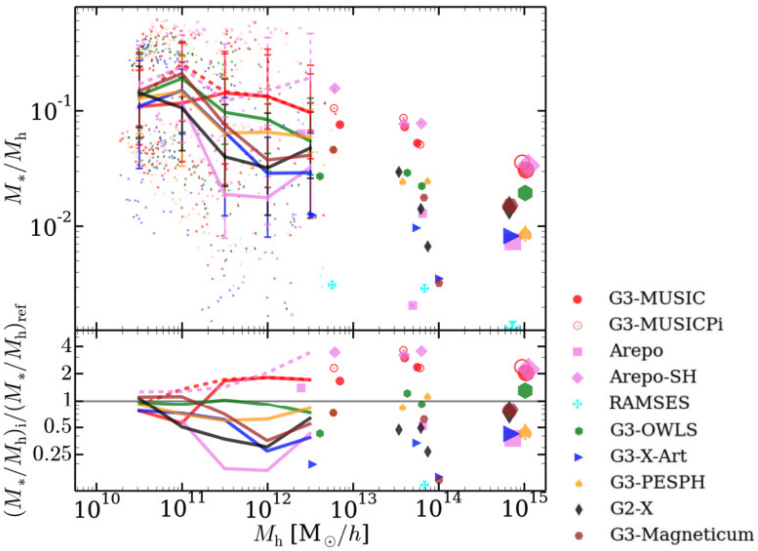

Figure 4.10: Stellar mass to host (sub)halo relation (top) and the residuals relative to the median calculated using all simulation halo catalogues – Credits : Elahi *et al.* [171]

Simulating galaxy clusters with RAMSES

5

In this chapter we will give an overview of the Ramses *code used in this work. We will explore the numerical schemes as well as the sub-grid models implemented in the code. Among many different applications, we will discuss the* Rhapsody-G *simulations, being the basis of this work.*

5.1 A parallel AMR code

Ramses, or Raffinement Adaptatif de Maille Sans Effort Surhumain for connoisseurs, is an N-body and hydrodynamical code written by Romain Teyssier [154] in Fortran 90 which run in parrallel on various different super-computer architectures using the message-passing interface (MPI)[1] . It is publicly available and can be found at https://bitbucket.org/rteyssie/ramses.

1: It can also be used on single processor machines without MPI.

The code is able to simultaneously follow particles which are gravitationally coupled to an inviscid fluid. This coupling occurs when solving the Poisson equation with a total density field (particle+fluid) to compute the gravitational potential and the force field.
As we saw in the previous Chapter 4, Ramses is an Eulerian code. It uses a mesh grid to compute the hydrodynamics but use a particle-mesh technique for the N-body solver (previously discussed in Section 4.2).

The Euler's equations are solved in their conservative form to guarantee that energy is perfectly conserved. The hydrodynamical solver is a second-order unsplit Godunov scheme made for perfect gases. As the fluid is discretized on the grid, the information of neighbouring cells is required to compute the partial differential equations at a given point. By using a piecewise linear method (PLM), the left and right cell values at the discontinuity used to compute fluxes, are approximated by a second order solution which approximates the initial function with a linear function (see Figure 5.1). Different types of slope limiter used in the Godunov scheme for the PLM reconstruction can be chosen either MinMod or MonCen TVD. The slope limiter prevents spurious oscillations to appear in the solution.

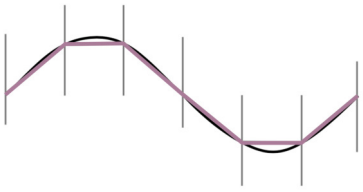

Figure 5.1: Reconstruction of an initial function (black) with a second order scheme (light pink)

To find the inter-cell flux, different Riemann solvers can be chose between the Harten-Lax-von Leer (HLL), the Global Lax-Friedrich (GLF), and HLL Contact (HLLC) solvers for instance. These solvers do not solve the original equation but, in fact include an additional numerical diffusion term needed to obtain a stable time integration. This numerical diffusion is proportional to the cell size : it converges to zero as the mesh size become infinitesimally small. Therefore to minimize numerical diffusion for these low-order (second) order schemes, the mesh size has to be reduced. This can be achieved by using a adaptative mesh refinement (AMR) technique.
The basic idea of AMR is to adaptively refine the mesh where numerical diffusion is too large.
Moreover, a uniform mesh is computationally inefficient because regions with low density will be as computationally expensive as regions of better interest. Hence, it is preferable to place higher resolution where needed and leave the rest at a coarser resolution to use efficiently the computational time.

In Ramses, the data is structured in a fully threaded tree, where the Cartesian mesh is refined on a cell by cell basis. The refinement criterion can be set according to the simulation needs. For instance, simulations with strong shocks will rather refine based on pressure or density gradient. Cosmological simulations will rather opt for an overdensity-based (i.e. 'Lagrangian') refinement which splits cells if they reach an user-defined overdensity. Truelove *et al.* [173] found that resolving the Jeans length with at least 4 cells prevents from an artificial fragmentation of a self-gravitating gas. Therefore one can also use a Jeans refinement strategy which splits a cell if its size exceeds a fraction of the local Jeans length.

The basic element in Ramses is called an oct. It is a grid composed of eight cells in 3D (four cells in 2D and two in 1D). Each cell stores all the variables (density, momentum, internal energy and metallicity, magnetic field and any other passive scalar) but also has the reference of its neighboring and parent cells.

The whole simulation box is 1 oct (i.e. 8 cells) at Level 1. Which is then homogeneously refined down to a minimum refinement level l_{min} where each oct is by refined to 2 cells along each direction. Therefore, at a given level l, the total of cells is $\left(2^l\right)^{n_{\text{dim}}}$, with n_{dim} is the number of dimension. As the result, the cell size at level l is set by :

$$\Delta x_l = \frac{L_{\text{box}}}{2^l} \tag{5.1}$$

The simulation will start at this level l_{min} and evolves, but as soon

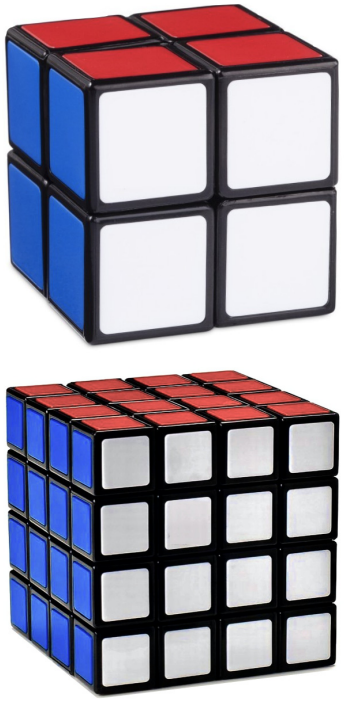

Figure 5.2: *Top* : The Ramses simulation box at Level $l = 1$ consisting of 1 oct of 8 cells. *Bottom* : The same simulation box refined at Level $l = 2$.

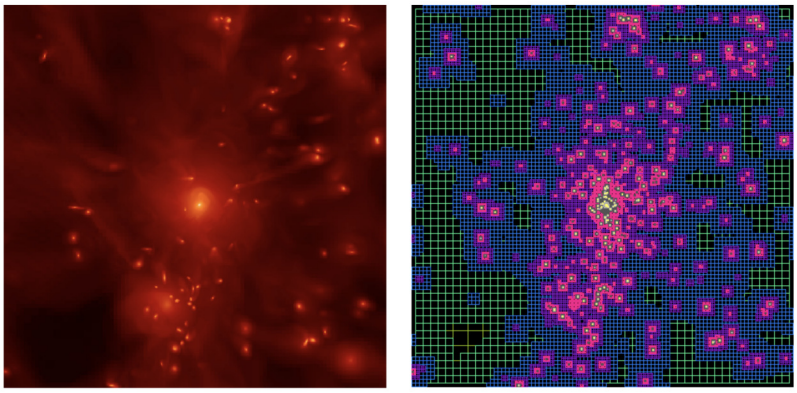

Figure 5.3: Gas density map (*left*) of Ramses galaxy cluster simulation with its corresponding AMR grid. We see that the refinement strategy allows to evolve the densest regions at the highest resolution while waisting a minimal computational effort in low density regions. – Credits : R. Teyssier

as a cell fulfills the refinement criterion it is refined to another level. However, this refinement is constrained by the scale factor in cosmological simulation and cannot exceed the defined maximum level of refinement $l_{\max}$.
If a cell has no children, it is called a "leaf" cell, otherwise it is a "split" cell.
Figure 5.3 illustrates such adaptative evolution of the grid which allows to put most of the computational effort on the densest regions.

Ramses evolves the fluid equations down the refinement tree as smallest cells do not share the same time step as the coarsest. As a matter of fact, the time step Δt is controlled by the Courant, Friederich and Lewy (CFL) condition which forbids the gas from travelling more than the length of the cell. Otherwise, we could end up in an unphysical negative mass in the cell. Therefore,

$$\Delta t \leqslant C \frac{\Delta x}{v} \tag{5.2}$$

where $C < 1$ is the Courant factor and v the gas velocity. Usually, it is required that the gas cannot move more than half a cell, i.e. $C = 0.5$. Hence, we can see that the most refined regions are updated more often than the coarsest ones. For each level, the time step is evaluated for all cells and the minimal value set the level's time step. The time step for all cells at a coarser refinement level l is twice as long as the time step for the level $l + 1$.

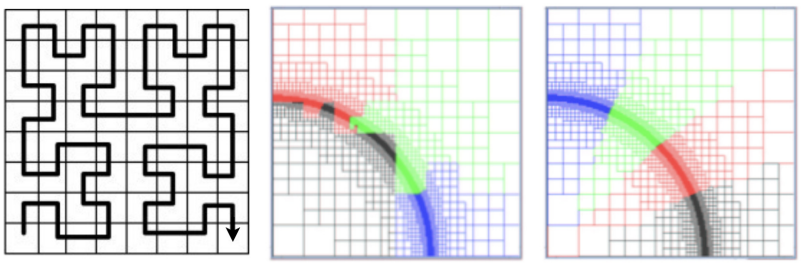

Figure 5.4: *Left* : The Hilbert curve, a continuous fractal space-filling curve used for ordering cells and portioning the simulation volume. *Middle* and *right* : Illustrations of load balancing strategies angular and hilbert respectively. Each colored portion is parsed to a central processing unit (CPU)

For expensive simulations, such as ours, computational tasks needs to be split across multiple processors. Using MPI, the simulation volume is split across computational domains[2] based on a cell ordering method such as the Peano-Hilbert curve shown in Figure 5.4 (planar and angular decomposition are also available). Such curve allows to link all simulation cells. The length of the curve is then split among the processors which all get an equal number of cells[3] .

2: they contain a volume of adjacent cells and particles, as well as ghost regions surrounding the domain.

3: This is the load balacing process.

5.2 Magnetic fields

The cosmological simulations carried out during this PhD contain DM and stars particles (treated by the N-body solver), and, a baryon component which behaves like an ideal, conducting plasma together with magnetic fields laid down on a grid. To treat all these components simultaneously in a self-consistent way, the MHD equations have to be solved in a cosmological setting. For this, the MHD equations are usually written in the comoving frame ($\mathbf{x} = \mathbf{r}/a$).

However, this formulation renders the equations with lots of additional factors with explicitly depends on the scale factor $a(t)$[4] . Martel & Shapiro [174] introduced a different transformation to so-called "super-comoving" coordinates which allows to cast the MHD equations into a more convenient form. It is defined in a similar way as the comoving coordinates but replaces the physical time t by a new function t_x which depends on the expansion factor as :

4: These equations no longer have the form of hyperbolic conservation laws

$$\mathbf{x} = \frac{\mathbf{r}}{a}, \qquad \mathrm{d}t_x = \frac{\mathrm{d}t}{a^2}, \tag{5.3}$$

Therefore, all the time derivatives in the MHD equations are now formulated with respect to this new function. Additionally, the quantities therein get substituted by new "super-comoving" quantities :

$$\begin{aligned} \rho_x &= \rho a^3, & T_x &= T a^2, \\ \phi_x &= \left(\phi + \frac{1}{2} a\ddot{a}x^2\right) a^2, & S_x &= S a^{-(3\gamma-8)}, \\ P_x &= P a^5, & B_x &= B a^{5/2}, \\ \epsilon_x &= \epsilon a^2, & \mathscr{H}_x &= a\dot{a}, \end{aligned} \tag{5.4}$$

where we have ρ the gas density, ϕ the total gravitational potential, ϵ the internal fluid energy, T the temperature, P the thermal pressure, $\mathscr{H}$ the super-comoving Hubble constant, B the magnetic field strength and S the modified entropy following Ryu *et al.* [175]

given by :

$$S = \frac{p}{\rho^{\gamma-1}}, \tag{5.5}$$

In this new super-comoving framework, most of the terms depending on the scale factor a cancel out and the equations in the MHD framework become[5] :

5: see appendixes of Doumler & Knebe [176] for their derivation

$$\Delta_x \phi_x = 4\pi \mathrm{G}\,(\rho - \bar{\rho})\, a(t), \tag{5.6}$$

$$\frac{\partial \rho_x}{\partial t_x} + \boldsymbol{\nabla}_x \cdot (\rho_x \mathbf{v}_x) = 0, \tag{5.7}$$

$$\frac{\partial \rho_x \mathbf{v}_x}{\partial t_x} + \boldsymbol{\nabla}_x \cdot \left[\rho \mathbf{v}_x \mathbf{v}_x + \left(P_x + \frac{B^2}{2\mu}\right)\mathbb{1} - \frac{\rho \mathbf{B}_x \mathbf{B}_x}{2\mu}\right] = -\rho_x \boldsymbol{\nabla}_x \phi_x, \tag{5.8}$$

$$\frac{\partial \rho_x E_x}{\partial t_x} + \boldsymbol{\nabla}_x \left[\mathbf{v}_x \left(\rho E_x + P_x + \frac{B_x^2}{2\mu}\right) - \frac{1}{\mu}\mathbf{B}_x\,(\mathbf{v}_x \cdot \mathbf{B}_x)\right] = -\rho_x \mathbf{v}_x \cdot \left(\boldsymbol{\nabla}_x \phi_x\right) + \mathscr{H}_x \frac{B_x^2}{2\mu}, \tag{5.9}$$

$$\frac{\partial \mathbf{B}_x}{\partial t_x} + \boldsymbol{\nabla}_x \times (-\mathbf{v}_x \times \mathbf{B}_x) = \frac{1}{2}\mathscr{H}_x \mathbf{B}_x, \tag{5.10}$$

$$\boldsymbol{\nabla}_x \cdot \mathbf{B}_x = 0, \tag{5.11}$$

where the spatial derivatives changed to :

$$\boldsymbol{\nabla}_x = a\boldsymbol{\nabla}, \tag{5.12}$$

$$\mathbf{v}_x = a\mathbf{v} - \dot{a}\mathbf{r}, \tag{5.13}$$

and the total fluid energy E_x is the sum of the kinetic, internal and magnetic energies. We see that if we drop the x subscripts, the above super-comoving ideal MHD equations in conservative form closely resemble their non-cosmological counterparts. The only noticeable differences are in Equation 5.6 where $\bar{\rho}$ is the average total density in the simulation box,

$$\bar{\rho} = \Omega_m \rho_{c,0} = \Omega_m \frac{3H_0^2}{8\pi \mathrm{G}}, \tag{5.14}$$

and the two magnetic Hubble terms in the right hand sides of Equation 5.9 and Equation 5.10. We see that this is the only time that the cosmology explicitly enters in the equations.
Therefore, this convenient set of equations is easier to implement in the code than the comoving equations while accounting for the same physics. Moreover, it makes it easier to employ numerical schemes which were originally designed for non-cosmological purposes.

Let us discuss now how Ramses solves the induction Equation 5.10 on the grid.
Based on the MUSCL-Hancock approach already used in the hy-

drodynamic version of Ramses, Fromang *et al.* [177] implemented a Godunov scheme to solve the ideal MHD equations. The induction equation is evolved in time using the standard CT scheme of Evans & Hawley [178].
By taking the induction equation[6] in the :

$$\frac{\partial \mathbf{B}}{\partial t} + \nabla \times (\mathbf{v} \times \mathbf{B}) = 0 \tag{5.15}$$

in its integral form (using Stoke's theorem) :

$$\frac{\partial}{\partial t} \int_S \mathbf{B} \cdot \mathrm{d}\mathbf{n} + \oint_L (\mathbf{v} \times \mathbf{B}) \cdot \mathrm{d}\mathbf{l} = \frac{\partial}{\partial t} \phi_B + \oint_L \mathbf{E} \cdot \mathrm{d}\mathbf{l} = 0, \tag{5.16}$$

this suggests a surface-average form.
$\mathbf{E}$ is the electric field defined by the relation $\mathbf{E} = \mathbf{v} \times \mathbf{B}$. This is why, opposed to cell-centered Euler-type hydro variables[7] , Ramses uses face-centred values for magnetic fields (a staggered mesh approach)[8] .
Then, the 2D Riemann problem at the cell edges has to be solved in order to obtain the time-averaged electric fields. The face-centered magnetic fields can be updated by a contour integral of the electric field at the cell edges. This is the constrained transport method.

By construction, the magnetic flux across each cell is conserved and allows $\nabla \cdot \mathbf{B}$ to vanish to machine precision.
Different 2D Riemann solvers are available in Ramses but during this work we only use the Harten-Lax-van Leer-Discontinuities (HLLD) solver[9] .

5.3 Thermal conduction

Thanks to the work of Dubois & Commerçon [179], the anisotropic thermal conduction as well as the cosmic ray (CR) diffusion is implemented in Ramses. We will only discuss the anisotropic thermal conduction scheme that the authors implemented as we did not use the CR module for the work presented in this thesis.
A limiting problem with the implementation of diffusion processes is that the stability criterion is given by :

$$\delta t_{\mathrm{diff}} = \frac{\Delta x^2}{2 D_{\mathrm{diff}}}, \tag{5.17}$$

where D_{diff} is the diffusion coefficient. Unlike the hydrodynamical CFL condition given is Equation 5.2, the diffusion stability does not scale linearly with the cell size Δx. Hence, it could be a bottleneck for an explicit diffusion scheme to verify, at all times, this condition (especially in galaxy clusters simulations where strong contrasts

6: Here, we only want to illustrate the motivation behind the constrained transort scheme, hence we use the classical induction equation here for clarity

7: density, velocities, total energy

8: On the other hand, cell-centred schemes are easier to develop but they require divergence cleaning methods which are time consuming, not robust and not conservative

9: The other 2D Riemann solvers available are HLL, LLF, Roe and upwind

in gas densities trigger refinements). For this reason, an implicit numerical solver was favoured and which does not need to fulfill a time step constraint at the expense of numerical complexity.
Thermal conduction appears in the energy conservation equation as :

$$\frac{\partial \rho \epsilon}{\partial t} + \boldsymbol{\nabla} \cdot \left[(\rho \epsilon + P)\, \mathbf{v} - \frac{\mathbf{B}\,(\mathbf{B} \cdot \mathbf{v})}{4\pi} \right] = -\boldsymbol{\nabla} \cdot \mathbf{Q}_{\rm cond}, \tag{5.18}$$

where $\mathbf{Q}_{\rm cond}$ is the heat flux carried by electrons. Thermal conduction, in the right hand side, is treated separately as a source term from the MHD solver of Fromang *et al.* [177].
In the presence of magnetic fields , the conduction of heat through electrons[10] in a fully ionised plasma is [179] :

$$\frac{\partial \rho \epsilon_e}{\partial t} = -\boldsymbol{\nabla} \cdot \mathbf{Q}_{\rm cond}, \tag{5.19}$$

$$= -\boldsymbol{\nabla} \cdot \left[-\kappa_{\parallel} \mathbf{b}\,(\mathbf{b} \cdot \boldsymbol{\nabla})\, T_e \right] - \boldsymbol{\nabla} \cdot \left(-\kappa_{\rm iso} \boldsymbol{\nabla} T_e \right), \tag{5.20}$$

where we have $\mathbf{b} = \mathbf{B}/|\mathbf{B}|$ the unit vector in the direction of the local magnetic field, T_e is the electronic temperature, $\kappa_{\rm iso}$ and $\kappa_{\parallel}$ are the isotropic and parallel conduction coefficient (with respect to the magnetic field lines) respectively with $\kappa_{\parallel} = \kappa_{\rm Sp} - \kappa_{\rm iso}$. In many astrophysical cases, $\kappa_{\rm iso}/\kappa_{\parallel} \ll 1$ since the Larmor radius is much smaller than the mean-free-path of electrons[11] .
For instance, in the hot ICM of galaxy clusters with $T_e = 3\,\mathrm{keV}$, electron density of $n_e = 10^{-2}\,\mathrm{cm}^{-3}$ and $B = 1\,\mu\mathrm{G}$, the Larmor radius is $10^8\,\mathrm{cm} = 3.24 \times 10^{-14}\,\mathrm{kpc}$ while the mean free path of electrons is $10^{21}\,\mathrm{cm} = 0.32\,\mathrm{kpc}$.
However, an isotropic conductivity of 1% was set to ensure numerical stability.

10: but this can be be also applied to ions and electrons by assuming a single temperature model

11: We will go through thermal conduction in a more theoretical setting in Chapter 8.

First, the anisotropic fluxes are computed at cell corners from the face-average magnetic fields. This step corresponds to the term in square brackets in Equation 5.20. Then, the anisotropic heat flux is evaluated at the cell interfaces from the the corner values.
Whereas, for the isotropic heat flux, it just follows the classical discretisation from left and right temperature values at the cell interface.
The discretisation of Equation 5.20 can be translated into a matrix system $A\mathbf{x} = \mathbf{c}$ where the matrix A includes the conduction coefficient, time step and cell size while the vectors $\mathbf{x}$ and $\mathbf{c}$ contain respectively the temperatures and the energy densities (more details can be found in the paper of Dubois & Commerçon [179]).
The conjugate gradient algorithm of Commerçon *et al.* [180] which was originally implemented for radiation hydrodynamics is used to solve this system of linearised equations.

The diffusion on the AMR is performed using Dirichelet boundary conditions where cell values at level boundaries are imposed for fine-to-coarse or coarse-to-fine interfaces.

This numerical implementation is augmented by modelling a multi-temperature component with temperature coupling of ions and electrons.
We will not go into further details, as we did not use this model in our work yet, but basically it allows to track the electronic and ionic temperatures separately.

Unfortunately the implementations of Dubois & Commerçon [179] were not available in the latest version of Ramses that benefit from upgraded physical models. Therefore, during this PhD we undertook the implementation of the anisotropic diffusion of heat and cosmic rays in the publicly available version of Ramses.

5.4 Heating & Cooling

As we discussed in the previous chapter, the process of gas cooling is central for star formation. We will now describe how Ramses treats the radiative cooling of the gas.

Cooling and heating rates depend on the gas density, temperature and ionisation state. However, by assuming collisional ionisation equilibrium, the ionisation state can be calculated as a function of density and temperature alone. Therefore, the ionisation state does not need to be tracked in the code. Moreover, we assume that for a gas with density ρ, temperature T and metallicity Z that the ion number densities are in equilibrium, values of the cooling function $\Lambda(\rho, T, Z)$ can be constructed for a given set (ρ, T, Z).

Ramses reads such tabulated values of the cooling function and interpolates across the table for given (ρ, T, Z) values. Such an approach is advantageous as it does not require a memory-intensive tracking of the chemistry of the gas.
Different gas atomic and metal cooling models are implemented in Ramses, but for this work, we adopted the standard H and He cooling from Katz *et al.* [181], with an additional contribution from metals based on the model of Sutherland & Dopita [182] above 10^4 K, while below 10^4 K rates of Rosen & Bregman [183] are used. Ramses does not evolve separately different metals, but advects a total gas metallicity with the hydrodynamical equations as a passive scalar. The metallicity is sourced by the SN feedback model

that will be explored in Section 5.5.3.
Moreover, a UV background is included separately assuming the parametrization of Haardt & Madau [184].

5.5 Sub-grid models

In addition to the treatment of magnetic fields, thermal conduction, and gas heating and radiative cooling, many other physical processes have been implemented in Ramses. We will present in this section the sub-resolution physical models that have been used for the work presented in this PhD thesis. We will see how stars are formed in Ramses simulations and how stellar feedback interacts with the surrounding gas. We will review the models of black hole (BH) seeding and growth and how feedback from active galactic nuclei (AGNs) is implemented.

5.5.1 The polytropic equation of state

The multiphase structure of the interstellar medium (ISM) is a crucial ingredient for star formation and the impact of SN and AGN feedback. However, cosmological simulations cannot resolve such scales hence they neglect various phenomena in the interstellar medium (ISM) such as thermal instabilities and turbulence which give rise to a complex multi-phase ISM structure.
The idea of a sub-grid multiphase ISM in Ramses translates into a heating due to an effective thermal pressure unresolved by the simulation, it takes the form of a polytrope with the equation of state :[12]

$$P = K\rho^{\gamma} \quad \Longleftrightarrow \quad T = K\rho^{\gamma-1}, \tag{5.21}$$

$$T = T_0 \left(\frac{\rho}{\rho_0}\right)^{\gamma-1}, \tag{5.22}$$

where K, is the proportionality constant, ρ_0 is the density threshold for SF, T_0 is the polytropic temperature and γ is the polytropic index which is also the heat capacity ratio.
Actually the constant K defines a pseudo-entropy. Indeed, the actual entropy of an ideal gas is given by

$$S = \ln\left(K^{1/(\gamma-1)}\right) + \text{cst}, \tag{5.23}$$

with :

$$K = \frac{k_B\, T}{n^{2/3}}, \tag{5.24}$$

which is commonly defined as the cluster specific entropy in X-ray astronomy [185].

12: We consider a monoatomic ideal gas undergoing a reversible adiabatic process (isentropic process), therefore the polytropic index equals the heat capacity ratio γ

This sub-grid multiphase ISM model will stabilise the gas against gravitational collapse. Springel & Hernquist [186] found for indexes $\gamma > 4/3$ that this effective pressure could provide enough vertical thickening to stabilise gaseous disks against rapid break-up into clumps due to dynamical instabilities. Below this value, the gas is unstable.

This can be understood by looking at the Jeans' mass (M_J) and length (λ_J) which describe a system where the gas pressure balances the gravitational collapse under its own weight.

$$\lambda_\mathrm{J} = c_s \sqrt{\frac{\pi}{\mathrm{G}\rho}} = \sqrt{\frac{\pi \gamma \mathrm{k_B}\, T}{\mathrm{G}\rho\mu m_h}}, \tag{5.25}$$

$$M_\mathrm{J} = \rho \lambda_\mathrm{J}^3 \tag{5.26}$$

which become by using the polytrope in Equation 5.22 :

$$\lambda_\mathrm{J} \propto \sqrt{\frac{T}{\rho}} \propto \rho^{\gamma/2-1}, \tag{5.27}$$

$$M_\mathrm{J} \propto \sqrt{\frac{T^3}{\rho}} \propto \rho^{3\gamma/2-2}. \tag{5.28}$$

Therefore, we see that the Jeans length become independent of the density for $\gamma = 2$ while for $\gamma = 4/3$ the Jeans mass is independent of the density. This is why γ is usually chosen between $4/3 \sim 1.333$ and 2 in numerical simulations.[13] In the simulations presented in this thesis, we adopt a value of $\gamma = 5/3 \sim 1.667$.

In a nutshell, this sub-grid multiphase ISM model is equivalent to an entropy floor K below which no gas can cool. The gas will be adiabatically heated along the adiabate defined in Equation 5.24 which raises the gas parcel temperature while lowers its density. Hence, objects are kept artificially big.

5.5.2 Star formation

Stars form in the very dense environment of molecular clouds. When the kinetic energy of the gas does no longer balance the potential energy, i.e. when the cloud mass is greater than the Virial mass, the molecular cloud collapses. During this collapse, the fragmentation of the gas leads to the formation of stars. The largest molecular clouds (called giant molecular clouds) have typical sizes of 5 to 200 pc which is far beyond what most cosmological

13: For instance, in Horizon simulations, the adiabtaic index is set to $\gamma = 7/4 = 1.75$

Figure 5.5: A star forming region in our Milky Way, a dark cloud of cosmic dust illuminated by the brilliant light of new stars. This dense cloud is a star-forming region called Lupus 3, where hot stars are born from collapsing masses of gas and dust. – Credits : ESO/VLT/R. Colombari

numerical simulations can resolve. Therefore, sub-grid models for star formation (SF) must be adopted guided by observational constraints.
Such a model requires an analytical expression which converts a given portion of gas in a cell into a stellar population as soon as criteria for star formation are met.
This is given by the Kennicutt relation [187] relating the surface density of SF, Σ_*, to the gas surface density, Σ :

$$\Sigma_* = 2.5 \times 10^{-4} \frac{\Sigma^{1.4}}{1 \mathrm{M}_\odot \, \mathrm{pc}^{-2}} \mathrm{M}_\odot \, \mathrm{kpc}^{-2} \, \mathrm{yr}^{-1}, \tag{5.29}$$

In simulations, such a relation can be similarly expressed in terms of a volume density where the SF rate in a cell is given by :

$$\dot{\rho}_* = \begin{cases} \epsilon_{\mathrm{SF}} \, \rho \, / \, t_{\mathrm{ff}}, & \text{if } \rho > \rho_0, \\ 0, & \text{otherwise}, \end{cases} \tag{5.30}$$

with ϵ_{SF} the SF efficiency being usually of the order of a few percent [188], and $t_{\mathrm{ff}} \propto (\mathrm{G}\rho)^{-1/2}$ is the local free-fall time which yields $\dot{\rho}_* \propto \rho_{\mathrm{gas}}^{1.5}$.

In simulations, the density threshold ρ_0 for the SF is typically set by the Jean mass at the highest resolution. As we saw in the first section of this chapter, Truelove *et al.* [173] found that artificial fragmentation can be avoided by resolving the Jeans length by at least 4 cells hence we should choose

$$\lambda_{\mathrm{J}} = N_{\mathrm{cell}} \Delta_x \propto \sqrt{\frac{T_0}{\rho_0}}, \tag{5.31}$$

with $N_{\mathrm{cell}} \geqslant 4$. Therefore, we can choose a density threshold for SF based on this Jeans criterion for a given temperature floor T_0.
Or equivalently, we can define an entropy floor, K_0, based on Equation 5.24 below which gas will be converted to stars, i.e. $K_0 \propto T_0 / n_0^{2/3}$.

As a result, the amount of stars created from the gas satisfying the SF threshold is given by Equation 5.30. Once stars are formed, they are decoupled from the gas as a "star" particles[14] which traces a continuous stellar mass distribution following the Salpeter [189] initial mass function. When a gas cell is eligible for star formation, collisionless star particles are spawned using a Poisson random process. In Ramses, SF is a stochastic process, therefore two simulations do not share the same SF. Hence, two simulations might not share the same stellar content and feedback.

14: The star particle is treated as an N-body particle in Ramses

5.5.3 Stellar feedback

Based on their spectral properties, supernovae (SNe) are divided into several classes. SNe of type I do no show any Balmer lines of Hydrogen in their spectrum, in contrast to those of Type II [190]. The type I of SNe is further subdivided : SNe Ia show strong emission of SiII (at 6150Å, [191]) where no SiII emission is visible in spectra of Type Ib,c.

SNe of type II and Ib,c are the final stages in the evolution of massive stars ($M \geqslant 8\mathrm{M}_{\odot}$). Once the fusion of of the Iron nucleus is reached, no more energy can be gained from fusion to heavier elements. The pressure inside the star can no longer balance the gravitational force which cause the star to collapse under its own gravity until the so-called rebounce occurs : a shock wave runs towards the surface and heat the infalling material. The star explodes. In its center, a neutron star remains (or black hole, depending on the mass of the Iron core). The major fraction of the binding energy is emitted in the form of neutrinos, which are later scattered and absorbed in the hot stellar envelope contributing to its explosion and the emission of photons. The explosion chemically enriches the ISM which mainly α elements (particles with an even number of protons and neutrons) [192].

Figure 5.6: The famous Crab nebula's neutron star (visible as a pulsar). The core-collapse SN explosion might be the one identified by Chinese astronomers in 1054. – Credits : Adam Block

On the other hand, SN of Type Ia are most likely explosions of white dwarfs (final evolution state of less massive stars). The compact star is stabilized by the electron degeneracy pressure[15] and can be stable if its mass does not exceed the Chandrasekhar mass[16] , otherwise the gravitational force wins. As the progenitors of SN Type Ia are low-mass star, the explosion does not produce strong winds in contrast to core-collapse SNe.

15: Phenomenon related to the Pauli exclusion principle

16: $M_{\mathrm{Ch}} \sim 1.44\mathrm{M}_{\odot}$

Therefore, we will focus on the modelling of core-collapse SNe (Type II and Ib,c). The strong shock escaping the stellar envelope can be modelled as a Taylor-Sedov blast wave [193, 194]. A method implemented in Ramses by Dubois & Teyssier [195], referred to "kinetic feedback", deposits mass, momentum, and energy of a pre-evolved Sedov-Taylor blast wave, onto the grid over 2-3 surrounding grid cells after 10 Myr[17] . Indeed, as the initial blast wave phase cannot be resolved in the simulation, the Sedov-Taylor blast wave is pre-computed and then placed on the grid cells around the star particle. Despite an accurate picture of the early SN evolution, Dubois *et al.* [196] shows that this kinetic feedback is unable to regulate remaining cold gas reservoirs in massive halos.

17: The assumption is that the star particle contains on average one Type II SN with a lifetime of $\sim 10\,\mathrm{Myr}$

Another model of SN feedback by Teyssier *et al.* [139] implemented in Ramses, referred to as delayed cooling, mimic non-thermal pro-

cesses[18] in the ISM that are able to dissipate on a much longer time scale (compared to the thermal component) before being radiated away (in the spirit of Stinson *et al.* [138]).
The SN energy is released both in the classical energy component and in a tracer component (passive scalar), which is denoted as "non-thermal" and is passively advected with the flow. This passive non-thermal energy decays on a time-scale defined by the user (but see in Appendix A of Dubois *et al.* [196] for a derivation of a dissipation timescale based on the resolution and the parameters of the kinetic SN feedback).

18: Such as X-ray , turbulent, magnetic, cosmic ray heating or radiative pressure for instance

In short, SN feedback is implemented based on the model in which each newly formed star particle releases a fraction $\eta_{\rm SN}$ of its mass and metals with a yield y into the surrounding gas cells through a kinetic SN feedback after 10 Myr. Gas cooling can be delayed on a timescale $t_{\rm diss}$ after the SN explosion to mimic non-thermal processes which cause the energy to be dissipated on longer timescales.

5.5.4 Black hole growth

Another way to deal with limited resolution in simulation of gravitation collapse than the Jeans heating presented in Section 5.5.1, is the use of sink particles. Instead of artificially stopping the gas collapse at a chosen scale, sink particles can approximate the small scale evolution, unresolved by the simulation, by a immediate collapse onto a point mass. This sink particle is collisionless and will interact with the gas that remains only through gravity, accretion and ejection of mass. It is therefore disconnected from the hydrodynamics and cannot be destroyed.
While these assumptions are extremes, sink particles are commonly used in astrophysical codes mainly in star formation schemes (used in Lagrangian SPH codes like Gadget [198] and Gasoline [199] but also in Eulerian codes like Enzo [200], Flash [201] or Athena [202] for instance).

Ramses uses collisionless sink particles to model black hole (BH) growth and evolution. The potential sites for BH seeding are found on the fly by the Phew clumpfinder implemented by Bleuler & Teyssier [197] in Ramses. We will describe the six main steps illustrated in Figure 5.7 leading to the seeding of a BH sink particle :

1) We start with a 3D density field on the AMR grid where the particles have been projected onto the grid beforehand.

2) Then, all cells above a a given density threshold are marked (shown in green in Figure 5.7).

3) Every cells is assigned to a peak by following the path of steepest gradient ascent (after having checked that the cell is not the local density maximum). All cells assigned to the same peak form a "peak patch".

4) All saddle point densities connecting each patch are identified. The saddle point are "significant" if the ratio of the peak density to the saddle density is greater than a pre-defined threshold (usually set to 2). If not, the peak patch will be merged to the one connected by the highest saddle point. For instance, the pink peak patch of step 3) in Figure 5.7 is merged to the turquoise peak patches with which it shares the highest saddle point. Peak patched are ordered by ascending peak density beforehand to make sure that no peak patch is merged with one that has already been merged into another one before.

5) After having merged the pink patch which have the lowest peak, the next patch having the lowest denisty peak is the yellow one which is then merged to the red peak patch with which it shares the highest saddle point.

6) The process is repeated untill the saddle density threshold is reached. It means that the merging process stops if the saddle density is below this defined threshold. For instance, the saddle point connecting the red to the blue patch in step 6) of Figure 5.7 have a density lower than the saddle threshold. Therefore, the two peak patches cannot be merged and only significant peak pacthed remains. Whereas, all insignificant peak patch have been either rejected or merged to form significant ones. These relevant patches are labeled as "clumps".

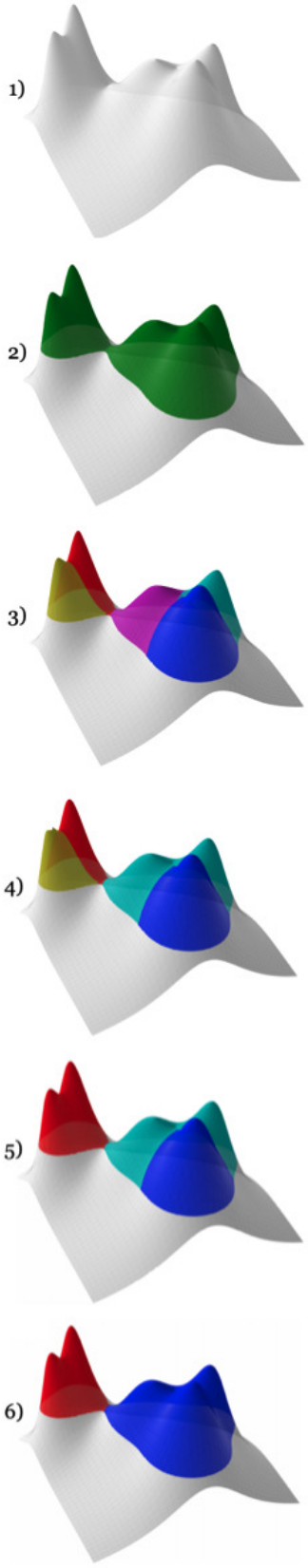

Figure 5.7: Working principle of the RAMSES clump finder represented on a 2D surface – Credits : Bleuler & Teyssier [197]

The PHEW algorithm identifies these clumps on the fly and requires 3 parameters to select potential BH formation sites : the density threshold, the relevance (or peak-to-saddle) threshold and the saddle threshold. The steps described above can be sum-up in 4 basic steps : watershed segmentation, saddle point search, noise removal and sub-structure merging. More technical aspects on the implementation can be found in Bleuler *et al.* [203].

The gas inside a sphere having a radius of 4 resolution elements surrounding the density peak is investigated[19] . First a Virial check which makes sure that the gravitational field is compressive and

strong enough to overcome internal gas support (it must be undergoing contraction along all directions). Secondly, a collapse check, which ensure that the gas is not only accelerated toward the centre of the considered volume but also that this gas is contracting. Finally, a proximity check, forbids the gas that is infalling to an already existing sink to create another sink (even if this density peak fulfills all criteria for sink formation).

19: We call this sphere the accretion sphere, with $4\Delta x$ is the accretion radius.

The choice for the initial seed mass is arbitrary. Biernacki *et al.* [204] indicated that setting the seed BH mass to the minimum Jeans mass of the simulation appears to be the right choice. A typical $M_{\rm seed} = 10^5 \mathrm{M}_\odot$ value is usually adopted in large-scale hydrodynamical simulations (e.g. in Booth & Schaye [144]). Indeed, direct collapse scenarios of SMBH formation do predict seed masses of this magnitude [205].

Once the SMBH is formed, it grows in mass thanks to the accretion of gas in its surroundings. While spatial and time scales relevant for SMBH accretion are far from being resolved, a model for gas accretion is needed. The most popular approach is the Bondi-Hoyle-Lyttleton formula (later Bondi for short; [206–208]) which gives a formula for the accretion rate (see review of Edgar [209] for its derivation) :

$$\dot{M}_{\rm Bondi} = 4\pi\rho_\infty r_{\rm Bondi}^2 v_{\rm Bondi}, \tag{5.32}$$

with $\rho_\infty = \bar{\rho}/\alpha(x_{\rm sink})$ where α is the dimensionless density profile of the Bondi self-similar solution (see [204] for more details), $\bar{\rho}$ the mean density inside the sink sphere[20] , $x_{\rm sink} = r_{\rm sink}/r_{\rm Bondi}$ and the sink radius and velocity defined as follows :

$$r_{\rm Bondi} = \frac{\mathrm{G}M_{\rm sink}}{v_{\rm Bondi}^2}, \tag{5.33}$$

$$v_{\rm Bondi} = \sqrt{c_s^2 + v_{\rm rel}^2}, \tag{5.34}$$

with $v_{\rm rel}$ the relative velocity the sink and the average gas velocity inside the sink sphere.

Springel *et al.* [135] and Booth & Schaye [144] proposed to boost the Bondi accretion rate in Equation 5.32 to account for unresolved fluctuations in the gas density and temperature at scale below the cell size. It replace the gas sounds speed by :

$$c_s \rightarrow \frac{c_s}{\beta(\bar{\rho})}, \tag{5.35}$$

20: The sink (or accretion) sphere is defined by a radius of $4\Delta x$ where an uniform distribution of cloud particles probe in the accretion region.

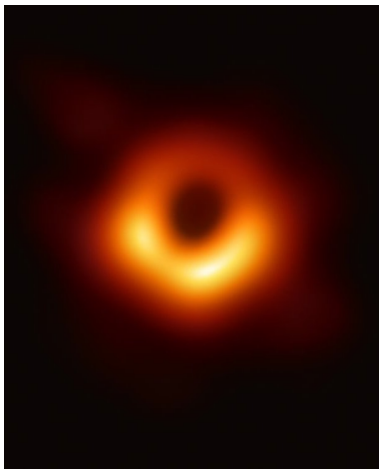

Figure 5.8: Direct visual evidence of the supermassive black hole in the centre of Messier 87 and its shadow It shows radio-wave emission from a heated accretion ring orbiting the object – Credits : The Event Horizon Telescope Collaboration

where β is the boost factor defined as :

$$\beta(\rho) = \max\left[\left(\frac{\rho}{\rho_*}\right)^{2/3}, 1\right], \tag{5.36}$$

with ρ_* is the SF density threshold.
The actual accretion rate is capped by the Eddington rate $\dot{M}_{\rm Edd}$ such that

$$\dot{M}_{\rm acc} = \min\left(\dot{M}_{\rm Bondi}, \dot{M}_{\rm Edd}\right) \tag{5.37}$$

with :

$$\dot{M}_{\rm Edd} = \frac{4\pi G M_{\rm sink} m_p}{\epsilon_r \sigma_T c} = \frac{M_{\rm sink}}{t_S}, \tag{5.38}$$

where σ_T is the Thomson cross-section, ϵ_r is the Shakura & Sunyaev [210] radiative efficiency[21] for a SMBH and $t_S \sim 45\,$Myr is the Salpeter time. The Eddington limit actually reflects that accretion energy is converted to accretion luminosity at high accretion rates. The pressure from this radiation actually removes the ionised gas in the SMBH vicinity by pushing it away. Because the scale at which the radiation pressure acts is not resolved, the net budget will be the Eddington-limited Bondi accretion.

21: $\epsilon_r = 0.1$

Once the the sink particle accretion rate is known, gas is removed from the cells falling into the sink sphere by integrating over a time step.

While the Bondi accretion model is of great simplicity it completely ignores rhe role of angular momentum[22] , turbulence and additional physics such as the magnetised and multi-phase nature of the ISM in the SMBH vicinity.
However, Rosas-Guevara *et al.* [142] showed that accounting for angular momentum has no effect on the Bondi accretion for halos larger than $10^{11.5}\mathrm{M}_\odot$, which is well below galaxy cluster masses that we are interested in. It should be noted that Negri & Volonteri [211] found that the Bondi formalism can, depending on the resolution, lead to both over- and underestimations of the BH growth in Zeus simulations.

22: Bondi studied a spherically symmetric accretion

Typically, the sink particle experiences two accretion regimes. First, the cold accretion regime where the gas cooling dominate over the AGN heating. The gas accretion rate is so high that it is considered to be Eddington-limited. As the sink grows and becomes massive enough, heating will dominate over gas cooling and the sink enters in the hot accretion regime. The gas temperature is considered to be large enough that the accretion rate is now given by the Bondi formula.

In addition to gas accretion, SMBHs can also grow via mergers. A "young" sink particle is merged to an "old" one if they are less than one accretion radius apart (i.e. $4\Delta x$). Two "young" sinks are merged if their distance is less than two accretion radii [197]. Before merging two sinks, an additional check on their relative velocity can be executed in order to determine if the system is actually bound.

5.5.5 Black hole dynamics

Unfortunately the dynamics of the SMBH cannot be properly resolved in cosmological simulations, with force resolution larger than a few parsec to kpc. Indeed, under the broad assumption that the conditions at the smallest resolution scale drive the SMBH evolution, the dynamics of a single SMBH object cannot be described properly. It results in spurious oscillations of the SMBH in the potential well of its host halo, due to external perturbations and the finite resolution effects, particularly during merger events. The dynamical evolution of the point mass particle is subject to the gravitational force of the gas, dark matter and star particles but also to a drag force due to the tight coupling of the sink and the accreted gas.

This drag force has often be invoked in the literature to justify different implementations to keep the BHs in their host halo.
One way is to resort to an ad hoc centering prescription designed to keep black holes very close to the potential minimum [212]. For instance in Illustris-TNG simulations, the SMBH is "pinned" to the local minimum of the potential field [143]. In gas-rich disk simulations, Gabor & Bournaud [213] chose to artificially push the BH in the direction of the stellar centre of mass to avoid its scattering by interactions with massive, dense, star-forming clouds. Another way is to use more sophisticated sub-resolution models for dynamical friction [214–216] such as in Horizon-AGN simulation [217].

However, Biernacki *et al.* [204] implemented in Ramses a physically motivated model based on the Eddington-limited accretion. They chose to treat the gravitational interaction between the sink and the matter distribution (as well as between the sink and possible other sinks) using a direct summation method with a softening radius set to $2\Delta x$ [197]. The choice of this approach over the Particle-Mesh method is motivated by more accurate sink particle trajectories.
The main assumption is that the gas accretion rate onto the accretion disc is set by the Bondi formula which corresponds to the large scale accretion flow. But the accretion onto the SMBH is set by the

Eddington value. The difference between the two rates is therefore the gas being decreted from the accretion disc by the radiation pressure which is redistributed on large scales, at a rate :

$$\dot{M}_{\rm dec} = \dot{M}_{\rm Bondi} - \dot{M}_{\rm acc} \tag{5.39}$$

where $\dot{M}_{\rm acc}$ is given by Equation 5.37.
This process of gas accretion and ejection leads to an additional momentum exchange between the gas and the sink particle, hence an additional drag force.
This additional drag force is modelled by requiring a fixed center of mass of the joint gas+sink system during the accretion and a conserved total momentum. More details on the implementation can be found in Biernacki *et al.* [204]. The advantage of such model is that it is a fully momentum conserving drag force.

We see that in the case of an unlimited Bondi accretion (i.e. $\dot{M}_{\rm Bondi} < \dot{M}_{\rm Edd}$), no gas is decreted from the accretion region. The momentum transfer only comes from the accreted gas mass onto the sink particle. In the opposite case of a strong Eddington-limited rate, $\dot{M}_{\rm dec}$ is maximal which result in a strong drag force between the gas and the sink particle.

However, the motivation for keeping BHs in the center of host halos is not obvious. Indeed, observations of AGNs in dwarf galaxies claim that BHs are not located at the centers of their host galaxies with an offset between tens of parsecs to a few kiloparsecs (see e.g. Shen *et al.* [218] and Reines *et al.* [219]). For instance, recent simulations of Pfister *et al.* [220] or Boldrini *et al.* [221] showed that BHs in dwarf galaxies are expected to be wandering around the central regions after the occurrence of mergers or due to tidal stripping or dynamical friction heating.

In our simulations, we implemented in Ramses yet another model which will be described in Section 9.2.2.

5.5.6 AGN feedback

Feedback from active galactic nuclei (AGNs) are believed to proceed in two distinct modes :

- Quasar mode (or thermal feedback), where large amount of radiation is emitted which is able to photoionise and heat the gas in the BH vicinity. This mode is essentially seen in the high redshift universe. The quasar mode occurs when gas accretion is comparable to the Eddington limit.

- Radio mode (or kinetic feedback), on the other hand, proceeds at a lower redshift. Typically, large radio bubbles (such as Figure 5.9) with inflated strong magnetic fields and high levels of cosmic-ray energy. This radio mode is preferentially triggered during low-accretion-rate episodes.

Very often, the ratio $\chi = \dot{M}_{\rm acc}/\dot{M}_{\rm Edd}$ is used to differentiate the two regimes. The threshold value of $\chi_{\rm Radio} = 0.01$ is used by Dubois *et al.* [222] which means that radio mode AGNs proceed at accretion rate lower than 1% of the Eddington value.

For both rates, the energy released to the ambient gas is given by :

$$\dot{E}_{\rm AGN} = \epsilon_f L_{\rm AGN}, \tag{5.40}$$

$$= \epsilon_f \epsilon_r \dot{M}_{\rm acc} c^2, \tag{5.41}$$

where ϵ_f accounts for the fraction of radiated energy $L_{\rm AGN}$ for the mode triggered by the accretion (with $\epsilon_{f,q}$ and $\epsilon_{f,r}$ for respectively the quasar and radio modes).
Meece *et al.* [223] recently showed that purely thermal feedback ($f_{\rm th} = 1$) produces very different results from feedback with even a small kinetic component. We will discuss it in detail in Chapter 9.
Both radio and quasar modes were implemented by Dubois *et al.* [222] in Ramses following the work of Teyssier *et al.* [224].

The radio mode or kinetic AGN feedback model was implemented to reproduce a jet-like outflow for $\chi \leqslant \chi_{\rm Radio}$. It deposits the AGN energy given by Equation 5.41 (with the prescribed fraction $f_{\rm k}$) into a bipolar conic outflows of angle θ inside the sink sphere. The jet velocity depends on the chosen kinetic mass loading factor. The quasar mode or thermal AGN feedback ($\chi \geqslant \chi_{\rm Radio}$) is very similar to the approach of Booth & Schaye [144] : the rest-mass energy of the accreted gas is stored until it would be enough to raise the temperature of the gas inside the sink sphere by ΔT (usually 10^7 K). However, with the implementation of Biernacki *et al.* [204] a continuous AGN energy injection is possible (i.e. setting $\Delta T = 0$). Dubois *et al.* [222] suggested that $\epsilon_{f,q}$, the coupling efficiency between the blast wave energy at small scales and the deposited thermal energy at large scales, should be set to $\epsilon_{f,q} = 0.15$ which is in agreement with the values found in the literature (from 0.05 [135] to 0.15 [144, 213]).

Both models can work at the same time where a fraction f_k of the feedback energy is added as kinetic energy, while the remaining fraction (i.e. $1 - f_k$) is added as thermal energy.
The AGN energy is deposited within the sink sphere (of radius

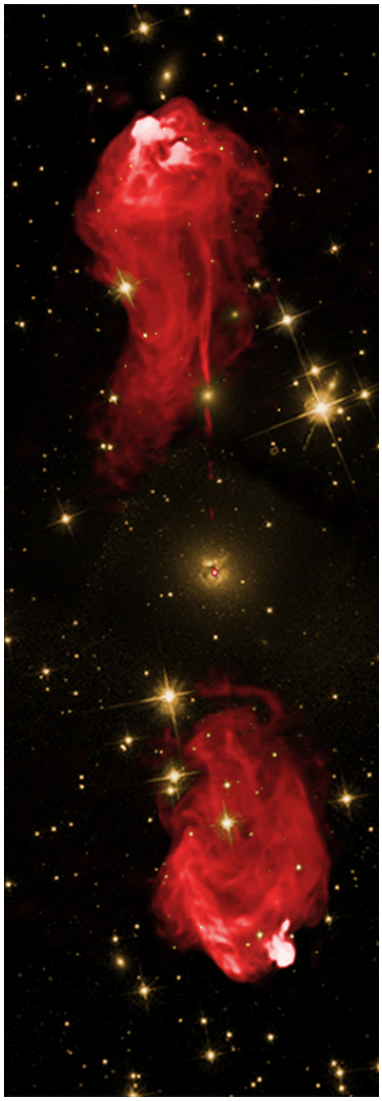

Figure 5.9: The large radio jets in Cygnus A glowing in red, overlaid on the optical image showing the center of the galaxy shrouded in dust. – Credits: NASA/STSiC (Optical) NSF/NRAO/AUI/VLA (Radio)

$4\Delta x$) at every fine time step [204] (i.e. the time step of the highest refinement level $l_{\max}$). By default, the energy injection is distributed in every gas cell proportionally to the gas density. This is a mass-weighted deposition scheme.

However, for the need of our work, we also implemented in Ramses a volume-weighted scheme where the AGN feedback energy is deposited homogeneously inside the sink sphere. This function has been added to the publicly available Ramses version.

5.6 The Rhapsody-G suite

The work presented in the next chapters follow the work of Hahn *et al.* [111], Wu *et al.* [164], and Martizzi *et al.* [225] on the Rhapsody-G simulations. In this section we will describe the Rhapsody-G sample of massive galaxy clusters as well as more technical details on the Ramses simulations. We will finally review the various results from these studies and state the starting point of this thesis.

5.6.1 Context and initial conditions

The Rhapsody-G simulation suite is constituted of hydrodynamical zoom-in Ramses simulations of 10 massive galaxy clusters. This sample of 10 clusters originates from the Rhapsody N-body simulations of Wu *et al.* [226, 227].
The Rhapsody precursor simulations consist of N-body simulations of 96 cluster-sized halos with masses $M_{\rm vir} = 10^{14.8\pm0.05}$. This large cluster sample have been identified in one of the Carmen simulations from the LArge Suite of DArk MAtter Simulations (Lasdamas)[23] .

23: http://lss.phy.vanderbilt.edu/lasdamas/

The Rhapsody[24] simulations of Wu *et al.* [226, 227] represents a sample of 96 zoom-in simulations in cosmological volume of $\left(1\,h^{-1}\mathrm{Gpc}\right)^3$ with 1120^3 particles.[25]
Each halo was simulated at two resolutions :

- Rhapsody 4K with a N-body particle mass resolution of $1.0\times10^9\,h^{-1}\mathrm{M}_\odot$ (equivalent to 4096^3 particles in the volume)
- Rhapsody 8K with a mass resolution of $1.3\times10^8\,h^{-1}\mathrm{M}_\odot$ (equivalent to 8192^3 particles)

24: Re-simulated HAlo Population for Statistical Observable-mass Distribution studY

25: Movies and images for each individual halo are available at http://risa.stanford.edu/rhapsody/

We summarise the simulation parameters in Table 5.1 The initial conditions were generated with the multi-scale initial condition generator Music [120] and the zoom regions consist of spheres of $8\,h^{-1}$Mpc centred on each selected cluster at $z = 0$. The particles

Table 5.1: Parameters of the Rhapsody simulations. The number of particles in the simulation gives the mean number of high-resolution particles in each zoom-in region and the number of particles in each halo gives the mean number of high-resolution particles within the $R_{\rm vir}$ of each targeted halo

Name	Mass resolution $\left[h^{-1}\mathrm{M}_\odot\right]$	Force resolution $\left[h^{-1}\mathrm{kpc}\right]$	Number of particles in the simulation	Number of particles in each halo
Rhapsody 4K	1.0×10^9	6.7	5.4M (equiv. 4096^3)	0.63M
Rhapsody 8K	1.3×10^8	3.3	42M (equiv. 8192^3)	4.9M

were then evolved using the public version of Gadget-2. The halo finding was performed with the phase-space halo finder Rockstar [228] and halo merger trees were constructed with the gravitationally consistent code of Behroozi *et al.* [229].

These 96 Rhapsody haloes were selected in a narrow mass bin of $M_{\rm vir} = 10^{14.8\pm0.05}$ at $z = 0$ from a previous Gadget-2 simulation of the full box using 1120^3 particles. The initial conditions from this full volume simulation were generated using the code of Crocce *et al.* [230].
We note that all initial conditions (both for the original box and all subsequent zooms) were performed using second-order Lagrangian perturbation theory at $z = 50$. Moreover, all simulations are based on the same ΛCDM cosmology as Carmen with the density parameters $\Omega_b = 0.045$, $\Omega_b = 0.25$ and $\Omega_\Lambda = 0.25$, a spectral index $n_s = 1$, an amplitude normalisation $\sigma_8 = 0.8$ and a Hubble parameter of $h = 0.7$. In this cosmology, the baryon fraction $\Omega_b/\Omega_m = 0.18$, is slightly higher that the value of the Planck Collaboration *et al.* [11] (~ 0.156).

From the full Rhapsody sample of 96 halos, only 10 halos were selected to be re-simulated with gas using Ramses. This Rhapsody-G sample of 10 clusters were selected in such a way that three of the main haloes have extreme concentrations[26] , two have an extreme number of subhaloes, and five have approximately the median concentration and and typical number of subhaloes .
We illustrated the selection strategy in Figure 5.10 as well as the whole original Rhapsody sample. On the same figure, we highlighted with colors the 10 halos of the Rhapsody-G sample in the concentration-number of subhalo plane.

Nine out of the 10 massive halos constituting the Rhapsody-G sample have similar mass of $M_{500} \sim 6 \times 10^{14}\mathrm{M}_\odot$ while the tenth has twice this mass ($1.3 \times 10^{15}\mathrm{M}_\odot$). The initial conditions were generated using Music [120] at a starting redshift of $z = 49$[27] . The local Lagrangian approximation (LLA) was used to generate a consistent initial density field of baryons on the grid (see in Hahn

26: The concentration parameter relates the virial radius ($R_{\rm vir}$) to the scale radius (R_s) as :

$$R_{\rm vir} = c\, R_s, \qquad (5.42)$$

of the Navarro *et al.* [125] density profile given by :

$$\rho(r) = \frac{\rho_s}{\frac{r}{R_s}\left(1 + \frac{r}{R_s}\right)^2}, \qquad (5.43)$$

with ρ_s, the amplitude of the density profile.

27: It is a convenient choice as the scale factor is $a(z = 49) = 0.02$.

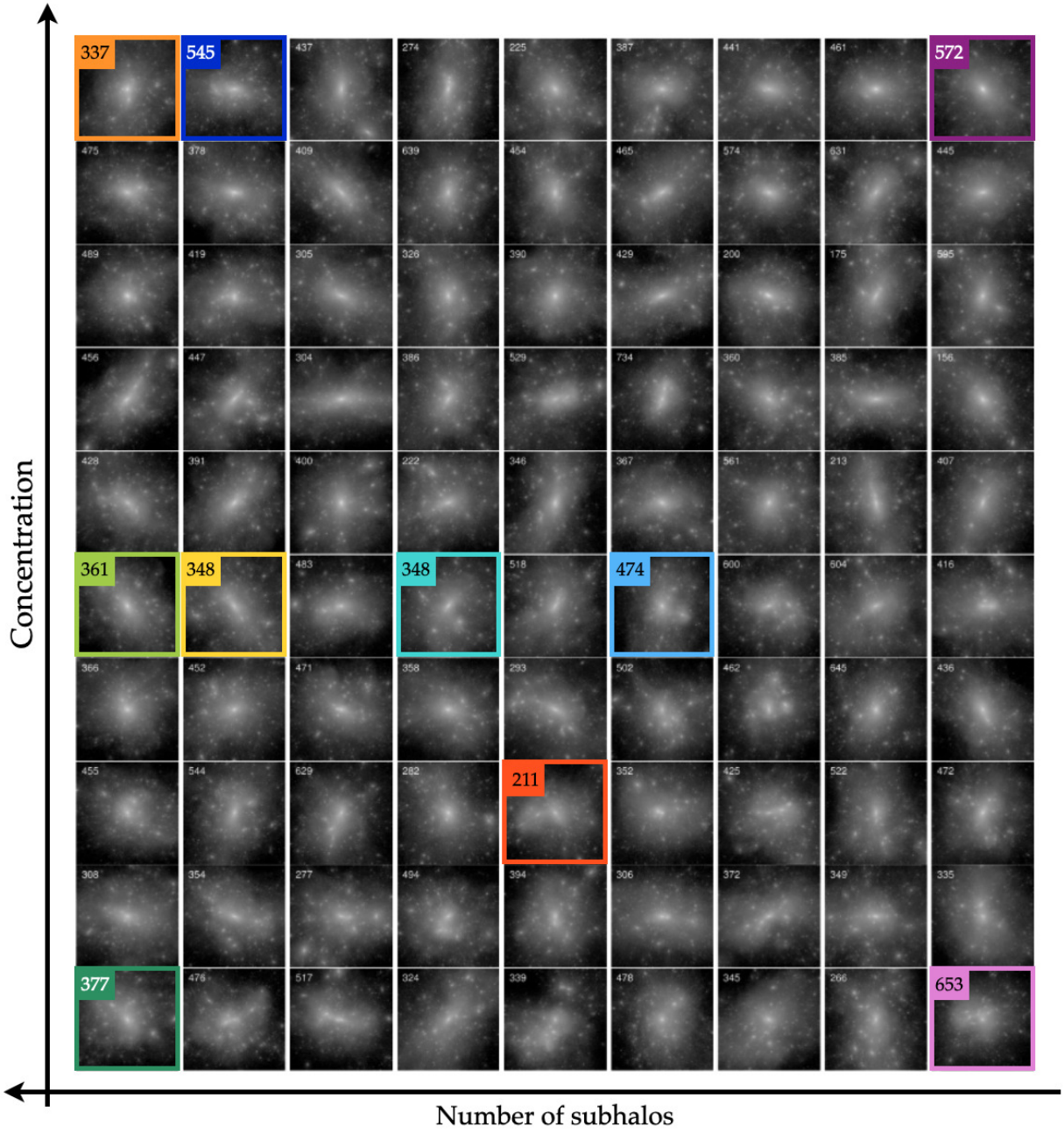

Figure 5.10: Images of 90 Rhapsody halos at $z = 0$, sorted by concentration (row-wise, ascending order) and by the number of subhalos (column-wise, descending order). Each thumbnail has a physical extent of 4 h^{-1}Mpc on a side (slightly larger than the average virial radius of 1.8 h^{-1}Mpc) – Credits : Adapted from Wu *et al.* [226]

& Abel [120] for more details). The Lagrangian volumes for the zoom simulations include a sphere of 8 h^{-1}Mpc, centered on each cluster at $z = 0$, in a cosmological box of $\left(1\ h^{-1}\text{Gpc}\right)^3$.

5.6.2 Numerical approach

From Figure 5.10, Rhapsody-G samples the extreme corners of the concentration-number of subhalos plane by the systems with IDs 337, 377, 653 and 572.[28] The system 545 was additionally included

to probe the high concentration, high substructure fraction region, similarly to the corner system 337.
This subset of "extreme" clusters was complemented with four more clusters taken from the central region of the plane with IDs 211, 348, 361 and 448.

All massive halos were simulated with Ramses and incorporate cooling, star formation, and purely (mass-weighted) thermal AGN feedback. The kinetic feedback of Dubois *et al.* [222][29] was not implemented yet.

28: The "fossil" system 572 (high concentration, low substructure fraction) is naturally included in this selection. As discussed in Wu *et al.* [226], this halo is curious outlier : it has the highest concentration, the least late-time accretion, and the most dominant central halo of our full sample. It is also the halo with the most massive progenitor at $z = 3$. While it has an atypical formation history, it does not particularly live in an atypical environnement on large scales.

29: it was shown to affect significantly the bulk gas and stellar mass

Thanks to their heavily modified version of the phase-space Rockstar halo finder [228], halo/galaxy finding was able to proceed with the Ramses AMR data. In this Rockstar-Galaxies version, all leaf-cells of the AMR-tree were converted to pseudo-particles of variable mass.
During the halo finding, halo/galaxy properties were calculated inside Rockstar-Galaxies to obtain masses, radii, centres and bulk velocities of the dark matter, stellar, gaseous and black hole content of each (sub)halo. But also, several galaxy-related quantities, such as the SFR, mean stellar age, surface brightness and magnitude in various photometric bands were computed.

5.6.3 Results

In Hahn *et al.* [111], it was established that the various results are numerically converged at the lower 4K resolution[30] .
Therefore, in what follows, the results presented here concerns the Rhapsody-G 4K simulations.

30: The comparison was done between all halos simulated at the 4K resolution and the 8K simulation of the `Halo653`

The galaxy formation models used in Rhapsody-G was shown to reproduce halos in broad agreement with the halo mass-stellar mass relation from the abundance matching results of Kravtsov *et al.* [231] and Behroozi *et al.* [232], shown in Figure 5.11.

Galaxies for all simulated clusters follow a narrow star-forming sequence which is consistent in both slope and normalization with the sequence of star-forming galaxies in the Sloan Digital Sky Survey (SDSS) [234]. On the other hand, few galaxies appear to be quenched with respect to the division of Woo *et al.* [234].
The star formation rate (SFR) of Woo *et al.* [234] is averaged over all field galaxies. But, the Rhapsody-G simulations probe the densest environments and therefore an higher quenched fraction should be expected. It seems that the Rhapsody-G simulations either lack the resolution or additional physical mechanisms are missed in

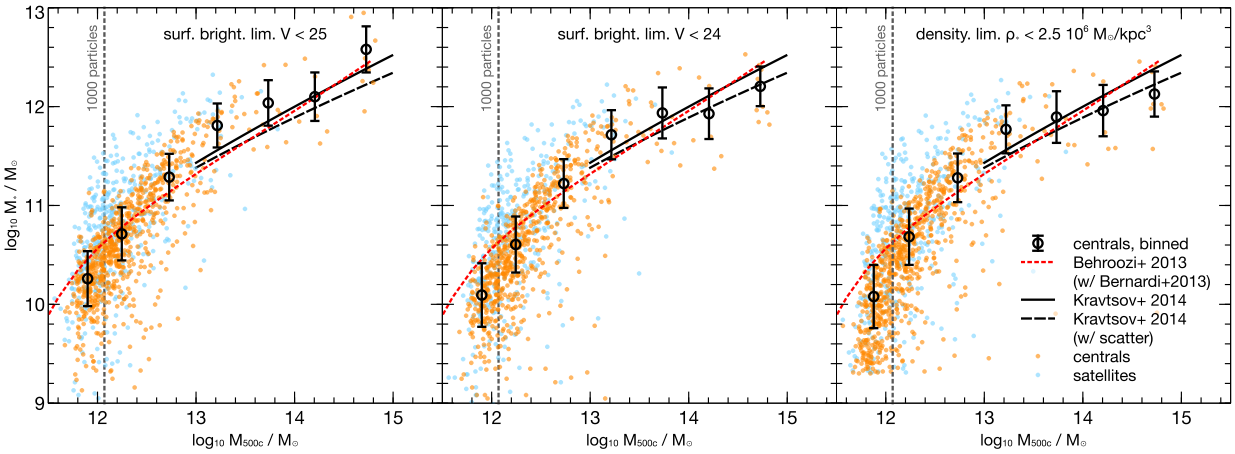

Figure 5.11: Comparison between the $M_* - M_{500}$ relation for central and satellite galaxies (respectively shown with the orange and blue dots) from all 10 RHAPSODY-G haloes at $z = 0$ with abundance-matching constraints. The black bold circles with error bars (1σ scatter) represents the mean stellar mass in bins of halo mass for central galaxies. See in the original paper for details on the comparison with published results. The stellar masses in the *left* and *middle* panel where measured using mock V-band images where the surface brightness was above 25 and 24 mag arcsec^2. The *right* panel shows the mass measurement using a simple overdensity of $2.5 \times 10^6 M_\odot$ kpc^{-3}. (see in Martizzi *et al.* [233] for the reason of this particular choice) – Credits : Hahn *et al.* [111]

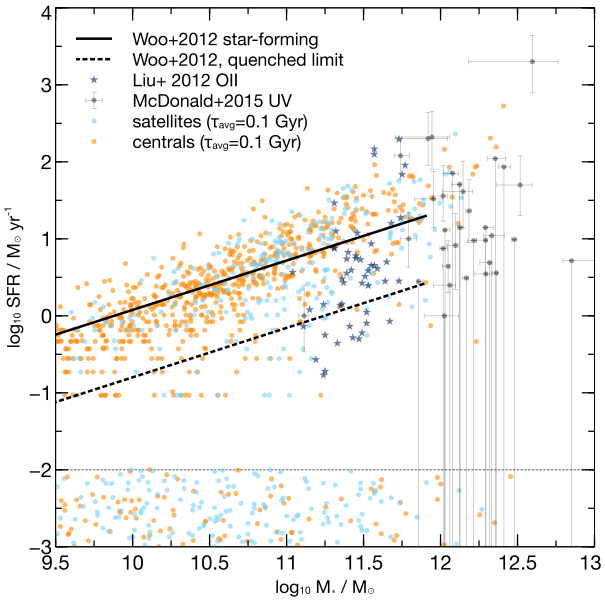

Figure 5.12: Star formation rates as a function of stellar mass for central (orange) and satellite (blue) galaxies for the 10 halos of the RHAPSODY-G sample at $z = 0$. The main sequence of star-forming galaxies in SDSS of Woo *et al.* [234] in show with the solid black line and the dotted black line shows the division between star-forming and quenched galaxies along with the measurement of Liu *et al.* [235] and McDonald *et al.* [236] – Credits : Hahn *et al.* [111]

these simulations to reproduce realistic quenched fraction. However, despite this high SFR in the cluster galaxies, Martizzi *et al.* [225] found that galaxy metallicities were ~ 0.5 dex lower than observational constrains. The stellar mass-metallicity relation at low redshift for all galaxies in the RHAPSODY-G sample is shown in Figure 5.13.

From the higher metallicities obtained in the 8K simulations, it seems that resolution affects the global metallicities of cluster galaxies. Martizzi *et al.* [225] claims that the potential well of galaxies is too shallow in low resolution simulations which prevent the

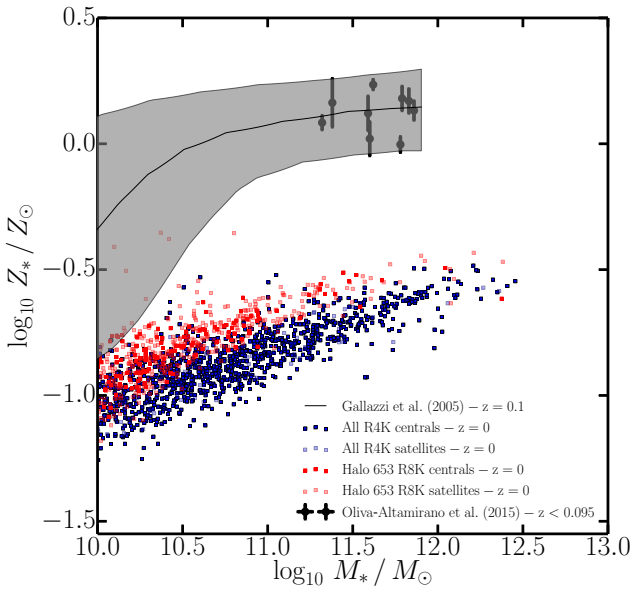

Figure 5.13: Stellar mass-metallicity relation for galaxies in the Rhapsody-G sample at low redshift. Galaxies shown at blue dots corresponds to all Rhapsody-G4K simulations, while the red dots shows the metallicities at the higher 8K resolution only for `Halo653` (run for convergence purposes). Comparison with the BCG data from Oliva-Altamirano *et al.* [237] and the local-universe relation of Gallazzi *et al.* [238] – Credits : Martizzi *et al.* [225]

metals from being confined in galaxies. Therefore, with a better resolution this problem might be alleviated. However, Dubois *et al.* [108] showed similarly low galaxy metallicity despite their higher resolution in the Horizon-AGN simulation[31] .

31: The Horizon-AGN simulation use Ramses with the same Salpeter [189] initial mass function.

The Rhapsody-G simulations however successfully reproduced the challenging cool-core (CC) / non-cool-core (NCC) dichotomy observed in galaxy clusters. Indeed, from the various radial profiles shown in Figure 5.14 we can clearly see a distinction in the central $\sim 100\,\mathrm{kpc}$, the cluster core. Hahn *et al.* [111] distinct CC clusters as having a central entropy of at most $40\,\mathrm{keV\,cm^{-2}}$ at $r = 10\,\mathrm{kpc}$ shown in Figure 5.14 as blue lines while NCC, in red.
We can clearly see the distinct CC/NCC populations by looking at central entropies and gas densities where CC clusters exhibit, respectively, lower and higher values compared to NCCs. The fraction of CC clusters is about 50%.
We note that Rhapsody-G haloes seems to have lower entropies and temperatures outside the core (i.e. above $\sim 100\,\mathrm{kpc}$) than the observed ACCEPT profiles.

Moreover, let us look at the (enclosed) gas fraction profiles (the ratio of the gas to the total mass) in the left panels of Figure 5.15, where NCC and CC clusters are plotted in the upper and lower part respectively. These gas depletion profiles are compared with the relaxed cluster sample of Mantz *et al.* [239] which is biased towards CC systems that systematically shows higher baryon fractions in the cores.
While NCC clusters have clearly lower gas fractions in the core (i.e. $0.1 - 0.2R_{\mathrm{vir}}$) than CC clusters, both population shows a high

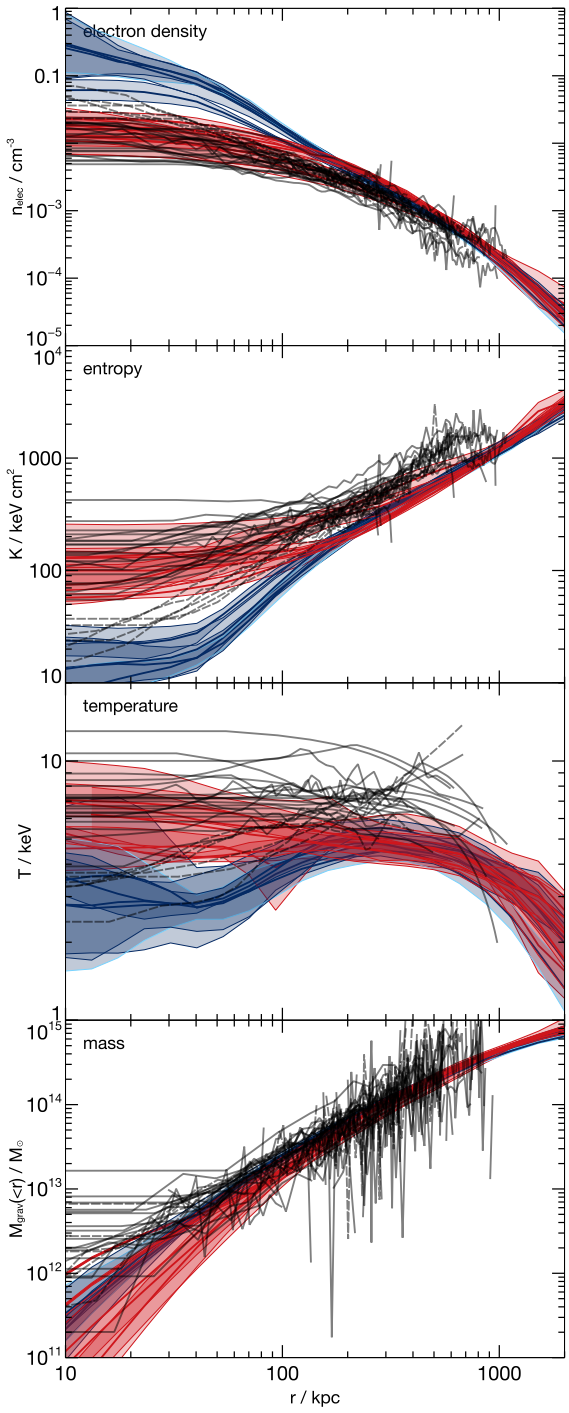

Figure 5.14: Comparison of the Rhapsody-G ICM radial profiles with observational data from their mass-matched subset of ACCEPT clusters. From *Top* to *bottom* : electron density, entropy profiles, temperature and total mass profiles. The simulated haloes were stacked individually for each cluster in same mass range as the ACCEPT subset. The shaded ribbons indicate the 1σ scatter in each stack, reflecting time variations in the profiles – Credits : Hahn *et al.* [111]

content of gas outside the core with respect to the observations of Mantz *et al.* [239]. It suggests that the AGN feedback model might be inefficient at preventing the build-up of gas in the ICM.
However, by testing various different models of thermal AGN feedback on a strong cooling flow cluster (`Halo 545`) they found that none had an effect outside the core.Hence, they argued that improvements in the AGN modelling, other forms of energy injection (through kinetic feedback e.g.) or additional processes (such as thermal conduction) might be needed to bring ICM gas fraction

in agreement with observational constraints.

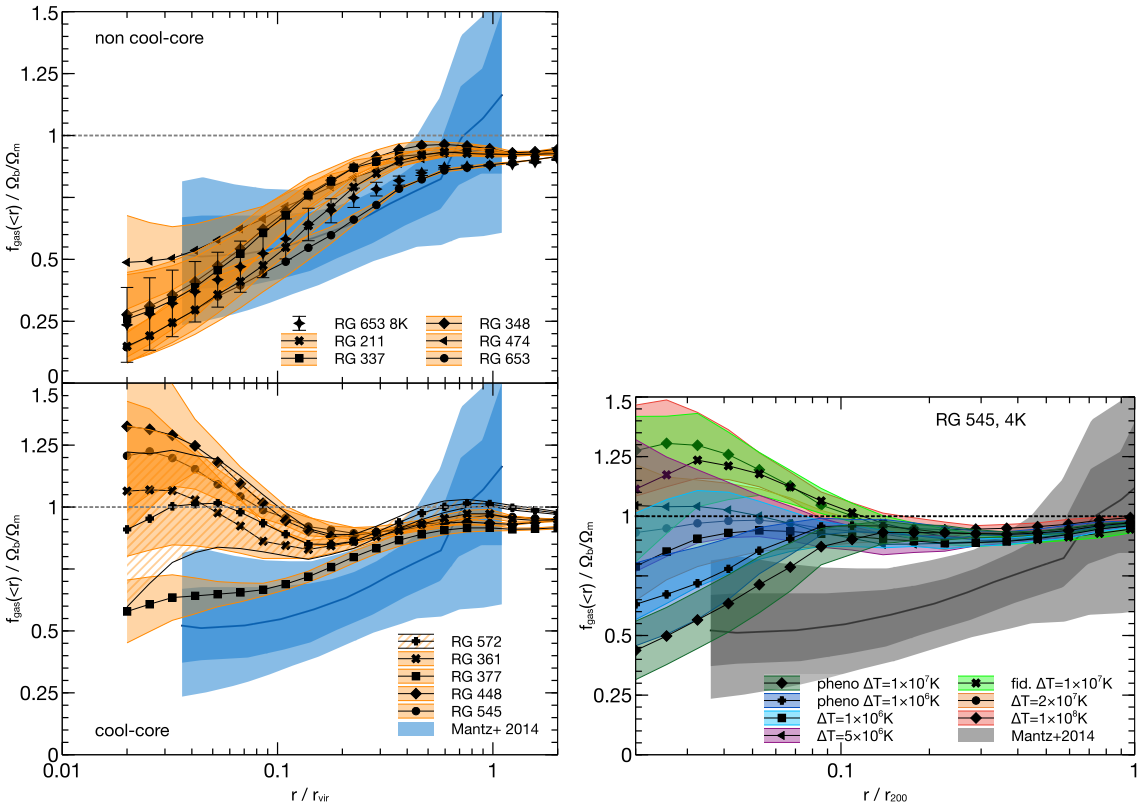

Figure 5.15: *Left* : Comparison of cumulative gas profiles for the same stacked clusters as Figure 5.14 for non-cool-core and cool-core clusters respectively in the upper and lower panels. *Right* : Same as the left pannels but for the CC cluster RG 545 only, where two different implementations and a range of parameters of the thermal blast-wave AGN model are used – Credits : Hahn *et al.* [111]

This study revealed that the transition from CC to NCC clusters was induced by the amount of angular momentum in major mergers. In more details, `Halo 545` and `Halo 348` show very similar assembly histories, but the later ends up into a NCC cluster while `Halo 545` remain with a CC. In fact, `Halo 348` experience a head-on major merger where the CC of the main halo got completely destroyed by the core collision. On the other hand, the major merger in `Halo 545` has a large angular momentum which only perturbs the CC but does not destroy it. This study showed that major merger was not the sole condition for CC/NCC transition but by how much the merger effectively perturbs the core[32] .

32: See in the original paper for the gas density and entropy maps illustrating the two mergers.

In this study, Hahn *et al.* [111] showed the cluster scaling relations for the Rhapsody-G sample which we collected in Figure 5.16. We will cover extensively in Chapter 11 details about the underlying assumptions, the derivation and the origins of possible scatter of cluster scaling relations as well as the methodology for the measurement of each global quantities (X-ray temperature, luminosity, integrated Y_{SZ}, ...). However, for now, we will discuss the general idea and the main findings from the various plots in Figure 5.16.

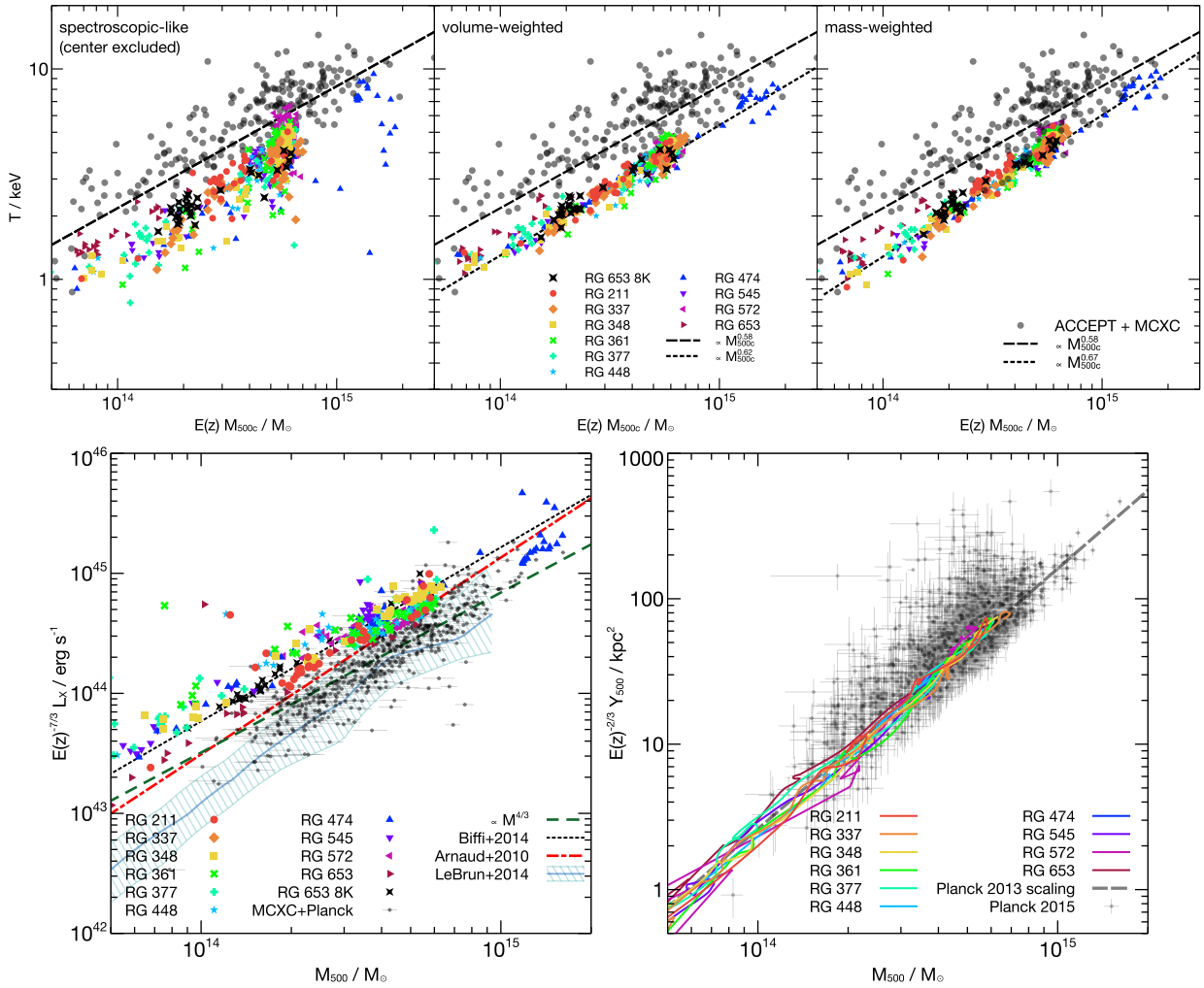

Figure 5.16: Comparsion of the cluster scaling relation of the RHAPSODY-G sample to various published results (see in the Hahn *et al.* [111] for more details on the various compared studies). *Top* : The top three panels shows the evolutionary tracks of the RG clusters in the gas temperature-halo mass plane. From left to right is the shown the core-excluded spectroscopic-like temperature, the volume-weighted gas temperature and the mass-weighted temperatures. *Bottom Left :* X-ray luminosty-mass scaling relation. All properties were measured inside R_{500} and rescaled to the expansion function $E(z)$ as appropriate. See also in Chapter 11 for more details on the cluster scaling relations – Credits : Hahn *et al.* [111]

All quantities are measured inside R_{500}, the radius enclosing 500 times the critical density at each redshift.

The top row, shows the evolution of each halo in the temperature-mass plane in comparison with the ACCEPT/MCXC sample[33] . The left panel shows the spectroscopic-like temperature [240] for the RHAPSODY-G sample at different redshift with the core[34] excluded from the temperature measurement. The middle and right panels show the volume- and mass-weighted (core-included) gas temperatures. As time evolves, each halo grows in mass, hence, we witness the evolution of each halo along the temperature-mass scaling relation.

RHAPSODY-G halo temperatures are systematically lower than observed values irrespective of the inclusion of exclusion of the

33: We refer the reader to the original paper for the details of each studies used for comparison. For clarity, we focus in this section to draw the results of the RHAPSODY-G simulations.

34: The core is defined to be $0.15 \times R_{500}$

core. However, if we assume that the observational mass measurements suffer from a hydrostatic bias, i.e. that the measured mass is underestimated, simulations and observations become concordant.

However, if we apply the same "mass-shift" to the Planck/MCXC data in the X-ray luminosity-mass scaling relation shown in the bottom left panel, it accentuates the gap even more. The Rhapsody-G data and published results from both observations and simulations cannot be reconciled : The Rhapsody-G luminosities are systematically too high.

In the lower right panel of Figure 5.16, the evolution of Rhapsody-G halo in the integrated Compton-Y Sunyaev-Zel'dovich-mass plane is surprisingly in good agreement with the unbiased (i.e. setting a zero hydrostatic mass bias, $b_{\rm HSE} = 0$) Planck Collaboration *et al.* [41] 2013 mean baseline relation plotted as the grey dashed line.

Rhapsody-G scaling relations show somehow contradictory results, and the causes of these discordances are not straightforward.

5.6.4 Perspectives

The Rhapsody-G simulations were able to reproduce a persistent CC/NCC dichotomy and provided an interesting scenario for the transition based on the angular momentum at which the major merger occurs.
However, we saw that galaxies were too massive with a very small fraction of quenched galaxies especially at high galaxy masses. The metallicity is at odds with observational data where Rhapsody-G cluster galaxies are systematically 0.5 dex lower.
On the other hand the gaseous component of Rhapsody-G clusters shows to be rather insensitive to the AGN feedback at large radii and realistic cluster gas fraction could not be reached.
The AGN feedback models tested in the Rhapsody-G simulations seems to be inefficient at quenching star formation and preventing the build-up of gas in the ICM.

Therefore, different and more sophisticated models of feedback need to be considered to reproduce realistic cluster galaxies and ICM properties. Moreover, additional physical processes such as thermal conduction, turbulence or cosmic rays might help to lower the burden of AGN at heating the ICM.
These exciting and open questions constitute the starting point of this thesis.

Moreover, having such detailed hydrodynamical cluster simulations are of importance for cluster cosmology. Indeed, they are used to calibrate cluster scaling relations that allows observers to derive cluster masses from easily observed quantities.
We saw that the Rhapsody-G simulations were able to reproduce the expected slopes of various scaling relations. More peculiar is the normalisation that cannot be consistently constrained. Hence, more effort is required to understand the origin of such offsets.

Scientific Results

Descriptions of the simulations 6

In this chapter we will gather all the details regarding the simulations used for this work. Unless specified otherwise, all simulations presented in the next chapters share the same resolution and physical models presented here.

6.1 Initial conditions

All initial conditions used in this work were generated with the Music code [120] using the same methodology as the previous Rhapsody-G simulations.
It consists of zoom-in simulations in a cosmological box of $\left(1\,h^{-1}\mathrm{Gpc}\right)^3$ based on two different flat ΛCDM cosmologies. The first one uses the same parameters as in the original Rhapsody simulations and the second cosmology the updated parameters found by the Planck Collaboration [241], 2015. The parameter values are given in Table 6.1 where we give the density parameters for baryon (Ω_b), total matter (Ω_m) and for the cosmological constant (Ω_Λ) as well as the long-wave spectral index (n_s), the amplitude normalisation (σ_8) and the Hubble constant (H_0).

In the Rhapsody New cosmology, the total matter density parameter is larger implying a lower baryon fraction of $f_\mathrm{b} = \Omega_\mathrm{b}/\Omega_\mathrm{m} \sim 0.1586$ compared to the original Rhapsody simulations ($f_\mathrm{b} = 0.18$). As a consequence, simulations with the updated cosmology will show more massive structures with less baryons.
In this Rhapsody New simulation of Buehlmann & Hahn [242, in prep.], we could find halos with similar properties and coordinates to the original Rhapsody-G halos. We will keep the same ID labels , although they are not strictly the same (i.e. more massive halos with less baryons).

The initial conditions were generated at $z = 49$, from the minimum bounding ellipsoid matrix retrieved from the cosmICweb database[1] [242] with a traceback-radius of $2R_\mathrm{vir}$. It means that the ellipsoid zoom region at the stating redshift of $z = 49$ contains all the matter that will end up within the halo $2R_\mathrm{vir}$ region at $z = 0$[2] . The high resolution ellipsoid patch, from which the halo will form, is in the center of the simulation box.

Table 6.1: Parameters of the two different ΛCDM cosmologies used in this work. The Rhapsody cosmology is the same used in the previous studies [111, 164, 225–227]. The Rhapsody New is updated to the Planck 2015 cosmology [241].

	Rhapsody	Rhapsody New
Ω_m	0.25	0.309
Ω_Λ	0.75	0.691
Ω_b	0.045	0.049
H_0	70.00	67.74
σ_8	0.8	0.8159
n_s	1.0	0.9667

1: https://cosmicweb.oca.eu/

2: For more technical details, we refer the reader to the forthcoming paper of Buehlmann & Hahn [242]

All initial conditions were performed using second-order Lagrangian perturbation theory (LPT) with dark matter and baryon perturbations at $z = 49$. However, we dropped the local Lagrangian approximation for the baryons.

Baryons and dark matter did not comove prior to recombination. However sub-percent effects are expected at cluster scale (see e.g. [243–245]). Therefore, we assume that baryons fully trace cold dark matter perturbations at our starting redshift, as these effects are not relevant.

We cover the full simulation box of side $1\,h^{-1}$Gpc with a coarse resolution at the level $l_{\rm min} = 7$. At this level, we have $2^7 = 128$ cells per box dimension. The lower and higher resolution versions of the simulations use then, respectively :

- $l_{\rm max,IC} = 12$ for the Rhapsody 4K simulations, which indeed yields an effective resolution of $2^{12} = 4096$ cells per dimension for the full box.
- $l_{\rm max,IC} = 13$ for the Rhapsody 8K simulations with 8192 cells per dimension.[3]

3: The majority of the work presented in this thesis was run at the 8K resolution, except for calibration of the star formation that we will present in Section 9.1.

The particular choice of $l_{\rm max,IC}$ sets the effective resolution in the refined ellipsoid region at the stating redshift.
It also gives the DM particle mass $m_{\rm DM} = 8.22 \times 10^8\,h^{-1}{\rm M}_\odot$ and $1.03 \times 10^8\,h^{-1}{\rm M}_\odot$ for the 4K and 8K simulations respectively.

Further dynamical adaptative refinement is allowed up to a maximum refinement level of $l_{\rm max} = 19$ according to a mass-based Lagrangian refinement criterion (see below). The maximal spatial resolution (or minimum cell size) is therefore[4] :

4: in physical units

$$\Delta x = \frac{1\,h^{-1}{\rm Gpc}}{2^{19}} = 1.9\,h^{-1}{\rm kpc}. \tag{6.1}$$

In general, because the Poisson equation is solved on the AMR grid, the cell size also provides the value of the gravitational softening length. Note that no dynamical refinement is allowed outside the zoom region.

We chose an overdensity-based refinement strategy (i.e. Lagrangian) which the AMR grid cells will be split if they reach an overdensity of 8. Therefore, as a grid cell will be split in 8, each split cells will get an overdensity of 1, i.e. the mean density $\bar{\rho}$. The DM particle mass are $m_{\rm DM} \sim 1 \times 10^8\,h^{-1}{\rm M}_\odot$ for 8K simulations and a factor 8 more massive in 4K simulations.

6.2 Gas cooling and chemical evolution

Our simulation follows the subgrid model implemented in Ramses using the cooling rates of Sutherland & Dopita [182] for Hydrogen, Helium and metal line cooling. Ramses does not separately follow metals, but the total gas metallicity is advected with the flow as a passive scalar. The gas metallicity can be sourced by supernova feedback only.
We consider the UV background radiation according to the Haardt & Madau [184] model. An instantaneous reionization takes place at $z = 10$ to take into account for an earlier reionization in the particularly overdense proto-cluster region that we simulate.

As we saw in Section 5.5.1, the unresolved cold and dense gas constituting the ISM can be modelled by using a polytropic temperature floor. Previously stated in Equation 5.22, we recall its formulation :

$$T_{\rm floor} = T_* \left(\frac{n_{\rm H}}{n_*} \right)^{\gamma_* - 1} \tag{6.2}$$

with $n_{\rm H}$ the Hydrogen number density. In our simulations, we always used $n_* = 0.1\,{\rm cm}^{-3}$ and $T_* = 10^4\,{\rm K}$ being respectively the star formation density threshold and the ISM polytropic temperature with $\gamma_* = 5/3$ being the ISM polytropic index.

6.3 Star formation

The sub-grid model for star formation will create a star particle wherever the gas density exceed the previously stated n_* density. We allow the star particle to carry 20% of the cell mean baryonic mass. Hence, the mass of this star particle depend on the DM particle mass, which is set by the DM particle mass and the cosmology as :

$$m_{\rm b} = \frac{\Omega_{\rm b}}{\Omega_{\rm m} - \Omega_{\rm b}} m_{\rm DM}, \tag{6.3}$$

$$m_{*,\rm min} = 0.2 m_{\rm b}, \tag{6.4}$$

which gives for instance a stellar mass of $m_{*,\rm min} \sim 3.8 \times 10^6\, h^{-1}{\rm M}_\odot$ in Rhapsody-GNew 8K simulations.

The local star formation rate expressed in Equation 5.30 is :

$$\dot{\rho}_* = \epsilon_* \frac{\rho}{t_{\rm ff}}, \tag{6.5}$$

where we set the star formation efficiency to $\epsilon_* = 0.01$. This value was set to reproduce a realistic population a cluster galaxies, see

later in Section 9.1.

6.4 Stellar feedback

Once a star particle is created, we assume that after 10 Myr, a fraction $\eta = 0.1$ of its mass is released into the surrounding cells with a metal yield of $y = 0.1$. In other words, $y\eta = 1\%$ of the time-integrated SFR is returned as metals in the ISM.
In addition to metals, the SN feedback injects in the surrounding gas cells an energy of 10^{15} erg.
We chose to enable the delayed cooling of the SN heated gas with a dissipation time scale of 20 Myr. This additional sub-grid model mimics the effect of non-thermal processes (e.g. turbulence, CRs) that are able to dissipate energy on longer time scales before being radiated away.

6.5 Black hole growth

Using the clumpfinder of Bleuler *et al.* [203][5] we identified potential SMBH formation sites where the gas density is higher than 8 times the mean density and we ask for a peak relevance of 3. We merged the identified peaks in the filtered density field based on a saddle threshold density of $20\bar{\rho}$.

5: We described in Section 5.5.4 the different steps of the Phew clumpfinder

The gas clump, from which the sink particle will be created, needs to be gravitationally bound and should not already contain another sink particle and have at least a mass of $10^9 M_\odot$. We also ask that the gas in this clump needs to be accelerated towards its center and contracting to form a new SMBH sink particle. We chose a SMBH seed mass to be roughly the same as our N-body DM particle mass, hence $m_{\mathrm{BH,seed}} = 10^8 M_\odot$. We do not check if two sinks form a bound system but directly merge if they are less than 2 cells apart.

SMBH then accrete at a Bondi-Hoyle accretion rate which can be boosted according to via the Booth & Schaye [144] boost factor defined in Equation 5.36. However, the sink accretion rate is always limited to the Eddington value.
Unless stated otherwise, we do not use the Booth & Schaye [144] boost and use the actual SMBH accretion rate.

6.6 AGN feedback

We do not redistribute the AGN energy in each time-step, but we accumulate the energy over time until :

$$E_{\rm AGN} > \frac{3}{2} m_{\rm gas} k_{\rm B} \Delta T \tag{6.6}$$

with ΔT is also called the energy accumulation threshold. We set it to $\Delta T = 10^7$ K. This parameter appears to be crucial. Indeed, Le Brun *et al.* [162] showed that this parameter allows a tuning of the bulk properties of the ICM in their SPH Cosmo-OWLS simulations. We redistribute this accumulated energy in a mass- and volume-weighted way in the sink sphere (i.e. a sphere of radius 4 cells). The temperature of this AGN blast is set to $T_{\rm AGN} = 1.5 \times 10^{11}$ K.

6.7 Magnetic fields

Except for some simulations that will be presented in Section 7.4, all simulations have a uniform seed magnetic field along the box z axis with a magnitude of 1.56×10^{-12} G.

6.8 Thermal conduction

For the simulations that include thermal conduction, the temperature of electrons is conducted at the Spitzer rate and couples with the ion temperature. We set a perpendicular conductivity coefficient of 1% to ensure numerical stability. Both ion and electron adiabatic indexes are equal to $\gamma = 5/3$.

6.9 Changes

In comparison with the original Rhapsody-G simulation, we added the treatment of magnetic fields. However, while being not dynamically important, their presence shapes transport processes in the ICM plasma.
Using the latest version of Ramses, we now benefit from various fixes and improvements in the subgrid models since the time at which the first Rhapsody-G simulations were ran.

On a more detailed level, we use a different and more robust black hole seeding strategy (see later in Section 9.2.1). We do not use any boost for the Bondi SMBH accretion. In the original Rhapsody-G simulations, only thermal AGN feedback with a mass-weighted energy desposition was used. In this work, we add the possibility of a volume-weighted energy injection (homogeneous deposition

in the sink sphere) and we will review in Section 9.3 the differences between the two models.
The star formation efficiency is a factor 2 lower (we now set $\epsilon_* = 0.01$, while 0.02 was used), and, we chose a higher metal yield of $y = 0.2$ ($y = 0.1$ in the original simulations).
The SN feedback is somehow different with the use of a delayed gas cooling now.

Additionally, we updated the ΛCDM cosmology to the more recent measurements of Planck Collaboration *et al.* [241]. The cosmology used in the previous Rhapsody-G simulation was based on relatively outdated parameters estimations.

The different changes and improvements, compared to the previous works on the Rhapsody-G sample, allow us to go towards more realistic hydrodynamical simulations of galaxy clusters. Especially, we will be interested to study the impact of the various baryonic processes on the intra-cluster medium at higher resolution than before.

The inclusion of magnetic fields will allow us to study the magnetic amplification with the Eulerian code Ramses and will be the topic of the next Chapter 7. The presence of these fields drives transport processes in the intra-cluster and we will study first in chapter Chapter 8, the anisotropic heat diffusion on idealised cases. Whereas, in Chapter 11, we will see wether it has an impact on full-physics simulations.

In Chapter 9, we will review in more details the impact of the galaxy-formation models, studied during the calibration phase of our simulations to both obtain a realistic ICM and cluster galaxies.

Magnetic field amplification 7

In this chapter, we will focus on magnetic fields in galaxy clusters. We will start by reviewing the various mechanisms relevant for the seeding and amplification of cosmic magnetic fields. We will discuss the various approaches in numerical astrophysics to tread the magneto-hydrodynamic equations. We will present our initial conditions of the seed field and their impact on the magnetic amplification in our simulations.

7.1 Magnetics fields in galaxy clusters

7.1.1 Overview

Magnetic fields are one of the fundamental and ubiquitous components of our Universe.
They are observed on a wide range of scales, from our solar system up to the largest structures (even in voids[1]) [247].

The presence of magnetic fields in clusters was demonstrated by Willson [248] who first detected in 1970 the presence of a diffuse synchrotron emission in the Coma cluster. Twenty years later, Kim *et al.* [249] estimated for the first time the intra-cluster magnetic field intensity within Coma ($\sim 2\mu G$) through Faraday rotation measures of background radio galaxies.
While being not dynamically relevant, their presence shapes the properties of the baryonic medium [250].

Today, dozen of studies have confirmed that cluster magnetic field intensities are at the micro-Gauss level and decline with cluster radius (see Govoni & Feretti [93] for a review). Current resuls indicate that magnetic fields fluctuate over spatial scales ranging from a few kpc to hundreds kpc. Cluster centres are characterized by small scale magnetic field structures, while filamentary magnetic field structures dominate on large scales [251].

Due to the complexity of non-thermal phenomena in cosmological context, connecting observations with theoretical expectations remains a major challenge.

1: Indeed, gamma ray astronomy started to detect the magnetization of void, with lower limits of 10^{-16} G have been derived from the spectra of high redshift blazar sources [246]

In the hierarchical scenario, gravity govern the CDM structure formation where small DM haloes forms first and baryon flows into their potential wells. Star and galaxies form through gravity and cooling, and will evolve into larger structures by mergers and infall [12].
These processes drive turbulence which is later amplified by the AGN and stellar feedback in galaxy clusters.

The ICM is one of the most ideal plasmas known with a Debye length[2] as short as $\lambda_D \sim 10^5$ cm. Therefore, the framework of magneto-hydrodynamics (MHD) remains a valid description for the dynamics of the ICM for scales larger than the Debye length. However the ICM is a high-β plasma with $\beta \sim 10^2$, where the magnetic pressure is negligible compared to the ICM thermal pressure.[3] Magnetic fields are therefore expected to have a weak impact on the dynamics of the intra cluster gas.

2: The Debye length is a rough measure of the size of the shielding cloud that the charged particle carries with itself.

3: We define β as the ratio of the thermal pressure to the magnetic pressure i.e. :

$$\beta = \frac{P_{\rm th}}{P_{\rm B}}, \tag{7.1}$$

$$= n k_{\rm B} T / B^2 \tag{7.2}$$

In this highly conducting IC plasma , magnetic field lines are entrained by (or "frozen into") the fluid motions. Therefore, turbulent gas motions stretch and bend magnetic field lines, which retroact on the gas by resisting to this deformation via the Lorentz force. This gives rise to a fully developed MHD turbulence (see Schekochihin & Cowley [250] for a review of turbulence and magnetic fields in astrophysical plasmas). This energy injected on large scales will be transferred and dissipated to smaller scales into thermal energy or, in case of a dynamo, into magnetic energy via the Lorentz force.

Despite significant progress in simulations of galaxy formation (with an emphasize on the subgrid models), simulations of non-thermal processes, magnetic fields and cosmic-rays remain challenging. In particular, resolving turbulence is a demanding numerical task where commonly used density adaptivity approaches are ineffective. But also, galaxy cluster simulations need to resolve an extremely large range of scales and incorporate various galaxy formation physics in a cosmological context.

From an observational point of view, the Square Kilometre Array Observatory (SKAO) will boost our capacity to analyse magnetic fields in galaxy clusters, as among other, it will allow us to :

- dramatically increase the number of Faraday rotation measures in each system [252],
- investigate turbulent fluid motions and large scale magnetic fields through the detection of polarised emission from diffuse radio sources in clusters (i.e. radio halos) [253],
- improve our ability to detect such radio sources up to high

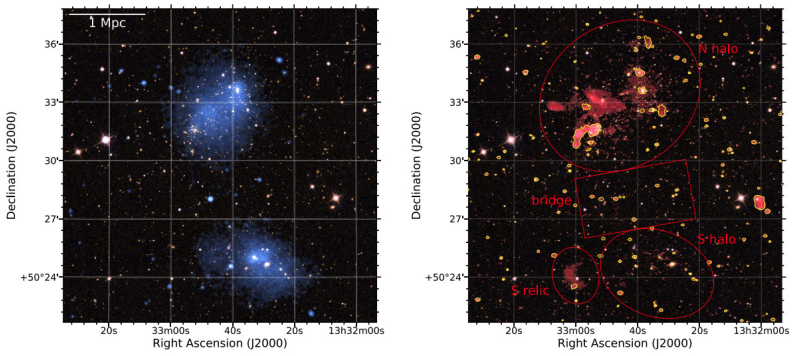

Figure 7.1: Composite images of the Abell 1758 galaxy cluster with the optical SDSS image. *Left* panel shows the X-ray emission in blue and the LOFAR image shown in red in the *right* panel. These images shows the radio bridge connecting two colliding galaxy clusters. It reveals that non-thermal phenomena in the ICM can be generated also in the region of compressed gas in-between infalling systems. – Credits : Botteon *et al.* [256]

redshift [254],
- study magnetic field intensities in large scale filamentary structures of the cosmic web [255].

In this respect, it is worth to be mentioned that the LOw Frequency ARray (LOFAR) SKA pathfinder already allowed us to discover diffuse radio emission in between clusters. Thus, it points out the presence of relativistic electrons and weak magnetic fields ($< 1\ \mu$G) in the detected ridge of radio emission [256, 257] as shown in Figure 7.1.

In the way to a successful theory of magnetic fields and non-thermal processes in astrophysical plasma, such as in the ICM, many open question need to be assessed :

- What is the origin of cosmic magnetic fields ?
- what are the properties of ICM turbulence and magnetic dynamos ?
- How does these processes amplify, sustain and shape IC magnetic fields ?
- How is the energy cascaded and dissipated in the ICM ?
- What is the magnetic field distribution and topology ?
- How does magnetic fields and turbulent flows enhance and inhibit the transport of cosmic ray, heat and momentum ?[4]

4: especially how viscous heating and thermal conduction balance the radiative cooling in the ICM ?

7.1.2 Mechanisms for seed fields and amplification

The origin of large-scale magnetic fields is strongly debated.
The analysis of the Planck CMB angular power spectrum excluded magnetic fields at $z \sim 1100$ with root mean square (rms) values larger than a few nG on scales larger than few megaparsec [258, 259].
Studying primordial magnetic fields (PMFs) is important to constrain the progenitors of the observed cosmic magnetic fields but they could provide a new potential observational window to the early Universe.

A vast range of mechanisms have been proposed for the origin of magnetic fields (see Subramanian [260] for detailed review). The main popular hypotheses are that the observed large-scale fields are remnants of fields that existed from the earliest times (primordial origin) or seeded at lower redshifts ($z \leqslant 6$) by galactic feedback processes (galactic origin).
We will give a short overview of these two proposed seeding mechanisms. However it is more likely that more than one of these mechanisms participate to the magnetisation of the large scale structures.

Different mechanisms have been proposed for the initial seed field in the early Universe which involve the generation of currents during inflation and phase transitions (see Subramanian [260] and references therein). These seed fields may produce either small ($\leqslant$ Mpc) or large coherence lengths whose structure may still persist today in the emptiest regions of the Universe.
In the case of inflationary generation, the different scenarios lead to field which are gaussian.[5]
Due to the uncertainties in the physics of the early Universe, the outcome of the above scenarios yields a rather large uncertainty of possible fields in the range of 10^{-10} down to 10^{-34} G [261].

5: For the inflationary generation, vacuum fluctuations of the electromagnetic fields that are amplified are Gaussian. For electroweak or quantum chromodynamics phase transitions, the fields generated on the small sub-Hubble scale might not be gaussian. But the large astrophysical scales of relevance may encompasse a large number of these domains. Hence, the central limit theorem implies that such fields average on these scale could be gaussian too.

On the other hand, they could have formed at a much later epoch during structure formation through microscopic processes such as the Biermann battery [262] or Weibel instabilities [263]. At low redshifts ($z \leqslant 6$), SN or AGN feedback can release magnetic fields generated inside stars or within galaxies through stellar or galactic dynamos respectively [264], into the interstellar medium and then into the IGM by galactic winds [265]. Indeed these astrophysical batteries are able to generate coherent seed magnetic fields in the late Universe. And if they did not exist, primordial fields originally seeded in the early Universe will decay if not sustained by any dynamo mechanisms.

Statistical analysis of Faraday measures jointly with MHD cosmological simulations could be the way to pinpoint and constrain primordial magnetic fields (more specifically in filaments or in the IGM). In that context, primordial fields are exciting because they could provide an interesting probe of the physics of the early Universe.

We will discuss in the next two sections, turbulent dynamos and amplification processes that are mandatory to maintain magnetic fields in the collapse of galaxies and galaxy clusters.

7.1.3 Quick words about cluster turbulence

Dynamos processes can arise from turbulent motions in the ICM. Indeed many processes in galaxy clusters drive turbulence such as the accretion of DM subunits and gas. The infalling gas will get shock heated around the virial radius with mach numbers $\mathscr{M} \sim 10$ and infalling structures inject turbulence via Kelvin-Helmholtz and Rayleigh-Taylor instabilities. Major mergers are also able to create eddies as large as the cluster core (e.g. Donnert & Brunetti [266]). On smaller scales, SN and AGN feedback as well as galactic winds inject turbulence in the ICM too. The interplay of all these processes on half-Mpc to sub-parsec scales are expected to include hydrodynamic shear and weak-to-moderately-strong shocks ($\mathscr{M} \leqslant 5$) which drive turbulence that cascades down to the dissipation scale.
Alfvén waves travelling in the ICM can generate small scale solenoidal motions. In fact, the solenoidal component drives a turbulent dynamo while the compressive component (fast and slow modes) will produce adiabatic compression and shock waves, which both fuel ICM turbulence.
The presence of CRs in the ICM modifies its plasma properties, which can further alter the turbulence on small scales (see Brunetti & Jones [92] for a review on CRs in galaxy clusters).

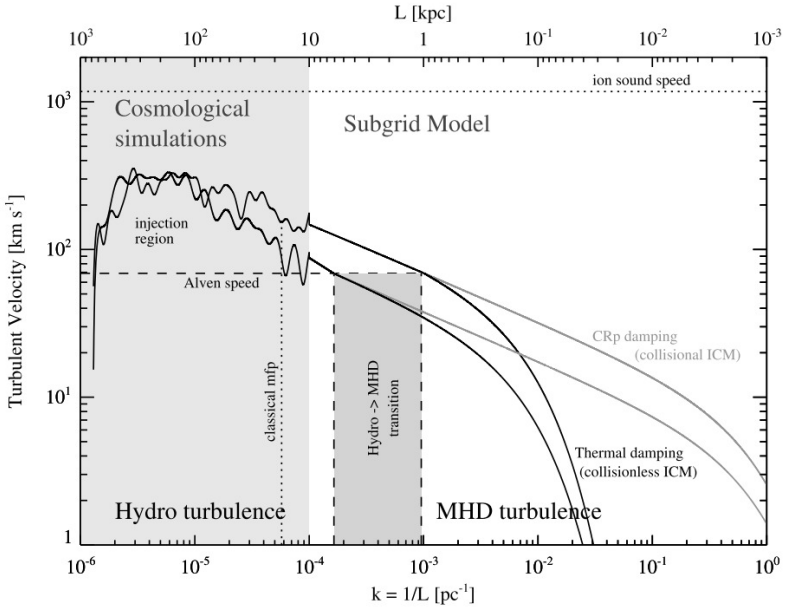

Figure 7.2: Illustration depicting the cascade of only compressive turbulence over length scale, considering damping from thermal ions and CR protons in galaxy clusters whose typical parameters are : $B = 1\,\mathrm{nG}$, $n_{th} = 10^{-3}\,\mathrm{cm}^{-3}$, $T = 10^8\,\mathrm{K}$, $\beta \sim 250$. The injection scale $\sim 300\,\mathrm{kpc}$, the classical mean free path $\sim 20\,\mathrm{kpc}$, the scale where the magnetic field modifies turbulent eddies $\sim 200\,\mathrm{pc}$ and the thermal dissipation scale $\sim 20\,\mathrm{pc}$ are indicated in this figure. In addition the sound speed $c_s = 1200\,\mathrm{km\,s^{-1}}$ and the Alvén speed $\sim 100\,\mathrm{km\,s^{-1}}$ are shown – taken from Donnert & Brunetti [266]

7.1.4 Amplification

We now give a short overview on the different mechanisms able to amplify seed magnetic fields. We will start by the above-stated dynamos that convert the kinetic energy associated with the fluid motion to magnetic energy by electromagnetic conduction.

We typically distinguish two turbulent astrophysical dynamos : fluctuation (or small-scale) and mean-field (or large-scale) dynamos.

In the former case, dynamos are caused by random fluid motions where magnetic fields lines are frozen in. In a simplified picture, field lines are therefore stretched and compressed by random fluid motions (see Figure 7.3) which amplifies the magnetic flux locally due to flux conservation.

To illustrate this process, let's consider a toy example of a flux tube of radius r_1 and length l_1 with a magnetic field strength B_1 being stretched to a length l_2 and radius r_2. The mass conservation gives :

$$\frac{r_2}{r_1} = \sqrt{\frac{l_1}{l_2}}, \tag{7.3}$$

And the magnetic flux, $S1 = \pi r_1^2 B_1$, is conserved in the high-β regime. Which, for an incompressible fluid, yields an amplified magnetic field B_2 :

$$B_2 = B_1 \frac{l_2}{l_1}. \tag{7.4}$$

This process is typically rapid compare to a cluster's age ($\sim 10^3$ yrs), thus repeating this process, leads to an exponential increase of the magnetic energy, in the case of the field does not back react on the fluid. This dynamo can saturate by the Lorentz force and concentrate on scales (that depend on the Prandtl number[6]) thus, leading to a certain degree of magnetic field coherence.

On the other hand, mean-field dynamos grow and maintain fields correlated on scales larger than the coherence length of turbulent motions. They typically require more special conditions (toroidal-poloidal-toroidal cycles of the field) but exponentially amplify fields on a much longer time scale ($\sim 10^8$ yrs).

On top of that, cosmic ray drifting in the ICM is able to drive instabilities. Indeed, the CR electric currents generate a return current in the ICM plasma which leads to a transverse force that can amplify transverse perturbations in the magnetic field [268, 269] (see also Marcowith *et al.* [270] for a review for these Bell instabilities in numerical studies). This amplification typically operates at scale comparable to the proton gyroradius.
Filamentation instabilities and other microphysical plasma instabilities could exist in the ICM, we will not describe it here but we refer the reader to the review of Donnert *et al.* [261] for more details.

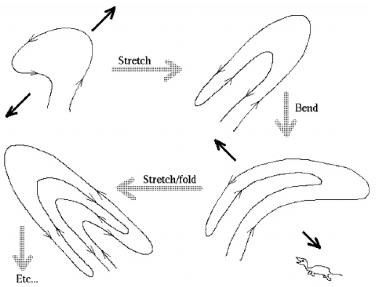

Figure 7.3: Folding-structure formation via stretching of the field lines. Bold arrows indicate directions in which volumes are stretched by random shear – Schekochihin *et al.* [267]

6: The magnetic Prandtl number relates the resistive to diffusive scale (respectively $_\nu$ and l_η) :

$$P_m = \frac{\nu}{\eta} = \frac{Rm}{Re} = \left(\frac{l_\nu}{l_\eta}\right)^{4/3} \tag{7.5}$$

where ν is the kinematic viscosity and η the diffusivity. Re is the Reynold number and Rm its magnetic analogue.

Magnetic amplification can also take place in shocks by mechanisms not yet well understood [271]. Small scales dynamos driven by turbulence are created at the shock front, which amplify fields downstream of the shock. While significant amplification is found in numerical simulations of SN remnants [272], it is unclear if this applies to galaxy clusters too (where Mach numbers are lower, $\mathcal{M} < 5$, and β parameters higher, $\beta \geqslant 100$).
Compression at shocks can also drive quasi-perpendicular field amplification, Iapichino & Brüggen [273] found that by pure compression :

$$B_{\rm ds} = B_{\rm us}\sqrt{\frac{2\sigma^2+1}{3}} \tag{7.6}$$

with σ being the shock compression ratio and $B_{\rm ds/up}$ the field strength in the downstream/upstream region.
This amplification must be rather low to be able to account for the large degree of polarisation in radio relics (except in the case of high $\mathcal{M} \sim 100$ such as recently found in the Sausage relic [274]).

The amplification can also arise from subsonic flows where magnetics fields can be amplified in localised regions in the cluster.
These motions were revealed by the presence of edges in the surface brightness of many clusters observed by Chandra. These features called cold front are believe to result from subsonic gas motions driven by cosmic accretions and clusters mergers (see e.g. Zuhone & Roediger [275] for a review).

At least three processes were identified to form such cold fronts : *remnant-core* fronts formed by galaxies of sub-clusters' cool core infall or merging with larger and more diffuse structures ; *sloshing* cold fronts are formed in cool core clusters by the displacement of the central low entropy gas from the dark mater potential minimum (see e.g. Perseus' cold front in Figure 7.4); and *stream* cold fronts formed by the collision between coherent gas streams (e.g. [277]).
Lyutikov [278] demonstrated that the cold dense subsonic motions of gas clouds through the ICM would amplify and stretch magnetic fields lines producing a thin magnetic draping layer along the contact discontinuity.

Sloshing cold front are very common in cool core clusters, which amplify magnetic fields. Mazzotta & Giacintucci [279] were the first to discover that these sloshing motions were bounding radio mini-halos in the core region of clusters. Indeed these sloshing motions could rapidly amplify magnetic fields and re-accelerates

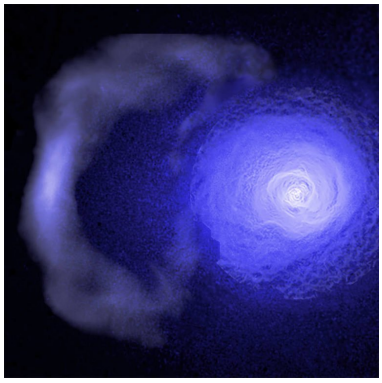

Figure 7.4: Cold front in the Perseus cluster from Walker *et al.* [276]. XMM-Newton mosaic of the Perseus cluster shown in blue, while the gaussian gradient magnitude filtering map of the Chandra (inner) and XMM (outer) mosaics or shown in white, pink and yellow. Clearly visible on the left, the ancient 730 kpc radius outer cold front. A video from Zuhone & Roediger [275] of the gas sloshing simulation reproducing this feature is available here : https://vimeo.com/236813999 and for the magnetic amplification see https://vimeo.com/78989618.

CRs in the core, as reproduced in the simulation of mini-halos of ZuHone *et al.* [280].

7.1.5 Evolution : MHD

If one wants to include the treatment of magnetic fields, one has to solve the MHD equations instead of Euler's. When written in conservative form and Gaussian units, the super-comoving MHD equations read[7] :

$$\frac{\partial \rho}{\partial t} + \boldsymbol{\nabla} \cdot (\rho \mathbf{v}) = 0, \tag{7.7}$$

$$\frac{\partial \rho \mathbf{v}}{\partial t} + \boldsymbol{\nabla} \cdot \left(\rho \, \mathbf{v}\mathbf{v} - \frac{\mathbf{B}\mathbf{B}}{4\pi} + P_{\rm tot} \mathbb{1} \right) + \rho \boldsymbol{\nabla} \phi = 0, \tag{7.8}$$

$$\frac{\partial E}{\partial t} + \boldsymbol{\nabla} \cdot \left[(E + P_{\rm tot}) \, \mathbf{v} - \frac{\mathbf{B}(\mathbf{B} \cdot \mathbf{v})}{4\pi} \right] + \mathbf{v} \cdot \boldsymbol{\nabla} \phi - \frac{1}{\rho} \mathscr{H} \frac{B^2}{4\pi} = 0, \tag{7.9}$$

$$\frac{\partial \mathbf{B}}{\partial t} - \boldsymbol{\nabla} \times (\mathbf{v} \times \mathbf{B}) + \eta \Delta \mathbf{B} - \frac{1}{2} \mathscr{H} \mathbf{B} = 0, \tag{7.10}$$

7: We dropped here the x subscripts compared to the equations in SI units given in Section 5.2

Where ρ is the fluid density and $\mathbf{v}$ its velocity, $\mathscr{H}$ is the super-comoving Hubble constant. $\mathbf{B}$ is the magnetic field, $\eta = c_s/(4\pi\sigma)$ the diffusivity, σ the conductivity and $P_{\rm tot}$ stands for the total pressure, being the sum of the magnetic ($P_{\rm B}$) and thermal pressure ($P_{\rm th}$):

$$P_{\rm tot} = P_{\rm th} + \frac{1}{8\pi} \mathbf{B} \cdot \mathbf{B}, \tag{7.11}$$

and E being the total fluid energy density :

$$E = \epsilon + \frac{1}{2} \rho \mathbf{v} \cdot \mathbf{v} + \frac{\mathbf{B} \cdot \mathbf{B}}{8\pi}, \tag{7.12}$$

with ϵ denoting the internal fluid energy given by the fluid equation of state i.e. $P = (\gamma - 1)\epsilon$.
This set of equation has to be complemented by the solenoidal constraint[8] which has to be satisfied at all times :

$$\boldsymbol{\nabla} \cdot \mathbf{B} = 0. \tag{7.13}$$

8: the divergence of the magnetic field has to vanish everywhere

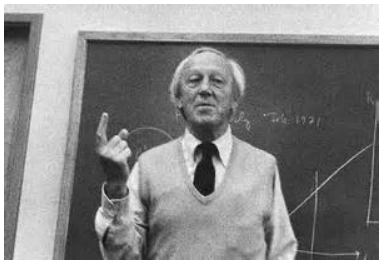

Figure 7.5: Hannes Alfvén, who initiated the field of magnetohydrodynamics for which he received in 1970 the Nobel Prize in Physics.

However due to numerical errors, this magnetic divergence constraint can be violated in simulations. Hence, different numerical schemes are used in different codes to overcome this issue. We will discuss in Section 7.2.1 the main schemes used in astrophysical codes.

The temporal evolution of the magnetic field with the flow is given by the induction Equation 7.10. When the conductivity is large, which is the case in galaxy clusters, the $\boldsymbol{\nabla} \times (\mathbf{v} \times \mathbf{B})$ term dominates

and can be regarded as the freezing of fields lines with the fluid. The diffusion term, coming from Ohm's law, indicates that the magnetic field lines will diffuse through the fluid.

The magnetic field generally decreases with as the Universe expands as [260] :

$$|\mathbf{B}|(t) \propto \frac{1}{a^2(t)}, \tag{7.14}$$

as one would naively expects from flux freezing of the magnetic field, as in an expanding universe all proper surface area increase as $a^2(t)$ (neglecting non-linear and dissipative effects).

We can define the dimensionless magnetic Reynolds number, Rm, being directly analogous to the fluid Reynolds number, Re, which can describe the relative importance of the flux freezing and the magnetic diffusion.
The Rm number is the ratio of the magnetic flux freezing term amplitude ($\boldsymbol{\nabla} \times (\mathbf{v} \times \mathbf{B}) \sim (U/L)B$) to the amplitude of the magnetic flux diffusion term ($\eta \Delta \mathbf{B} \sim \eta B/L^2$) that appear in the induction equation. It gives :

$$\mathrm{Rm} = \frac{UL}{\eta}, \tag{7.15}$$

where U and L are the characteristic velocity and length scale of the flow respectively.
When $\mathrm{Rm} \gg 1$, the field lines are frozen in the fluid while in the case of $\mathrm{Rm} \ll 1$, the Ohmic diffusion dominates and the field line diffuse easily through the fluid.

If we develop the curl in the induction equation we get :

$$\frac{\partial \mathbf{B}}{\partial t} = -\mathbf{v} \cdot \nabla \mathbf{B} + \mathbf{B} \cdot \nabla \mathbf{v} - \mathbf{B} \nabla \cdot \mathbf{v} - \eta \Delta \mathbf{B} - \frac{1}{2} \mathscr{H} B \tag{7.16}$$

Where the field evolution is determined by the four terms in the right hands side where we will describe now their physical meaning :

- The first term accounts for the advection of field lines with the flow,
- The second term for the stretching of the magnetic field lines by shear motions in the fluids,
- The third term relates to the the compression,
- The fourth term, as said before, is the magnetic dissipation into the fluid,
- And the fifth term is the Hubble drag term. It does not have a physical meaning but ensures that the field scales properly

with the scale factor a. Indeed, this term appears because the frame of reference is comoving with the magnetic energy density, and not with the magnetic field strength.

If we consider now in more detail the fourth term in Equation 7.16, we note that a net inflow i.e. $\nabla \cdot \mathbf{v}$ induces a magnetic field growth. As the magnetic flux, Φ_B, is a conserved quantity within the MHD framework, we have a scaling between the magnetic field strength and the density :

$$\Phi_B \propto BR^2, \tag{7.17}$$

$$R^3 \propto (M/\rho), \tag{7.18}$$

$$\implies B \propto \left(\frac{\rho}{\langle\rho\rangle}\right)^{2/3}. \tag{7.19}$$

Hence, we have an amplification of the field purely driven by the adiabatic compression of the fluid.

However, for a galaxy cluster with an average overdensity of $\Delta = \rho/\langle\rho\rangle \sim 100$, this adiabatic compression can only amplify seed fields by a factor of 20 or up to ~ 180 in the cluster core [261]. We see that only the adiabatic compression will not be able to amplify seed fields of $\mathcal{O}(10^{-10})$ (in the optimistic case) to the μG values commonly observed in the ICM. Therefore, dynamo processes as described above in Section 7.1.4 must occur to explain the observed cluster amplified magnetic fields.

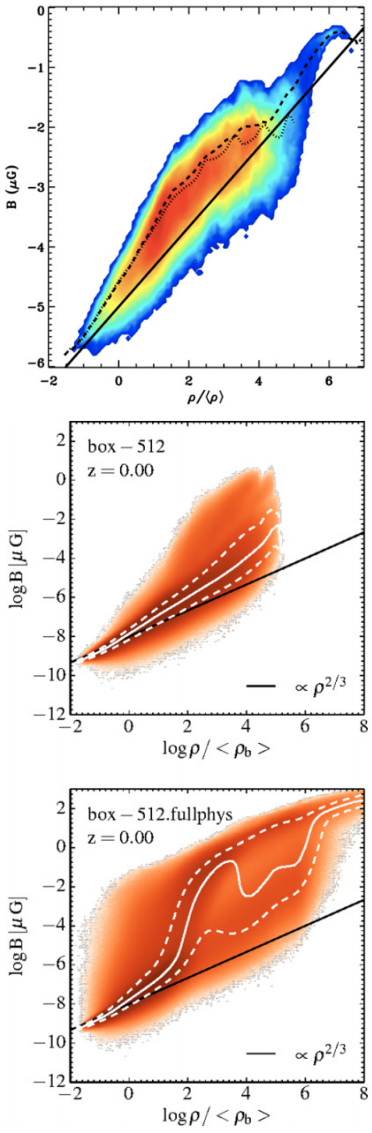

Figure 7.6: Phase diagrams of the magnetic field strength versus gas overdensity for different cosmological simulations. The solid line show the adiabatic collapse expected scaling $B \propto \rho^{2/3}$. Amplification of B fields are visible at high overdensities where the median steepens. *Top* : Dubois & Teyssier [281] Ramses simulation of a cooling-flow galaxy cluster. *Middle* and *bottom* : shows the Arepo simulations of Marinacci *et al.* [145] in the adiabatic case and with fiducial feedback model of the Illustris respectively. We can see that galaxy formation physics provides additional amplification. simulation

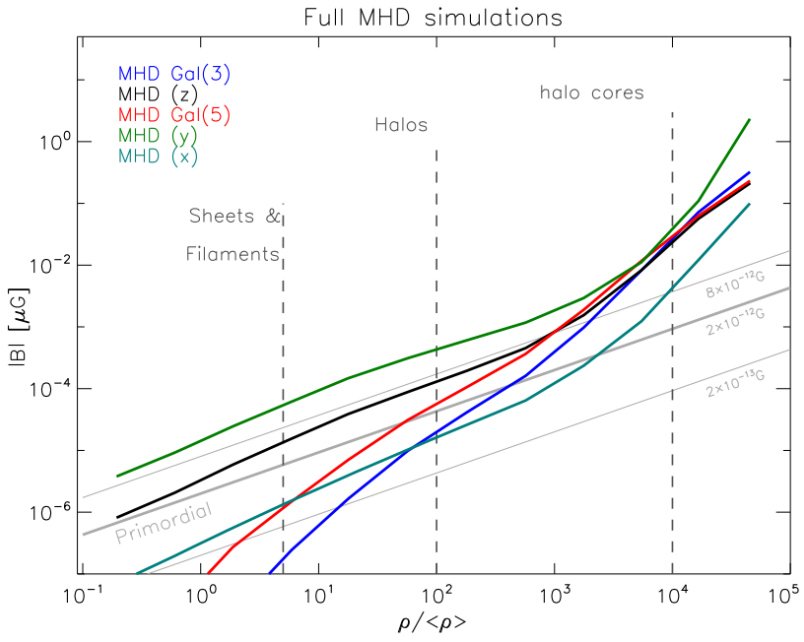

Figure 7.7: Magnetic field strength as a function of the overdensity in SPH simulations of Dolag *et al.* [282] and Dolag *et al.* [283]. Starting from 3 different seed field strength at $z = 20$ of $2{\times}10^{-13}$,$2{\times}10^{-12}$ and $8{\times}10^{-12}$ shown respectively in dark green, black and green. Blue and red line shows the results from galactic seeding. The analytical scaling of Equation 7.19 is shown in grey. We can see that at overdensities $\Delta < 10^3$, the amplification is mainly driven by adiabatic compressions. On the other hand, at typycal cluster core overdensities ($\Delta > 10^3$), all the different seeding mechanisms with different strengths reach amplified magnetic field of $10^{-1} - 10^{0}\,\mu$G where the seeding models are almost indistinguishable. In this regime, the amplification is mainly driven by turbulence (see Section **??**).

7.2 Simulations of turbulence and magnetic fields in galaxy clusters

We saw that the concept of dynamos is directly tied to turbulence. In order to explain the observed μG fields, these dynamo processes must have occurred to amplify and maintain tiny seed magnetic strength ($B \leqslant 10^{-10}$ G).
Cosmological numerical simulations can be used to capture these complex processes. In this section we give an overview of the various numerical studies in the field of turbulence and magnetic amplification. More details can be found in Donnert *et al.* [261].

Cosmological simulations of cluster turbulence

Dolag *et al.* [283] first studied turbulence in SPH cosmological simulations who found $400 - 800\,\mathrm{km\,s^{-1}}$ subsonic velocity dispersion on a scale of 20 to 40 kpc. They found higher turbulent energies in higher mass clusters with turbulent energy fractions of $5 - 30\%$. Their turbulent energy spectra showed to be flatter than Kolmogorov's [284] (but might be due to numerical limitations). Extending this study, Vazza *et al.* [285] provided scaling laws for turbulent energy with cluster mass.

Using Eulerian cosmological simulation, Ryu *et al.* [286] studied the generation of magnetic fields and their evolution. They found that cluster turbulence is largely solenoidal, not compressive with trans-sonic velocities in filaments and subsonic velocity in clusters.

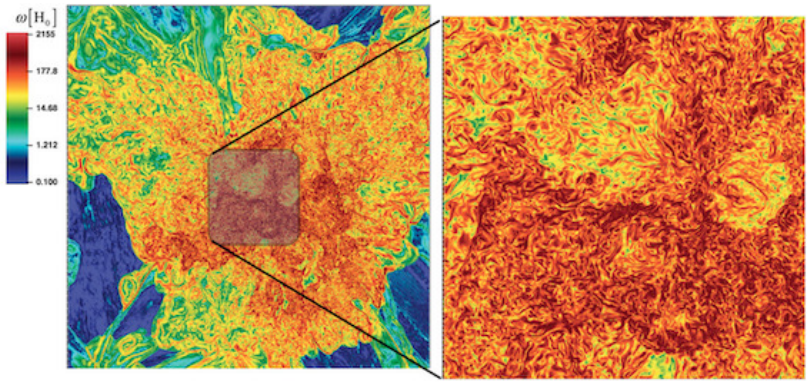

Figure 7.8: Slice of the vorticity magnetitude ω in the cluster centre of a massive galaxy cluster in the Matryoshka runs of Miniati [297, 298]. A high resolution is kept fixed throughout the cluster regions.

They also found a clear trend of rms velocity dispersion with mass and turbulent energy fraction of $10-30\%$ in agreement with prior studies.
They established the connection between magnetic field amplification and shock driven vorticity in cluster merger events. Using a semi-analytical model of small scale dynamo coupled to turbulence, they were able to derive a μG field in clusters.

Turbulence also provides a non-negligible pressure support in clusters, and various studies showed this influence on cluster scaling relations[9] (e.g. Nagai *et al.* [287], Battaglia *et al.* [288], Nelson *et al.* [289], and Schmidt *et al.* [290]). An increase of turbulent pressure with radius is consistently observed : Xu *et al.* [291] and Vazza *et al.* [292] derived first kinetic spectra in Eulerian cosmological simulations of clusters and found to roughly follow the Kolmogorov scaling. They found a Reynolds number of $10-100$ with an injection scale for turbulence larger than 100 kpc and a dissipation scale below 10 kpc (scales in-between correspond to their initial range)
In the last decade, simulations of cluster turbulence were able to reach higher Reynold numbers due to the increasing computational power (e.g. up to $Re = 10^3$ [293]). Turbulent energy was found to peak at the redshift of the formation of the underlying halo [294] and only reach a few percent in relaxed clusters [293].

9: Which will be discussed in Chapter 11

Ruszkowski *et al.* [295] found that long-term galaxy motions induced by minor mergers can excite subsonic turbulence ($\sim 100-200\,\mathrm{km\,s^{-1}}$) in idealised cool core cluster simulations including anisotropic thermal conduction. But the main driver of turbulence is found to be major mergers and cosmic accretions events [296].
The Matryoshka runs of Miniati [297, 298] were able to reach ~ 10 kpc peak resolution throughout the entire virial radius of a massive $\sim 10^{15}\mathrm{M}_\odot$ galaxy cluster. It was found that shocks generated 60% of the vorticity. In the cluster, the induced turbulence was

shown to be solenoidal/incompressible with a Kolmogorov slope. While in the outskirts, the turbulence was found to be compressive with a Burgers slope [299].
Suggested by the name of the "Matryoshka" runs, a hierarchy of energy component was suggested to exist in clusters : gravitational energy is mostly dissipated in thermal energy, then dissipated in turbulent energy and finally in magnetic energy (with a constant efficiency) [297, 298].

Cosmological simulations of cluster magnetic fields

The SPH simulations of Dolag *et al.* [300, 301] were the first full MHD simulation of magnetic fields in clusters with cosmological nG seeds. They found a scaling of the magnetic strength with gas density with an exponent of 0.9 which is close to the expectation from pure compression (2/3, see Equation 7.19). They found strengths of $3-6\,\mu$G in cluster centres over a wide range of masses, being in agreement with rotation measure observations.
Many works used these simulations to model giant radio haloes [302] to show the field influence of cluster mass estimates [303, 304], model the propagation of cosmic rays [305] and the distribution of fast radio bursts Dolag *et al.* [306].
On the other hand, Donnert *et al.* [307] and Beck *et al.* [308] studied the scenario of magnetic seeding by galaxy feedback and draw the conclusion that the same magnetic field is achieved irrespective of the employed seeding model.
AGN seeding in Eulerian MHD simulations of Xu *et al.* [291, 309] also showed to reproduce cluster magnetic fields strengths of $1-2\,\mu$G.

It is also interesting to point out that Ruszkowski *et al.* [295] were the first to incorporate anisotropic thermal conduction in full physics MHD simulation of galaxy clusters. They find a greater dynamo amplification with thermal conduction which also remove directional bias in the velocity and magnetic fields (without thermal conduction, magnetic fields tend to be radial especially at large radii).

Overall, all simulations agrees on the fact that adiabatic compression is the dominant amplification mechanism across most of the cosmic volume. Departures from this expected amplification ($B \propto \rho^{2/3}$) are found at high overdensities when $\rho/\langle\rho\rangle \geqslant 100$ where dynamo amplification seems to be at work (as we already see in Figure 7.7). Galaxy feedback can also provide significant

additional amplification as shown in the Lagrangian simulation of Marinacci *et al.* [145].
In their simulations, Vazza *et al.* [310] estimated that $\sim$ 4% of turbulent kinetic energy was converted to magnetic energy.
Recent cosmological simulations of galaxy cluster with SN and AGN feedback all agrees to the presence of dynamo amplification which allow to reach μG fields values in clusters at low redshifts (e.g. Vazza *et al.* [310] and Domínguez-Fernández *et al.* [311]).

However, we have to keep in mind that, while these above mentioned studies provide encouraging results on magnetic amplification, they use various reformulations of the MHD equations to ensure a divergence-free magnetic field. As we will see in the next section, the solenoidal constraint poses a real challenge for the numerical discretization of the MHD equations. If not treated accurately, a spurious artificial growth of the magnetic field can exist. [312].

7.2.1 Alternative approaches

One of the main limitation of a numerical simulation is its resolution. Indeed, resolving the whole turbulent cascade is out of reach for current simulations. Hence, it sets an upper limit on the effective Reynold number[10] such simulations can resolve :

$$\mathrm{Re}_{\mathrm{min}} = \left(\frac{L}{\epsilon \, \Delta x} \right)^{4/3}, \tag{7.21}$$

where Δx is the resolution element, ϵ is a factor depending on the numerical diffusivity[11] and L is the outer (injection) scale of $300 - 500$ kpc for clusters (as we can see in Figure 7.2).

Indeed as we can see in the example of Figure 7.9 with simulations of Bauer *et al.* [317], each code has its own implementations and different time and spatial integrations allow to reach smaller dissipation scales. As the effective viscosity reduces with the dissipation scale, the velocity power on small scales increases leading to a larger available inertial range. Thus, the higher effective Reynold number reached in less diffusive methods permits more tangled fields and faster amplification at a same resolution.

The treatment of the solenoidal constrain $\boldsymbol{\nabla} \cdot \mathbf{B} = 0$ is also a central issue in the treatment of the MHD equations. Indeed, smooth particle magnetohydrodynamic simulations[12] of Stasyszyn & Elstner [318] and Dobbs *et al.* [319] found that some amplification of the field is purely numerical. They found that schemes they used did not guarantee to recover the consistent solenoidal solution. There-

10: The Reynolds number, Re, is a dimensionless quantity that helps to predict flow patterns in different fluid flow situations. It is the ratio of inertial forces to viscous forces given by :

$$\mathrm{Re} = \frac{uL}{\nu} = \frac{\rho u L}{\mu}, \tag{7.20}$$

with ρ the fluid density, u the flow speed, L a characteristic linear dimension, μ and ν are respectively the dynamic and kinematic viscosities.

11: In modern SPH codes $\epsilon \geqslant 10$ [313], for difference/volume codes it often assumed $\epsilon \sim 7$ [314, 315] and for hybrid methods $\epsilon \sim 10$ [316]

12: using the Dedner cleaning method

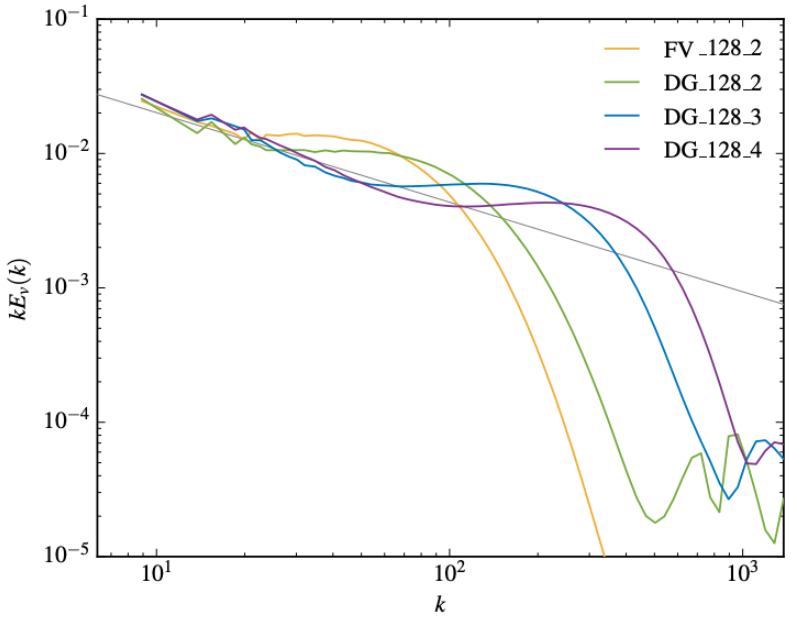

Figure 7.9: Velocity power spectra of driven compressible turbulence from Bauer *et al.* [317] in a simulation box of 128^3 cells. It shows the 2^{nd} order finite volume (FV) code Arepo in yellow and 2^{nd}, 3^{rd} and 4^{th} order discontinuous Galerkin (DG) code Tenet in green, blue and purple respectively. The grey line shows the Kolmogorov scaling of $k^{5/3}$. All simulation share the same Nyquist scale ($k_{\mathrm{Nyquist}} = 2\pi N/(2L)$, with N being the number of cells per dimension, and L the simulation box length)but the (temporal and spatial) integration order increases. Even at the same order, the DG scheme haas more power near the dissipation scale hence it allows to reach larger Reynold number. Therefore it yields faster amplification and more tangled field at the same resolution.

fore, claims of dynamo amplification in numerical simulations have to be taken with a pinch of salt.

Such schemes mainly come in two flavours : divergence cleaning schemes and constrained transport.

- *Constrained Transport* (CT) e.g. Evans & Hawley [178] exploits Stokes' theorem which uses a face-averaged representation of the magnetic fields (called the 'staggered-mesh' approach) to enforce $\nabla \cdot \mathbf{B} = 0$ to machine-precision. In CT, an initial zero divergence is conserved by a specific finite difference discretization on top of a staggered grid.

- The *Divergence Cleaning* method reformulates the MHD equations including additional divergence-waves (Powell *et al.* [320]) or divergence-damping terms (Dedner *et al.* [321]) to enforce the solenoidality constrain. In the case of the Dedner cleaning scheme, the magnetic field is projected into the space of divergence-free vector fields, where any non-zero divergence is eliminated, i.e. cleaned. It introduces an arbitrary function Ψ that is included in the induction equation Equation 7.10 and in the divergence free constrain Equation 7.13. Different choices for the Ψ function can be used between elliptical, parabolic (Marder [322]) and hyperbolic (Dedner *et al.* [321]).

Astrophysical codes make use of these two methods, for instance :

- *Constrained Transport* is used in Ramses (Fromang *et al.* [177]

and Teyssier *et al.* [323]), Athena (Stone *et al.* [324]), Gizmo (Hopkins [325]).

- Different *Divergence cleaning* schemes are used in other astrophysical codes. Arepo uses a Powell divergence cleaning scheme ([326]). The hyperbolic Dedner *et al.* [321] cleaning scheme is used in Gadget(-3) (Dolag & Stasyszyn [327]), Phantom (Price *et al.* [328]), Masclet (Quilis *et al.* [329]), while Flash (Waagan *et al.* [330]) uses a parabolic Marder [322] cleaning.

The Enzo code implements both methods (see Collins *et al.* [331] and Wang & Abel [332] for respectively the CT and Dedner cleaning schemes).
Tricco & Price [333] also developed a constrained formulation of Dedner divergence cleaning scheme for smoothed particle magnetohydrodynamics simulations. It was shown to be numerically more stable at density jumps and free boundaries (as opposed to periodic boundaries).

We note that Mocz *et al.* [312] also implemented a CT scheme in Arepo. They found that in turbulence simulations with a Powell cleaning scheme, the mean magnetic field artificially grows compared to the CT scheme which conserve the mean magnetic field of ideal MHD.
Moreover in their disc simulations, the divergence cleaning scheme shows a faster magnetic field growth and that the magnetic pressure dominates the gas pressure by a factor of 5 (whereas the CR simulations saturates to equipartition).

Mocz *et al.* [312] concluded that CT is preferred over cleaning technique as the latter, with its non-conservative formulation (divergence correcting source-terms), produce artificial magnetic field growth due to the source terms and can quickly transfers magnetic energy to the largest scales.
However, the Arepo CT implementation has not been used (except in simulation of the same principal author [334, 335]).
See also Hopkins & Raives [336] that identified problems where using only Powell or "8-wave" cleaning can produce order-of-magnitude errors.

7.3 Our Initial conditions for seed magnetic fields

To our knowledge, all current galaxy cluster cosmological simulations use a uniform magnetic seed field i.e. a constant value B_0 along a given axis (e.g. [145, 281, 291, 311, 329, 337]).
However, was saw in Section 7.1.2 that inflationary generation of magnetic fields should lead to gaussian random seed fields. Moreover, if magnetic fields originate for a much later epoch via Biermann battery, Weibel instabilities, or with the first stars, the initial magnetic fields would rather be randomly distributed than uniform.

This issue motivated our first study where we investigated the impact of the seed fields on the magnetic field evolution.
We investigated the evolution of the magnetic fields for different initialisation of the magnetic fields. We study the evolution of 3 different seed fields, being :

- *Uniform* seed field : a homogeneous magnetic field in the box along a prescribed direction,
- *Gaussian random* seed field that fluctuates on *large* scales: each component of the seed field follows a given power spectrum,
- *Gaussian random* seed field that fluctuates on *small* scales: same as above but the power spectrum has more power on smaller scales.

The magnetic field is initialised at the beginning of the simulation, i.e. $z = 49$.

By default, Ramses sets a uniform value along the box z axis. We use this simple initialisation for our uniform field :

$$\mathbf{B} = B_0 \hat{\mathbf{z}}. \tag{7.22}$$

where B_0 is the inital magnetic strength and $\hat{\mathbf{z}}$ is the unit vector along the z axis.

For the other two random seed fields, we use a more subtle approach.
When field fluctuations happen on too small scales, the magnetic fields can reconnect. Thus, the magnetic strength can quickly vanish. Therefore, we need a seed field that fluctuates on relatively large scales compared to the cell size.

To ensure the divergence free constraint of our initial seed field, we use a magnetic vector potential $\mathbf{A}$. Indeed, by definition, the

curl of the vector potential gives us the solenoidal constraint of the magnetic field :

$$\mathbf{B} = \boldsymbol{\nabla} \times \mathbf{A} \implies \boldsymbol{\nabla} \cdot \mathbf{B} = \boldsymbol{\nabla} \cdot (\boldsymbol{\nabla} \times \mathbf{A}) = 0. \tag{7.23}$$

Hence, using a magnetic vector potential guarantees that no magnetic monopoles can exist.

The potential magnetic fields are generated outside the Ramses code and we will describe now our methodology.

In order to generate a gaussian random (potential) seed field, we work in Fourier space to specify its power spectrum. Indeed, the field fluctuations are fully described by a power spectrum as we already saw in Section 2.2.2.

To avoid magnetic recombination, we would like the fluctuation to be on sufficiently large scales with respect to our cell resolution. Hence, we chose a power law power spectrum for which we could specify the scales on which the field fluctuates.
This is given by the slope of the power spectrum as illustrated by Figure 7.10. The steeper the slope is (i.e. higher spectral index n_A), the more power there is on large scales (i.e. small wavevectors k). On the other hand, for a shallower power spectrum, more power is given on small scales (large k).

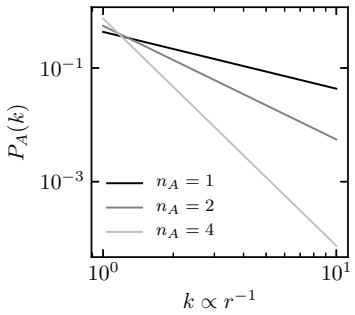

Figure 7.10: Illustration of power spectra with increasing n_A indexes. Low values of n_A gives more power on large k i.e. small scales r, on the other hand lower n_A values assign more power on large scales. An infinite index value, put all power on only one scale : this will correspond to an uniform field. Illustrations for Gaussian random fields are shown in Figure 7.11.

Hence, for our magnetic potential $\mathbf{A}$, we require such power spectra :

$$P_A(k) \propto |\mathbf{A}|^2 \propto k^{-n_A}, \tag{7.24}$$

Since the $\mathbf{B}(k) = \mathrm{i}k\mathbf{A}(k)$, we also have a power law spectrum for the magnetic field :

$$P_B(k) \propto k^2 P_A(k) \propto k^{-n_A+2} \tag{7.25}$$

To get the magnetic potential field in real space, we performed an inverse fast Fourier transform (FFT).

We treat all three components of the magnetic potential field independently. It ensures that the final distribution of $\mathbf{A}(\mathbf{r}) = \big[A_x(\mathbf{r}), A_y(\mathbf{r}), A_z(\mathbf{r})\big]$ has independent phases.

As the result, for all positions $\mathbf{x}$ in our simulation box of size N, we store a set of three independent values of A_x, A_y, A_z. In total, $3 \times N^3$ values needs to be read and parsed to Ramses.

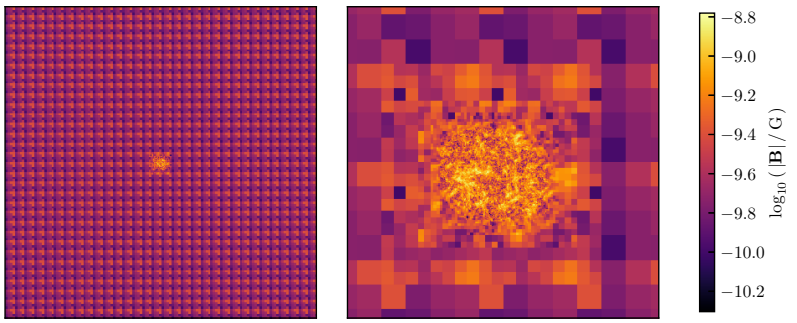

Figure 7.12: Magnetic field strength slices of the 1 Gpc full box (*left*) and 3 Mpc wide (*right*) showing our initialisation at $z = 49$ of gaussian random magnetic seed field.

In our case, we have a box size of $N = 2^{13}$ thus $3 \times 2^{13\times3}$ double precision numbers need to be stored in memory which yields a total size of ~ 13 To !
We had to cut down the size of the stored fields.Therefore, we chose to generate smaller boxes and replicate them throughout the full simulation box. We reduce to a more reasonable size of $\tilde{N} = 256^3 = (2^8)^3$ (~ 400 Mo). As the result, the smaller box needs to be replicated $(2^{13-8})^3 = 32^3$ times.

In panels of Figure 7.11, we show the slices of the smaller 256^3 boxes that respond to different power spectra.

The replication is performed within a Ramses routine.[13] After completing the replication, we loop over all hydro cells and compute the curl of the potential vector in Ramses.
We carefully check after this step that the divergence of the initial magnetic field is indeed zero.

We normalise the initial magnetic field **B** by setting its root mean square to the same initial magnetic field strength B_0 of the uniform field (Equation 7.22). As we said in Section 7.1, it is reasonable to expect cosmic magnetic fields in the order of $|\mathbf{B}| \sim 0.1$ nG comoving. Hence we set $B_0 = 0.1$nG. This guarantees that the magnetic energy at the grid scale is constant.

As the result, we show in Figure 7.12 the magnetic field initialisation at the start of the simulation. We can clearly see the 32^3 replicas of our small 256^3 boxes. In the zoom region, best visible in the right panel, we can see the field fluctuations on scales larger than the resolution. Hence the large magnetic field coherence length elude numerical field recombination.

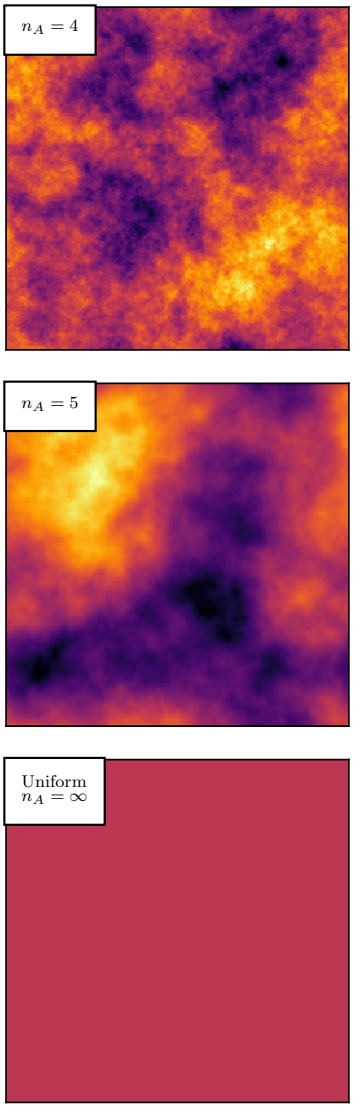

Figure 7.11: Slices of the magnetic potential seed field that follow a power spectrum of Equation 7.24 with the spectral index, n_A, given in the top left inserts. Low indexes favour small scales amplitudes whereas higher n_A will favour larger scales fluctuations. A power spectrum of infinite slope correspond to an absolute uniform field.

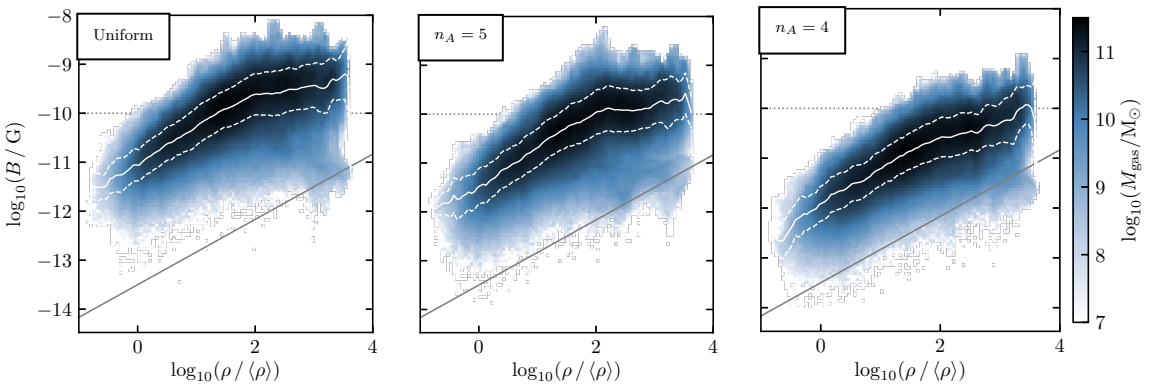

Figure 7.13: Phase diagrams of the magnetic field versus the gas density inside the virial radius at $z = 0$ for adiabatic simulations with different seed fields. The grey solid line shows the expected scaling from a pure adiabatic collapse. The grey dotted line shows the average strength $B_0 = 0.1\,\mathrm{nG}$ of the initial field seeded at $z = 49$ and follow different the power spectra given by Equation 7.25 where the spectral index is shown is the top left insert. White lines represent the median (solid), the 16^{th} and 84^{th} percentiles (dashed). We do not observed any difference compared to the expected slope of 2/3. The change in the relations is only an overall rescaling the magnetic field, which is due to the seed field configuration. The uniform seed field (left) show higher B than the random seed fields at $z = 0$. However, we note a higher normalisation for larger scale fluctuations in the seed field, i.e. larger n_A.

7.4 Magnetic amplification

In this section we will study the evolution of the magnetic fields for three simulations with different seed fields described in the previous Section 7.3. We consider only adiabatic physics and run each simulation from $z = 49$ to $z = 0$.

We show in Figure 7.13 the two-dimensional histograms of the magnetic strength versus the gas overdensity for all gas cells inside the virial radius at $z = 0$. We colour coded according to the mass of gas falling on to each bin. We show the expected $|\mathbf{B}| \propto \rho^{2/3}$ pure adiabatic collapse amplification as the solid grey lines. We indicated with dotted grey lines the initial average magnetic field strength $B_0 = 0.1\,\mathrm{nG}$.

We can see that our data roughly follows the expected scaling of amplification via gravitational collapse. In contrast to other studies, we do not see any additional amplification via small scale dynamo as reported in studies of amplification in galaxy clusters of Dubois & Teyssier [281] and Vazza *et al.* [310, 337] or Marinacci *et al.* [145] (see Figure 7.6 for [281] and [145]).
Moreover, we do not get any magnetic field strengths of the order of μG. Therefore, our simulations do not reproduce the observed μG values in galaxy clusters.

From Figure 7.16, we clearly see that the simulation with the uniform seed fields shows higher magnetic field strengths overall. While the simulation with the Gaussian random field fluctuating on smaller scales (i.e. lower $n_A = 4$) shows the lowest $|\mathbf{B}|$ values.

13: We thank Yohan Dubois for giving us access to his Ramses replication routine for setting initial conditions

We conclude that the more coherent the seed field on large scales, the stronger is the magnetic amplification. Hence, the simulation with the uniform seed field provides the maximal amplification. Therefore, such simulations set an upper limit on the amplified magnetic fields at $z = 0$.
Moreover, it is not unexpected that numerical diffusion leads to the reconnection on small scales, which has a stronger effect for smaller n_A.

We observe a pure collapse amplification for overdensities lower than ~ 100. At higher overdensities, the magnetic strengths show lower values than the expected scaling. We argue that, at such overdensities, the magnetic field lines are very close and tangled. Hence we suppose that magnetic reconnection is at play and magnetic energy is diffused in the ICM.

We shown in Figure 7.14 the radial profiles of the magnetic field strength of our three simulation. We see a clear offset in the normalisation with the simulation with the uniform seed field shows the highest strengths at all radii.

We show in Figure 7.15 slices of 10 Mpc size[14] of the magnetic field strength at $z = 0$. We see strongly magnetised cores and lower fields in the cluster outskirts. The cluster magnetic fields show a very tangled structure with large coherence lengths.

14: The cluster virial radius is 1.7 Mpc

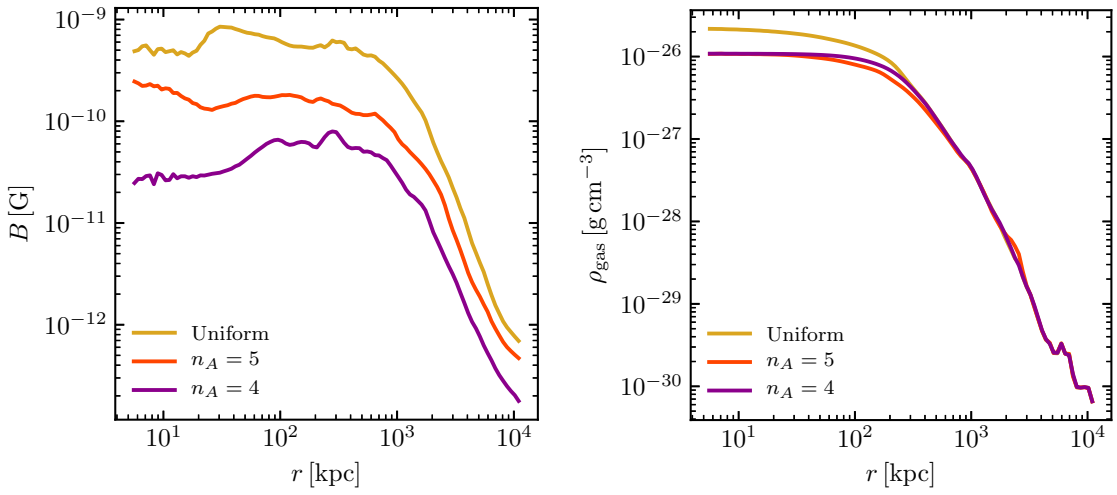

Figure 7.14: Volume averaged radial profiles for the magnetic field strength (*left*) and gas density (*right*) at $z = 0$ for the three non-radiative simulations having different magnetic seed fields. The golden line represents an uniform seed field, while the orange and purple represent gaussian random fields with the former ($n_A = 5$) having magnetic fluctuations on larger scales than the latter ($n_A = 4$). We can see that the different initialisation of the magnetic field result in different normalisations of the cluster magnetic fields. The lowest magnetic fields are observed for the small scale fluctuating seed field ($n_A = 4$) where the uniform initial field shows the largest strengths. The initial seed field determine the overall cluster magnetic strength.

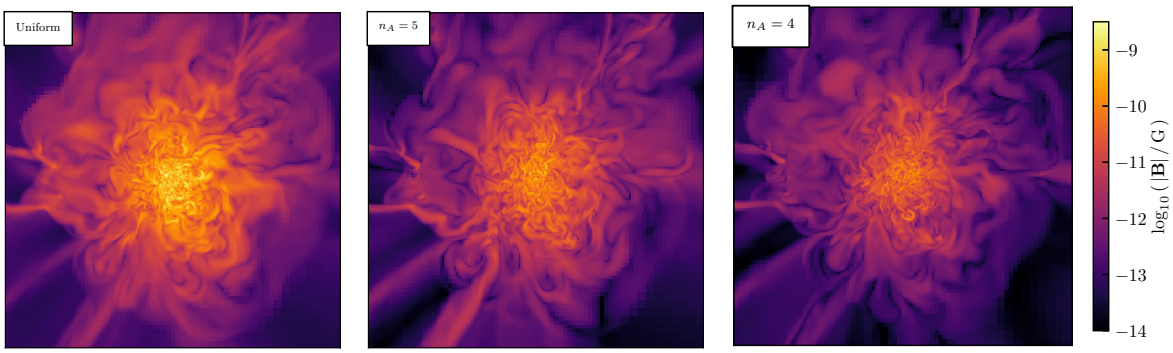

Figure 7.15: 10 Mpc Volume-averaged 10 Mpc wide slices of the magnetic field strength at $z = 0$. The upper left inserts shows the index of the prescribed power spectrum of the initial magnetic potential field. In the left panel, the uniform magnetic field ($n_A = \infty$) shows the greatest amplification in the cluster centre as well as large radii. In the middle and right panels, the index decreases. We observe overall lower magnetic fields with the lowest strengths for $n_A = 4$. As the result, more coherent the magnetic field is on large scales, greater is the amplification. An uniform initial field provides maximum amplification. However, we do not observe any significant magnetic amplification from the initial average value of 0.1 nG.

For the radial profiles and the maps of the magnetic fields strength, we do not see any difference between uniform or gaussian random seed field. The initial topology only impacts the overall normalisation and the memory of the field initial structure of is lost by $z = 0$.

Amplification with AGN feedback

Marinacci *et al.* [145] ran the first large-scale cosmological simulations of magnetic fields with inclusion of mordern galaxy formation physics (gas cooling, SN and AGN feedback). They argued that when feedback physics and gas cooling are included, magnetic fields are amplified to larger strengths (up to a factor 10^3) with respect to their non-radiative run. They reach strengths of a few up to tens of μG in the centres of massives haloes.
They found a saturated magnetic amplification at all overdensities to the same strengths irrespective of the uniform seed field (which varies from strengths of 10^{-16} to 10^{-12} comoving G).
They attribute this additional amplification to the increased level of turbulent and shear gas motions triggered by galactic outflows and AGN feedback.

These simulations were run with the Arepo code using Powell *et al.* [320] divergence cleaning technique [326] to ensure the $\nabla \cdot \mathbf{B} = 0$ constraint. They seeded a homogeneous magnetic field in their 100 h^{-1}Mpc box at the starting redshift $z = 127$ along a prescribed direction.[15]
They use the galaxy formations physics developed for the Illustris simulation suite [338] at two different resolutions : First, $2{\times}256^3$ DM and gas particles with respective mass resolution of $4.2{\times}10^9\ h^{-1}\mathrm{M}_\odot$

15: They found that the direction of the uniform seed field does not play any role inside haloes on the averaged B properties and orientations, due to the turbulent gas motions that rapidly erase any memory of the initial direction. On the other hand, filaments and voids retains its original orientation.

and $7.9 \times 10^8\, h^{-1}\mathrm{M}_\odot$. And, 2×516^3, with $5.3 \times 10^8\, h^{-1}\mathrm{M}_\odot$ and $9.8 \times 10^7\, h^{-1}\mathrm{M}_\odot$ DM and gas particle mass resolutions.

To our knowledge, the work of Marinacci *et al.* [145] remains the only study of simulations including baryonic physics with AGN feedback in a cosmological context.
However, as we said in Section 7.2.1 the solenoidal constrain treated with the Powell cleaning scheme in their simulations may produce artificial magnetic field growth due to the presence of divergence correcting source-terms [312].

In Ramses, the constrained transport scheme of Fromang *et al.* [177] guarantees the solenoidal constrain at machine precision. It was indeed confirmed by Mocz *et al.* [312], that this scheme is more accurate than the divergence-cleaning technique for Arepo too.

As we saw in the previous section, we do not observe significant magnetic field amplification at high overdensities for non-radiative simulations.
In this context, we would like to test wether baryonic physics provide significant turbulent dynamos to reach magnetic amplification of few orders of magnitude.

In the previous section we found that the topology of the magnetic seed field only provide a change in the normalisation, with the uniform field providing a maximum amplification.
For convenience, we will now use an uniform seed field. For these simulation, we chose to set a lower magnetic seed field strength of :

$$B_0 = 1.5 \times 10^{-12}\,\mathrm{G} \tag{7.26}$$

We will present the results for a set of 4 different simulations that we named : `NR`, `VW`, `MW` and `MC`, with :

- Non-radiative (`NR`) where the gas evolves adiabatically,
- Then we add baryonic physics : radiative gas cooling, star formation, stellar feedback, black hole formation and AGN feedback. We will review in great details the specification of all models in Chapter 9. We assume for now that these models are calibrated to reproduce the observed properties of a galaxy population and the ICM thermodynamics. As we will see extensively in Section 9.3, the way of redistributing AGN feedback energy into the ICM can have a great impact on the intra-cluster gas properties. We have two different models for the AGN energy injection : a volume-weighted (`VW`) and a mass-weighted (`MW`) deposition.

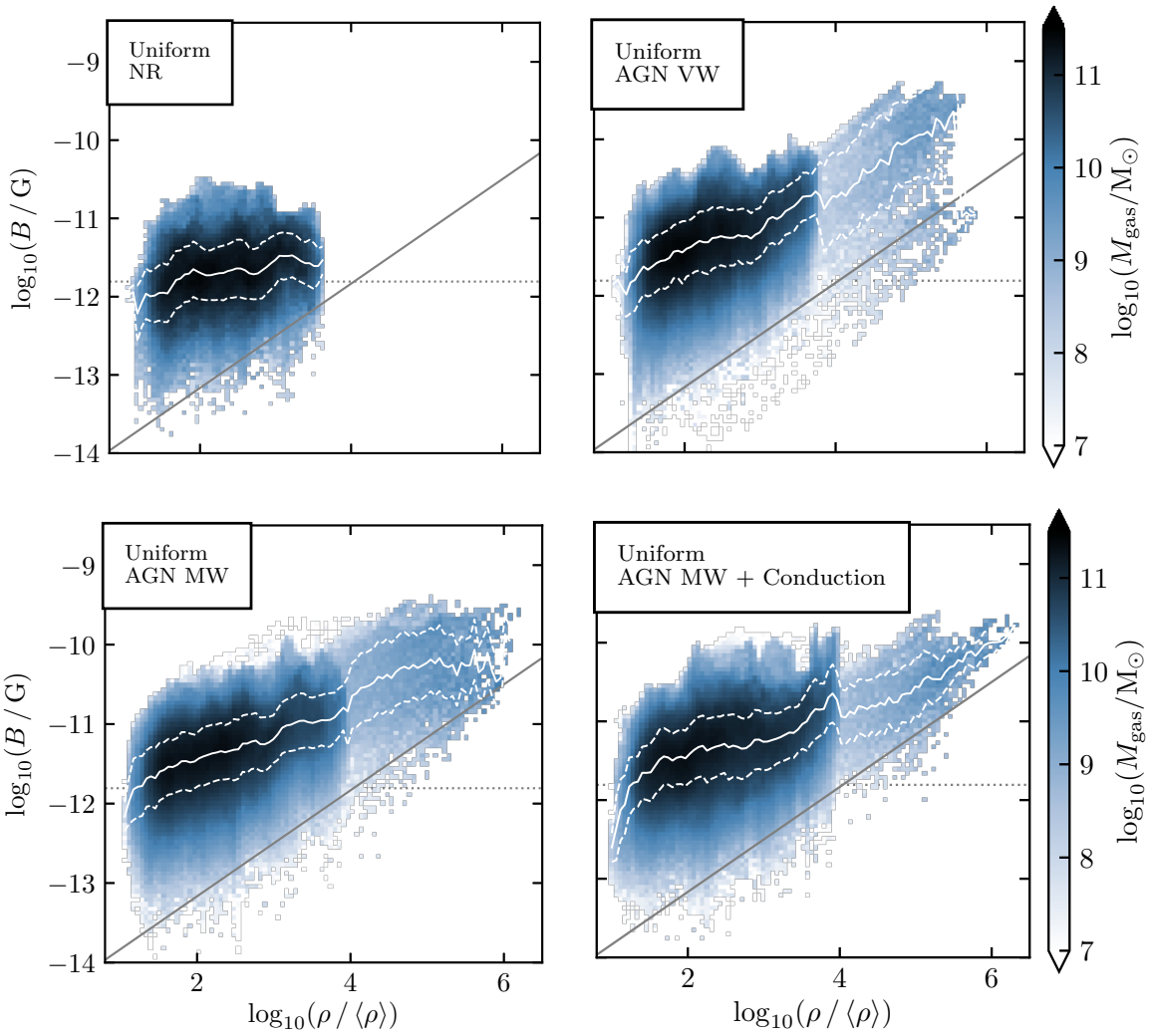

Figure 7.16: Same as Figure 7.13 but for our full physics simulations with an uniform seed field with a lower strength of $B_0 = 1.56 \times 10^{-12}$. The *left* panel show the phase diagram for the full physics simulation with a volume-weighted (VW) AGN energy injection. Both *middle* and *left* panels show simulations with mass-weighted (MW) energy injection while the former include anisotropic thermal conduction.

Simply put, on one hand, the VW model yields an efficient heating in the ICM out to large radii enhancing gas mixing. On the other hand, the MW AGN model injects feedback energy rather locally. Thus, significantly less shear and turbulent gas motions are observed in the ICM compared to the VW model.

- Finally, we add to the galaxy formation models with MW AGN feedback, the anisotropic thermal conduction (MC) that we will detail in the next Chapter 8.

We show in Figure 7.16 the 2D histograms of the magnetic strength and gas density of cells within the virial radius of our halo.
In the top left panel of Figure 7.16, we plot the phase diagram for the non radiative simulation. It seems that the median relation shown as the solid line is somehow shallow than the expected

amplification by compression.

The other three panels shows the effect of galaxy formation physics. We see that due to gas cooling, the gas condense and now reach higher overdensities.
As stated above, the efficient VW AGN feedback model induce more gas mixing. Hence, we see larger scatter in the magnetic field strength at overdensities larger than 10^4.

For simulations with the MW model, as the AGN heating is inefficient at large radii, gas cools and can condense to even higher densities. As the result, the magnetic fields from different magnetic domains are more spliced to one another due to the high densities. This magnetic reconnection happening at the resolution scale lead to a lower strength and magnetic energy is transferred into kinetic and thermal energy in the ICM.

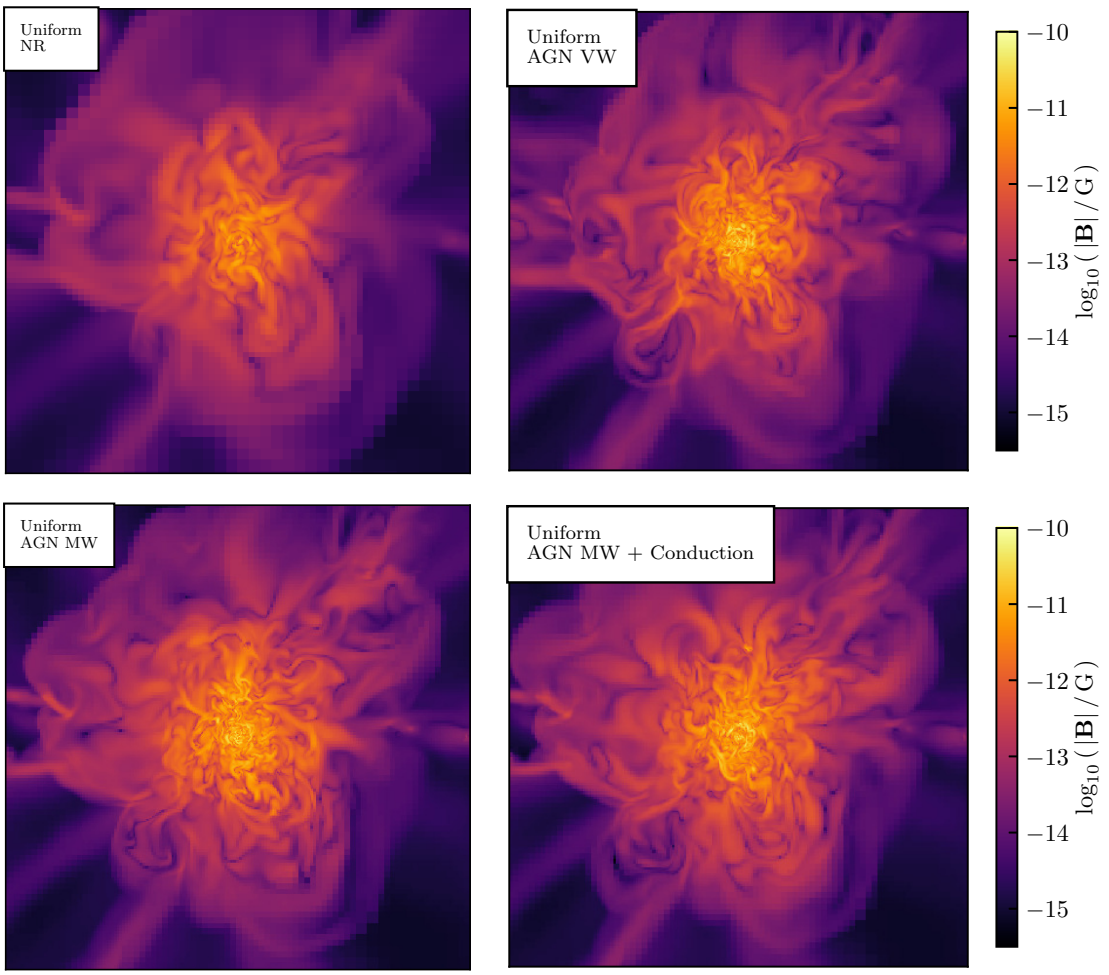

Figure 7.17: Same as Figure 7.15. 10 Mpc Volume-averaged 10 Mpc wide slices of the magnetic field strength $|\mathbf{B}|$ at $z = 0$ for the different simulations incorporating baryonic physics. See text for details.

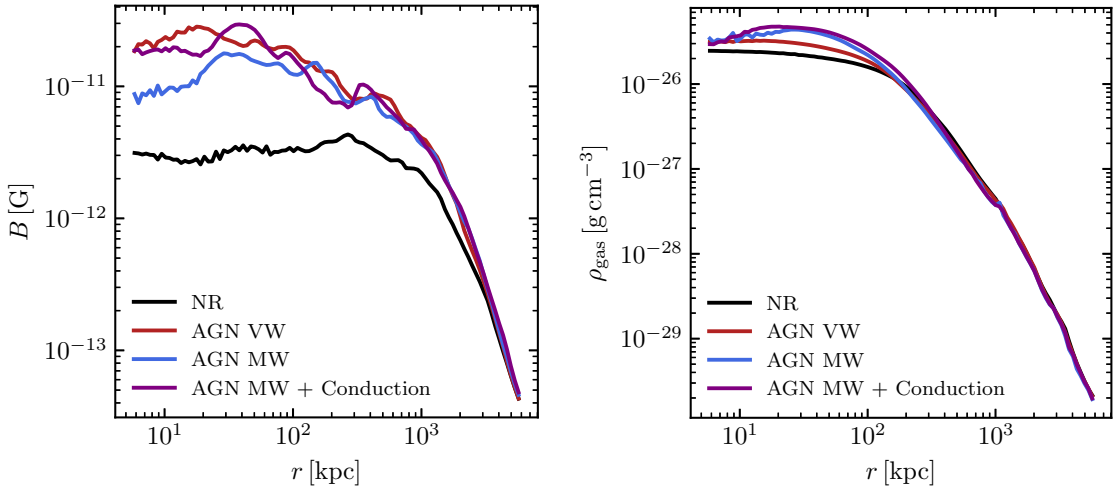

Figure 7.18: Same as Figure 7.14 for the radial profiles of the magnetic field strength (*left*) and the gas density (*right*).

7.5 Summary

Most studies of magnetic amplification in galaxy clusters use divergence cleaning schemes and uniform magnetic seed fields [145, 281, 291, 311, 329, 337]. However, we saw in Section 7.1.2 that Gaussian random magnetic seed fields are expected in different inflationary generation scenarios.
Moreover, these studies mainly use divergence cleaning schemes to ensure the solenoidal constraint, which was shown to produce artificial magnetic field growth [312].

For these reasons we investigated if the initial seed field topology has an effect on the magnetic amplification in clusters, using a constrained transport scheme were the $\nabla \cdot \mathbf{B} = 0$ constraint is enforced to machine precision.

We found that the uniform seed field provides the maximum amplification compared to Gaussian seed fields. For random initial fields, we found that the more coherent the initial field is on large scales, the greater is the amplification. Indeed, if the seed field fluctuates on small scale, magnetic reconnection might occur at the resolution scale. Thus, uniform seed fields provide an upper limit on the expected amplification.

However, we do not observe any amplification above what is expected from the pure compression of the gas ($B \propto \rho^{2/3}$).

Because we do not observe it, we can suspect that some of the observed amplification reported in other studies originates from the divergence cleaning schemes that could produce artificial mag-

netic field growth (as reported in Mocz *et al.* [312]).

Our simulations are very similar to the cosmological simulations of Dubois & Teyssier [281] as we both use Ramses' constrained transport schemes with comparable models of radiative physics[16] and value of the initial magnetic strength. However, we do not see any amplification to μG they observed (we reach maximum values of 10^{-2} μG).
This difference might be due to the fact that Ramses did not include the Hubble drag term in the induction Equation 7.10 at the time of the study of Dubois & Teyssier [281], which might results in the magnetic field amplification that they observed.

16: Simulations of Dubois & Teyssier [281] includes atomic cooling, UV heating, and star formation but not AGN feedback.

Marinacci *et al.* [145] argued that AGN feedback can provide significant additional magnetic amplification in galaxy clusters. However, we saw that when including galaxy formation physics (cooling, SF, feedback for SN and AGN) in our simulations, we do not observe any dynamo amplification.

As we can see on Figure 7.19, our simulations shown non-negligible vorticities with a tangled structure similar to what is observed on the magnetic field slices in Figure 7.17. Therefore, the observed fluid rotationality indicates for turbulent gas motions which should actually amplify magnetic field by dynamo processes. The fact that we do not observe the dynamo amplification claimed by various studies such as Marinacci *et al.* [145] might originate from numerical issues which deserve consideration.

To sum-up, we do not observe any dynamo amplification of cluster magnetic fields in our simulations including full galaxy formation sub-grid models with a constrained transport scheme[17] .

17: which correctly account for the Hubble drag therm in the super-comoving induction equation too

We also argue that the commonly used uniform seed field provide a maximum amplification. However, regardless of the initial fields, the field topology is lost by $z = 0$ which is of great importance for the transport of charged particles in the ICM.

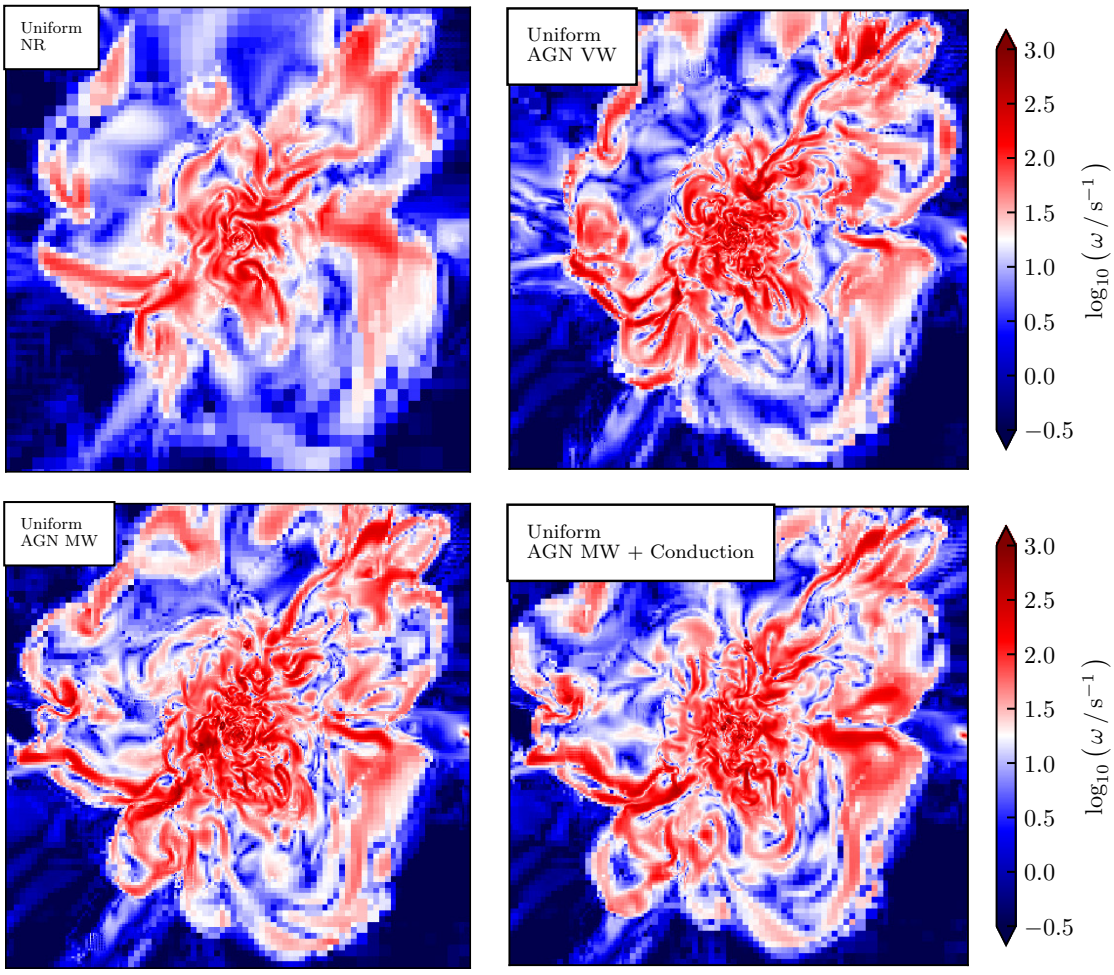

Figure 7.19: Same as Figure 7.17. 10 Mpc volume-averaged 10 Mpc wide slices of the vorticity strength $|\boldsymbol{\omega}|$ at $z = 0$ for the different simulations incorporating baryonic physics. The vorticity is defined as the curl of the gas velocity.

Anisotropic thermal conduction 8

After discussing processes related to the anisotropic transport of heat, we will explore the effect of such processes on the thermodynamics of the intra-cluster medium.

8.1 Phenomenology of thermal conduction

Diffusion processes are ubiquitous in nature. Especially, it arises when the temperature, density and average velocity are not the same throughout a gas. Transport processes are particularly important when the mean-free-path of particles is not negligibly small like in the ICM plasma. To approach an equilibrium, these non-uniformities have to be smoothed out through the transport of energy, mass and momentum from one part of the gas to another. Particularly, thermal conduction is the process through which internal energy is diffusively transported by collision of particles.

This process is of importance as many studies invoke thermal conduction to explain the short cooling times (shorter than ~ 500 Myr in the centre of clusters) while not observing at the same time large amount of cold gas in cluster cores that one expects in a cooling flow [339, 340].
Indeed, to prevent the cooling catastrophe, radiative losses must be offset by heating sources such as AGN feedback or by thermal conduction which can transport heat from the thermal reservoir at large radii.

In high energy plasma such as the ICM, electrons are the main carriers for this heat transfer.
However, as we just saw in Chapter 7, the ICM is permeated by magnetic fields. Therefore, due their presence, charged particles of the intra-cluster plasma preferentially move along the field lines. Hence, the heat transport become highly anisotropic which complicates its theoretical modelling.

Moreover, the combined effect of gravity and transport processes in stratified medium, such as the ICM, can trigger instabilities in the plasma which can drive thermal circulation in the ICM.

We start with a brief introduction of the physical properties and concepts of isotropic as well as anisotropic conduction.

8.1.1 Isotropic conduction

When a homogeneous plasma such as the ICM is out of thermal equilibrium, elastic collisions transfer energy to relax the ICM particles to a Maxwellian distribution. We will review particle collisions, which drive thermal conduction, to derive basic properties of this process in galaxy clusters.

Let us start by considering an ICM electron moving with a speed v.
The electron e flies by an ion with charge Z which is at rest[1] . The electron, with an impact parameter b, is scattered by the Coulomb field of the ion as illustrated in Figure 8.1. This discussion is following the derivation of Rutherford [341] for the first derivation of thelastic scattering of charged particles by the Coulomb interaction.

1: As the proton masses are much greater than that of the electron, the field ion moves much more slowly (if the electrons and ions are near thermodynamic equilibrium) and we can be treated as at rest for the moment.

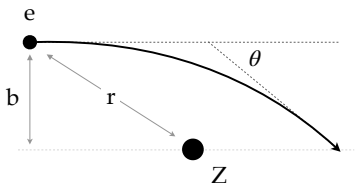

Figure 8.1: The geometry of a Coulomb collision

The perpendicular component of the Coulomb force, with respect to the electron motion is given by :

$$F_{\perp} = \frac{b}{r}\frac{Z^2e^2}{r^2}, \tag{8.1}$$

and acts over a time $\Delta t \sim b/v$, deflects the electron velocity vector at an angle θ.[2] The change in the perpendicular electron velocity is :

$$\Delta v_{\perp} = \frac{1}{m_e}F_{\perp}\Delta t = \frac{Ze^2b^2}{m_e v r^3} \sim \frac{Ze^2}{m_e b v}, \tag{8.2}$$

2: We assume that the deflection angle is so small that absolute velocity almost does not change.

Therefore, the parallel component of the electron velocity changes by :

$$\Delta v_{\parallel} = v\,(1-\cos\theta) \sim v\frac{\theta^2}{2} \sim \frac{\Delta v_{\perp}^2}{2v} \sim \frac{Z^2e^4}{m_e^2 b^2 v^3}. \tag{8.3}$$

Integrating over all impact parameters, we can obtain the change in the parallel momentum over the time Δ_t of an electron beam of number density n_e :

$$\Delta p_{\parallel} = \int_{b_{\min}}^{b_{\max}} \mathrm{d}b\, 2\pi b\, n_e m_e v \Delta v_{\parallel} = \frac{n_e Z^2 e^4}{m_e v^2}\ln\Lambda. \tag{8.4}$$

where $\ln\Lambda = \ln(b_{\max}/b_{\min})$ is the Coulomb logarithm.

The maximum impact parameter $b_{\max}$ is the Debye length λ_D, since for impact parameters $b \gg \lambda_D$ the Debye shielding screens out a particle's Coulomb field.[3]
The minimum impact parameter $b_{\min}$ is the distance b_0 of closest

3: The Debye length is a measure of a charge carrier's net electrostatic effect in a plasma and how far its electrostatic effect persists.

$$\lambda_D = \sqrt{\frac{\mathrm{k_B}\,T}{8\pi\bar{n}e^2}}. \tag{8.5}$$

We refer to reader to the book of Fitzpatrick [342] for related plasma quantities and more rigorous definitions.

approach, obtained by equating the initial kinetic energy to the Coulomb energy at closest approach

$$\frac{1}{2}m_e v^2 = \frac{1}{4\pi\epsilon_0}\frac{Ze^2}{b_0}, \tag{8.6}$$

$$\implies b_0 = \frac{Ze^2}{2\pi\epsilon_0 m_e v^2}, \tag{8.7}$$

But, due to the quantum mechanical wave packet spreading, the nearest the electron can go is the de Broglie wavelength $\lambda_e = \hbar/(m_e v)$. Therefore, $b_{\min} = \max[b_0, \lambda_e]$.
For numerical values of $\ln\Lambda$ in a thermalised plasma, see Spitzer [343]. At typical cluster densities and temperatures, we have $\ln\Lambda \sim 40$.[4]

4: More precisely for temperature above 10^6 K :

$$\ln\Lambda = 37.8 + \ln\left[\left(\frac{T_e}{10^8\,\mathrm{K}}\right)\left(\frac{n_e}{10^{-3}\,\mathrm{cm}^{-2}}\right)^{-1/2}\right]$$

which is nearly independent of the temperature

We can define the collision rate as the rate of loss of the parallel beam momentum :

$$\nu^{ei} = -\frac{1}{p_\parallel}\frac{\Delta p_\parallel}{\Delta t} \sim \frac{n_e Z^2 e^4}{m_e^2 v^3}\ln\Lambda, \tag{8.8}$$

We must also consider the repulsive collision of our test electron with field electrons. Although the assumption that field electrons are at rest is no longer justified, the impact for large angle deflection is still $\sim b_0$, hence Equation 8.8 is still appropriate, as an order of magnitude estimate :

$$\nu^{ee} \sim \frac{n_e e^4}{m_e^2 v}\ln\Lambda, \tag{8.9}$$

The intra cluster plasma is dominated by hydrogen ($Z \sim 1$) and we have :

$$\nu \sim \nu^{ei} \sim \nu^{ee} \sim \frac{n_e e^4}{m_e^2 v}\ln\Lambda \tag{8.10}$$

As the result, the electron can travel on average a distance λ_{mfp} in the ICM before experiencing a Coulomb collision with a particle. This distance is the mean free path and for an electron we have :

$$\lambda_{\mathrm{mfp}} \sim \frac{v}{\nu} \sim \frac{(\mathrm{k_B}\,T_e)^2}{n_e e^4 \ln\Lambda} \tag{8.11}$$

where we used the thermal velocity of electrons $v \sim \sqrt{2\mathrm{k_B}\,T_e/m_e}$.
In a more rigorous derivation by Spitzer [343], one finds :

$$\lambda_{\mathrm{mfp}} = \frac{3^{3/2}}{4\pi^{1/2}}\frac{(\mathrm{k_B}\,T_e)^2}{n_e e^4 \ln\Lambda}, \tag{8.12}$$

$$\sim 23\,\mathrm{kpc}\left(\frac{T_e}{10^8\,\mathrm{K}}\right)^2\left(\frac{n_e}{10^{-3}\,\mathrm{cm}^{-2}}\right)^{-1}, \tag{8.13}$$

Electrons will finally reach an equilibrium among themselves on a time scale τ^{ee}, roughly set by the mean free path and the root mean squared electron velocity[5] :

$$\tau^{ee} = \frac{3}{4\pi^{1/2}} \frac{m_e^{1/2} (\mathrm{k_B}\, T_e)^{3/2}}{n_e e^4 \ln\Lambda}, \tag{8.14}$$

$$\sim 0.326\,\mathrm{Myr} \left(\frac{T_e}{10^8\,\mathrm{K}}\right)^{3/2} \left(\frac{n_e}{10^{-3}\,\mathrm{cm^{-2}}}\right)^{-1}. \tag{8.15}$$

ICM protons will equilibrate for $\tau^{pp} = \sqrt{m_p/m_e}\,\tau^{ee} \sim 43 \times \tau^{ee}$ while electrons and protons will reach equipartition (i.e. $T_e = T_i$) for $\tau^{ei} = (m_p/m_e)\,\tau^{ee} \sim 1840 \times \tau^{ee}$.[6]
As the result, thermal conduction happens roughly on time scales of $1840 \times 0.33 \sim 600\,\mathrm{Myr}$ which is much shorter than the age of clusters, but not short enough to be irrelevant.

5: $\langle v \rangle_{\mathrm{rms}} = \sqrt{3 \mathrm{k_B}\, T_e}$

6: For heavier ions in the ICM (being nearly fully stripped), equilibration time scales are generally at least this short as the increased charge makes up more than the increased mass.

Because, the mean free path of electrons given in Equation 8.13 is much shorter than the length of the temperature gradient $l_T = T_e/|\nabla T_e|$, heat diffusion can occur. For a non-magnetized plasma, the heat flux is given by Fourrier's law :

$$\mathbf{Q} = -\kappa \boldsymbol{\nabla} T_e, \tag{8.16}$$

with a conduction coefficient κ. In an idealised plasma, the conductivity is given by the Spitzer value :

$$\kappa_{\mathrm{Sp}} = 20 \left(\frac{2}{\pi}\right)^{3/2} \frac{(k_B T_e)^{5/2}\, k_B}{m_e^{1/2} e^4\, Z \ln\Lambda} \tag{8.17}$$

which strongly depends on the electron temperature. Therefore, we see that thermal conduction might play an important role in the presence of AGN heating for instance.
We can derive the conduction timescale characteristic of the ICM :

$$t_{\mathrm{cond}} \sim \frac{n_e l_T^2}{\kappa_{\mathrm{Sp}}} \sim 10\,\mathrm{Myr} \left(\frac{n}{10^{-3}\,\mathrm{cm^{-3}}}\right) \left(\frac{l_T}{100\ \mathrm{kpc}}\right)^2 \left(\frac{T_e}{10^6\,\mathrm{K}}\right)^{-5/3} \tag{8.18}$$

which is small compared to cluster dynamic time scales.

However, we observe various temperature substructures such as cold fronts or filaments as shown in Figure 8.2. Hence, if thermal conduction was so efficient, these features should not have survived during cluster evolution.

Indeed, this idealised thermal conductivity needs to be multiplied by a factor ζ which has been calculated by Spitzer & Härm [345]. This factor highly depends on the proton number density : from $\zeta = 0.225$ for a pure electron-proton plasma to values $\zeta \sim 1$ for large Z.

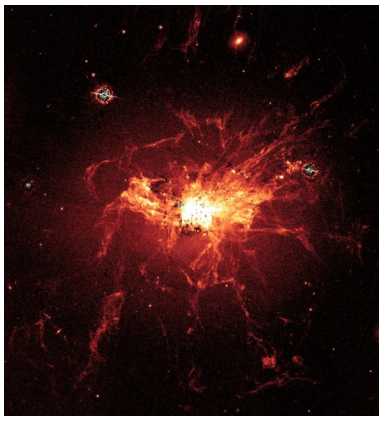

Figure 8.2: Hα emission from the core of the Perseus cluster showing cold gas filament of size $\sim$ 10 kpc. The filaments might be tracing magnetic fields of the ICM, it could explain the peculiar horseshoe shaped filament in the top right corner. See also radiation-hydrodynamic simulations of AGN feedback in cool-core cluster by Qiu *et al.* [344].

Another correction needs to be made. For a plasma with very low density, and even at high temperatures, one cannot expect that the conductivity as Coulomb scattering should happen only at a very low rate. In this case we have the saturated heat flux derived by Cowie & McKee [346] :

$$Q_{\rm sat} = 0.4 n_e k_B T \left(\frac{2k_B T}{\pi m}\right)^{1/2}, \tag{8.19}$$

An interpolation between the idealised and saturated case, yields a conduction coefficient [347, 348] :

$$\kappa = \frac{1}{1 + 4.2\frac{\lambda}{l_T}} \kappa_{\rm Sp}. \tag{8.20}$$

This modified Spitzer conduction is valid for galaxy clusters in the absence of magnetic fields. Yet, clusters do host magnetic fields, and their presence forces charged particles to move primarily along the field lines.
Consequently, this non-thermal diffusion process become highly anisotropic and the above derived heat flux cannot be valid.

8.1.2 Anisotropic conduction

The original formulation of the so-called Spitzer conductivity assumes an isotropic movement.
However, in the presence of magnetic field lines, the motion of particles perpendicular to the field lines is restricted. The assumption of isotropic collisions in the previous Section 8.1.1 no longer holds and the coupling of thermal conduction with magnetic field topology has to be considered. This results in different heat transfer in the direction perpendicular or parallel to the field line with different conduction coefficients $\kappa_\perp$ and $\kappa_\parallel$ respectively.

Braginskii [349] in the full derivation of anisotropic transport coefficients in a magnetized plasma, presented three terms of conductive heat flux :

$$\mathbf{Q} = -\kappa_\parallel \boldsymbol{\nabla}_\parallel T - \kappa_\perp \boldsymbol{\nabla}_\perp T - \kappa_\Lambda \mathbf{b} \times \boldsymbol{\nabla} T, \tag{8.21}$$

with $\mathbf{b} = \mathbf{B}/|\mathbf{B}|$, the unit vector in the direction of the local magnetic field.

Note that the particle movement parallel to the magnetic field is not restricted, the diffusion along the field lines should not be affected.

Specifically, electrons move on spiral trajectories around magnetic field lines due to the Lorentz force. The radius of this circular motion is the gyroradius (or Larmor radius) given by :

$$\rho_g = \frac{m v_\perp}{ZeB} \sim 10^{-13}\ \mathrm{kpc}\ \frac{1}{Z}\left(\frac{m}{m_e}\right)^{1/2}\left(\frac{T_e}{10^8\,\mathrm{K}}\right)^{1/2}\left(\frac{B}{1\,\mu\mathrm{G}}\right)^{-1}, \quad (8.22)$$

and is much smaller then any length scale of interest in clusters and the mean free path in Equation 8.13. Nevertheless, because ions have larger gyroradii, they are more effective in transport processes perpendicular to the field line. In practice, the gyroradii are so small in the ICM that thermal conduction perpendicular to field lines is almost totally suppressed.[7]
The last term in Equation 8.21, does not arise from particle collisions but comes from the Hall effect that transports energy in a direction perpendicular to both the temperature gradient and the magnetic field. We will not go into detail here, as the Hall conductivity plays no significant role in the ICM.

7: Indeed, the perpendicular condictivity is :

$$\kappa_\perp \sim n_e \rho_g^2 \nu^{ee}, \quad (8.23)$$
$$\sim n_e \left(\frac{\rho_g}{\lambda_{\mathrm{mfp}}}\right)^2 \kappa_{\mathrm{Sp}}, \quad (8.24)$$
$$\ll \kappa_{\mathrm{Sp}}. \quad (8.25)$$

As the result, for the ICM it is reasonable to assume that the heat flux is only driven by the component of the temperature gradient parallel to the magnetic field :

$$\mathbf{Q} = -\kappa_\parallel\, \mathbf{b}\,\mathbf{b}\cdot\boldsymbol{\nabla}T. \quad (8.26)$$

8.1.3 Tangled magnetic fields

In the ICM, tangled magnetic fields concentrated on a scale l_B develop. This scale can be comparable to or even shorter than the mean free path of the electrons λ_{mfp}. Chandran & Cowley [350] show that the thermal conductivity κ is reduced by a tangled magnetic fields. They specifically applied their theory to galaxy cluster cooling flows and derived a reduction of the Spitzer value by a factor of order 10^2 to 10^3.

As the electron is moving along field lines on a scale $\sim l_B$, it also drifts a distance $\sim \rho_g$ perpendicular to the magnetic field due to field strength gradients and field line curvature. Such displacement is shown in Figure 8.3 where the electron travels the distance l_B from P to Q. At point Q, the electron drifts a distance ρ_g from the magnetic field line and starts to follow a new neighbouring field line. After a distance l_B along this new line, it diverges (exponentially) from the initial solid line by a distance $d(l) \sim d(0)e^{l/L_K}$ (where L_K is the Kolmogorov-Lyapunov length [351]) to arrive at point R. At this point, the electron's subsequent motion is not correlated with its initial field line. The distance

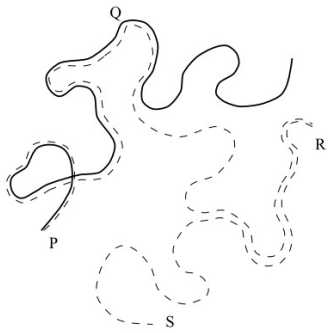

Figure 8.3: An electron tajectory (dashed) along a tangled magnetic field line (solid) – Credits : Chandran & Cowley [350]

between points P and R is the Rechester-Rosenbluth [352] length:

$$L_{\mathrm{RR}} \sim l_B \ln\left(\frac{l_B}{\rho_g}\right) \tag{8.27}$$

However this value is slightly overestimated as the electron constantly drift away from magnetic lines [350].

Let us consider that at point R, the electron is reflected by a collision or a magnetic mirror. Then it will not return to point P, as it would have done in the case of no transverse diffusion, but travels to point S along a new magnetic field line.

We see that a very small amount of transverse diffusion, can restore an isotropic random walk of the electron in space.
Therefore, the effective transverse electron diffusion is greatly enhanced by the stochasticity of the field lines. Applying to galaxy clusters, Chandran & Cowley [350] used Monte Carlo particle simulations to find that the diffusion coefficient is about two orders of magnitude smaller than the Spitzer value.

However, the ICM can be turbulent in a wide range of scales. Narayan & Medvedev [353] found that in MHD turbulence, the Kolmogorov-Lyapunov length is $L_{\mathrm{RR}} \sim l_B$ which yields a less reduced diffusivity of $D_{\mathrm{turb}} \sim D_{\mathrm{Sp}}/5$.

See also Shalchi [354] for a recent review of perpendicular transport of energetic particles in magnetic turbulence. We will not discuss these aspect further here but these processes are relevant for the study of cosmic rays.

8.1.4 Instabilities

In the previous Section 8.1.2, we explored the Braginskii MHD which describes the anisotropy of heat transport directed along the magnetic field lines. While this framework describes some features or weakly collisional systems, it does not captures the micro-scale instabilities that the ICM could support. On the other hand, fully collisionless plasmas are better described by the Vlasov-Maxwell equations. In this case, these equations can be used to derive the linear theory of kinetic instabilities such as the firehose and mirror instabilities, driven by anisotropies in the velocity space with respect to the magnetic field [355]. In particular, studies have shown that such instabilities in collisionless plasma can suppress heat conductivity in the case of an ion mirror instability [356] and an electron whistler instability [357].

In the ICM, the weak magnetic fields conspire with the low collisionality to make the plasma prone to these kinetic instabilities, where their presence could influence the ICM dynamics.

The picture gets more complex with the introduction of anisotropic thermal conduction in a stratified medium. Actually, convection motions can be triggered in the presence of a entropy gradient in a stratified fluid. In plasma, situations where the temperature increase in the direction of gravity with no heat flux in the background give rise to a magnetothermal instability (MTI). Balbus [358] showed that the plasma with an anisotropic thermal conduction is buoyantly unstable to the convective-like motions.
Quataert [359] extended the analysis of Balbus [358] in the presence of background heat flux. A new heat-flux-driven buoyancy instability (HBI) arises because of the background heat-flux cooling or heating a perturbed fluid element in a way to become buoyantly unstable. This happens in the opposite situation where the temperate decreases in the direction of gravity.
As the result, the entire intra-cluster plasma is unstable : in the outskirts the ICM is MTI instable and while cluster cores are MTI stable, HBI takes over ($0.1 - 100$ kpc) as the temperature decreases inwards.
Moreover, these instabilities might reorient magnetic field lines. The MTI is found to reorient field lines rather radially, thus allowing a heat flow along the temperature gradient. The instability does not saturates and sustain the convective motions in the ICM. The HBI on the other hand saturates by reorienting the magnetic fields perpendicular to gravity.
Finally, as the kinetic instabilities (discussed in the previous paragraph) have an effect on the plasma conductivity and they also impact the MTI and HBI.

We see that the effect of thermal conduction in the ICM is not straightforward. Moreover, large scale plasma motions induced by mergers, AGN and SN feedback could impact the evolution and saturations of these instabilities. In short, the introduction of anisotropic thermal conduction fundamentally change the response of the intra-cluster plasma to perturbations.

8.2 Numerical implementations

Many astrophysical codes treat the anisotropic thermal conduction and applied it to the study of galaxy clusters. For instance:

- Parrish & Stone [360], Bogdanović *et al.* [361], Avara *et al.* [362], Berlok *et al.* [363] for the Athena code
- Ruszkowski *et al.* [295] for Flash

- Dolag *et al.* [364], Arth *et al.* [348] for GADGET
- Kannan *et al.* [365], Barnes *et al.* [366], Kannan *et al.* [114] for AREPO
- Smith *et al.* [367] for ENZO
- Dubois & Commerçon [179] for RAMSES

In more details, Dolag *et al.* [364] reported the first hydrodynamical simulations of the formation of clusters with anisotropic thermal conduction (shown in Figure 8.4). While thermal conduction was argued to help preventing the overcooling problem in cluster cores [340], they found that conduction does not change the baryonic fraction in the inner regions. They also found that it breaks the observed self-similarity of cluster profiles.

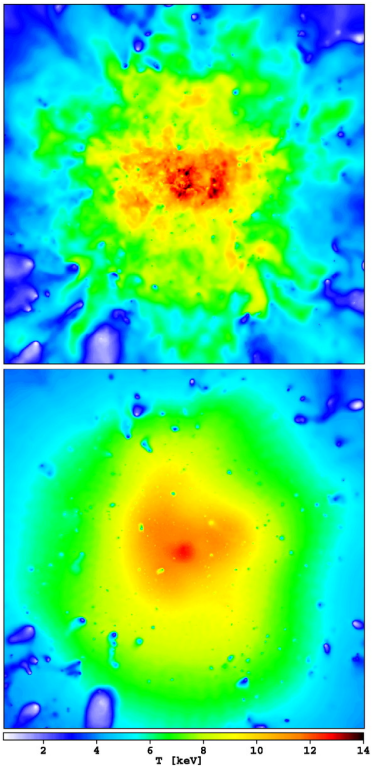

Figure 8.4: Projected maps of mass-weighted gas temperature of a hot cluster in the study of Dolag *et al.* [364] simulated without (*top*) and with thermal conduction (*bottom*). We can see the small-scale pattern of temperature variations are wiped out in the simulation with conduction.

Simulations of Ruszkowski *et al.* [295] and Yang & Reynolds [368] yield a similar result : thermal conduction alone cannot offset the cooling losses even at a full Spitzer conductivity along field lines. Yang & Reynolds [368] found however that the conduction could provide part of the heating, reducing the burden on AGN feedback. Moreover this study found that the AGN-driven turbulence can randomize magnetic field lines effectively and sustain conductivity. In Sharma *et al.* [369] and Banerjee & Sharma [370], it was shown that thermal conduction, in the presence of external sources of turbulence, enhances the mixing of the thermal plasma.
Kannan *et al.* [114] also show that the inclusion of the anisotropic thermal conduction results in a greater level of mixing which efficiently redistributes the AGN kinetic energy more isotropically. As the result, the improved coupling between the feedback energy and the ICM facilitates an earlier disruption of the cool-core and star formation quenching.
Barnes *et al.* [366] also found a higher level of mixing in the presence of the anisotropic thermal conduction. They show that its inclusion produces larger fractions of cool-core clusters, as with thermal conduction, central gas fractions increase in the clusters cores. They found a flatter CC fraction redshift evolution being more in agreement with observations. They also found an increased AGN-ICM coupling which reduce the feedback energy required for reaching self-regulation (also found by Rasia *et al.* [153] with an artificial thermal diffusion).

8.3 Simulations of the ICM

In this work, we aim at to investigate the effect of thermal conduction on the RHAPSODY-G galaxy clusters.
Before adding more sophisticated physics to our simulations, we would like to understand the impact of the anisotropic thermal conduction on the intra-cluster gas in simple settings.

These simulations were run at the lower 4K resolution (see Chapter 6 for details).

8.3.1 Effect of the anisotropic thermal conduction

We start with a non-radiative cosmological simulation of a galaxy cluster where we are only interested in the adiabatic evolution of the gas. During the cluster formation, the gas gravitationally collapses towards the potential minimum. While the gas is gradually collapsing, it gets adiabatically heated. At the end of the simulation, we have a hot cluster centre. Then, the gas temperature decreases at larger radii.

Then, we run a new simulation with the exact same set-up but we allow the anisotropic thermal conduction with a Spitzer conductivity. For numerical stability reasons, we also allow one percent of the heat to diffuse also perpendicularly to the magnetic field lines.

We illustrate the comparison between the two simulations in Figure 8.5. It shows the mass-weighted averaged gas entropy in a slice of 1.5 Mpc wide and 10 kpc deep through the cluster center.

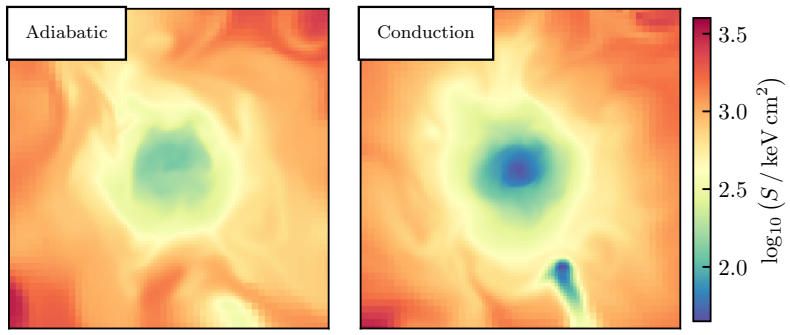

Figure 8.5: Maps of the mass-weighted average entropy in a slice of 1.5 Mpc wide and 10 kpc deep centered at $z = 0$. The *left* panel shows the end result of the adiabatic simulation while the *right* panel shows the same simulation but where the anisotropic thermal conduction was enabled. As the result, the conduction run shows a larger amount of low entropy gas in the centre, inducing a cooler cluster core. In this case, thermal conduction act as a cooling source by transportinh heat outwards.

We can see in the *left* panel of Figure 8.5, the lower entropy core surrounded by higher entropy gas heated by its adiabatic compression. In the *right* panel, we see a much larger amount of low entropy gas in the center with an infalling substructure in the lower right.
While the cluster forms and the intra-cluster gas is collapsing towards the center, heat generated during this gas compression is transported outward were the gas temperature is lower. As the result more low-entropy gas fall inwards and the cluster centre gets denser. We also see that low entropy gas clumps forms. We see that the heat generated by the gas compression during the cluster

evolution is transported to the colder outskirts.
Indeed, thermal conduction's general effect is to make the gas more isothermal by smoothing out temperature gradients in the ICM. In that case, the thermal diffusion is actually behaving like a gas cooling source.

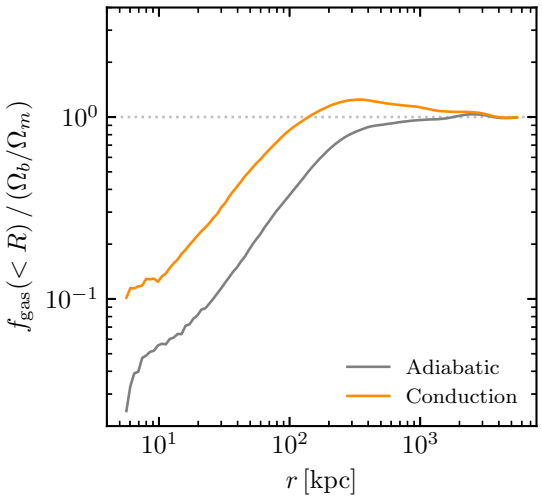

Figure 8.6: Gas fraction profiles in unit of the universal baryon fraction. The grey line shows the adiabatic simulation while the orange line shows the anisotropic thermal conduction. We notice the large amount of gas, above the universal expectation (shown as the horizontal grey dotted line), at radii above ~ 150 kpc. The gas profile is higher at all radii for the simulation with thermal conduction. We explicitly see here the contraction of the cluster raising its overall gas density.

Indeed, the transport of heat lowers the pressure support in the cluster center, hence more gas flows inwards with lower temperatures.
This behavior is well shown in Figure 8.6 where we plot the radial profiles of the gas fraction, $f_{\rm gas}$, in unit of the universal baryon fraction. The gas fraction profile shows the ratio of the total mass enclosed at each radii to the total, i.e. gas and dark matter, enclosed mass. It provide a measure of the relative contribution of the collisional to the non-collisional matter with respect to the universal fraction.

We see that, the simulation with anisotropic thermal conduction enabled, shows a higher gas fraction at all radii. Especially, at radii above ~ 150 kpc the gas fraction is above the universal value. We have a gas rich cluster with a much denser core (< 100 kpc). The intra-cluster gas in contracting much faster than to the transport of heat towards cluster outskirts.

To conclude, the anisotropic thermal conduction in this case, acts as a cooling source : the clusters is cooler and denser.

8.3.2 Combination with radiative cooling

We push a step further by allowing the gas to radiatively cool. At high temperatures, such as in the ICM, the gas cools mainly through Bremsstrahlung (free-free emission).
We saw in Section 3.1.2, that this process is quadratically sensitive to the gas density. Therefore during the collapse, as the gas is getting denser it also cools faster. And because this gas is colder, it contracts to get even denser which cools at even greater rates, leading to a runaway instability : the cooling catastrophe.

As we are still considering only the cluster gas, we need to set an artificial limit to prevent overcooling. In more realistic simulations, the gas cooling is stopped as soon as star formation is triggered which turns this dense cold gas into stars.
This artificial limit is set by imposing a cooling (or pressure) floor. It means that no gas cools below this limit, which is set by the star formation threshold defined in Chapter 6. Due to this restriction, the gas can only increase its density along the adiabat $P \propto \rho^{\gamma}$.

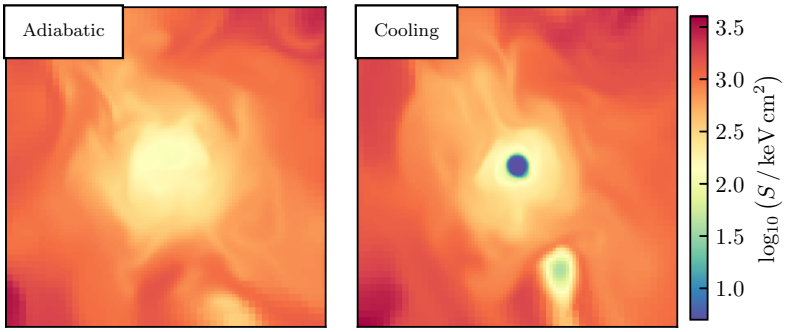

Figure 8.7: Same as Figure 8.5 with a wider color scale. We compare the adiabatic simulation with a simulation where the radiative cooling is enabled. When the gas cools, it get denser hence cooling at higher rates. Therefore in the dense regions such as the core or the infalling gas clump in the lower right corner, gas density dramatically increase while the temperature drops. As the result we have the formation of a low entropy core where cooling is artificially stopped with a pressure floor (see text for details).

Illustration of this process is shown in Figure 8.7, where we see the excess of low entropy gas in the core. The cluster core is extremely rich in gas with a steep temperature gradient : the cluster outskirts are still hot while the core is overcool (albeit limited by the artificial floor, explaining the constant core entropy).

Let us examine the effect of anisotropic conduction in this new configuration. We again show in Figure 8.8 the entropy maps, as it is a good measure of both gas density and temperature.

First, we observe a larger core with an increased entropy. Secondly, the ICM seems more diffuse where substructures tend to be smoothed out. Especially in the upper part of the *left* panel of Figure 8.8 we observe a steeper entropy gradient than in the *right* panel.

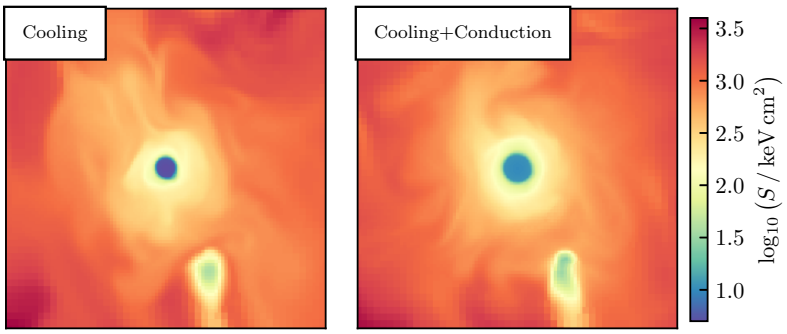

Figure 8.8: Same as Figure 8.8. We study now the effect of thermal conduction in combination with the gas radiative cooling.

Thermal conduction in this case is working to transport heat toward the overcooling core. Therefore, during the cluster evolution, as the ICM is getting denser by gas accretion, it shows a steeper decreasing temperature profile towards the center. On the other hand, thermal conduction constantly transports inwards the heat generated during this gas compression, to ease the core cooling. As the result, while the core is getting warmer and less dense, the outskirts tend to have colder temperatures hence getting denser than in the cooling-only simulation.

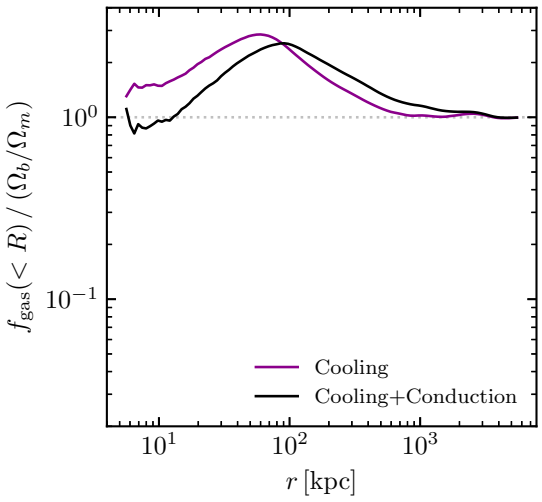

Figure 8.9: Same as Figure 8.6 but for the simulation with radiative gas cooling. We observe a lower core density with denser outskirts for the simulation incorporating thermal conduction. Thermal conduction slows down the gas cooling hence the cluster is collapsing at a lower rate. As the result, we have an extended core shown by the maxima of the gas fraction profiles (100 kpc, compared to $\sim$ 60 kpc in the cooling only simulation) with a smoother ICM (where outside the core, we have a shallower slope toward the universal baryon fraction.)

We observe this easily in the gas depletion profiles shown in Figure 8.9.

In the cooling-only simulation, we see a high fraction of gas peaking at 60 kpc, defining the extent of the core. While at larger radii from this core, the amount of gas decrease to reach the universal baryon faction at 700 kpc.

With the addition of thermal conduction, the core extends now to 100 kpc while showing a lower amount of gas . Then, the fraction of gas slowly decreases towards Ω_b/Ω_m at a much larger radius of $\sim$ 2 Mpc.

Thermal conduction has an effect on the whole ICM. By attempting to slow down the cooling in the core via the transport of heat from

larger radii, the outskirts get slightly denser/cooler but smoother.

Interestingly, we see that the simulation having thermal conduction shows now an opposite behavior compared to Section 8.3.1. It now acts as transporting heat inward to heat the core. It is now behaving like a heating source.

We gather in Figure 8.11 the entropy and density maps plotted with the same color scale. We also show the gas fractions of the four simulations in Figure 8.10

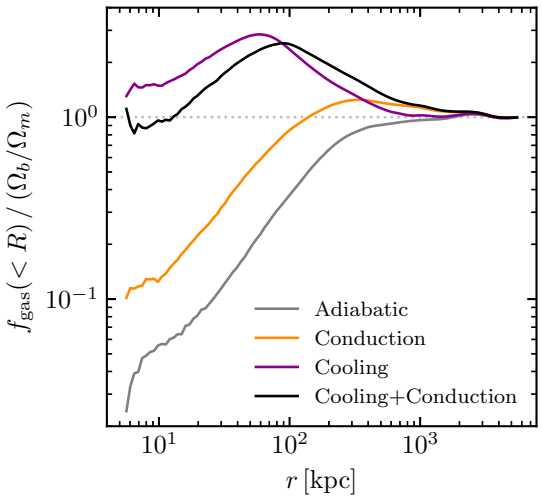

Figure 8.10: Gas depletion profiles for our 4 different simulations studied in this chapter. The grey line shows the adiabatic simulations and in orange when thermal conduction is enabled. Purple and black lines show respectively simulations with radiative gas cooling with and without thermal conduction. We see the contraction of the gas rich core in orange compared to grey, while an opposite trend with the black line compared to the purple line. Depending on the temperature gradient in the core ($\leqslant$ 200 kpc), anisotropic thermal conduction can act as a cooling or heating source and endeavours to smooth out substructures in the ICM.

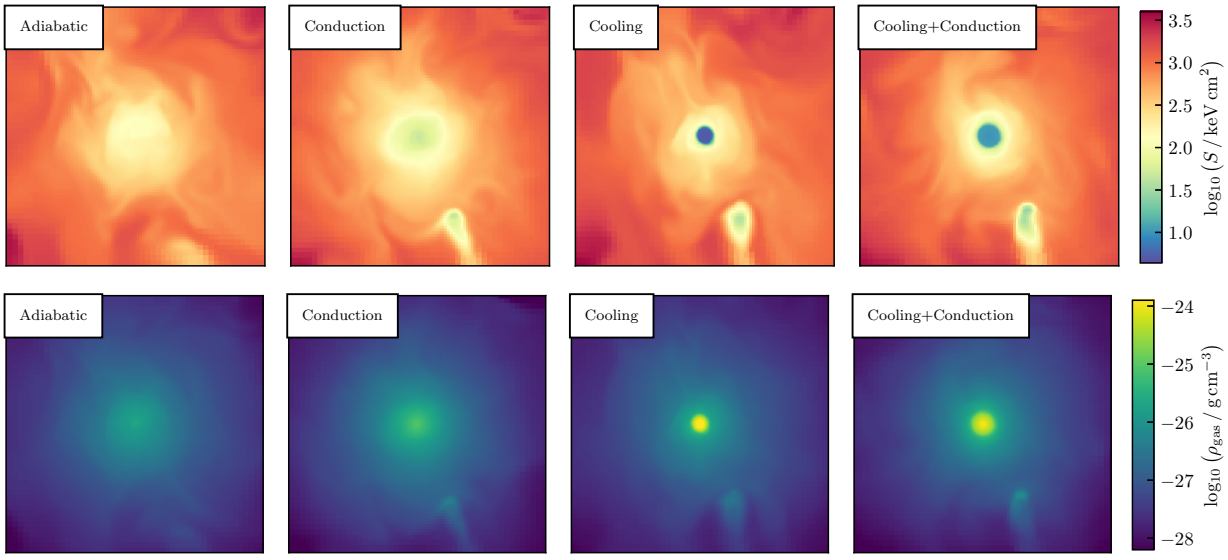

Figure 8.11: In this figure we gather the entropy (*top row*) and density (*bottom row*) slices of 1.5 Mpc wide and 10 kpc deep. Each property is (mass-weighted) averaged along the line of sight. All maps share the same color scale which allows to put in perspective the different processes at play in this simulations. We see that thermal conduction alone transports heat outwards to cool down the core. When radiative cooling is added, the cluster core overcools and gets extremely gas rich. Coupled to gas cooling, thermal conduction shows the opposite behavior by transporting heat inwards to warm the gas in the inner region to the detriment of the surrounding intra-cluster gas.

8.4 Summary

In this chapter, we reviewed the phenomenology of thermal conduction. We explored its origin using the kinetic theory to understand the transport of energy by the collisions of particle in the intracluster plasma.
The presence of magnetic fields in the ICM obliged the consideration of the anisotropy in this diffusion process. Indeed, charged particles of the ICM (electron and ions) moves preferentially along magnetic fields lines. The energy transport parallel to the field lines seems however to be a crude assumption where magnetic fields in the ICM tend to be highly tangled on a wide range of scales and to large radii. We discussed that in this case, the conductivity can be reduced by few orders of magnitude.
Therefore, the assumption of isotropic thermal conduction at the Spitzer value might not hold. How far the true ICM conductivity is from the ideal Spitzer value remains uncertain.

We discussed possible thermal instabilities that can arise in a stratified plasma where anisotropic thermal conduction and gravity couple. On one hand, in the absence of heat flux and when the entropy increases in the direction of gravity, the plasma becomes buoyantly unstable.[8] On the other hand, the presence of heat flux an analogous instability is presence when the temperature now decreases in the direction of gravity.[9] The latter instability is predicted to be present at radii of $\sim 0.1 - 100\,\mathrm{kpc}$ (in the core), while the former is expected at radii above ~ 100. It is thought that the entire intracluster plasma is unstable to magnetically mediated buoyancy instabilities.
Such instabilities drives turbulence in the ICM which could participate to the amplification of magnetic field in the ICM at all radii. Moreover, they can reorient field lines with different trends, which can have an immediate effect on the transport of heat. Therefore, thermal conduction in cluster might be less effective at heating cool cores in cluster as expected.

8: This is the magneto-thermal instability (MTI).

9: This is the heat-flux-driven buoyancy instability (HBI).

But, before going to simulations of galaxy clusters with galaxy physics, we ran idealised simulations to grasp the effect of thermal conduction.
Interestingly, we saw that thermal conduction can act as a cooling source by transporting heat from the core to larger radii, or, as a heating source by transporting heat inwards. This behaviour is dictated by the sign of the temperature gradient in the inner cluster region. More generally, thermal conduction is effective at flattening out temperature substructures in the ICM.

As the result, we see how subtle is the process of thermal conduction in the intra-cluster medium. It might help to lower the burden of the AGN to heat the ICM by transporting heat from larger radii, or, by coupling to it to redistribute AGN energy more efficiently. The global effect of the anisotropic thermal conduction in the ICM is not clear and thermal instabilities could also play an important role. How thermal conduction acts throughout the cluster evolution or its impact on star formation, and feedback from stars and AGN will be investigated later in Chapter 9 and Chapter 11.

Toward realistic galaxy clusters 9

In ths chapter we will review the impact of the different sub-grid models used in our simulations on the intra-cluster medium of one halo in the Rhapsody-G *sample.*

For an effective theory of galaxy formation and evolution, several key astrophysical processes need to be modelled. These processes include star formation, stellar evolution, chemical enrichment, primordial and metal line gas cooling, stellar feedback, and supermassive black hole formation, growth and feedback.
The spatial and mass resolutions of cosmological large-scale simulation such as ours ($\sim$ kpc), still remain much arger than typical scales of the turbulent interstellar medium ($\sim$ pc) and, in particular, scales at which the formation of stars and black holes occurs ($\lesssim$ pc). Therefore, inspired by the outcome of observations and theoretical models, these baryonic processes are implemented a sub-grid manner and operate in a cosmological context.

We described in Chapter 5 the implementation of the different sub-resolution physical models in the Ramses code. Then, in Chapter 6, we reviewed the changes from the original Rhapsody-G simulations as well as the specific parameters of each sub-grid model.
We will now discuss the impact of these various models on galaxy properties as well as the ICM. This chapter presents and discusses the calibration of these models in our simulations, by a parameter-space exploration, to get closer to realistic clusters with respect to observational constraints.
We will then present in the following Chapter 10 the simulations resulting from this study that will be analysed to derive cluster observables and scaling relations.

9.1 Formation of stars and supernova feedback

We discussed in Section 6.3 the sub-grid models for star formation and stellar feedback which was slightly modified from the original Rhapsody-G simulations. However, we set a lower star formation efficiency of $\epsilon_* = 0.01$ compared to the standard value of 0.02 previously used in the original Rhapsody-G simulations. We also set a factor 2 higher metal yield to overcome the low metallicity of

Rhapsody-G halos found by Hahn *et al.* [111]. The low metallicity was originally thought to be due to low metal yields. However, after a few tests, increasing the metal yield did not lead to an overall increase in stellar metallicities comparable to observed values. Actually, this issue might originate from the choice of the Salpeter [189] initial mass function (IMF) in Ramses which decreases the total energy released by a stellar particle by a factor of 3 compared to a Chabrier IMF [108, 371].

The star formation efficiency, i.e. the ratio M_*/M_h, peaks at halo masses of $10^{12}\mathrm{M}_\odot$ and decreases at both smaller and larger masses [231, 372]. It translates into a knee at $10^{12}\mathrm{M}_\odot$ in the stellar mass-halo mass (SMHM) relation. Below this mass, stellar feedback is expected to regulate star formation.
However, supernova-driven winds cannot escape from the gravitational potential of higher mass halos as already pointed out by Dekel & Silk [373]. It is commonly acknowledged that AGN feedback must threfore play a key role in shaping the baryonic properties of massive halos and their star formation efficiency [374–376].

Therefore, one common procedure to calibrate both SN and AGN feedback is by comparing simulated galaxy to the SMHM relation. Specifically, to calibrate our SN feedback sub-grid model, we tracked the evolution of halos until $z = 3$.
Indeed, around and below $z = 3$, AGN feedback starts to dominate the quenching of star formation in particularly massive halos in our proto-cluster environments.

The parameter exploration for the SN feedback model was carried out at the lower 4K resolution. We found it to be robust against change to the higher 8K resolution.
In a relatively low number of simulations we found a satisfying parameter set which is found to be in agreement with abundance matching studies[1] of Behroozi *et al.* [372] and Legrand *et al.* [377], and, the IllustrisTNG100 simulations at $z \geqslant 3$.[2]

As we can see in Figure 9.1, where we plotted the total and stellar mass inside R_{200} of all galaxies at $z = 3$.[3] For consistency, we also compare the total and stellar mass inside R_{200} for the IllustrisTNG100 simulations. For comparison, we plotted the recent abundance-matching results of the Universe Machine of Behroozi *et al.* [372] and of Legrand *et al.* [377] which use precise galaxy stellar mass function measurements in the COSMOS field.

We can see that our stellar masses are systematically low with respect to the IllustrisTNG100 halos. In fact, as we are simulating a

1: Abundance matching relations are derived by assigning galaxies to dark matter halos based on their cosmic abundance in large-volume N-body simulations

2: We thank Jolanta Zjupa for kindly helping us with access to the IllustrisTNG100 data

3: Here, we measure the total mass as being the sum of the mass of gas cells, dark matter and star particles enclosed in R_{200}. The stellar mass only accounts for the total mass of the star particles within R_{200}.

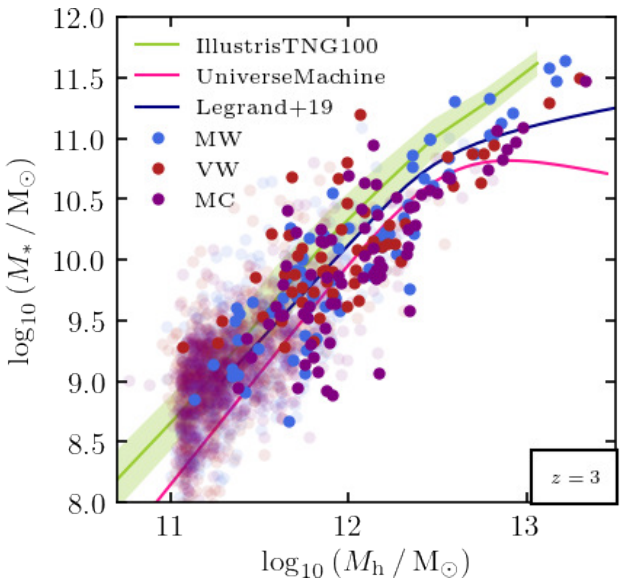

Figure 9.1: Comparison of the $M_* - M_\mathrm{h}$ relation for galaxies from our simulations of Rhapsody-G `Halo 545` at $z = 3$ with abundance-matching constraints and IllustrisTNG100 simulations. We show the total mass (M_h) and stellar mass (M_*) inside R_{200}, the radius enclosing 200 times the critical density at $z = 3$ for our halos. Galaxies are shown for three different types of simulations (that we will describe slightly later in this chapter) where the opaque and transparent dots shows respectively central and satellite galaxies. We plot in green, the mean relation with the standard deviation (shaded area) for the IllustrisTNG100 halos with $\Delta = 200$. The Universe Machine relation of Behroozi *et al.* [372] (pink) and Legrand *et al.* [377] (navy) show the median relation for peak historical halo mass using Bryan & Norman virial overdensity which we computed at $z = 3$.

denser system it is expected that our galaxies are more quenched than galaxies in the field, therefore our mean relation is biased low compared to the large volume IllustrisTNG100 simulation.
On the other hand, we measure the total stellar mass in our halos which include the intra-halo light and the galaxy mass. Therefore it is expected to be slightly higher than the galaxy masses measured in Behroozi *et al.* [372] and Legrand *et al.* [377].
Taking this into account, we can see that our data is in broad agreement with published SMHM median relations especially at lower halo masses. Therefore, we can assume that our star formation and SN feedback models are tuned to reproduce reasonably realistic stellar masses.

However, at higher halo mass, the AGN feedback is thought to be the main mechanism that suppress star formation. In the next sections, we will study the effect of SMBH evolution and AGN feedback required to properly reproduce galaxy masses in high mass halos.

9.2 Black hole growth

SNe have little impact on the formation of massive galaxies [375]. On the other hand, AGN feedback from SMBHs provides enough energy to quench star formation in high mass halos. Therefore, the sub-grid models for the formation and growth of black holes need

to be discussed next.

9.2.1 Seeding

As previously discuseed in Section 6.5, SMBHs with an initial mass of $10^8 M_\odot$ are seeded in the simulation according to a specific set of rules.
We had to revisit the seeding prescription of black holes from the original Rhapsody-G simulations as it was found to be unstable : starting from exact same initial set-ups, we found that some SMBHs were not seeded in specific locations where they should have.
This effect arises from the stochastic nature of star formation, where SN feedback couples differently to the gas from one simulation to another. As the result, the local gas properties can be slightly different between two simulations, and the original SMBH seeding procedure was not found to be robust enough against such slight changes. As a consequence, in two identical simulations, the same halo could end up with a SMBH and the other one without.

While looking for a better BH seeding model, we actually found that it can have a crucial impact on the star formation in the protocluster by significantly changing the AGN energy injection into the intra-cluster gas.
We tested different way to select the potential SMBH formation sites. As we discussed extensively the Phew clumpfinder in Section 5.5.4, we can directly detail the characteristics of the simulations that we will presented here. Simulations with different parameters are labelled by two digit binary numbers. We have :

- **00** : This simulation shares the same parameter for the Phew clumpfinder as the original Rhapsody-G simulations. It has low values of the density, saddle and an usual relevance threshold value. As a consequence, a large fraction of the simulation volume is marked by the clumpfinder. Then, due to the low saddle threshold value, many peaks are merged which results in a low number of potential SMBH formation sites. Hence few BH sink particles will be seeded in the simulations.
- **01** : This simulation has a much higher density[4] and saddle threshold values (~ factor 10) which allow to select only the highest density peaks in the simulation. We also ask for a larger relevance threshold to reduce the noise in the analysed density field. As the result, more peaks are found (in a smoother field) due to the higher saddle threshold value which allows to seed more SMBH in the simulation.

4: The density threshold was set to 8, which is also the same criteria for the mesh refinement.

- **10** : Here, we increased by another factor of 10 the saddle threshold compared to the **01** simulation. As the result, much less substructure are merged which results in an increased number of sink formation sites.
- **11** : In this simulation, compared to **00**, we only lowered the saddle threshold by 25%. Following the same logic, this loosens the criteria for peak merging hence more substructure can be merged resulting in a lowered number of SMBH seeds in the simulation.

To sum-up, compared to the original RHAPSODY-G simulation (**00**) clumpfinder parameters, we chose to increase the robustness of the peak finding and to focus on the highest density peaks using respectively higher relevance and density thresholds. Then, we control, by increasing the saddle threshold value, the number of SMBH sink particles seeded in the simulation. Where in simulations **00**, **11**, **01** and **11**, we respectively have an increasing number of SMBH seeds in our simulations.

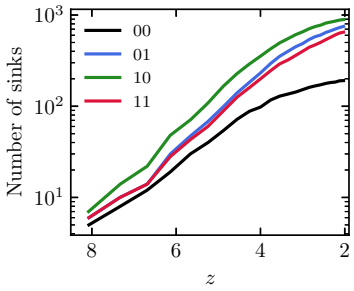

Figure 9.2: Evolution of the number of SMBH in the simulation box as a function of redshift. The **00**, **01**, **10** and **11** simulations have at $z = 2$, respectively, 191, 750, 892, 649 SMBH sink particles.

Indeed, as we can see from the evolution of the number of sink particles in each simulation in Figure 9.2, the original seeding model (**00**) forms ~ 200 SMBHs by $z = 2$ which is more than 4 times less than the other simulations. It illustrates that, by increasing the saddle threshold, the overall number of sinks in the simulation is increased.

Let us now discuss the impact the number of SMBH sinks has on the stellar content of our proto-cluster `Halo 545` at $z = 2$. We specifically chose $z = 2$ as it corresponds to the peak of the AGN activity. Thus, at $z = 2$, we should easily see the impact of the different seeding scenarios on the proto-cluster properties.
Figure 9.3 shows the cumulative stellar mass profile corresponding

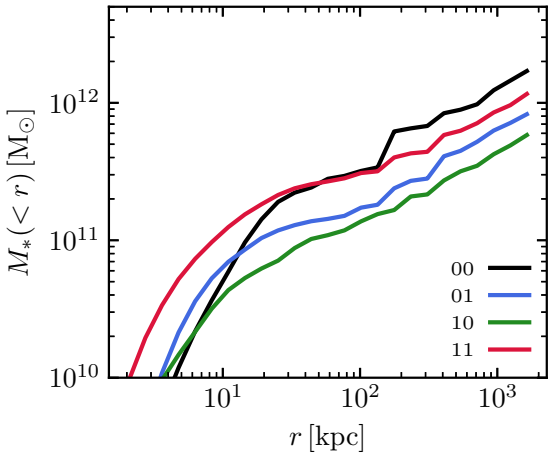

Figure 9.3: Cumulative stellar mass radial profiles for the simulations sharing different seeding scenarios at $z = 2$. We can see that it has a direct impact on the star formation on the protocluster.

to our four simulations using the same color-coding as in Figure 9.2. We can see that the total stellar mass in protocluster is reduced with an increasing number of SMBHs present in the simulations. Indeed, the **00** simulation has the lowest number of black holes (~ 200) and shows the highest total stellar mass of $1.7 \times 10^{12}\,\mathrm{M}_\odot$ inside $\sim 2\,\mathrm{Mpc}$, while, the **10** simulation shows a lower stellar mass by a factor of 3 (for ~ 900 SMBHs).
We see that by controlling the number of seeded SMBHs, we can control the star formation in the protocluster.

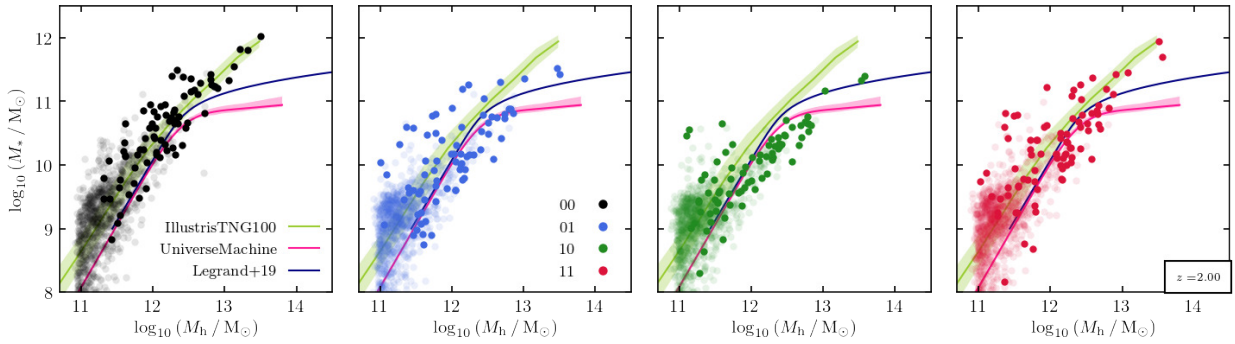

Figure 9.4: Stellar mass as a function of halo mass for the **00**, **01**, **10** and **11** simulations (from *left* to *right*) at $z = 2$. Similarly to the Figure 9.1, we also compared to the results of Behroozi *et al.* [372], Legrand *et al.* [377] and the IllustrisTNG100 simulation computed as $z = 2$.

In order to decide on the set of parameters for the seeding of SMBHs, we compare the output of each simulation in the stellar mass-halo mass plane with published results similarly to Section 9.1. In Figure 9.4, we show the stellar mass versus halo mass of our halos in our four simulations and we can easily see the impact of the BH seeding on the galaxy masses.
We can see that the **00** original simulation's model shown in black, forms too massive galaxies with stellar masses above the IllustrisTNG100 median relation. Similarly, the **11** simulation produces too massive galaxies (shown in red). Therefore, we discarded these two models.
We notice that the **10** simulation (shown in green) shows more strongly suppressed star formation than the **01** simulation (shown in blue) and stellar masses are lower in the **10** simulation. Indeed we see in the simulation **10**, that the majority of the halos with $10^{12} \leqslant M_\mathrm{h} \lesssim 10^{13}\mathrm{M}_\odot$ lies below the UniverseMachine median relation. But, we should expect stellar masses to lie slightly above it as we measure the total amount of stars in halos and not the galaxy mass as they do (indeed, we incorporate the intra halo light).

As a consequence, we chose the parameters of the **01** simulation for the sub-grid model of black hole seeding.
Interestingly, we see that the number of seeded SMBH have a

crucial impact on the star formation in the protocluster, which can be easily controlled by the clumpfinder parameters. Seeding more BHs at early times allows to heat the gas and quench efficiently the star formation at later times. Indeed, while individual SMBHs have lower masses and accretion rates, the large scale heating is more efficient.

9.2.2 Decayed orbits

During the calibration phase of the AGN models (that we will detail in the next Section 9.3), we realized that the outcome of our simulations was inconsistent due to a inefficient gas accretion.
Actually, the dynamics of the sink particles were found to be unstable and easily perturbed by infalling cold and dense clumps of gas onto the SMBH. As a result, sink particles were wandering around and could not efficiently accrete the cold and dense gas that piles up in halo centers.
Consequently, this build up of gas in the halos fuels star formation that should have been suppressed by an AGN feedback.
Therefore, it was necessary to revise our sub-grid BH model to better "trap" sink particles in their host halo. The problem of migrating SMBH sink particles is well known in the simulation community and several solution have been adopted such as dynamical friction models for instance (see discussion in Section 5.5.5).

As we discussed in Section 5.5.5, resolving scales of SMBH dynamics in cosmological simulations is out of reach. Various sub-grid models of dynamical friction and centering prescription are therefore implemented to avoid spurious oscillations of the BH sink particles. More generally, this issue is crucial to understand the formation of SMBHs from a rapid growth of less massive seeds as it requires BHs to efficiently sink and be trapped in the galactic center via dynamical friction [378].
For instance, recent works of Biernacki *et al.* [204] and Ogiya *et al.* [379] showed the impact of the embedding nuclear star cluster at decaying efficiently BH orbits towards the halo center and stabilising it.
Therefore, we would like to approach such orbital decay with a sub-grid model to account for the unresolved dynamical friction between the SMBHs and the surrounding (infalling) dense gas and/or nuclear star clusters.

We therefore model such effect with a new "orbital decay" model where SMBHs descent along the potential gradient, towards their local potential minima. The displacement is calculated using a hybrid formula similar to the Barzilai & Borwein [380] method.

This Barzilai-Borwein technique was found to be extremely efficient and having the great advantage of being easily extended to solve a wide class of constrained optimization [381].

Similarly to the classical steepest descent method proposed by Cauchy [382], we search to minimize the SMBH potential at every fine time step Δt i.e. the time step of the level $l_{\max}$, as all sink variables are always updated at the highest resolution level. Hence the SMBH displacement, $\Delta\mathbf{x}$, along the steepest gradient is computed at a time t and the SMBH position is updated at the next time iteration $t + \Delta t$.
Let $\mathbf{x}_n$ be the sink position at the time t and $\mathbf{x}_{n+1}$ at the next time step $t + \Delta t$. The potential $\phi(\mathbf{x}_{n+1})$ that we wish to minimize can be approximated by :

$$\phi(\mathbf{x}_{n+1}) = \phi\left(\mathbf{x}_n + \Delta\mathbf{x}_n\right), \tag{9.1}$$

$$\approx \phi(\mathbf{x}_n) + \Delta\mathbf{x}\nabla\phi(\mathbf{x}_n) + \frac{1}{2}\Delta\mathbf{x}^{\mathrm{T}}\mathbf{H}_\phi(\mathbf{x}_n)\Delta\mathbf{x}. \tag{9.2}$$

Where $\mathbf{H}_\phi(\mathbf{x}_n) = \nabla\nabla\phi(\mathbf{x}_n)$ is the Hessian matrix of the potential at the position $\mathbf{x}_n$.

Minimising the above potential with respect to the SMBH displacement translates to :

$$\frac{\phi(\mathbf{x}_{n+1}) - \phi(\mathbf{x}_n)}{\Delta\mathbf{x}} = 0, \tag{9.3}$$

which implies that (omitting a factor of 2) :

$$\Delta\mathbf{x} = \mathbf{x}_{n+1} - \mathbf{x}_n = \mathbf{H}_\phi^{-1}(\mathbf{x}_n)\,\nabla\phi(\mathbf{x}_n), \tag{9.4}$$

$$\implies \mathbf{x}_{n+1} = \mathbf{x}_n - \mathbf{H}_\phi^{-1}(\mathbf{x}_n)\,\nabla\phi(\mathbf{x}_n), \tag{9.5}$$

that (roughly) gives an updated position of the SMBH that gradually minimises its potential. We see that $\nabla\phi(\mathbf{x}_n)$ is the force exerted on the SMBH sink particle, $\mathbf{f}(\mathbf{x}_n)$. Therefore we can rewrite the last equation as :

$$\mathbf{x}_{n+1} = \mathbf{x}_n - \gamma_n\mathbf{f}(\mathbf{x}_n) \tag{9.6}$$

where the term $\gamma\mathbf{f}(\mathbf{x}_n)$ is subtracted from $\mathbf{x}_n$ because we want to move against the gradient, towards the local minimum. We can see that the factor γ has the dimension of a time squared. It actually defines a time step on which the displacement towards the potential minimum occurs.
In some cases, the Hessian matrix can be difficult to invert, hence many algorithms provide different formulas which approximate its value. Barzilai & Borwein [380] provide a robust form that converges remarkably fast to the minimum of the studied function.

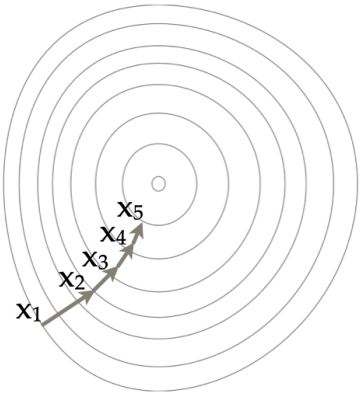

Figure 9.5: Illustration of gradient descent. The successive displacements lead to the bottom the the potential well.

In our case, their adaptative time step reads :

$$\gamma_n = \frac{|(\mathbf{x}_{n+1} - \mathbf{x}_n)^{\mathrm{T}} \, [\mathbf{f}(\mathbf{x}_{n+1}) - \mathbf{f}(\mathbf{x}_n)]|}{\|\mathbf{f}(\mathbf{x}_{n+1}) - \mathbf{f}(\mathbf{x}_n)\|^2}, \tag{9.7}$$

where we identify a form of the Hessian of the potential multiplied by convenient form of the unity vector :

$$\mathbf{H}_{\phi}^{-1}(\mathbf{x}_n) \sim \frac{\mathbf{x}_{n+1} - \mathbf{x}_n}{\mathbf{f}(\mathbf{x}_{n+1}) - \mathbf{f}(\mathbf{x}_n)} \cdot \frac{\mathbf{f}(\mathbf{x}_{n+1}) - \mathbf{f}(\mathbf{x}_n)}{\mathbf{f}(\mathbf{x}_{n+1}) - \mathbf{f}(\mathbf{x}_n)}, \tag{9.8}$$

The Barzilai & Borwein [380] time step given in Equation 9.7 varies, in our case, depending on the difference of the force exerted on the SMBH at the positions $\mathbf{x}_n$ and $\mathbf{x}_{n+1}$. We can see that the "descent" Δx mimics an unresolved tidal force experienced by the SMBH during its motion[5] .
This sub-grid model only involves positions and forces which therefore ensures the "descent" to be fully momentum conservative (i.e. Galilean invariant).

5: Indeed, the Hessian of the gravitational potential is the tidal tensor

We implemented in Ramses this "tidal friction" model in a hybrid form that depends on the local simulation time step Δt. We rename the hybrid step $\tilde{\gamma_n}$ and is given by :

$$\tilde{\gamma}_n = f_d \sqrt{\gamma_n \Delta t}, \tag{9.9}$$

where f_d is a dimensionless control parameter which takes values between 0 and 1. It allows to adjust the effective displacement as we found the SMBH descent to be very effective.
This "tidal friction" is implemented by updating the SMBH sink particle positions, similarly to Equation 9.6 with the adjustable time step $\tilde{\gamma}_n$, at the end of the original sink position update as :

$$\mathbf{x}_{n+1} = \mathbf{x}_n - \tilde{\gamma_n} \mathbf{f}(\mathbf{x}_n). \tag{9.10}$$

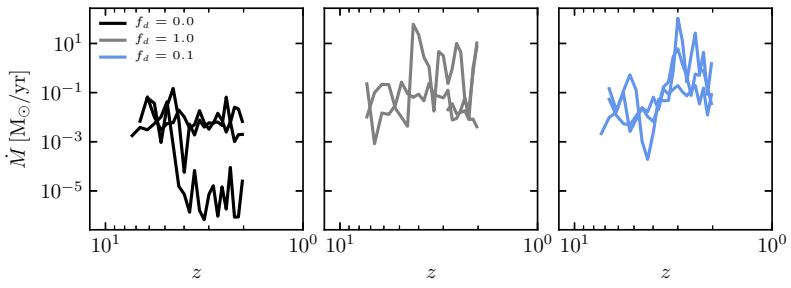

Figure 9.6: Redshift evolution of the gas accretion rate onto the three most massive black hole in the simulation with no "tidal descent" (black, $f_d = 0$), a maximal (grey, $f_d = 1$) or mild (blue, $f_d = 0.1$) descents. For clarity, we only show the 3 most massive black holes as the effects of our sub-grid model is easily seen.

We show in Figure 9.6, the accretion rates as a function of redshift for the three most massive SMBHs in three simulations with a different value of our adjustable f_d parameters.
As we can see, the simulation with no "tidal friction" (i.e. with

$f_d = 0$) in black, shows steady and decreasing accretion rate onto the SMBHs as a function of time. On the other hand, simulations with $f_d = 1$ and 0.1 (in grey and blue respectively) show higher gas accretion rates which tend to increase with time.
We can also see this behaviour by looking a the SMBH masses plotted in Figure 9.7, where we see dramatic differences.

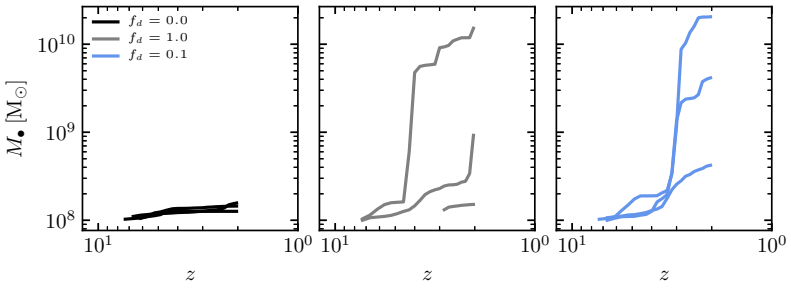

Figure 9.7: Same as Figure 9.6 for the time evolution of the SMBH masses of the three most massive SMBHs in each simulation. We can directly see the effect of the our sub-grib model on the SMBH mass growth.

We notice that the SMBH masses increase only slightly and slowly from the seed mass of $10^8 M_\odot$ in the $f_d = 0$ case. Indeed, we know that in this case the SMBHs oscillate around their host halo and cannot efficiently accrete the cold and dense gas that piles up in the halo center. Therefore, the SMBH sink particle can only accrete gas each time they cross the gas rich center. In this case, if one SMBH is lucky enough to meet many times the halo center it can keep its gas accretion at a steady rate. On the other hand, if the SMBH stays in the halo periphery (or even escapes it), the gas accretion can no longer proceed at a reasonable rate and the black hole mass stagnates.

On the other hand, we see that the other two simulations show a greater mass for the most massive SMBH by more than two order of magnitude from the simulation without any tidal descent. The difference between these two simulations (blue and grey) is more subtle. When $f_d = 1$, the SMBHs are robustly glued to the halo center directly from the start of the simulation. As a result, it leads to a strong early gas accretion around $z \sim 4$ (shown by the peak in the accretion rate in Figure 9.6) which leads to a rapid mass growth seen in Figure 9.7. As the AGN feedback energy is proportional to the gas accretion rate (see in Equation 5.41), it also leads to a strong AGN feedback event which efficiently heats the ICM in the protocluster. Consequently, the ICM is more diffuse and the gas accretion onto the other two SMBH shown in Figure 9.7 is hindered. But we also see that the third BH forms much later and struggles to find cold gas to accrete.

The simulation with $f_d = 0.1$ allows the SMBHs to oscillate somewhat more freely while being kept close to the halo potential

minimum. In that case, the gas accretion is gradual which allows a SMBH to simultaneously grow and redistribute more efficiently AGN feedback energy throughout the protocluster.

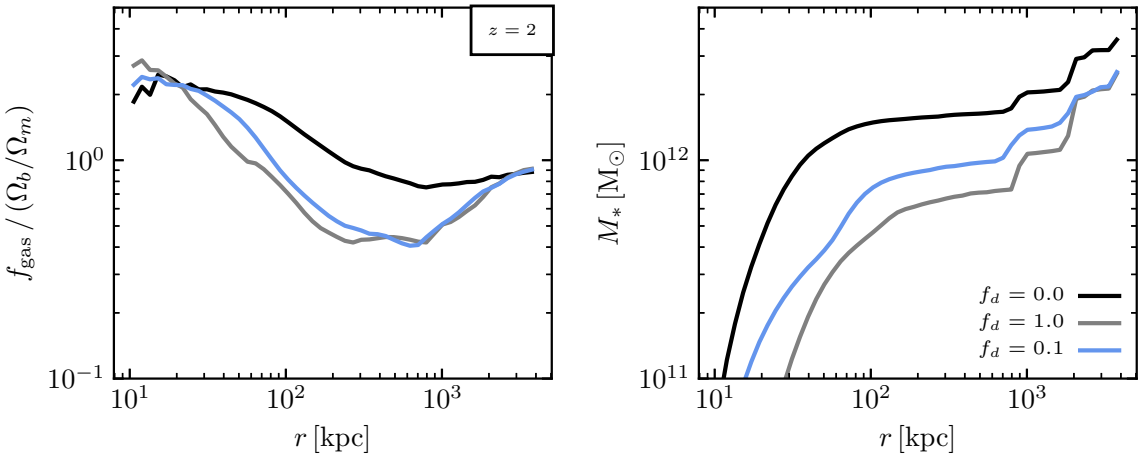

Figure 9.8: Gas depletion and stellar mass radial profile for the simulation with no (black, $f_d = 0$), maximal (grey, $f_d = 1$) or mild (blue, $f_d = 0.1$) tidal friction.

We can see the impact of our sub-grid model for unresolved tidal friction on the gas and stellar content of the protocluster at $z = 2$ in Figure 9.8. We just saw that, by keeping the SMBHs closer to their host halo potential minima, the gas accretion rate and thus the AGN feedback is dramatically boosted. As a result, this large amount of feedback energy allows to deplete gas in the protocluster at all radii in both the $f_d = 1$ and $f_d = 0.1$ simulations compared the the one without "tidal friction". As a consequence, we can see in the *right* panel of Figure 9.8 that the star formation is efficiently smothered inside the whole protocluster depending on the amplitude of the descent given by the f_d parameter. Indeed, at $z = 2$ the protocluster virial radius is about ~ 400 Mpc (physical), we can see that at this radius the total amount of star is directly impacted by to the amplitude at which the decay the SMBH orbits. With the lowest stellar mass is observed for a maximal descent and a largest stellar mass for the original simulation with no SMBH orbital decay.

We found that the simulation with $f_d = 0.1$ reproduce SMBH orbits that seems reasonable in the sense that we have boosted feedback without effectively glueing the SMBH to the potential minimum. On the other hand, the simulation with $f_d = 1$ appears unrealistic as SMBH are tightly anchored at the potential minimum and the simulation without descent shows spurious oscillations of the SMBHs around halo centres (which lead to extremely low accretion rates).

9.2.3 (Boosted) Accretion

Above, we discussed how our "tidal friction" model dramatically boosts the gas accretion onto the SMBHs. Therefore, we could ask if the Booth & Schaye [144] boost[6] is still needed ?

6: We remind that the Booth & Schaye [144] boost is to increase the SMBH gas accretion in a density-dependant fashion given by Equation 5.36. This boost was used in the original Rhapsody-G simulations.

Let us study now two simulations of again the same `Halo545` incorporating both the **01** seeding and the $f_d = 0.1$ SMBH descent: one uses the boosted Bondi accretion according to Booth & Schaye [144] and the other one does not. In Figure 9.9 we plotted both the time evolution of the accretion rate and the SMBH mass of the three most massive sink particles in the two simulations.

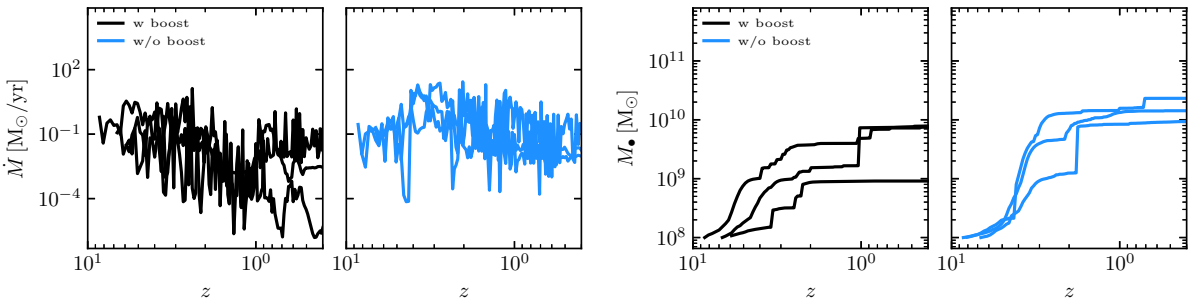

Figure 9.9: : Evolution of the gas accretion rate (*left*) and the mass (*right*) of the three most massive SMBHs in the simulation with (black) and without (blue) Booth & Schaye [144] boost.

By comparing the gas accretion rates, we can see that the simulation with the boost starts with higher rates compared to the simulation without boost. Therefore the SMBH mass growth faster, which fuels earlier and more intense AGN feedback. Therefore, the injected AGN energy heats the gas surrounding the SMBH which stifles further efficient cold gas accretion. Consequently, we see that the accretion rate declines and, after a rapid growth, the SMBH masses evolve only middly (except via mergers with other SMBHs).

On the other hand, without the boost we see that the accretion rate remains steady across all redshifts, peaking around $z \sim 3-2$. Thus, we see a smoother mass growth that is able to reach reasonably high enough SMBH masses. Here, the use of the boost actually "backfires" on a long-term AGN heating by preventing too early the SMBH gas accretion. It thus halts the SMBH growth that prevents further efficient AGN heating.

Therefore, we decided to drop the Booth & Schaye [144] boost in our simulations because the unboosted accretion is already high enough once the SMBH particles are more stably constrained in the gas rich centre of halos thanks to the "tidal friction" model.

9.3 Feedback from active galactic nuclei

In this section, we will study the impact of different models of AGN feedback energy injection.
As discussed in Section 5.5.6, Ramses by default uses a mass-weighted AGN feedback energy injection. It deposits the AGN energy, at every fine time step, proportional to the gas density in a cell i as :

$$E_{\mathrm{AGN},i} = E_{\mathrm{AGN}} \frac{\rho_i \Delta x_i^3}{\sum_i \rho_i \Delta x_i^3}, \tag{9.11}$$

where ρ_i is the gas density of a cell i inside the sink accretion sphere (i.e. a sphere of radius 4 resolution elements, Δx). As a result, this model injects AGN energy preferentially in gas rich regions hence accretion regions fueling the SMBH growth. Hence, the heated gas quickly thermalise with the surrounding dense and cold gas. Therefore, the heating of accretion regions can prevent the cold gas accretion and reduce the overall AGN feedback. Then, the ICM can efficiently cool which leads to massive galaxy masses and steeply decreasing entropy profiles towards the cluster core.

On the other hand, if the AGN energy is redistributed in a volume-weighted manner, the AGN feedback deposition is homogeneous within the sink sphere :

$$E_{\mathrm{AGN},i} = E_{\mathrm{AGN}} \frac{\Delta x_i^3}{\sum_i \Delta x_i^3}. \tag{9.12}$$

Therefore, this AGN feedback model deposits less energy in the gas rich regions in favour of less dense regions. Thus, AGN energy can escape more easily the accretion sphere to reach larger radii than the mass-weighted deposition.

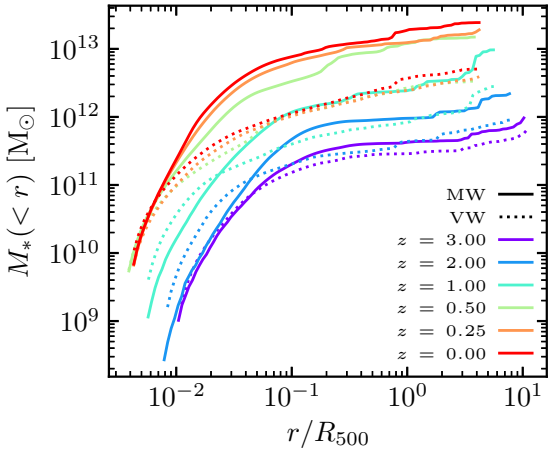

Figure 9.10: Cumulative stellar mass radial profiles rescaled by the halo R_{500} corresponding to the radius enclosing 500 times the critical density at that redshift. We roughly have $R_{\mathrm{vir}} \sim 1.7 - 2R_{500}$. Solid and dotted lines show the radial profiles of the `MW` and `VW` simulations respectively. The line color indicates the redshift at which the radial profile is computed. We see the great effect of the AGN with a volume weighted energy deposition at quenching star formation throughout the cluster.

Let us next discuss the impact of such changes on the stellar and

gas content of the simulated cluster. We simulated `Halo545` with the mass-weighted AGN feedback energy injection model (labelled as `MW`) and with the volume-weighted model (`VW`).
We plotted in Figure 9.10 radial profiles of the (cumulative) stellar mass.
In the stellar mass profiles, we notice that the stellar content in the cluster has been reduced by a factor of $\sim 6-7$ at $z = 0$ ($R_{\rm vir} \sim 2\,R_{500}$) for the simulation using a `VW` AGN feedback model.

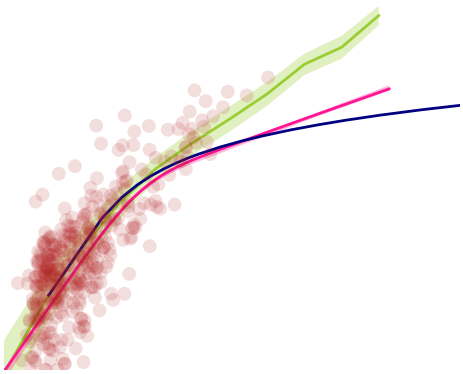

$0.15R_{500}$. In that case, we see that the entropy profiles for the MW simulations do not significantly change out to the virial radius (being, 1.6 R_{500} and 1.9 R_{500} at $z = 3$ and $z = 0$ respectively).
On the other hand, the VW simulation shows higher entropy in the ICM at high redshifts, which drops by $z = 0.5$ to values similar to the MW simulation.
Simulation with a VW AGN model allows a more efficient heating at all radii which is able to raise the ICM entropy. This heating can also be seen in the right panel of Figure 9.12. Indeed, focusing again in the $r > 0.15R_{500}$ region, we clearly see that the gas fraction drops below the universal value (i.e. Ω_b/Ω_m) at $z > 0.5$ for the VW simulation whereas the MW simulation shows a higher amount of gas.

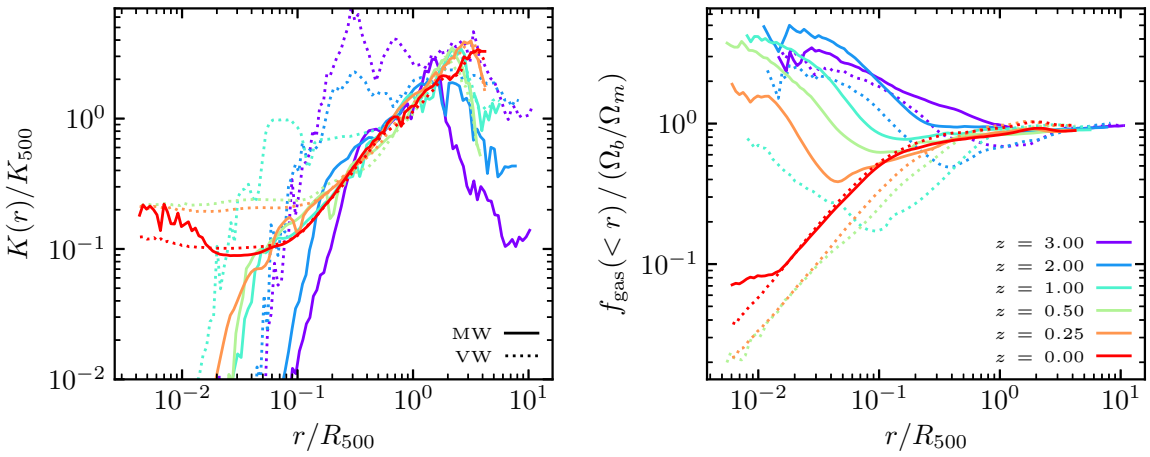

Figure 9.12: ICM entropy (*left*) and enclosed gas fraction (*right*) radial profiles. Radii have been normalised to R_{500}, the radius enclosing 500 times the critical density at the indicated redshift. The entropy profiles has been rescaled by the self-similar values of Nagai *et al.* [287] (see Equation 10.7 in the next chapter) which allow to compare profiles at different redshifts more easily. Solid and dotted lines show respectively profiles in the MW and VW simulations while the line color indicates the redshift. We can see in the entropy profiles that the VW AGN feedback heats the ICM up to large radii compared at $z < 1$ to the MW one. It allows an earlier transition to a NCC cluster already by $z = 0.5$, while the MW simulation still shows a very low core entropy.

Starting from $z = 0.5$, we see that in the core the entropy profiles of the VW simulation flatten, while in the MW simulation, entropies are very low. They become similar at $z = 0$ reaching values of $\sim 10^2$ keV cm^2.
We see that the VW AGN feedback can balance the gas cooling in the core from $z = 1$ in contrast to the MW simulation.
Indeed, the MW AGN feedback model injects its energy in the cold dense accreting region which difficultly escapes the sink accretion region (i.e. where the sphere in which AGN energy is injected). The AGN energy is rapidly thermalised by the large amount of cold gas in which the SMBH sits. Therefore, the gas accretion onto the SMBH is limited at early times. In the meanwhile, the gas continues to cool outside the accretion region that will later fuel a greater

SMBH gas accretion. Hence, AGN feedback will eventually be able to heat the core to temperatures equivalent to the VW simulation at low redshift by the increased cold gas accretion rates.
It explains why compared to the VW simulation, the entropy profile of the MW simulation at $z = 0$ shows a high entropy inner core (due to the immediate AGN heating) embedded in a colder core.

In a nutshell, we have the VW AGN feedback which allows to better heat the less dense regions. The AGN energy escapes the accretion region and can efficiently heat the whole cluster at high $z \geqslant 1$. As the result, the ICM being hotter and more diffuse, the cold gas accretion fuelling further strong AGN events is reduced, which lowers the AGN heating at low redshifts.

On the other hand, the MW AGN feedback model injects energy in the dense accretion regions, which rather prevents the accretion at high redshifts until the cold gas can reach the inner core (shown by the excess of gas in the right panel of Figure 9.12 at $z = 0$). The presence of the immediate large reservoir of cold dense gas at the immediate surroundings of the SMBHs allows an efficient heating at low redshifts able to bring the ICM entropy of the MW simulation comparable to the VW one.

Despite the relative similarity of the entropy profiles at $z = 0$, the AGN heating histories in the cluster significantly differ.
In the MW simulation, the inefficient AGN feedback at early times does not regulate the star formation in the proto-cluster which leads to the over-massive cluster galaxies. Whereas, in the VW simulation we see strong quenching of the star formation at earlier times because of a very efficient feedback.
As we can see in the first and second panels of Figure 9.13, the gas distribution differs substantially between the VW and MW respectively. Thanks to the heating at large radii of the VW AGN model, the pile up of cold gas observed in the MW simulations has been prevented.

Consequently, we can see in the stellar maps of Figure 9.13 that the stellar content has been greatly reduced in the VW simulation as well as a lower number of galaxies.

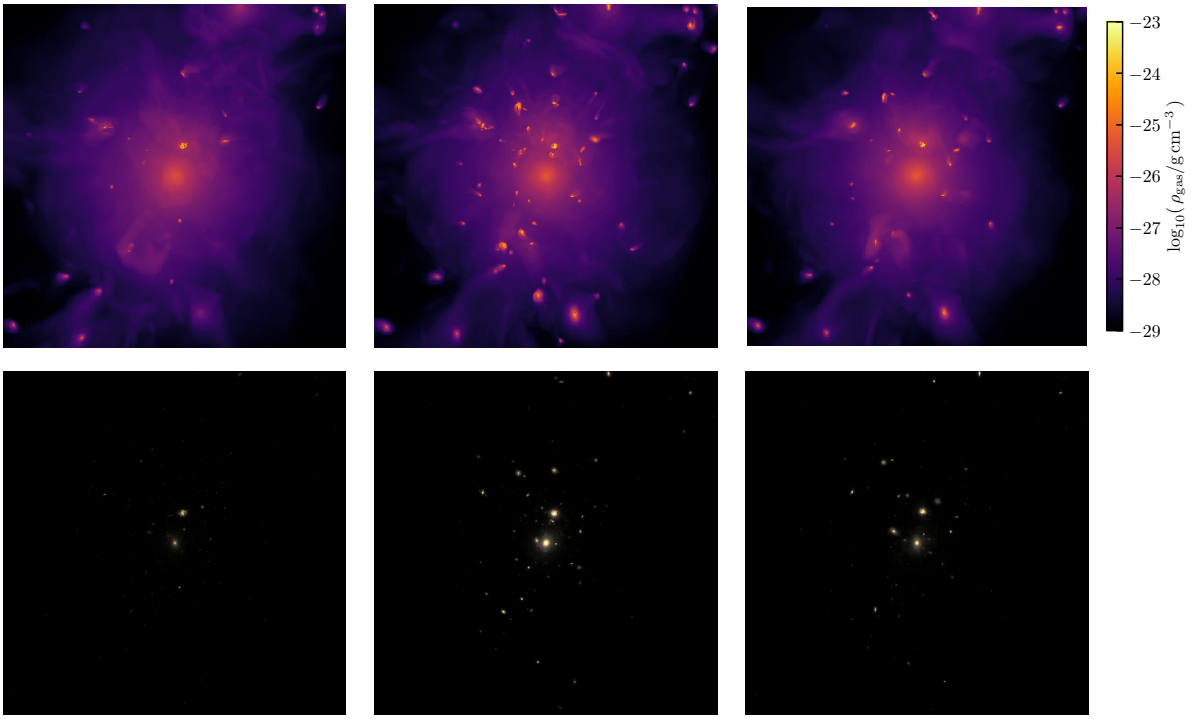

Figure 9.13: Maximal intensity maps of the gas (top panels) and stellar (bottom panels) density in a box of 4 Mpc on the side at $z = 0$. We have from *left* to *right*, the `VW`, `MW` and `MC` simulations. We can see the effect of the `VW` AGN feedback at removing the cold dense gas clumps compared to the `MW` AGN model. We can also notice a similar effect, albeit lower, of the anisotropic thermal conduction in the `MC` simulation at preventing the pile up of gas in dense clumps. As a result, the stellar content in the `VW` simulation is greatly reduced compared to the `MW` one. The `MC` shows a lesser density of stars too.

9.4 Anisotropic thermal conduction

Starting from the `MW` simulation which shows the largest amount of cold gas, we investigate in this section, wether anisotropic thermal conduction is able to offset the radiative losses in the ICM.
We named the simulation using the MW AGM model and thermal conduction, `MC` which will be compared to the `MW` simulation.

We recall that the effect of the anisotropic thermal conduction studied in Chapter 8 is to transport heat in order to smooth out temperature gradients.
Therefore it can act as a cooling or heating source depending on the sign of the temperature gradient. As the `MW` simulation studied in the previous section, shows a strong inner core heating (as we can see in the higher entropy in the $r/R_{500} < 2 \times 10{-}2$) we would like to know if thermal conduction is able to transport the AGN energy at larger radii. Also, as the `MW` simulation shows the highest stellar masses and a large amount of cold gas, it would be interesting to test wether thermal conduction can ease the observed overcooling. Indeed, Ruszkowski *et al.* [295] found that thermal conduction was able to noticeably reduce the gas accretion driven by overcooling.

We will start by looking at the impact of the anisotropic thermal conduction on the stellar content of our `Halo545`. We plot in Figure 9.14 the cumulative stellar mass profiles of the `MW` and `MC` simulations.

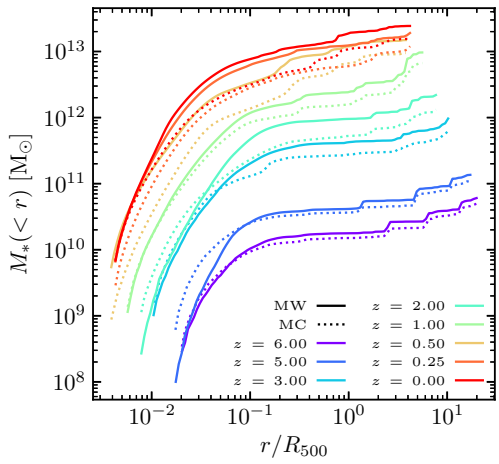

Figure 9.14: Comparison of the cumulative stellar mass radial profiles for the simulations with (dotted) and without (solid) anisotropic thermal conduction both using a MW AGN feedback energy deposition. The line colors indicate for the redshift at which the radial profile is computed. The anisotropic thermal conduction allows to reduce the stellar content of the ICM by a factor of ~ 2.

Less dramatic than the VW AGN energy injection, the anisotropic thermal conduction allows to reduce by a factor of ~ 2 the stellar content in the ICM. We can see in Figure 9.14 that the amount of star is already lower at high redshifts, before the peak of the AGN activity ($z \sim 2$). Equivalently, the galaxy masses in the `MC` simulation, shown in Figure 9.15, are lower compared to the `MW` one. It means that star formation in the forming proto-cluster is reduced with thermal conduction which smooths out temperatures gradients. Indeed, the amount of cold gas in galaxies necessary for star formation is reduced due to the transport of heat.

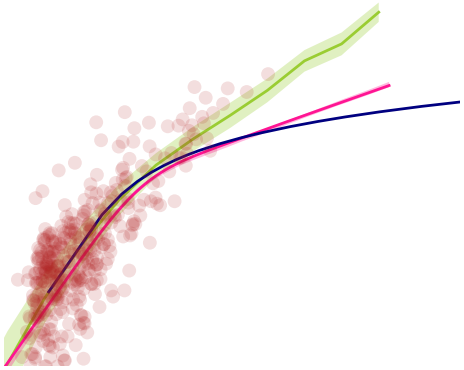

helps to reduce star formation, it also suppresses the amount of cold gas available for the accretion onto the SMBHs fuelling AGN activity.

Kannan *et al.* [114] found in their Arepo simulation of a galaxy cluster that anisotropic thermal conduction isotropises the injected AGN feedback energy in the ICM. They found that an enhanced coupling between the feedback energy and the ICM reduces the SFR by an order of magnitude while the overall amount of AGN feedback energy injected into the ICM is lower. They found that the earlier quenching comes with an earlier transition to a NCC cluster.

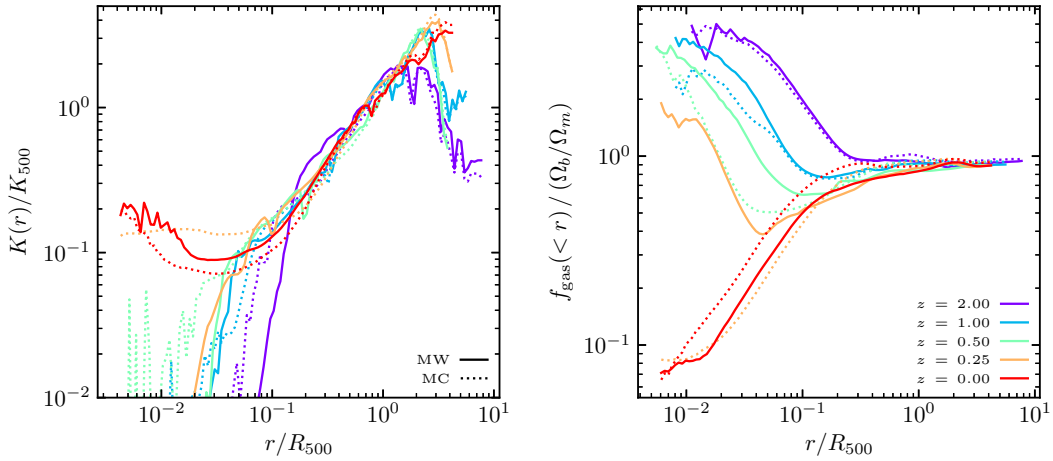

Figure 9.16: Radial profiles of the gas density (*left*) and enclosed gas fraction (*right*) of the `MW` and `MW` simulations at different redshifts shown respectively with solid and dotted lines. We can see the earlier transition from a cool to an hotter core at $z = 0.25$ (orange lines) in the simulation incorporating anisotropic thermal conduction.

As we can see in Figure 9.16, we also witness an earlier transition to a NCC cluster. We see that at $z = 0.25$ (orange lines), the `Halo 545` in the `MC` simulation (dotted line) shows already a high core entropy compared to the `MW` simulation. We observed that, at this redshift, the gas depletion profile shown in the right panel of Figure 9.16 are drastically different with the `MW` simulation showing a higher amount of cold gas in the core compared to the `MC` simulation.

As discussed earlier, we do observe a lower SFR in the ICM by roughly a factor of two which is five times less than what Kannan *et al.* [114] observed in their simulations.
However, the strong quenching of Kannan *et al.* [114] by a greater AGN heating efficiency is not observed in our simulations. By looking at the cumulative AGN energy injected by the SMBH in our simulations we find that the `MC`, compared to the `MW` simulation, shows a lower injected AGN energy by a factor of 2.

Thermal conduction actually reduces the AGN activity in our simulations.
The SF quenching is rather attributed to thermal conduction which smoothes the ICM. Therefore, the condensation of gas is prevented and the birth of stars is consequently reduced.

We also notice that by comparing the entropy radial profiles of the MW and MC simulation, we see that the entropy is slightly lower in the MC simulation for $r \lesssim R_{\rm vir}$ and higher at $r \gtrsim R_{\rm vir}$ (with $R_{\rm vir} \sim 1.9 R_{500}$).
Indeed as we can see, in the gas temperature profiles of Figure 9.17 at $z = 0$ and radii lower than the Virial radius, that lower temperatures in the ICM in the simulation with thermal conduction and slightly higher above $R_{\rm vir}$.
We know that thermal conduction works at flattening temperature gradients. As the ICM temperature is decreasing with radius, thermal conduction transports heat outwards. As a result, the cluster gas shows lower temperatures and a smoother radial distribution. However, the induced cooling in the ICM raises the gas density as we can see in the gas depletion profiles in Figure 9.16.

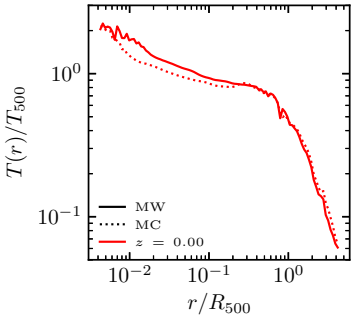

Figure 9.17: Radial profiles at $z = 0$ of the gas temperature normalised by the self-similar values T_{500} calculated according to Equation 10.6. We show the MC simulation with dotted lines while the MW simulation is shown with solid lines.

In the MW AGN model used in these two simulations, the injected energy stays confined to the accretion sphere ($\sim 10^{-2} R_{500}$). Anisotropic thermal conduction does not transport the AGN energy on sufficiently small timescales (compared to the central cooling times) to effectively diffuse the AGN heating on large distances.
In this case, it seems that thermal conduction shows an opposite behaviour compared to what Kannan *et al.* [114] found : conduction slows the SMBH gas accretion which lowers the injected AGN energy and permits a greater cooling in the ICM.

9.5 Summary

In this chapter, we have studied the impact of our sub-grid models of galaxy formation on the stellar content of our halos as well as the intra-cluster gas properties. This step is crucial to understand the impact, success and shortcomings of the models that we use. Hence, we can better adjust model parameters to produce simulated galaxy clusters close to observed ones as much as possible.

In Section 9.1, we showed that the model of star formation and supernova feedback that we use is able to reproduce realistic galaxy masses in agreement with abundance matching constraints.[7]

7: See Figure 9.1 for the SMHM relation for the MW, VW and MC simulations.

Shortcomings in the Rhapsody-G simulations of Hahn *et al.* [111] motivated the revision of our models of SMBH growth and AGN feedback.
We saw in Section 9.2 that the seeding of black holes in the original Rhapsody-G simulations was unstable and inefficient. By adjusting the SMBH seeding in our simulations we saw that we can efficiently control the star formation in our protocluster. Indeed, we now robustly seed more SMBHs in our simulations. It also allows to reproduce realistic galaxy masses at the AGN activity peak, $z = 2$.

We had to develop a new model for the SMBH dynamics to conserve stable orbits inside halos. We showed that our model of "tidal friction" in Section 9.2.2 drastically boost the SMBH gas accretion and SMBH growth. As the result, the Booth & Schaye [144] boost used to compensate for the unresolved gas accretion was dropped. The implementation of this tidal model for the SMBH growth allow to significantly lower the amount of gas in the ICM as well as the stellar mass which were the main flaws in the original Rhapsody-G simulations.

Our 'tidal friction" model has been successfully implemented in the current version of Ramses. It was made publicly available on the online repository[8] and has been already used by other scientists in the field.

8: bitbucket.org/rteyssie/ramses

We later investigated the effect of AGN feedback in our simulation which benefit from the above-mentionned improvements.

Figure 9.18: Similarly to Figure 9.13, we show the stellar density in a smaller box of 1.5 Mpc on the side at $z = 0$ of the same halo in the `VW` (*left*), `MW` (*left*), and `MC` (*right*) simulations

We found in Section 9.3 that the slight change in the AGN energy injection within the sink sphere dramatically changes the stellar content in the ICM as well as its heating history. A VW AGN injection strongly heats the ICM at early times and prevent the build up

of cold gas. It allows to efficiently quench star formation early-on. By injecting more AGN energy in the less dense regions, the AGN energy is able to escape and reach large radii (even beyond the virial radius). However the early strong AGN heating prevents a later AGN activity as it reduces the amount of cold and dense gas in the ICM. Thus, the ICM is left to cool without forming stars.

MW energy injection does not allow the heating beyond the SMBH accretion region at high redshifts. Hence, the ICM cools and the formation of star abounds. This early cooling will however fuel a strong AGN activity at low redshifts which allows to reproduce a similar entropy profile as the `VW` simulation at $z = 0$.
Despite this late-time agreement, the galaxy masses significantly differ in the two simulations. Illustrated in Figure 9.18, we found ~ 6 times less massive galaxies in the `VW` simulation (early strong AGN heating) as well as a lower number of cluster galaxies (see also Figure 9.11).

The anisotropic thermal conduction allows to quench star formation in the protocluster by almost a factor of 2 at $z = 3$. Indeed, thermal conduction smooths out temperature gradients which prevent the clumping of the gas in the ICM that would lead to the formation of stars.
However, the reduced ICM clumpiness weakens the SMBH cold gas accretion, which consequently decrease the AGN heating. As a result, the ICM cools and get denser. This result is amplified by the effect of thermal conduction at transporting heat of the central regions to the cluster outskirts.
Hence, thermal conduction effectively reduces the early star formation but participates in the late time cooling of the ICM.

To sum-up, we studied the properties of galaxies and the ICM based on three simulation flavours :

- `VW`, which represents an extreme case of strong AGN heating at large radii and early times. For this feedback model, we found that star formation was quenched too early, leading to under-massive galaxies.

- `MW` produces a confined AGN energy deposition in the cluster core. Here we did not observed a significant quenching leading to over-massive galaxies.

- `MC` leads to a quenching of star formation but does not significantly increase the AGN heating efficiency.

To span the range of uncertainties in astrophysical modelling in

cluster simulations, we will use this set of three simulations for each halo of the Rhapsody-G sample and study their respective evolution.

Global properties of the simulated clusters

10

In this chapter we will give an overview of our new Rhapsody-G *simulations. We will discuss the properties of the cluster galaxies, black holes as well as the thermodynamics of the intra-cluster medium in the simulations using different physics. We will see the global impact of thermal conduction, a volume-, or a mass-weighted AGN energy deposition on the cluster sample properties.*

10.1 Sample overview

We start by showing in Figure 10.1 the mass assembly of our halos in dark matter-only simulations. We can see that, at $z = 0$, all clusters share roughly the same mass with the exception of `Halo 474` which is about a factor 2 more massive than the rest of the sample.

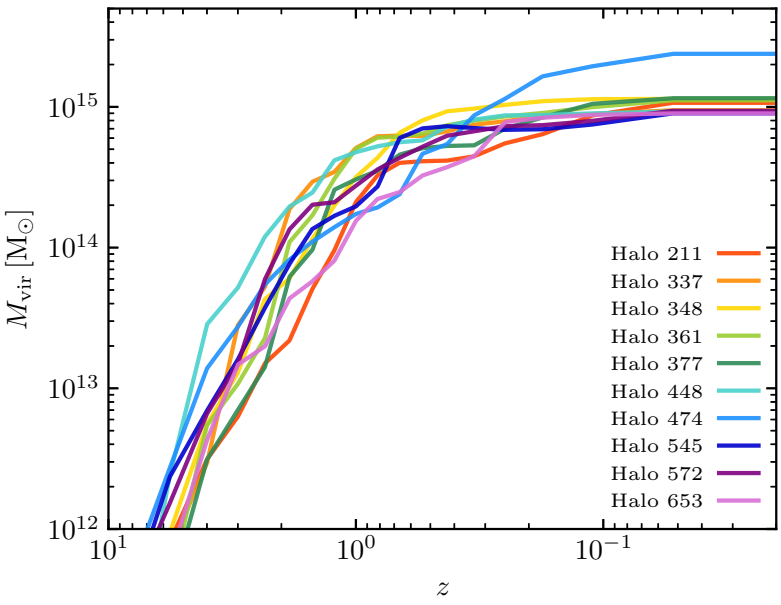

Figure 10.1: Mass assembly histories in the (new) Rhapsody-G sample with updated cosmology. We see the difference in mass evolution in our sample which will allow to study galaxy cluster properties at cosmic variance.

Figure 10.1 demonstrates the variety of halo assembly histories at fixed $z = 0$ mass. For instance, we can see the relatively rapid mass growth of `Halo 448` compared to a smoother mass increase of `Halo 211`.

We saw in Figure 5.10[1] that halos of the Rhapsody-G sample probe

1: In this thesis, we will consistently use the same colors and symbols that corresponds to an unique halo in the Rhapsody-G sample. Therefore, the colors of the frames in Figure 5.10 are consistent with the color lines of Figure 10.1 or the colored symbols of Figure 10.2

Name	z	$M_{\rm vir}$ [$M_\odot / 10^{14}$]	$R_{\rm vir}$ [Mpc]	M_{500} [$M_\odot / 10^{14}$]	R_{500} [Mpc]
Halo211	0.00	11.57	2.77	7.56	1.42
Halo337	0.00	10.08	2.64	6.32	1.33
Halo348	0.00	11.96	2.80	6.98	1.38
Halo361	0.00	11.86	2.78	7.55	1.41
Halo377	0.00	12.22	2.82	6.80	1.37
Halo448	0.00	9.78	2.62	6.24	1.33
Halo474	0.50	4.80	1.55	3.87	0.94
Halo545	0.00	9.88	2.62	6.73	1.36
Halo572	0.00	9.96	2.63	6.62	1.35
Halo653	0.00	8.62	2.51	5.19	1.25

Table 10.1: Properties of the Rhapsody-G halos in our new simulations with updated cosmology, all computed at $z = 0$ except for Halo474 which did not reach it yet. For each halo, we give its virial mass and radius as well as the radius R_{500} enclosing 500 times the critical density at redshift z (given in the second column) and the total mass M_{500}.
These properties are computed for the MW simulations, but do not significantly change in the VW simulations.

Name	z	$M_{\rm vir}$ [$M_\odot / 10^{14}$]	$R_{\rm vir}$ [Mpc]	M_{500} [$M_\odot / 10^{14}$]	R_{500} [Mpc]
Halo211	0.25	5.48	1.86	3.64	1.02
Halo337	0.15	8.94	2.32	5.36	1.20
Halo361	0.50	6.90	1.75	4.78	1.01
Halo377	0.20	8.24	2.20	5.10	1.16
Halo448	0.10	9.23	2.42	5.57	1.24
Halo545	0.00	9.86	2.62	6.68	1.36
Halo572	0.02	9.67	2.57	6.34	1.32
Halo653	0.15	8.54	2.29	5.57	1.22

Table 10.2: Same as Table 10.1 but for the MC simulations. As these simulations are more expensive, all but one (Halo545) did not reach yet $z = 0$. We give in the second column the redshift of the latest available simulation snapshot at which cluster properties are computed.

extreme cases of the formation history but also more average clusters. This explains the observed scatter in the mass assembly histories of the Rhapsody-G sample between $z \sim 6$ and $z \sim 0.2$.

We listed in Table 10.1, the properties of these clusters at $z = 0$ in the MW simulations. We remark that these properties do not change significantly in the VW simulations.

At the time we write this thesis, all except one MC simulation have not yet reached $z = 0$. A simulation implementing anisotropic thermal conduction is on average a factor $\sim 3 - 4$ more expensive than a simulation without. The MC simulations were run to $z \gtrsim 0.2$. We give in Table 10.2, properties of halos in the MC simulations with, in the second column, the redshift of the latest simulation snapshot available.

Thanks to the diversity of the Rhapsody-G sample, we are in a position to study the impact of (non-thermal) astrophysical processes at variance with cosmological formation histories on the properties of massive galaxy clusters.

Constraining the amount of non-thermal energy related to mass accretion, merger activity, or galactic feedback events is crucial for

cluster cosmology. As the true mass of a cluster is not accessible in observations, we need to understand how biased is the mass inferred by a gas proxy assuming hydrostatic equilibrium (as this assumption does not hold in reality due to the rich nature of galaxy clusters, c.f. Chapter 11).

In our set of simulations (`VW`, `MW` & `MC`) we can study the role of mergers vs. AGN vs. thermal conduction in shaping the thermodynamic structure of massive galaxy clusters. A particular focus on understanding the respective impact on cluster scaling relations will be explored in the next Chapter 11. But, first, let us discuss in this chapter the properties of the stellar and gaseous components of the simulated galaxy clusters.

10.2 Cluster galaxies

In this section, we will start by looking at the stellar properties of our sample. We show in the top panels of Figure 10.2, the stellar-mass vs the halo mass of the halos in each of our Rhapsody-G simulations. We show all halos and subhalos masses in all Rhapsody-G simulations with, from left to right, the `VW`, `MW` and `MC` physical models.
We distinct halos by using the same color coding as in Figure 10.1.

We notice in this figure the relatively high number of sub-halos in the `Halo 348` simulation compared to `Halo 211` or `Halo 653` simulations for instance. It again shows the diversity of our simulated cluster with different number of substructures (c.f. Figure 5.10).

From the comparison of the three panels of Figure 10.2, we can see that the `VW` simulations have a systematically lower number of halos with stellar masses above $\sim 10^{10.5}\mathrm{M}_{\odot}$. Futhermore, the stellar masses are systematically lower by a factor of ~ 2 compared to the `MW` simulations. Consistently with the findings of Section 9.3, we see that the VW AGN energy deposition is effective at quenching the star formation compared to a MW energy injection for all halos in our sample. In comparison with IllustrisTNG100 data or abundance matching results, halos in the `VW` simulations have a factor $\sim 5-10$ lower stellar masses. We have to keep in mind that we measure the total stellar mass inside R_{200} i.e. stars in the central galaxy and in the intra-halo light. We also measure the total stellar mass for IllustrisTNG100 halos but abundance matching results provide the mass of the central galaxy only. For the `VW` simulations and for $M_{\mathrm{h}} \leqslant 10^{13}\mathrm{M}_{\odot}$, we see that our stellar masses

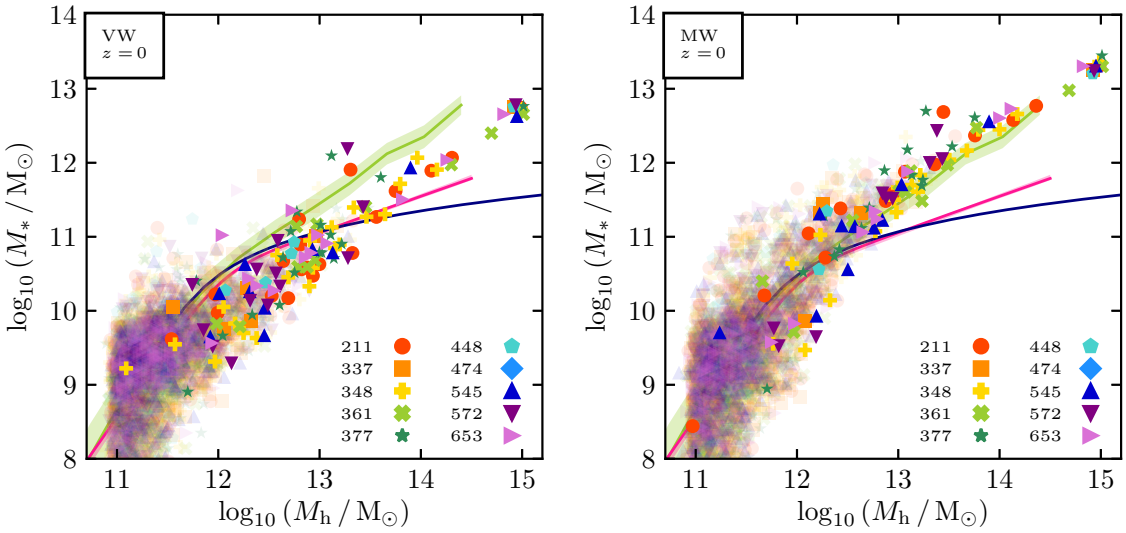

Figure 10.2: Total mass of stars inside R_{200} as a function of the halo mass for the VW (*left*) and MW (*right*) simulations. As in Figure 9.1, we show abundance matching results of the Universe Machine [372] (pink) and Legrand *et al.* [377] (navy). In green, we plot the mean relation with the standard deviation (shaded area) for the IllustrisTNG100 simulations. The opaque and transparent symbols indicate respectively for central and satellite galaxies.

are systematically lower than the IllustrisTNG100 simulations, the Universe Machine [372] and Legrand *et al.* [377] studies, up to a factor of 10, which is unrealistic.
In contrast, the stellar masses of the MW simulations agree at the high mass end, with the IllustrisTNG100 mean relation with a significantly smaller scatter compared to the VW simulations. We notice in the MW simulations, the larger stellar masses at all halo mass compared to the VW simulations.

As a result, consistently with the conclusions of Section 9.3 we see that the different AGN models differently impact the stellar content of the cluster at $z = 0$.
If we look at the star formation rates in Figure 10.3, we can see that the VW energy injection model suppresses efficiently the star formation in the cluster down to $z = 0$ compared to the MW model. We measure the star formation in our halos as the mass of star particles in each halo that have an age less than 500 Myr divided by 500 Myr. We stress that we do not measure the central galaxy SFR but the total SFR in the halo which include more stars.
We compare our data with the main sequence of star formation of Noeske *et al.* [383] and the quenched limit of Woo *et al.* [234] in the Sloan Digital Sky Survey (SDSS) along with the sample of central cluster galaxies from SDSS of Liu *et al.* [235].
We can easily see that the SFRs of the VW simulations are greatly reduced compared to the MW simulation, where only few halos with $M_* \leqslant 10^{11}\mathrm{M}_\odot$ persist. We see that a large fraction of central halos are below the quenched limit of Woo *et al.* [234] compared to the MW simulations. However, we can see that halos with stellar

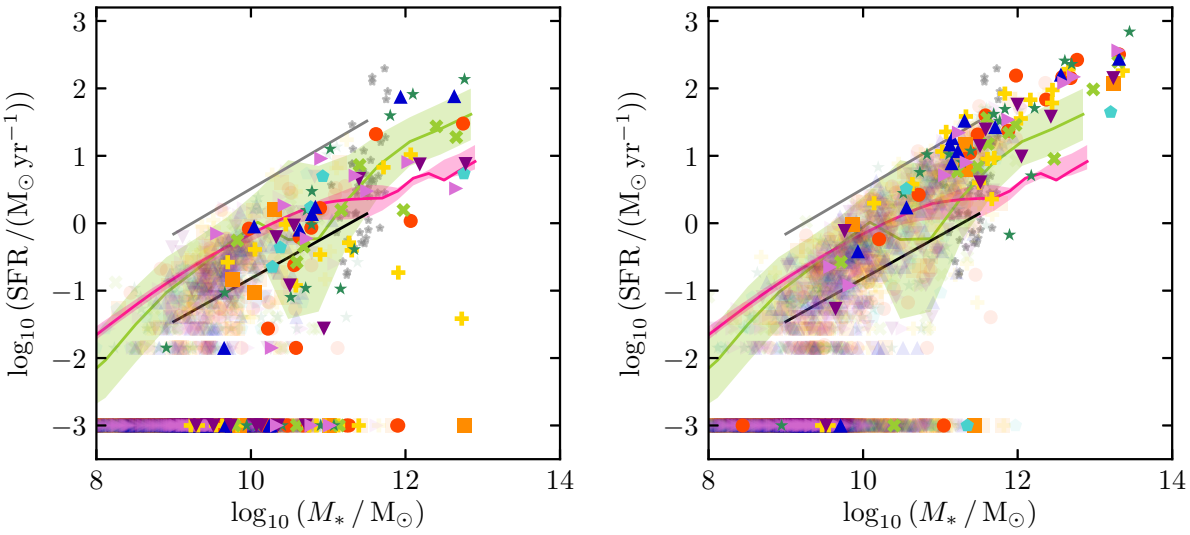

Figure 10.3: Total star formation rates in the last 500 Myr for the VW (*left*) and MW (*right*) simulations as a function of stellar mass at $z = 0$ for central (opaque) and satellite (transparent) galaxies for all the Rhapsody-G halos. We assigned a constant value of 10^{-3}M$_\odot$/yr for halo with no detectable star formation. We compare our results to the Universe Machine [372] (pink), the main sequence of star formation of Noeske *et al.* [383], the quenched limit from Woo *et al.* [234] (black), the OII-derived SFRs for the BCG samples of Liu *et al.* [235] along with the mean relation of the IllustrisTNG100 simulation.

mass $M_* \leqslant 10^{11}$M$_\odot$ broadly agree with the comparison studies but, SFRs in the MW/VW simulations tend to be slightly biased high/low. Indeed, SFRs of the MW simulations show high values compared to the other studies especially at the high mass end.

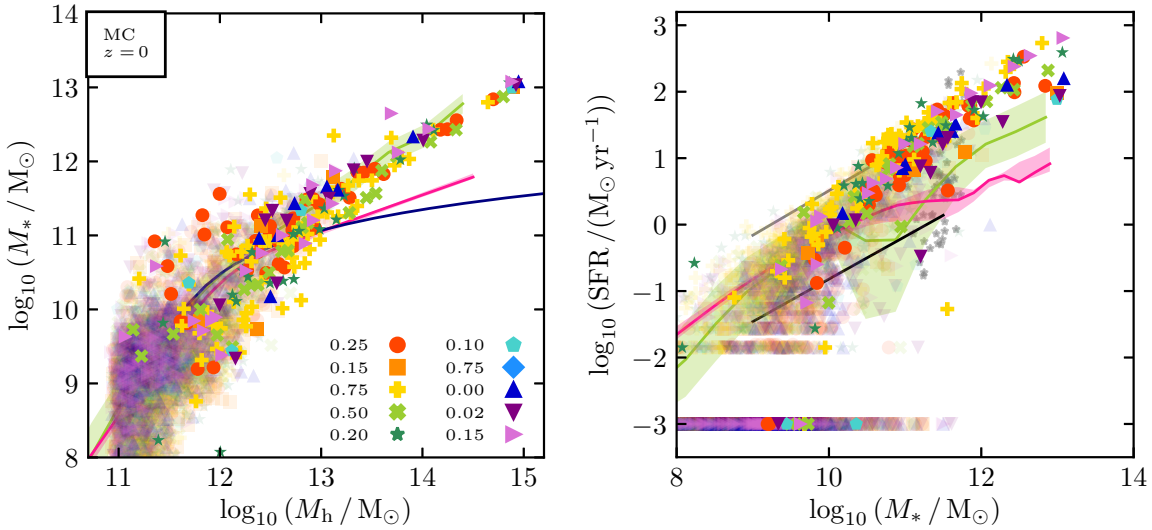

Figure 10.4: Same as Figure 10.2 (*left*) and Figure 10.3 (*right*) for the MC simulations which incorporate anisotropic thermal conduction. Because most of the MC simulations did not reach $z = 0$, we plot halo properties at the lowest available redshift given in the legend of the *left* panel. For comparison, we plotted the IllustrisTNG100 mean SMHM, UniverseMachine and Legrand *et al.* [377] relations at $z = 0$. The results of Noeske *et al.* [383] ($z \lesssim 1.1$, grey), Liu *et al.* [235] ($0.1 < z < 0.4$, grey stars) are valid for the redshift range covered by the various MC simulations. The quenched limit of Woo *et al.* [234] (Black) plotted here is only valid for $0 < z < 0.2$.

Because not all the Rhapsody-G MC simulations reached $z = 0$, a direct comparison with the VW and MW cannot be performed. There-

fore, we show in Figure 10.4 the stellar properties in the latest available snapshot of each halo simulation in order to illustrate how do halos in these simulations compared to the comparison studies.
We can see that stellar masses and star formation rates roughly agrees with the simulations, abundance matching and observational results. However, we still have to keep in mind that these studies rather probe galaxies in the field. We can see that only `Halo545` was run to $z = 0$ which allowed the comparative analysis of Section 9.4. Therefore, we can see that the `MC` simulations show higher rates of star formation, expected at higher redshifts. SFRs are in agreement with the main sequence of Noeske *et al.* [383] and show some quenched star formation for masses $M_* < 10^{12}\mathrm{M}_\odot$.

10.3 Black hole scaling relations

In their centers, host galaxy properties correlates with the mass of supermassive black holes (see Kormendy & Ho [384] for a review). Out of the many black hole scaling relations, the $M_\bullet - \sigma$ relation, linking the BH mass ($M_\bullet$) to the stellar velocity dispersion (σ), has been established as the strongest and most universal relation [385, 386].

Therefore, we show in Figure 10.5 how do our SMBHs in our three set of simulations (`VW`, `MW` and `MC`) compare to the published results of van den Bosch [387]. The study of van den Bosch [387] combines 230 BH masses and host galaxy velocity dispersions from the literature.

For all SMBHs in our simulation, we find their host halo and measure the velocity dispersion of gas and stars inside the virial radius of this halo.
If more than one SMBH sits in the same halo, we only keep the SMBH closest to the halo center.
We are aware that this might not be the most accurate method, but we are interested here to see how "central" SMBHs compares to the literature.

We can see that SMBHs in our simulations, agrees within the scatter well with the data of van den Bosch [387]. We can see that for the `VW` simulations, SMBHs tend to be less massive than the `MW` and `MC` simulations by almost a factor 10. Indeed, as we saw in Section 9.3, the VW AGN model, is efficient at depleting the gas in the accretion region, hence slowing dramatically its mass growth. Whereas, `MW` and `MC` simulation both use the MW AGN model that

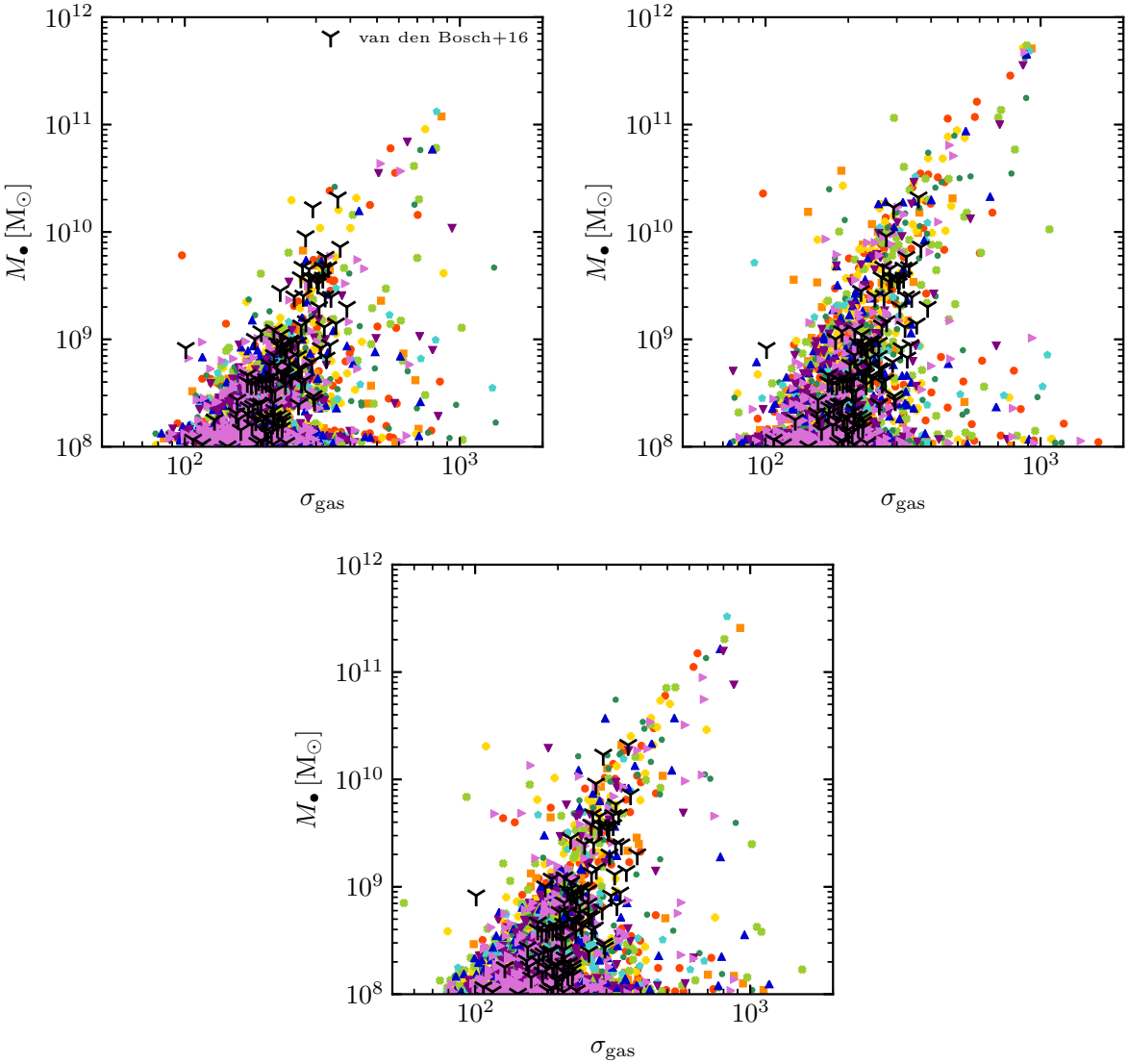

Figure 10.5: SMBH mass vs. the velocity dispersion of gas and stars for the simulation using the VW AGN deposition model (*top left*), the MW deposition (*top right*) and the simulation with thermal conduction (*bottom*). For comparison, we plotted the collected data from the litterature of van den Bosch [387] in the foreground black symbols. For the `MC` simulations, not halos are at $z = 0$. We show here the last available snapshots for the `MC` simulation which redshift are given in the legend of the upper right panel of Figure 10.2.

does not allow the AGN energy to escape far from the accretion region. Therefore, the cold gas accretion onto the SMBHs is not as much reduced as in the `VW`. Hence, SMBH masses can effectively grow to higher masses.
We can also see a factor ~ 2 decrease of SMBH masses in the `MC` simulations compared to the `MW`. With the incorporation of thermal conduction the cold gas content in the ICM is reduced and consequently the fuelling of the SMBH. Indeed, we show in Figure 10.6, the amount of cold gas in the `Halo 545` (the only one that reached $z = 0$) at different redshifts.

We can see in Figure 10.6 that the amount of cold gas in the ICM

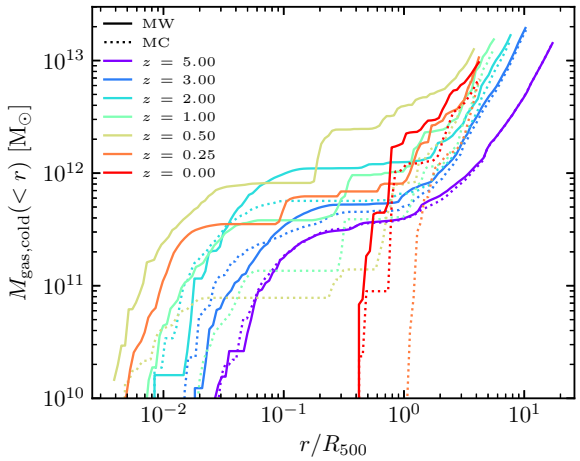

Figure 10.6: Comparison of the cumulative mass radial profiles of the cold ($< 10^6$ K) gas in the ICM between the simulation without (MW) and with (MC) thermal conduction at different redshift. We can see that thermal conduction significantly prevent the build up on cold gas in the core ($r/R_{500} \lesssim 0.3$)

is significantly reduced by $z = 2$ in the MC simulation. However, we see during most of the AGN activity (i.e. $z \gtrsim 2$) that the MC simulation shows the highest amount of cold gas in the very inner region of the cluster center, where the accretion happens. This is because the MW simulation has a stronger AGN activity that depletes the cold gas more efficiently. However, the surrounding ICM is colder and denser. Therefore, as we can se in the maps of Figure 10.7, very dense clump of gas at larger radii fuels the central SMBH mass growth in the MW simulation (*left*).
As a result, SMBH masses in the MC simulations are lower than the MC because of a reduced gas accretion in a smoother ICM.

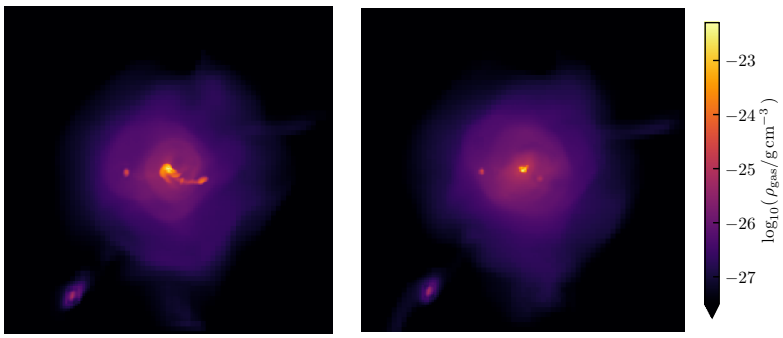

Figure 10.7: Mass weighted density maps of Halo 545 in a box of 2 Mpc (comoving) on the side at $z = 2$, corresponding to the peak of the AGN activity. The *left* panel show the simulation without thermal conduction (MW) and the *right* panel shows the simulation with conduction (MC). We see that the amount of dense gas fuelling the central black hole is reduced in the MC simulation. Consequently, the SMBH mass growth is slower in the MC simulation than in the MW simulation.

10.4 Intra-cluster gas profiles

10.4.1 Impact of the physical models

In this section, we investigate the effects of the physical models used in our simulations on the ICM properties of our sample. As the number of simulation snapshots (i.e. stored redshifts), halos and physical model is high, we decided to show the mean profiles of all our Rhapsody-G sample for each of the VW, MW and MC simulations at low redshifts ($z \leqslant 0.5$) to provide a time-averaged view.

The mean profiles were obtained by first normalizing the ICM profiles of each halo at R_{500} and then averaging over the RHAPSODY-G sample for each of the 3 types of simulations.
In order to reduce the scatter and suppress the mass dependance, the temperature, entropy (defined as $K = k_B T/n_e^{2/3}$), and pressure profiles are normalized to the self-similar value values computed for the given cluster mass using a simple the Kaiser [388] model (see Section 11.1.1 in next chapter; [287, 389]) :[2]

$$T_{500} = 11.05 \text{ keV} \left(\frac{M_{500}}{10^{15} h^{-1} M_\odot}\right)^{2/3} E_z^{2/3}, \quad (10.6)$$

$$K_{500} = 1963 \text{ keV cm}^{-2} \left(\frac{M_{500}}{10^{15} h^{-1} M_\odot}\right)^{2/3} E_z^{-2/3}, \quad (10.7)$$

$$P_{500} = 1.45 \times 10^{-11} \text{ erg cm}^{-3} 1 \left(\frac{M_{500}}{10^{15} h^{-1} M_\odot}\right)^{2/3} E_z^{8/3}. \quad (10.8)$$

Rescaling the ICM profiles by the self-similar values at R_{500} given by Nagai *et al.* [390] is common in the literature. This is why, we also use this normalisation to compare later with published studies.
In addition, we normalise the density profile by the self-similar cosmological dependance on $E(z)^2$ (see later in Equation 11.9).

We show in Figure 10.8, the rescaled mean ICM thermodynamic profiles for the `VW`, `MW`, `MC` and the non-radiative (`NR`) simulations.[3]
For each simulation, the mean radial profile is computed for $z \leqslant 0.5$ for all halos of our RHAPSODY-G sample in 50 logarithmic radial bins out to 4 Mpc-comoving. We also show the 1σ rms scatter around the mean profile.

From the analysis of the four radial profiles we can draw the same conclusions as in the previous Chapter 9[4] for the whole RHAPSODY-G sample.

Let us first compare the mean profiles of the `VW` and `MW` simulations. We can see that the cluster core ($r \lesssim 0.2 R_{500}$), in the `VW` simulations, is on average less gas-rich with a factor ~ 2 higher core temperature. As the result, we see a factor ~ 2 higher entropy core. We directly see the strong impact of the energy deposition method. The VW injection allows to deposit more energy in less dense regions which therefore allows the AGN energy to escape the SMBH accretion region and reach larger radii. However, the strong AGN heating at higher redshifts prevented the formation of stars out of the ICM gas. This can be seen from the steeper decrease of the stellar fraction with radius shown in the right panel of Figure 10.9. Therefore the cluster outskirts are more gas-rich in the `VW` simulations than in

2: The numerical coefficients in the above equations follow :

$$K_{500} = k_B T_{500} n_{e,500}^{-2/3}, \quad (10.1)$$

$$P_{500} = n_{\text{gas},500} k_B T_{500}, \quad (10.2)$$

with

$$n_{e,500} = \frac{\mu}{\mu_e} n_{\text{gas},500}, \quad (10.3)$$

$$= \frac{1}{\mu_e m_p} \frac{\Omega_b}{\Omega_m} 500 \rho_c(z), \quad (10.4)$$

from the definitions of Nagai *et al.* [287] which adopted values the values of :

$$f_b = 0.175,$$
$$\mu = 0.59,$$
$$\mu_e = 1.14.$$

The characteristic temperature is :

$$k_B T_{500} = \mu m_p \frac{G M_{500}}{2 R_{500}}, \quad (10.5)$$

being the temperature of a singular isothermal sphere with mass M_{500}.

3: We also show, in Figure A.1 the radial profiles which we do not rescale by R_{500} and by the associated self-similar quantities.

4: Especially, the results of Section 9.3 and Section 9.4 being respectively, the analysis of the VW vs. MW AGN feedback injection models and the effect of thermal conduction.

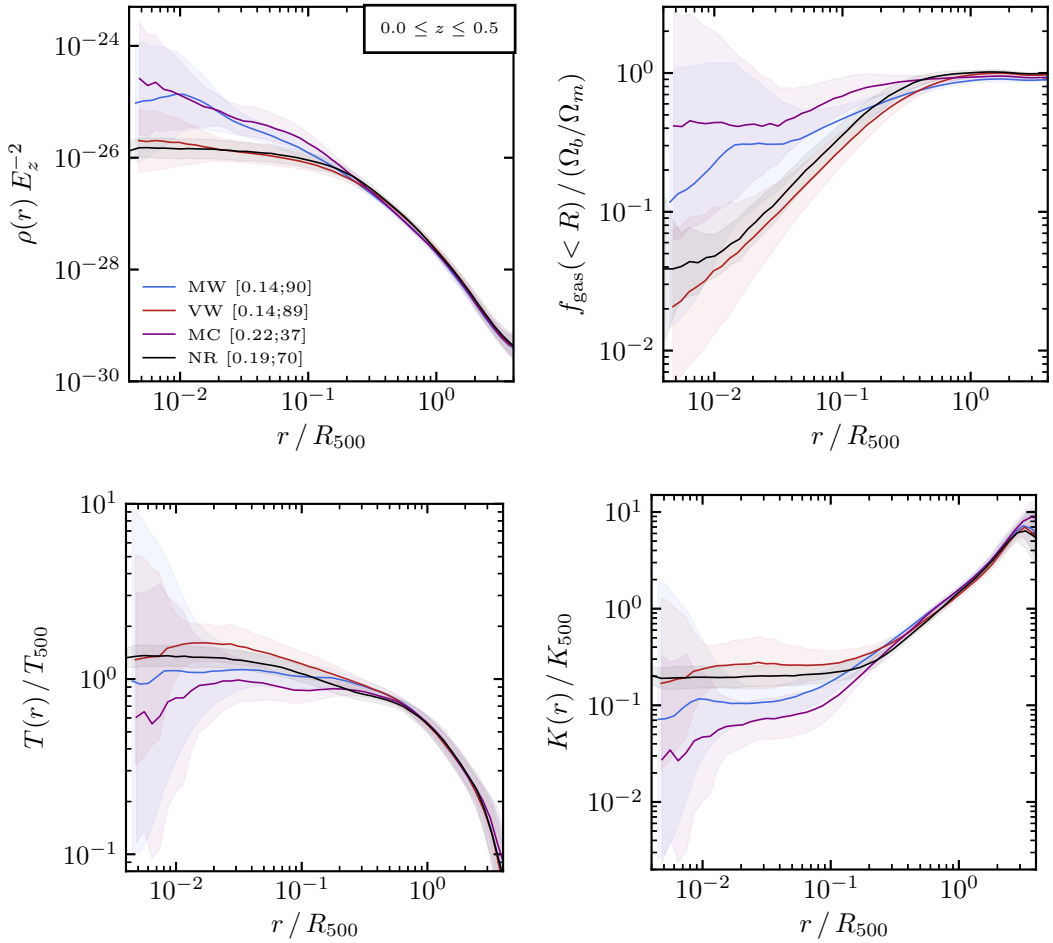

Figure 10.8: Mean radial profiles of ICM thermodynamic quantities rescaled by the self-similar values for our RHAPSODY-G sample at $z \leqslant 0.5$. We shows the mean profiles for the VW (red), MW (blue), MC (purple) and NR (black) simulations being respectively simulations using a volume-weighted AGN energy deposition, a mass-weighted AGN energy deposition with and without thermal conduction as well as an adiabatic simulations. We shows as shaded areas, the 1σ scatter around the mean profiles. We also give, in the first panel, the mean redshift and the number of analysed snapshots for each mean profile. We shows the (scaled) mean radial profiles of the density (*top left*), gas fraction (*top right*), temperature (*bottom left*) and entropy (*bottom right*) of the intra-cluster medium. The radii are scaled to R_{500} and the thermodynamic quantities by the self-similar values T_{500} and K_{500} as well as the density by E_z^2 (see text). It allows to reduce the scatter by suppressing the mass dependance of all studied halos in our sample at different redshifts. We note the lower number of snapshots for the MC simulations available at low redshifts. See Figure A.1 for the profile not scaled with self-similar quantities.

the MW. The gas-rich ICM in the VW simulations will therefore cool at higher rates than in the MW simulations. This is the reason why we observe, at low redshifts, the higher gas fraction at $r \gtrsim 0.3R_{500}$ and a higher gas entropy.

By comparing the mean temperature profile of the simulations without (MW) and with (MC) thermal conduction, we can see the the MC simulation shows a roughly flat profile out to $r \sim 0.6R_{500}$. Whereas in the simulations without conduction, the mean temperature profile steepens from smaller radii $r \sim 0.2R_{500}$. It shows the ability of the anisotropic thermal conduction at smoothing temperature gradients by transporting heat on large distances.

However, the temperature smoothing also prevent star formation at higher redshift which results in a more gas-rich ICM as we can see by comparing the MW and MC mean gas fraction profiles up to $R_{500}/2$.

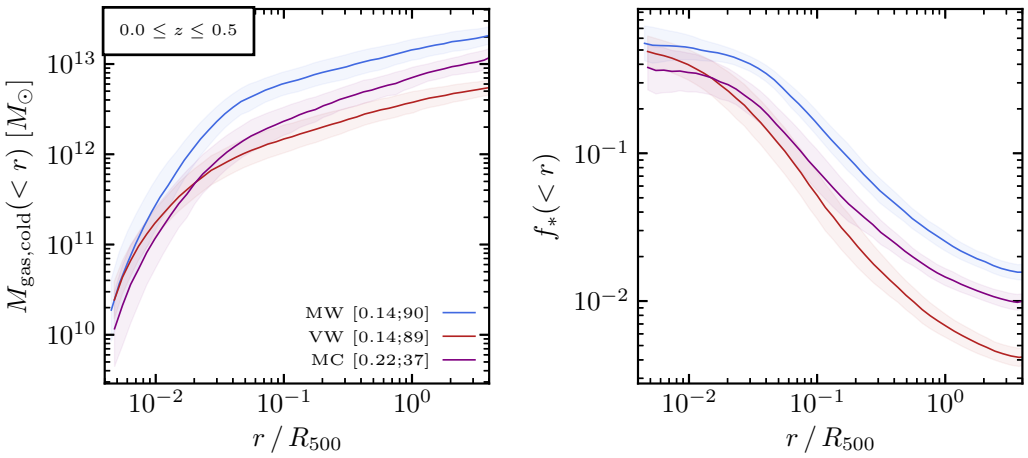

Figure 10.9: Same as Figure 10.8 for the radial profiles of the enclosed mass of cold ($< 10^6$ K) gas (*left*) and the stellar fraction (*right*), with, $f_* = M_*(< r)/M_{\rm tot}(< r)$). We can see the effect of the VW AGN feedback model at suppressing the radiative gas cooling in the cluster core at low redshifts compared to a MW injection model. At higher redshifts, the VW model was efficient at quenching the star formation at large radii which can be seen from the steeper decrease of the gas fraction for the VW simulation compared to the MW. Thermal conduction contributes to reduce both the amount of cold gas and stars in the intra-cluster medium which can be easily seen by comparing the simulations with (MC) and without (MW) thermal conduction.

By looking at the amount of cold gas in the ICM, we see that the simulations with thermal conduction showing slightly a higher fraction of gas in the ICM and also shows a lesser amount of cold gas in the ICM by a factor 2. Therefore, we see that thermal conduction acts at slowing the gas cooling in the ICM which suppresses consequently the star formation by a similar amount.

However, we can see in the mean temperature profile of the MC simulation a dip at $r \sim 0.1R_{500}$ and at the very centre. We saw in Section 8.3 that thermal conduction can either cool or heat the gas depending on the heat transport direction. The central dip is caused by the transport of the AGN energy out of the accretion region which induces an increased gas cooling in the very centre. The second dip is caused by the transport of heat from the core to the colder outskirts. Therefore, the gas at the outer shell of the core cools at the expense of the heated surrounding out to $r \sim 0.6R_{500}$. Thermal conduction strongly acts in the regions where the temperature gradients are the strongest i.e. the AGN immediate surroundings and the outermost shell of the cluster core. Thus, it seems that the ICM becomes unstable to the heat transport processes within.

To conclude, we see that our three different sets of galaxy formation physics provide systematic differences in cluster evolution :

- `VW`: Due to an strong efficient AGN heating, at high redshifts on large cluster distances, the star formation is markedly supressed in the ICM which results in under-massive galaxies. However, the cluster core is very hot with an entropy comparable to the non-radiative[5] simulation.

- `MW`: As the AGN energy is confined near the SMBH, the ICM is free to cool and stars form at a high rate. As a result, `MW` simulations show a lower entropy core with a denser, cooler ICM with overly-massive galaxies.

- `MC`: With conduction added to a MW AGN energy deposition model, the star formation is reduced in the ICM at higher redshifts. Therefore, the ICM is slightly more gas-rich than in the `MW` simulations. Combined with the fact that thermal conduction slows the AGN activity, the ICM cools slightly more than the `MW` simulations. As a result, gas densities in the `MW` and `MC` simulations are comparable but `MC` shows lower gas temperature (hence, lower entropies).

5: In the `NR`, the gas cooling is not allowed and the gas evolves adiabatically. Therefore, as the cluster forms and the ICM is being compressed, the ICM temperature rises in the core.

10.4.2 Comparison to published studies

We will finally compare our ICM radial profiles with published data in order to conclude on wether our simulations reproduce realistic galaxy clusters.
We compare our intra-cluster profiles to the following studies :

- Voit *et al.* [389] who analysed the intra-cluster entropy profile of 71 clusters in AMR and SPH simulations.

- Pratt *et al.* [391] who studied the gas entropy profiles of the 31 nearby galaxy of the REXCESS sample ($z = 0.055 - 0.183$).

- The study of Planck Collaboration *et al.* [392] gave a mean pressure profile from a sample of 62 nearby massive clusters. The majority of objects lies at a redshift lower than 0.3 (and all have $z < 0.5$).

- McDonald *et al.* [96] combined a samples of 8 massive galaxy clusters at $z = 1.2 - 1.9$ (SPT-Hiz), with 49 (X-ray-selected) galaxy clusters at $z = 0 - 0.1$ and 90 (SZ-selected) at $z = 0.25 - 1.2$ to derive mean gas density profiles in different redshift bins.

- Ghirardini *et al.* [70] presented various radial profiles of the ICM thermodynamic properties for 12 galaxy clusters in the X-COP sample with $z = 0.04 - 0.1$.

- Gianfagna *et al.* [393] studied radial pressure profiles for a sample of 260 synthetic clusters from the MUSIC simulation project at $z = 0 - 0.82$.

Additionally, we compare our simulations to the publicly available data from the ACCEPT[6] Chandra archival project described in Cavagnolo *et al.* [185].
From the 242 galaxy cluster profiles available in the table downloaded from the project website, we have matched 141 objects to the MCXC sample of Piffaretti *et al.* [394] which gives access to radius and mass estimates.
The match between ACCEPT and MCXC catalogues was performed using the right ascensions, declinations and redshifts of the objects. As the result, our matched sample "ACCEPTxMCXC" includes 141 objects and we show the mass and redshift distribution in the two panel of Figure 10.10.

6: Archive of Chandra Cluster Entropy Profile Tables (ACCEPT), see the homepage of the project at http://www.pa.msu.edu/astro/MC2/accept

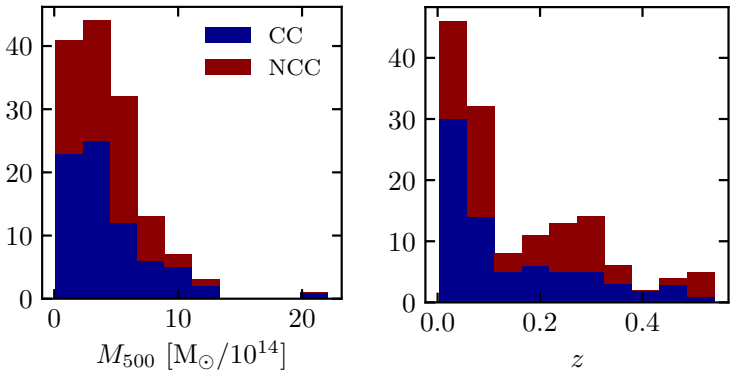

Figure 10.10: Mass (*left*) and redshift (*right*) distribution of our matched ACCEPTxMCXC cluster sample. The blue and red color show the relative contribution of cool-core (CC) and non-cool-core (NCC) to the total distribution.

Cavagnolo *et al.* [185] found a bimodality in the central entropy excess K_0[7] distribution with two distinct population separated at $K_0 \sim 30 - 50\,\mathrm{keV\,cm^2}$.
We therefore classified the ACCEPTxMCXC clusters as cool-core (CC) and non-cool-core (NCC) if the the core entropy excess K_0 is respectively below or above $50\,\mathrm{keV\,cm^2}$. Hence, we will be able to compare how our simulated ICM compared to CC and NCC ACCEPTxMCXC clusters.

7: K_0 does not represents a minimum core entropy or the entropy at $r = 0$ but represents the typical excess of core entropy above the best-fitting power law at larger radii. The determination of the K_0 comes from a fit between the observed entropy profile and a simple model that is a power law at large radii and approaches a constant value at small radii :

$$K(r) = K_0 + K_{100}\left(\frac{r}{100\,\mathrm{kpc}}\right)^{\alpha} \quad (10.9)$$

with K_{100}, a normalization for entropy at 100 kpc, and α, the power-law index.

The highest redshift in the ACCEPTxMCXC sample is 0.54, while the range of clusters masses is $M_{500}/10^{14}\mathrm{M}_\odot = 0.12 - 13.18$ in addition to one massive cluster with $M_{500} = 2.21 \times 10^{15}\mathrm{M}_\odot$.
Thus, we chose to select only the simulation snapshots of our simulated cluster which have $z \leqslant 0.54$. We show in Figure 10.11 how our total cluster sample i.e. `VW`, `MW`, `MC` and `NR` simulations of all halos in the Rhapsody-G sample compare to the distribution of the ACCEPTxMCXC's.

We can see that our halos are more massive and rather lie at lower redshifts. Unfortunately, due to our storing strategy we could not sample the whole $z = 0 - 0.5$[8] redshift range, so our redshift distribution is more scattered than the ACCEPTxMCXC sample. The upper limit of 0.5 on cluster redshifts is also consistent with the above-mentioned studies.

8: In this range, we stored only snapshot with redshifts of 0.5, 0.25, 0.2, 0.15, 0.1, 0.075, 0.05, 0.025, 0.01, 0.005, 0.

The ACCEPTxMCXC sample has a mean (median) M_{500} mass of $4.1(4.0) \times 10^{14} M_\odot$ and values of 0.16(0.09) for mean (median) redshift. Our Rhapsody-G sample with $z \leqslant 0.5$ has respectively $6.2(6.0) \times 10^{14} M_\odot$ and 0.13(0.05) for mean(median) values on M_{500} and z. While our clusters are more massive than the ACCEPTxMCXC sample, we approach reasonably their redshift distribution.

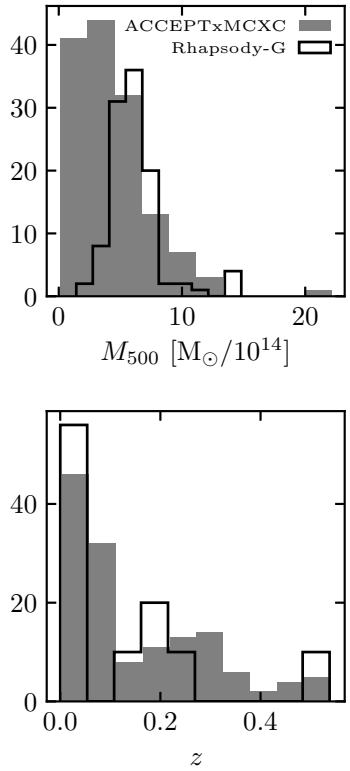

Figure 10.11: Mass (*top*) and redshift (*bottom*) distribution of the Rhapsody-G and matched ACCEPTxMCXC cluster samples.

We show in Figure 10.12, the comparison of the mean radial profiles presented in the previous section (without their 1σ ribbon) to the literature.
From the electronic number density shown in the *top left* panel of Figure 10.12 we can see that the simulations with a MW AGN model (`MW` and `MC`) show a factor $\sim 2-3$ denser core[9] than the CC fraction of the ACCEPTxMCXC sample. In the core, the `VW` simulations are consistent with the NCC ACCEPTxMCXC population within the 1σ scatter shown by the ribbon in transparency. The `VW` simulation approach the mean radial profile of McDonald *et al.* [96] while indicating for a flatter core electronic density. The non-radiative simulations shows the flattest core mean density profile being still consistent with the NCC ACCEPT clusters.
On the other hand, outside the core and especially at $r > 0.7R_{500}$, our simulations consistently indicate a steeper decrease of the density with radius compared to the mean profile of McDonald *et al.* [96]. Both CC and NCC ACCEPTxMCXC clusters show a denser ICM.

9: We remind that we define the core by the region encolse by $r \leqslant 0.15R_{500}$

In the *top right* panel, we can see the large scatter in the ACCEPTxMCXC pressure profiles. Both are consistent with our `VW` and `NR` simulations. The mean pressure profiles of Planck Collaboration *et al.* [392], Ghirardini *et al.* [70] and the MUSIC simulated clusters [393] agrees out to large cluster radii with our simulations. The `VW` and `NR` simulation show good agreement with these studies with a sightly higher core pressure. On the other hand, the `MW` and `MC` simulations show a factor 4 higher core pressure, but, meet at $r \geqslant 0.2R_{500}$ the `VW` and `MC` profiles.

In the ICM temperature profiles, we can see that both ACCEPTxMCXC clusters and Ghirardini *et al.* [70] shows large uncertainties. Both ACCEPTxMCXC CC and NCC clusters shows flat temperature profiles with high ICM temperature out to R_{500}, discrepant to

both our simulations and the mean profile of Ghirardini *et al.* [70]. However compared to Ghirardini *et al.* [70], we observe lower ICM temperatures in the outskirts too. But in the core region, our mean VW, NR and MW temperature profiles agree with the local clusters of Ghirardini *et al.* [70], with the latter showing however a steeper profile with a hotter inner core. On the other hand, the MC shows a factor 2 lower ICM temperature up to $0.5R_{500}$. Similarly to the density profiles, our simulations indicate for a steeper decrease of the ICM temperature with radius than Ghirardini *et al.* [70].

As a result, the steep temperature profiles indicated by our simulations also translate into steep increasing entropy profile in clusters outskirts. The slope is consistent to the simulations of Voit *et al.* [389] but is larger than the slope found in the REXCESS cluster sample [391] or by Ghirardini *et al.* [70]. The ACCEPTxMCXC entropy profile shows shallower slope with a higher normalisation (consistent with the found high ACCEPTxMCXC ICM temperatures). However, the VW simulation agrees well to the NCC ACCEPTxMCXC population within scatter while the MW simulations better match the CC cub-sample. The NR simulation is somehow in between but the MC shows low core entropy still compatible the CC ACCEPTxMCXC clusters.

Compared to the ACCEPTxMCXC sample, we see that our VW simulations reproduce the ICM of the NCC population while the MW and MC simulations approach the CC fraction. The study of Ghirardini *et al.* [70] is somehow in between the CC and NCC cluster population. They give outer slopes for the intra-cluster temperature, pressure and entropy in better agreement to our simulations.
Similarly to our new Rhapsody-G simulations, Hahn *et al.* [111] found lower temperatures and entropies outside the core compared to ACCEPTxMCXC which they attributed to a either missing physics or due to their higher baryon fraction ($f_b = 0.18$). In this new simulations, we updated the cosmological parameters to the Planck Collaboration *et al.* [241] (which provide a lower value of $f_b = 0.146$) but our ICM temperatures are still below the ACCEPTxMCXC ones. Indeed probing the ICM out the R_{500} is challenging in X-ray cluster astronomy, so we suspect that the ACCEPTxMCXC temperatures being somehow biased high as they are also at odds with the results of Ghirardini *et al.* [70] and their masses to be under-estimated.
By the analysis on the thermodynamic profiles shown in Figure 10.12, we see that the ICM of the MW and MC simulations suffer from overcooling in the core with high densities and low values of the temperature/entropy for $r \lesssim 0.2R_{500}$. Interestingly, the adiabatic

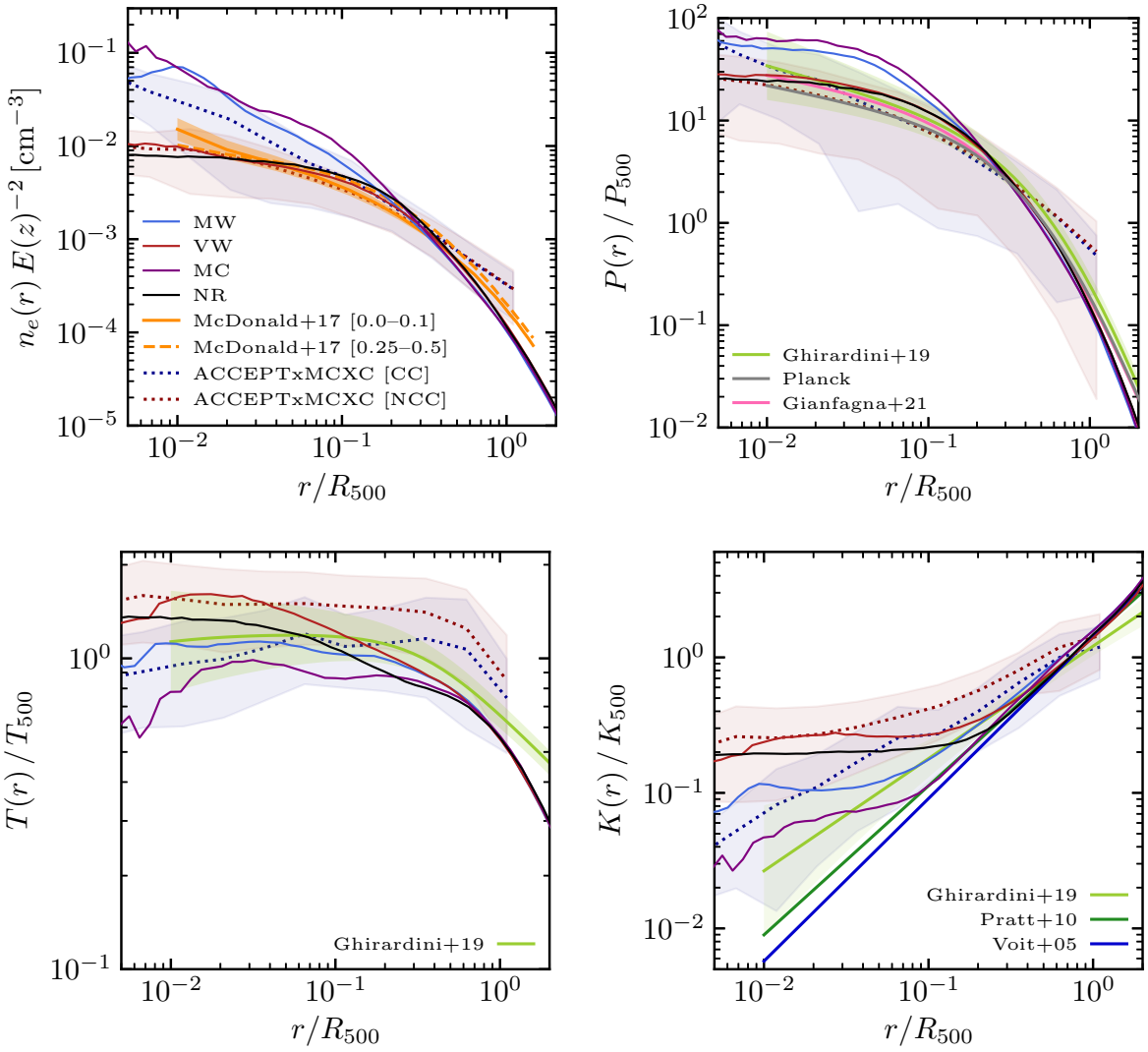

Figure 10.12: Scaled radial profiles of the electronic number density (*top left*), dimensionless pressure (*top right*), temperature (*bottom left*) and entropy (*bottom right*) of our `VW`, `MW`, `MC` and `NR` simulations (with $z \leqslant 0.5$) in comparison with the matched sample of ACCEPT [185] and MCXC [394] and the sample of McDonald *et al.* [96] (we give the redshift range of the mean profile in the brackets). We show the best fit thermodynamic profiles of Ghirardini *et al.* [70], the pressure profiles of Planck Collaboration *et al.* [392] and Gianfagna *et al.* [393] as well as the entropy outer slopes of Pratt *et al.* [391] and Voit *et al.* [389].

simulations (`NR`) are also found to be in agreement with the comparison studies. As being much less computationally expensive than their full-physics counterpart, they still provide insightful results on the ICM structure at our resolution.

We therefore see that reproducing a realistic ICM is a difficult task. Slight changes in the AGN feedback model can drastically change the structure of the simulated ICM and the cluster galaxies.

10.5 Summary

In this chapter, we extend the conclusions of the Chapter 9 on the impact of AGN energy deposition scheme or thermal conduction of the simulated ICM and cluster galaxies.

We found for the Rhapsody-G sample, that the VW and MW AGN energy injection models probe extremes of AGN activity. Indeed, the VW simulations show an AGN activity efficient to heat the ICM out to large radii which quench dramatically the star formation. As a result, the ICM of the VW simulations shows a hot ICM with high entropy and fewer cluster galaxy with too low masses. However, while the ICM can be compatible with observed NCC cluster, the galaxy population is unrealistic with too low masses.
Interestingly, the non-radiative simulations still provide a good approximation of the ICM of NCC clusters.

When, the AGN energy is deposited in dense regions, the feedback energy difficultly escape the accretion region. Consequently, the ICM cools rapidly which permits high star formation rates. As a result, the ICM of MW simulation shows a very dense core and lower ICM temperatures. Due to the inability of the MW AGN model to heat the ICM, star formation in the ICM is high and cluster galaxies are very massive at all redshifts.

Adding thermal conduction, does not help in preventing the ICM overcooling. However, it allows to reduce the galaxy masses by a factor of 2 due to the smoother ICM densities and temperatures at early times. Interestingly, thermal conduction acts in slowing the AGN activity compared to the MW simulations due to slower mass growth of the SMBHs. Thus, the ICM is even colder and denser than in the MW simulations. Counterintuitively, thermal conduction participates to the cooling of the ICM even more and seems to provoke some level of thermal instabilities. However, the star formation seems to be more realistic.

We see here, the complex interplay of the different physical models tested in this work. Reproducing both a realistic intra-cluster medium and a cluster galaxy population is an arduous task and requires a finer modelling of the ICM physics.
However, the different physical models tested here in our VW, MW and MC simulations probe extremes of the ICM structure and galaxy population and can provide insightful results which can put constraints on the ICM physics.

Scaling Relations 11

In this chapter we will explore the concept of the self-similar evolution of galaxy clusters. We will show the scaling relations resulting from our simulations and how do they compared to the theoretical expectations. We will discuss possible deviations from cluster self-similarity as well as their origin.

11.1 Self-similarity

Before we delve into the detailed results of cluster scaling relations, it is helpful to introduce the simplest model of galaxy cluster evolution based on the assumption of self-similarity. We need to discuss to some extent the assumptions behind the self-similar model to interpret the expected cluster scaling relations. These relations are crucial ingredients for cluster cosmology. Indeed observers heavily rely on these scalings to relate observed quantities to the cluster mass. Therefore it is if great importance to understand the underlying details of this theoretical model for using clusters as cosmological probes. We will show the expected parametric scalings that this model predicts.

11.1.1 Kaiser's model

Let us consider first what we should expect in the case of a simple model in which only gravity is important. This leads to a so-called self-similar model as shown by Kaiser [388].

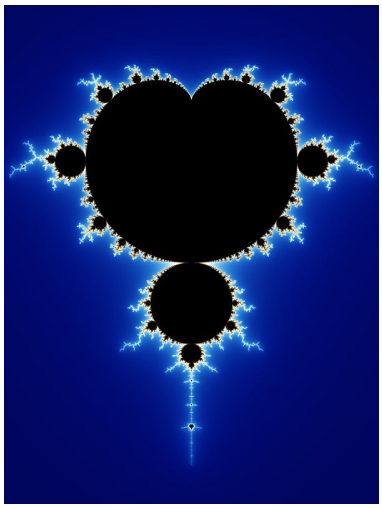

Figure 11.1: The self-similar Mandelbrot set. One of the best-known example of a complex structure arising from the application of simple rules.

In general, an object is self-similar when it is exactly or approximatively similar to a portion of itself [395]. Mathematically, self-similar functions are invariant under dilation such as :

$$f(x) = f(\alpha x), \tag{11.1}$$

Scaling the argument by a constant factor α only causes a proportionate scaling of the function itself.
Power laws are typical self-similar functions :

$$f(\alpha x) = (\alpha x)^n = \alpha^n x^n \propto f(x). \tag{11.2}$$

In nature, we mostly encounter statistical self-similarity, where

only statistical quantities are the same for an object and its rescaled version.

Following Kaiser [388], we start by considering the case of an Einstein-de Sitter Universe (closure density, $\Omega_m = 1$). The initial fluctuation density spectrum, $P(k)$, follows a power law over some range of wave-number k such as :

$$P(k) \propto k^n, \tag{11.3}$$

The mass variance of the fluctuations, σ^2, then scales as :[1]

$$\sigma^2(k) \sim k^3 P(k) \propto k^{n+3} \propto r^{-(n+3)} \propto M^{-(n+3)/3}, \tag{11.4}$$

As the result, the amplitude of the fluctuations (σ) is a power law in mass M or scale r. These self-similar fluctuations grow in time as :

$$\sigma(M, t) \propto a(t)\, M^{-(n+3)/6}, \tag{11.5}$$

The perturbation becomes non-linear when $\sigma = 1$, from which we obtain a scaling of the non-linear mass, M_{NL}, given by :

$$M_{NL} \propto a^{6/(n+3)}. \tag{11.6}$$

As the result, this scale (marking the transition from the linear to the non-linear regime) will be the only scale of all statistical quantities of the evolved non-linear fluctuation field.[2]
This means that this non-linear mass encapsulates the dependance on the normalisation and shape of the power spectrum.
In such a model, halo properties and abundance become universal functions of the ratio M/M_{NL}.[3] Hence, for example, two clusters at two different redshifts z_1 and z_2 with respective masses of $M_1(z_1)$ and $M_2(z_2)$ that correspond to the same ratio $M_1(z_1)/M_{NL}(z_1) = M_2(z_2)/M_{NL}(z_2)$, will have the same dimensionless properties (e.g. concentration or gas fractions) or abundance under the assumption of self-similarity.[4]

In a way, the universe is self-similar if it starts from a power law power spectrum. But as discussed by Kaiser [388], this is not expected at all scales but remains a good approximation on galaxy cluster and group scales.

We will now sum up the assumptions and the induced control parameters of the self-similar model developed by Kaiser [388] :

- *Assumption 1* : Clusters forms via gravitational collapse from the initial density peaks in an Einstein-de Sitter Universe.[5]
- *Assumption 2* : The amplitude of the density fluctuations is a

1: We have the proportionalities $k \propto r^{-1}$ and $M \propto r^3$ between the mass M and a physical scale r and the wave number k.

2: i.e. the halo number density of a given mass at a given time

3: The only dependence of the ratio M/M_{NL} is on $a(t)$ which is, in fact, a power law of time i.e. $a \propto t^{2/3}$.

4: Halo statistical properties are generally expressed as a function of a density contrast $\Delta(r, t)$ at a given time t and (comoving) scale r .

5: In such Universe, the gravitational collapse is scale-free or self-similar.

power law of their size, $\sigma^2(k) \propto k^{n+3}$.

- *Assumption 3* : Physical processes shaping cluster properties do not introduce new scales.

- *Parameter 1* : The normalisation of the power spectrum of initial density perturbations at an initial time.[6]
- *Parameter 2* : The slope of this power spectrum.

6: The defined characteristic non-linear mass encapsulates the dependance of these two parameters.

Galaxy clusters are dominated by collisionless dark matter and gravity is the only force that these particles experience. Gas in galaxy clusters can also be considered as weakly collisional because the ion Larmor radius is much smaller than the mean free path (as we saw in Chapter 7). It was shown in early numerical simulations [396] that the self-similarity also holds when gravity and shock heating are included. Hence, when disspative, non-gravitational effects are neglected, cluster dimensionless properties can be expected to be roughly self-similar in time and that $M_{\mathrm{gas},\Delta} \propto M_{\mathrm{DM},\Delta}$.

A consequence of Equation 11.4 is that the variance is the largest on small scales i.e. the amplitude of small scale fluctuation is the largest. These scales reach the non-linear mass faster which causes them to collapse. This is the "bottom-up" scenario of hierarchical structure formation in which small structures forms first and provide the building blocks for the larger ones. Hence, these small structures are expected to be scaled-down version of the bigger ones.

In this convenient framework, simple relations can be predicted as two halos that have formed at the same epoch must have the same mean density, yielding :

$$\frac{M_{\Delta_z}}{R^3_{\Delta_z}} = \text{constant}, \tag{11.7}$$

Where the mass M_{Δ_z} of within a sphere of radius $R^3_{\Delta_z}$ encompassing the density contrast Δ at redshift z :[7]

7: Δ is commonly expressed with respect to the critical density at the cluster's redshift

$$M_{\Delta_z} = \frac{4\pi}{3}\,\Delta\,\rho_{\mathrm{crit},z}\,R^3_{\Delta_z} = \frac{4\pi}{3}\,\Delta\,\rho_{\mathrm{crit},0}\,E_z^2 R^3_{\Delta_z}, \tag{11.8}$$

Where we used :

$$\rho_{\mathrm{crit},z} = \frac{3H_z^2}{8\pi G} = \rho_{\mathrm{crit},0}\frac{H_z^2}{H_0^2} = \rho_{\mathrm{crit},0}\,E_z^2. \tag{11.9}$$

with E_z is the expansion function that describes the evolution of the Hubble parameter with redshift.[8]

8: $E_z = E(z) = H(z)/H_0$

Assuming that the cluster gas is an ideal fluid[9] in a gravitational potential ϕ, we have the following Euler equation :

$$\frac{\partial \boldsymbol{v}}{\partial t} + (\boldsymbol{v} \cdot \nabla)\, \boldsymbol{v} = -\frac{1}{\rho_{\rm gas}} \nabla P_{\rm gas} - \nabla \phi, \tag{11.10}$$

If we assume the gas to have a spherical distribution and setting the velocity to zero, it yields the ICM hydrostatic equilibrium (HSE) equation:

$$\frac{1}{\rho}\frac{{\rm d}P_{\rm gas}}{{\rm d}r} = \frac{{\rm d}\phi}{{\rm d}r} = -\frac{{\rm G}M_{\rm tot}}{r^2}, \tag{11.11}$$

where G is the gravitational constant. Using the previous hydrostatic equation and the following perfect gas law :[10]

$$P_{\rm gas} = n_{\rm gas} {\rm k_B} T_{\rm gas} = \frac{\rho_{\rm gas} {\rm k_B} T_{\rm gas}}{\mu m_{\rm u}}, \tag{11.12}$$

we can rewrite the total cluster mass within R_Δ as :

$$M_{\Delta_z} = -\frac{{\rm k_B} T_{\rm gas}(R_{\Delta_z}) R_{\Delta_z}}{\mu m_{\rm u} {\rm G}} \left(\frac{\partial \log T_{\rm gas}(r)}{\partial \log r} + \frac{\partial \log n_{\rm gas}(r)}{\partial \log r} \right)\Bigg|_{r=R_{\Delta_z}} \tag{11.13}$$

Hence, we have a proportionality between the mass enclosed in R_{Δ_z} with $T(R_{\Delta_z}) \times R_{\Delta_z}$ and the sum of the logarithmic slopes of the gas temperature and gas density profiles at R_{Δ_z}.
A key assumption in Kaiser's model is that these slopes are independent of M [9], hence :

$$T_{{\rm gas},\Delta_z} \propto \frac{M_{\Delta_z}}{R_{\Delta_z}} \tag{11.14}$$

which combined with Equation 11.8[11] allows us to write the first expected scaling relation between mass and temperature :

$$T_{{\rm gas},\Delta_z} \propto M_{\Delta_z}^{2/3}\, E_z^{-2/3}. \tag{11.15}$$

Using this first proportionality, we can construct other cluster properties that scales with mass. Let us start with the ICM luminosity emitted due to radiative cooling. In massive system, the ICM is shock heated to temperatures of $10^7 - 10^8$ K that radiates due to thermal Bremsstrahlung. Its total emissivity[12] ϵ can be written as (c.f. Section 3.1.2) :

$$\epsilon \propto n_{\rm e} n_{\rm ion} T_{\rm e} \propto \rho_{\rm gas}^2 T_{\rm gas}^{1/2}, \tag{11.16}$$

where we implicitly assume thermal equilibrium i.e. electrons and ions sharing the same temperature. Another key assumption in Kaiser's model is the proportionality between the $M_{\rm gas}(< R_{\Delta_z})$ and $M_{\rm tot}(< R_{\Delta_z})$ (i.e. a constant gas fraction $f_{\rm gas}$, defined as the ratio of the two previous masses). It allows us to relate the X-ray

9: i.e. a fluid in which thermal conductivity and viscosity do not play a relevant role

10: where $m_{\rm u}$ is the atomic mass unit (a.m.u.) and μ, the mean molecular weight in a.m.u. which is equal to $\mu = (2X + 3/4Y + 1/2Z)^{-1} \sim 0.594$ with X, Y and Z being respectively the mass fraction in Hydrogen, Helium and heavier elements.

11: i.e. $R_{\Delta_z} \propto M_{\Delta_z}^{1/3} E_z^{-2/3}$

12: luminosity per unit volume

luminosity to the gas temperature :

$$L_{X,\Delta_z} \sim \epsilon R^3_{\Delta_z} \sim \rho^2_{\rm gas} T^{1/2}_{{\rm gas},\Delta_z} R^3_{\Delta_z}, \tag{11.17}$$

$$\propto f^2_{\rm gas} T^{1/2}_{{\rm gas},\Delta_z} R^3_{\Delta_z}, \tag{11.18}$$

$$\propto M_{\Delta_z} R^{-3}_{\Delta_z} T^{1/2}_{{\rm gas},\Delta_z}, \tag{11.19}$$

By means of Equation 11.14 and Equation 11.8, we get the X-ray luminosity scaling with cluster mass or temperature :

$$L_{X,\Delta_z} \propto M^{4/3}_{\Delta_z} E_z^{7/3}, \tag{11.20}$$

$$\propto T^2_{{\rm gas},\Delta_z} E_z. \tag{11.21}$$

We derived here the most common X-ray scaling relations. We can also obtain the Sunyaev-Zel'dovich scaling relation of the integrated Comptonization parameter with mass, where we have :[13]

$$Y_{{\rm SZ},\Delta_z} \propto T_{\rm e} \int n_{\rm e} {\rm d}V \propto T_{\rm e} M_{\rm gas} \propto T^{1/2}_{{\rm gas},\Delta_z} M_{\Delta_z}, \tag{11.22}$$

13: see Section 3.1.3

Where again we assume thermal equilibrium and a constant gas fraction. Using Equation 11.14, we finally get :

$$Y_{{\rm SZ},\Delta_z} \propto M^{5/3}_{\Delta_z} E_z^{2/3} \propto Y_{{\rm X},\Delta_z}. \tag{11.23}$$

Indeed, we have the similar equation for the X-ray analogue, $Y_{{\rm X},\Delta_z}$, which is the product of the X-ray temperature and the gas mass. [14]

14: The proxy $Y_X = M_{\rm gas} T_X$ was first introduced by Kravtsov *et al.* [397] and was found to be a low scatter mass indicator.

From the combination of the basic scaling relations derived in this section, many other possible scaling relations can be derived. We have to keep in mind that these scaling relations were derived under additional assumptions :

- *Assumption 4* : Dimensionless cluster gas temperature and density profiles (i.e. absence of scaling with cluster mass).
- *Assumption 5* : The ICM is in thermal equilibrium.
- *Assumption 6* : Pure Bremsstrahlung emission
- *Assumption 7* : A constant gas fraction

These assumptions may not hold exactly and possible deviations may arise due to physical processes that violate self-similarity.[15] Indeed, galaxy clusters sit at a unique place where their dynamics induced by the gravitational collapse also interacts with the complex baryonic processes associated with galaxy formation and physical processes within the ICM. These very energetic phenomena should violate the simplified assumptions of the self-similar model and should participate to the offset from the self-similar scaling relations.

15: Extensions to the Kaiser model were derived in Borgani & Kravtsov [9] where extra evolutions are considered.

11.1.2 Deviations from self-similarity

Galaxy clusters are not isolated entities but located at the nodes of a complex filamentary cosmic web. The distribution and orientation of these filaments should introduce a non-zero level of triviality which may violate the assumption of spherical symmetry. The connectivity[16] of a given halo was predicted to scale with halo mass [398] and to increase its ellipticity [399]. A recent study by Malavasi *et al.* [400] on the densely connected network of the Coma cluster has shown a connectivity of 2-3 coinciding with the location of significant accretion. The presence of these filaments should introduces a preferred direction for matter infall.

16: The number of filaments connected to a halo

Moreover, the continuous accretion of gas drives some level of turbulence into the cluster and mergers or infalling galaxies stir the ICM. In addition, supersonic and superalfvenic gas motions accompanying cluster formation (especially in major mergers) produce shock waves with a wide range of strengths. This kinetic energy will be dissipated into the ICM and, as we saw in Section 7.1.4, will contribute to the amplification of magnetic fields and to the acceleration of particles. Such cosmic rays are expected to contribute non-negligibly to the energy budget of galaxy clusters.

Last but not least, processes related to galaxy formation break the self-similarity of the ICM by introducing new scales. Radiative gas cooling selectively removes low entropy gas from the hot X-ray emitting phase making room for higher entropy gas from larger radii to fall in. Counterintuitively, the cooling leads to an increased entropy of the hot X-ray emitting ICM and acts as a non-gravitational heating source.
This also leads to a large amount of gas that will be turned into stars. Hence, more non-gravitational heating is required to balance cooling losses and regulate star formation. Such heating processes as SN and AGN feedback inject thermal and kinetic energy into the ICM. Besides an efficient gas heating, it also leads to an increased amount of gas motions and participate to the acceleration of particles. These non-gravitational processes linked to galaxy formation evolve with redshift. Therefore, it may lead to a non-constant and/or redshift-dependent halo gas fraction hence contradicting the seventh assumption in the above Section 11.1.1.

We see that galaxy clusters are a place where complex processes are at play. In this respect, thermal and dynamical equilibria may not be fulfilled as residual gas motions can exist as well as dissipative non-thermal processes.
Each phenomenon should offset cluster properties from their self-

similar prediction with a possible dependence with halo mass or redshift. Therefore, it is of paramount importance to understand the exact amount of uncertainties, bias or scatter these processes induce.

We see that, more generally, these scaling relations are not simply a tool for cosmology but could provide precious diagnostics on the thermodynamic history of the ICM.

Given that galaxy clusters constitute highly non-linear collapsed systems, numerical simulations appear as the method of choice for their theoretical study. Indeed, in such closed laboratory, it is possible to study the relative importance of each process at shaping the ICM properties by comparing observational and cosmological results.

We aim in the following sections to understand how exactly all the physical processes studied in the previous chapters of this thesis contribute to deviations from the expected cluster scaling relations.

11.2 Cluster observables

We will start by describing the methodology of the measurement of cluster observables used in the scaling relations from our simulations.
We recall that the physical processes behind cluster observables were discussed in Section 3.1.

11.2.1 X-ray temperature

11.2.1.1 Methodology

From the simulation, we can estimate an "X-ray" ICM temperature by taking the gas temperature average for X-ray emitting cells. We need to exclude for this analysis the cold gas cells with temperature below 0.5 keV as they do not participate to the X-ray emission[17] .
We perform the following weighted average on the temperature T_i of all the gas cells i within the region of interest (e.g. a sphere of radius R_{500} or R_{200}) :

$$T_w = \frac{\sum_i w_i T_i}{\sum_i w_i}, \tag{11.24}$$

A volume averaged temperature, $T_{\rm vw}$, is given by setting the weights to the volume of gas cells : $w_i = \mathrm{d}V_i$ where $\mathrm{d}V_i$ is the AMR cell

17: We recall that the ICM X-ray emission is due to thermal Bremsstrahlung which is dominant at temperature above $0.5\,\mathrm{keV} \sim 6 \times 10^6\,\mathrm{K}$

volume determined by the local resolution of the simulation. In our case, it corresponds to $\sim 6.8\,h^{-1}\mathrm{kpc}^3$ in the finest resolution (and $\sim 54\,h^{-1}\mathrm{kpc}^3$ for the second finest).
Another common option is to weight by the mass of gas enclosed in this cell i.e. $w_i = \rho_i \mathrm{d}V_i$. This mass-weighted temperature,T_{mw}, emphasizes dense regions that participate more to the X-ray emission and gives a more "physical" average.
The emission-weighted (EMW) temperature will accentuate even more the X-ray emitting gas by weighting the temperature by its emissivity being $\epsilon \propto \rho^2 \Lambda(T)$ where Λ is the temperature dependant optically thin cooling function.
Because Bremsstrahlung emission[18] is the dominant process, we can approximate $\Lambda(T) \sim \sqrt{T}$. It yields $w_i = \rho_i^2 \sqrt{T_i} \mathrm{d}V_i$ for the emission-weighted temperature, T_{ew}.
However, this weighting emphasizes the dense and hot gas while X-ray observations are rather sensitive to *cold* dense gas. Indeed, the Bremsstrahlung emissivity depends quadratically on the gas density.
Mazzotta *et al.* [240] have studied the impact of such weighting methods and shown that the emission-weighted temperature overestimates the spectroscopic temperature. This discrepancy is due to the thermal inhomogeneity of the observed multitemperature source which is not accounted for in observations (single temperature fit). They proposed to choose $w = n^2 T^{-3/4}$ in Equation 11.24 to better approximates the observed X-ray temperatures. This weighting, beside being biased toward the densest regions of the clusters (as the EMW), will also be biased toward the coolest regions. They showed that this temperature weighting approximates the spectroscopic to a level better than 10 percent.

18: The formula for the Bremsstrahlung emissivity gas given in Equation 3.7

To circumvent the shortcomings of simple weighting schemes, we instead seek to produce an X-ray spectrum from which estimation of the temperature and density can be performed as close as possible to the observers' methodology.

To compute the ICM thermal emission for a gas cell, we use the AtomDB atomic database [19] . It is designed for the spectral modeling of X-ray collisional plasma, where hot electrons colliding with astrophysically abundant[20] elements and ions create X-ray emission. It includes the Astrophysical Plasma Emission Database (APED) and the spectral models output from the Astrophysical Plasma Emission Code (APEC).
APEC produces separately line and continuum emissivity tables from the APED atomic data by computing the interplay between the different rates (such as atomic radiative transition rates and collisional excitation rates) and energies of the ions involved.

19: http://atomdb.org/

20: such as those of Anders & Grevesse [401]

To model the ICM X-ray spectra, we read the temperature of each gas cell and compute its continuum and line emission.[21] We compute the APEC spectra for gas cells having $T \geq 0.05\,\mathrm{keV}$ at a given metallicity Z. Therefore, we have the continuum and line emissivity $\epsilon(T, Z)$ in each spectral bin from which we can compute the emitted photon rate :[22]

$$\phi = \epsilon(T_e, Z) \int n_e n_H dV, \quad [\mathrm{ph\,s^{-1}}] \tag{11.25}$$

where the integral over $n_e n_H dV$ is the emission measure in cm^{-3}. In this way, we produce a mock X-ray spectrum by summing the individual rest frame spectra of each gas cell that falls in the desired radial range.
In order to compared with observational results, we chose to produce spectra inside the sphere enclosing 500 times the critical density, ie. only up to R_{500} without including the core, i.e. in the range :

$$0.15 \leq r/R_{500} \leq 1.0, \tag{11.26}$$

Indeed, X-ray observations typically resolve the ICM up to $\sim R_{500}$, while the core exclusion is to avoid being biased by any AGN activity happening in the cluster centre or any cooling flow. A resulting spectrum measured from our simulations is shown in Figure 11.2[23]

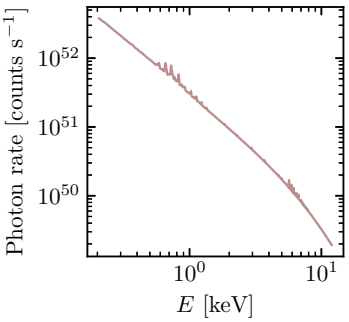

Figure 11.2: Typical ICM photon emission rate computed from the the simulation in the core-excised R_{500} sphere.

21: We use APEC equilibrium line and continuum fits files from the 3.0.9 version of AtomDB.

22: We omit any dependence with redshift or column density

23: For a more detailed analysis, we could also convolve the obtained spectra by Chandra or XMM-Newton response functions.

We chose to simulate spectra at a lower resolution for computational reasons (at level $l = 15$ where gas cells have minimal size of $\sim 30\,\mathrm{kpc}$). We carefully checked that the obtained spectra are about the same as the ones obtained at highest resolution level (at $l = 19$ for a minimal size of $\sim 2\,\mathrm{kpc}$).

To obtain the temperature and density of the observed ICM from X-ray observations, the most common method is to fit the observed spectra by a single temperature APEC model. Here we follow a similar methodology and chose to perform fits using a Monte Carlo Markov Chain (MCMC) sampling method.

We use the `emcee`[24] python library that has already been used successfully in many published research works in astrophysics. The `PyAtomDB`[25] python library is used to model a single temperature spectra using only two parameters : the temperature and the metallicity.
Then, we translate into a global photon rate emission by multiplying such a spectrum with the global emission measure of the gas inclosed in the core-excised R_{500} sphere. This step adds a third

24: Foreman-Mackey *et al.* [402]

25: Since 2015, PyAtomDB is develloped to replace the APEC code for a more flexible python interface. https://atomdb.readthedocs.io

parameter : the mean gas density.

As a result, we have three parameters to fit based on minimising a likelihood function. Using `emcee`, we sample the parameter space assuming a flat prior distribution in, respectively, the $1 - 16$ keV range for the temperature, the $10^{-30} - 10^{-22}\,\mathrm{g\,cm^{-3}}$ range for the mean gas density and the $0.001 - 0.5\,\mathrm{Z_\odot}$ range for the metallicity.

To illustrate our fitting procedure, we will start by showing a difficult fit with the ICM spectrum shown in grey in Figure 11.3.

The ICM emission is dominated by thermal Bremsstrahlung which is proportional to the density squared and depends only slightly on the gas temperature ($\propto \sqrt{T}$). As we want to fit such emission, the MCMC converges faster towards the gas density that the temperature.
In the case shown in Figure 11.3, we see a ICM spectrum with a high fraction of cold gas. This low energy bump in the spectrum can bias the MCMC solution to a high density value to minimise the likelihood function.
Consequently the temperature, which converge at a lower rate (see Figure 11.4 for the time series), will tend to be underestimated (i.e. a steeper cutoff, see later) to compensate for the overestimation of the gas density.
Therefore, the MCMC sampling could converge to a non-optimum set of gas density, temperature, metallicity.

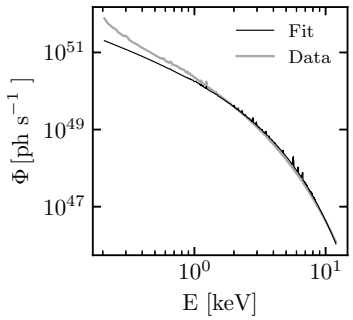

Figure 11.3: Result of the fit for `Halo 361`. The presence of the bump at low energies (caused by the high fraction of cold gas) could induce the fit to converge to high values of the density (i.e. spectrum normalisation). In order to maximize the likelihood, the MCMC chain will later try converging to lower temperatures (i.e. steeper cutoff) to compensate for the overestimated density.

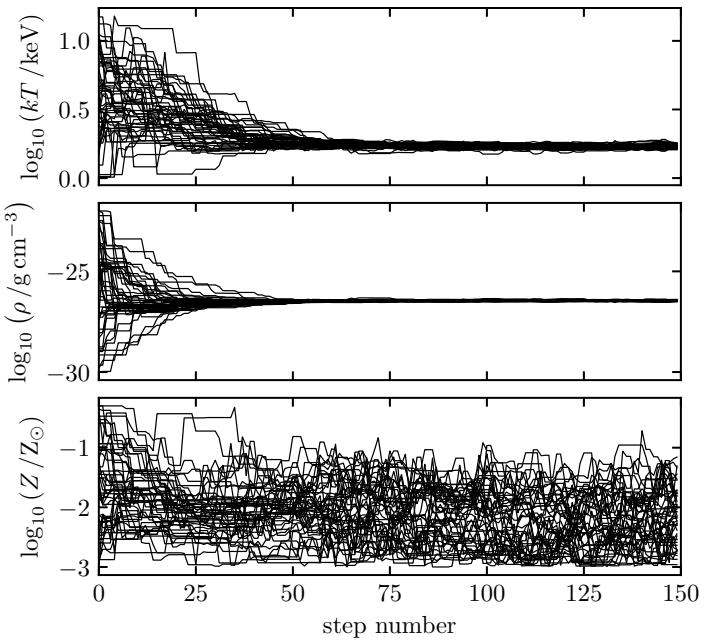

Figure 11.4: Time series of the MCMCs for the three fitted parameters.

To infer robust constrains, we chose to split the fitting procedure in two steps.

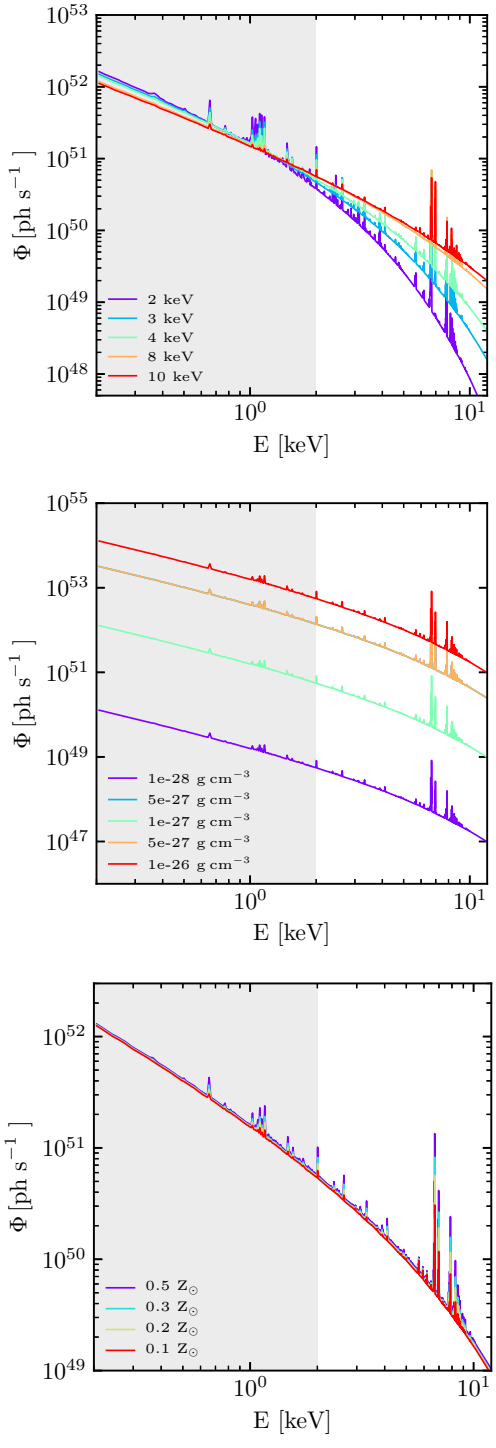

Figure 11.5: From left to right, we test in the top, middle and bottom panels the dependance of the APEC spectra with, respectively, the temperature, density and metallicity. Grey shaded region highlights the energy band on which the first step of the MCMC fit is performed. We see that the temperature has a bigger impact outside this $0.2 - 2\,\mathrm{keV}$ band while the density clearly affect the overall normalisation. Changing the metallicity has an impact on the metal line emission but not significantly affect the continuum emission. When unchanged, fiducial parameters are $T = 6\,\mathrm{keV}$, $\rho = 10^{-27}\,\mathrm{g\,cm^{-3}}$ and $Z = 0.3 Z_\odot$.

Using `PyAtomDB`, we study the behavior of an ICM spectra to gas density, temperature or metallicity changes.
As one can see in Figure 11.5, the X-ray flux is not very sensitive on the plasma temperature and metallicity in the $0.20 - 2.00$ keV band (show by the shaded region). We can see that the normalisation is

mainly set by the density.
Hence to prevent an erroneous (overestimation) of the gas density as before, we chose to only fit the mean gas density in this $0.20 - 2.00$ keV band first. The gas temperature and metallicity are set to average ICM values of 5 keV and $0.3 Z_{\odot}$.

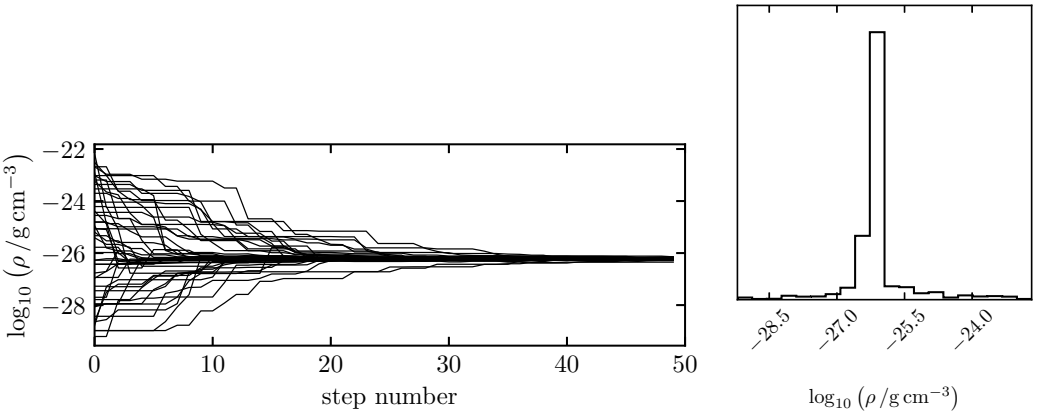

Figure 11.6: *Left*: Time series of the MCMC for the density fitting in the first step. *Right*: Posterior distribution of the density. This distribution will be used as a prior in the next MCMC (instead of a uniform prior).

The resulting MCMC chain, shown in the left panel of Figure 11.6, quickly converges to a first good approximation for the density. Purposely, we chose to run the MCMCs on a small number of steps, to get a posterior distribution with a relatively wide standard deviation. We will use now this posterior distribution of the MCMC chain of the density as the prior distribution for the second MCMC chain (instead of previously assumed flat priors). Hence, we will still be able to sample a broad range of density values in the next MCMC while privileging a density value close to the correct one.

In the second step, we now fit all parameters simultaneously. We use flat priors for the metallicity and temperature, but, priors on the density are set by the previously found posterior distribution (shown in the left panel of Figure 11.6).
We plot in Figure 11.7, the time series of the parameters in the chains for the three parameters. Posterior probability distributions of the parameters can be found in Figure 11.8 along the covariances between parameters.

The resulting best fit solution which was shown in black in Figure 11.4 is shown to be in good agreement with the simulation data on a wide range of energies.
However, the low energy bump cannot be constrained with a single temperature model and a double (or multi) temperature model would be more suited. However, to be consistent with the observers'

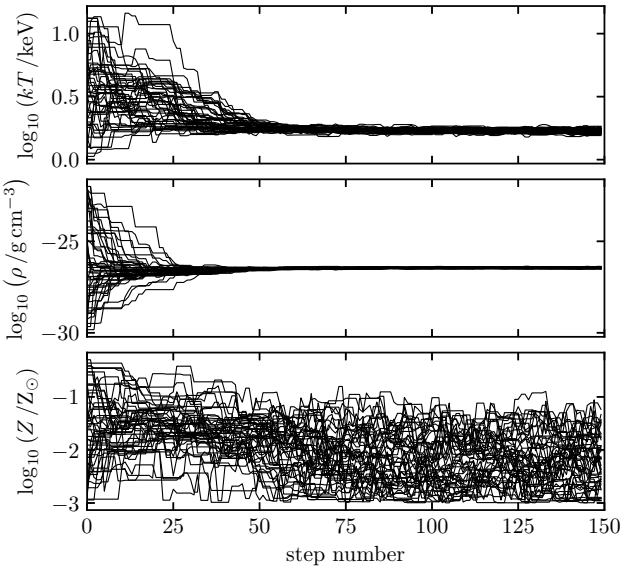

Figure 11.7: Time series of the MCMCs for the three simultaneouly fitted parameters.

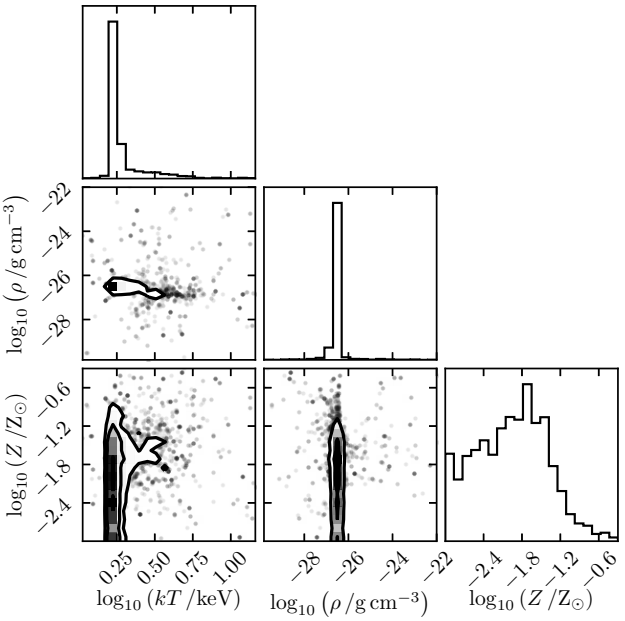

Figure 11.8: Posteriors distributions and covariances between fitted parameters.

methodology we derive the ICM temperature by using a single temperature model.
With the two-step MCMC procedure, we overcome the issue of overestimated densities which is crucial to not underestimate the ICM X-ray temperature.

11.2.1.2 Results

We show in Figure 11.9, the value of the χ^2 statistics for all halos in the different set of simulations `MW`, `VW`, `MC` and `NR` as a function of redshift (We gave in Chapter 10 the meaning of each simulation acronyms, but see also in the beginning of Section 11.3 for a

short summary). The χ^2 statistic is computed between the derived spectrum from the simulation and the fitted APEC spectrum model by the two-step MCMC procedure as :

$$\chi^2 = \sum_i \frac{[\Phi_{\rm APEC}(E_i) - \Phi(E_i)]^2}{\Phi(E_i)} \tag{11.27}$$

We can see in Figure 11.9 that the VW spectra yield best fit compared to the other ones with systematically lower χ^2 statistics. We can see systematic differences between the different feedback models. This is because, the VW AGN feedback model is the most effective at heating the cluster ICM and thus producing a flatter ICM spectrum. A flatter spectrum is easier to fit and the degeneracy between the temperature and density parameters decreases.

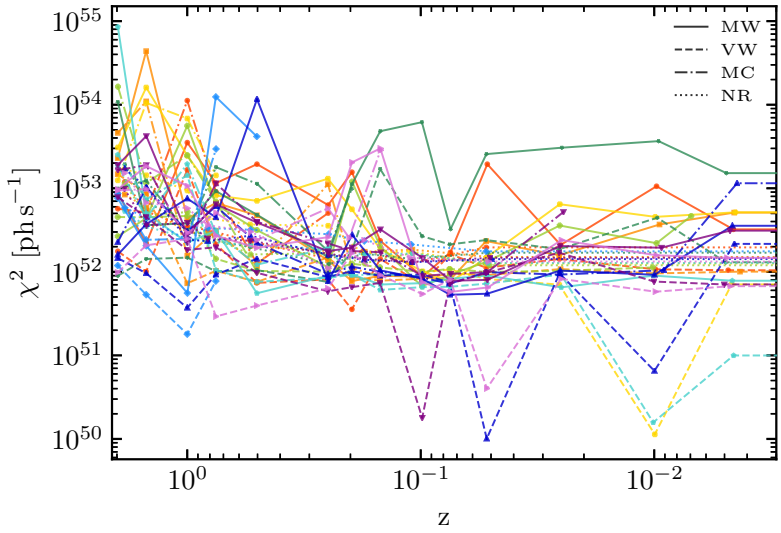

Figure 11.9: The χ^2 statistic for all our halos (color coded) in each simulation set : solid lines for the MW simulations, dashed lines for the VW one, dash-dotted lines for MC and finally dotted lines for the NR simulations. We can see at $z \lessapprox 0.7$ that our fits converge relatively low χ^2 values. On the other hand we can see that at $z \gtrapprox 1$, fits for the MW and MC perform poorly. We attribute to the presence of relatively high amount of dense cold gas in these simulations.

Indeed, the MW runs are the ones showing an excess of emission at low energy and a steep cutoff induced by the larger fraction of dense cold gas present in these simulations. This type of spectrum (low energy bump + steep cutoff) is typically more difficult to fit as the mean density converges to high value (caused by the dense cold component). The temperature can converges to a lower value, i.e. a steeper cutoff, to compensate for the constrained high spectrum normalisation. We observe the same behavior for the MC simulations that show also a fair amount of ICM overcooling.[26]
MCMC fits for the NR are consistent over a large redshift range ($z \lessapprox 1$) and provides relatively robust constraints.

Of course, there are simpler ways to measure a temperature from the simulation. As we explained earlier, we can measure the average ICM temperature using different weighting schemes.
Despite being straightforward, these averaged temperatures do not quite reflect what observers measure as we explained in Section

26: Unfortunately, from the lower number of MC snapshot that we have, we cannot strictly confirm the goodness of the fit for $z \lesssim 0.25$

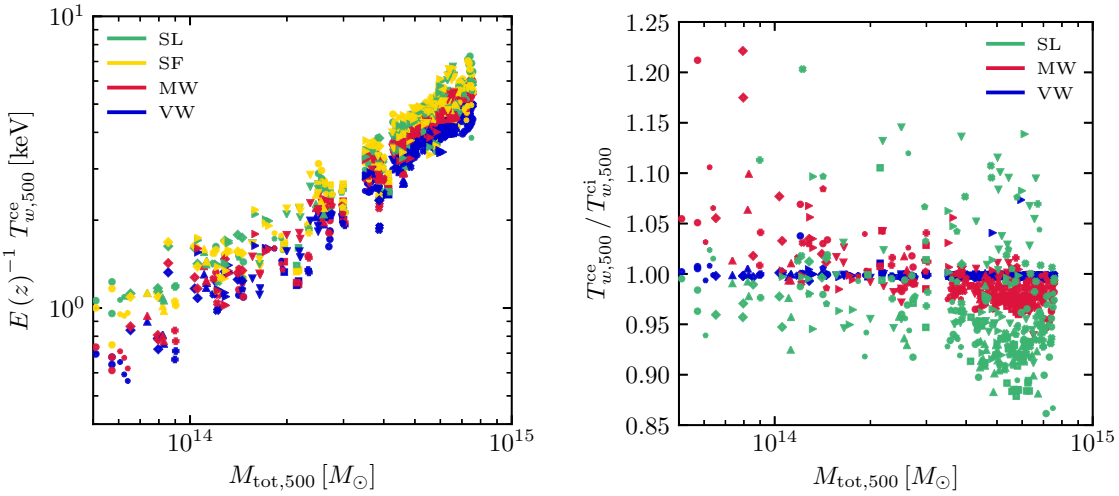

Figure 11.10: *Left :* Different ICM temperature estimates as a function of the total halo mass for all our full-physics simulated halos. We plot the spectroscopic-like (SL) temperature of Mazzotta *et al.* [240] in green, temperatures estimated via the spectrum fitting (SF) and finally the mass- and volume-weighted (MW and VW) temperatures respectively in red and blue. We can see here for example the difference of almost a factor 2 between the mass-weighted and spectroscopic like temperature commonly used to measure ICM temperatures in simulations. On average, our SF temperatures are in good agreement with the SL temperatures. *Right :* Ratio of the core-excluded to the core-included temperature within R_{500}. We can see that halo masses lower than $2-3\times10^{14}\,\mathrm{M}_\odot$, the exclusion of the core tend to increase the MW temperature. On the other hand, for $M_{500}\gtrsim 3\times10^{14}\,\mathrm{M}_\odot$ the MW temperature is few percent lower when the core is excluded. While showing a big scatter, the core-excluded SL temperature are on average up to 10% lower for the highest masses. But we see that this SL weighting scheme shows the largest positive and negative fluctuations (with respect to unity). The VW temperatures are widely insensitive to the core inclusion/exclusion because the volume inside $0.15\,R_{500}$ represents only a tiny fraction of the total R_{500} sphere. See discussion in the text for outliers and trends.

11.2.1.1. In order to quantify the difference between all these different methods, we plot in the left panel of Figure 11.10 the various temperature estimates as the function of the total halo mass for all our halos.
We see that, for our sample, the volume-weighted (VW) temperature is consistently the lowest, and the spectroscopic-like (SL) temperatures of Mazzotta *et al.* [240] fairly well approximates the temperature resulting from our spectral fit (SF). We observe that the flattening in the slope of the SL and SF temperatures at lower halo masses. Hence, at lower mass halo, the SL and SF temperatures most differ from the simple mass-weighted (MW) or VW estimates. The MW temperature seems in between spectroscopic temperatures and the low VW one with a the largest scatter.

We see that the metallicity is not constrained as metal lines participate very little in the total emissivity. However, it does significantly affect the temperature estimation which is what really matters here. We do not use the metallicity found values in our analysis.

11.2.1.3 Core exclusion

As some works in the literature use core-included X-ray temperature, we would like to know how much scatter the presence of the core induces. As the computation of the SF temperature is expensive, we will focus on the other three computations. We show in the right panel of Figure 11.10 the ratio of the core-excluded to core-included temperature as a function of the cluster total mass.

As the core represent only 0.3% of the considered volume (a sphere of radius R_{500}), the volume weighted temperature is not sensitive to what is happening in the core. On the other hand, the core contributes $\sim 10\%$ to M_{500}.
Hence we see that the of the core-excluded to core-included volume-weighted temperatures is roughly constant to 1.[27] .
The behavior for the MW temperature is different where the ratio of the core-excluded to core-included temperature is a decreasing function of the halo mass. The equivalence of the two is roughly at $M_{500} \sim 2 - 3 \times 10^{14} \mathrm{M}_{\odot}$. On average, below this mass the MW core-excluded temperature is greater than the core-included one and the opposite trend is observed above this mass.
We can explain this because in this lower range, halos host in their core a reservoir of cold and dense gas that fuels AGN activity. The presence of this cold gas in the core biases the MW core-included temperature to lower values than the core-excluded counterpart. At higher masses, the whole ICM is cooling and especially in the outskirts because the AGN heating is inefficient at large radii and cold gas accretion persists. Hence the relative amount of cold gas is greater in the core excised region than the core-included one.

27: We note however that some snapshots show a very high AGN activity in the core that can considerably boost the VW temperature. We can see this in the blue outliers in the left panel of Figure 11.10 at $M_{500} \sim 10^{14}\,\mathrm{M}_{\odot}$

Studying in details the difference in the weighting schemes can be useful to understand and compare with the different published results. Indeed, as will will see in Section 11.3.3, authors can use different temperature estimates for their simulations. It is therefore helpful to understand how biased can be our measurements with respect to their results.

11.2.2 X-ray luminosity

We compute the X-ray luminosity by integrating the spectrum directly obtained from the simulation on the desired band. We compute the soft X-ray luminosity by integrating spectrum such as the one in Figure 11.2 in the $0.5 - 2\,\mathrm{keV}$ band. Observational works also use the $0.1 - 2.4\,\mathrm{keV}$ luminosity band. We prefer to use the $0.5 - 2\,\mathrm{keV}$ band in order to to be less sensitive on the cold gas that could eventually boost the measured luminosity due to the n^2 sensitivity).
We could also compute the hard X-ray luminosity in the $2.0{-}7.0\,\mathrm{keV}$

or the bolometric luminosity (0.01 − 100.0 keV) that however require an extrapolation. We chose to not do it here.

To understand how much the core inclusion affects the X-ray luminosity, we compare directly the core-included (L_{500}^{ci}) and the core excluded luminosity (L_{500}^{ce}). We compute the APEC emissivity in each cell and integrate the emission measure over the specified radial range :

$$L_{500}^{\rm ci} = \sum_{i}^{r_i \leqslant R_{500}} n_{{\rm H},i}\, n_{{\rm e},i}\, \epsilon(T_i, Z_i)\, {\rm d}V_i, \tag{11.28}$$

$$L_{500}^{\rm ce} = \sum_{i}^{0.15 \leqslant r_i/R_{500} \leqslant 1} n_{{\rm H},i}\, n_{{\rm e},i}\, \epsilon(T_i, Z_i)\, {\rm d}V_i. \tag{11.29}$$

We plot in the left panel of Figure 11.11 the core included and core-excised X-ray luminosities as a function of halo mass. We can see that the inclusion of the core typically boost the X-ray luminosity. Moreover, we see that $L_{500}^{\rm ci}$ typically show a much greater scatter than $L_{500}^{\rm ce}$. This is striking evidence that the thermodynamic state of the cluster core can dramatically boost the global luminosity. On the right panel of the same figure, we show the distribution of the ratio of $L_{500}^{\rm ce}/L_{500}^{\rm ci}$ for all our snapshots. We see that the exclusion of the core decreases on average the X-ray luminosity by 40% with a scatter spanning the entire range from $\sim 0 - 1$.

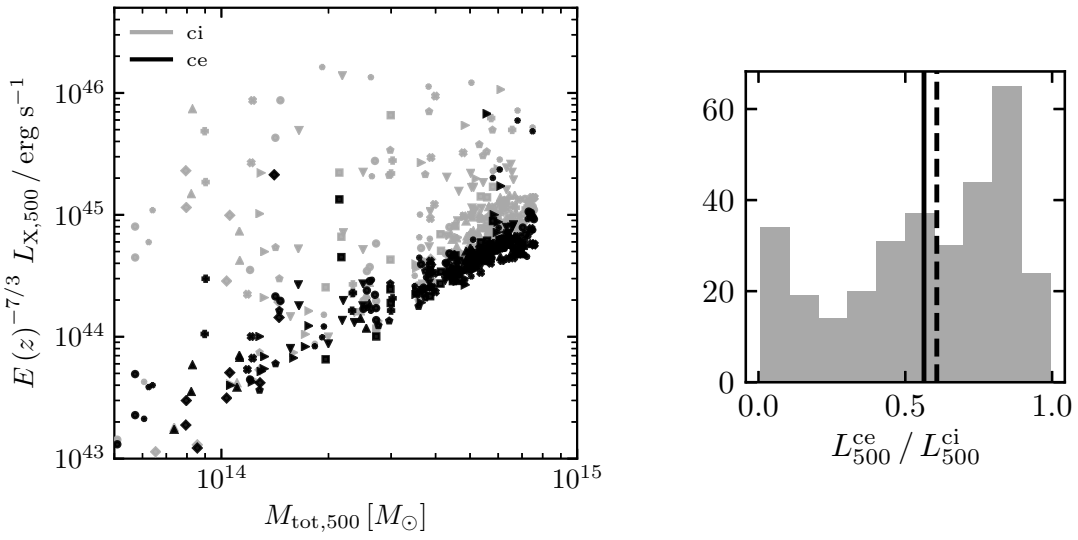

Figure 11.11: (a): Mass versus X-ray luminosity (normalised by the expansion function to cancel out cosmology and redshift dependance). The grey symbols show the core-included X-ray luminosity within R_{500} and the black symbols shows the luminosity in the core-exluded region ($0.15 \leqslant r/R_{500} \leqslant 1$). *Right*: Ratio of core-excluded to core-included X-ray luminosity for all our snapshots. We show the mean value of 0.56 as a solid vertical black line and the median value of 0.60 as a dashed line. We can see that the inclusion of the core typically boost the X-ray luminosity. We show only here the full-physics simulations.

Hence, core-excluded X-ray luminosities are more suited for galaxy cluster sample studies where clusters can have very different central states, which is consistent with the finding of e.g. Pratt *et al.* [391] and Mantz *et al.* [403]. Especially, we can see from the n^2 dependance of L_X and that the spectrum, cool-core clusters will have high luminosities compared to non-cool cores. Moreover, we saw in the panels of Figure 11.5, that gas with high temperatures (and metallicities to a lesser extent) will also yield higher luminosities. Hence, AGN activity surrounding black holes can increase significantly the cluster luminosity.

For these reasons, we chose to use only the core-excluded X-ray luminosity for what will follow.

11.2.3 Sunyaez-Zeldovitch

We calculate, $Y_{\mathrm{SZ},500}$, the integrated Compton-Y parameter directly from the cell density and temperature as :

$$Y_{\mathrm{SZ},500} = \frac{\sigma_T}{\mathrm{m_e\,c^2}} \sum_i^{r_i \leqslant R_{500}} \mathrm{k_B}\, T_i\, n_{e,i}\, \mathrm{d}V_i. \tag{11.30}$$

Y_{SZ} is less sensitive to the gas density (compared to L_X) due its linear dependance. Therefore, there is no need to exclude the core here. This parameter encompasses the total ICM pressure observed at millimeter wavelengths and do show any particular scatter as ICM pressure profile tend to be universal within R_{500} as we saw in Section 10.4..

11.2.4 Note for non-radiative simulations

For computational reasons, we ran our non-radiative simulations at the lower $4K$ resolution for all the Rhapsody-G halos. We carefully check on one halo that both simulation reproduced the same ICM profiles and global properties at our fiducial resolution and at the lower one. As an example, we can see in Figure 11.12 that the ICM spectra agreed to a level of better than 10% between the high resolution (L_{13}) and the lower one (L_{12})

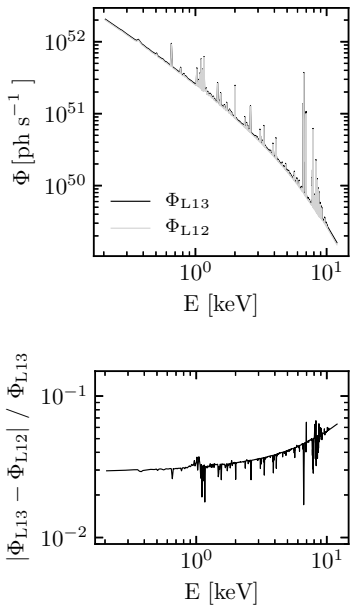

Figure 11.12: Top panel : Spectra generated from the non-radiative simulation at the fiducial $8K$ resolution and at the lower $4K$ one, respectively named L12 and L13. In the bottom panel, we see that the relative difference between these spectra is of the order of 5%. We see that in the soft X-ray band the difference is negligible $\sim$ 3%.

11.3 Results for the Rhapsody-G sample

We will present in this section the scaling relations of our Rhapsody-G cluster sample.
Due to our large number of simulations for the different Rhapsody-G halos and studied sub-grid models, we had to store a limited number of snapshots. We choose to store snapshots at the following

redshifts : 49, 10, 8, 6, 5, 4, 3, 2, 1.5, 1.0, 0.75, 0.50, 0.25, 0.20, 0.15, 0.1, 0.075, 0.05, 0.025, 0.01, 0.005, 0.

In the allocated time, it was not possible to run down to $z = 0$ the simulations with anisotropic thermal conduction (MC) being the most expensive ones. We shown in Figure 11.13, the redshift distribution of all our available snapshots for the different types of simulations.

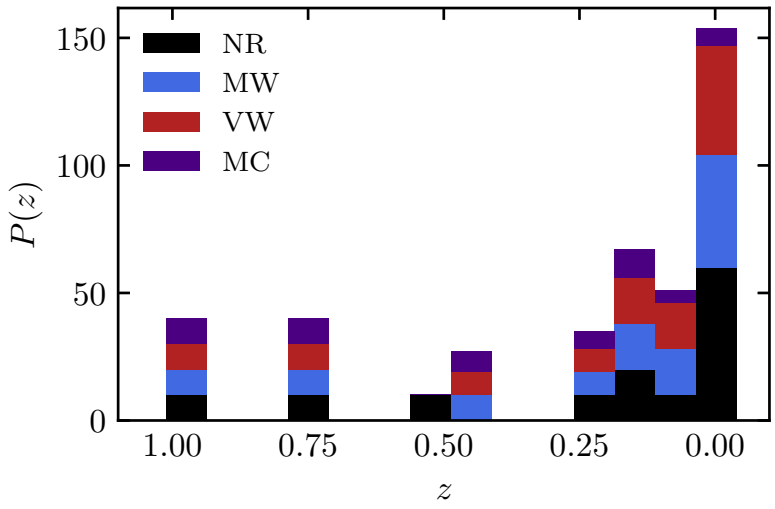

Figure 11.13: Distribution of the redshifts of our simulations snapshot used for this work. We only show the distribution at lower redshifts as MC simulation snapshots start to be missing at roughly $z \lesssim 0.25$.

We keep the same labels defined in Chapter 10 for the simulations using different sub-grid models. Except for the non-radiative (NR) simulations, we recall that all simulations share the same models for gas cooling, star formation, stellar feedback, black hole seeding and growth. The only differences are in the AGN feedback model which use different injection schemes and wether anisotropic thermal conduction was included or not.
We sum-up the different simulation types :

- NR: Non-radiative
- MW: Mass-weighted AGN energy deposition
- VW: Volume-weighted AGN energy deposition
- MC: Mass-weighted AGN energy deposition with anisotropic thermal conduction.

Let us now look at the scaling relations for our Rhapsody-G sample incorporating different sub-grid models.

11.3.1 Fitting for scaling relations

For each set of parameter observable (Y, X) (where often, X is the total cluster mass and Y an ICM observable), we fit our data as :

$$Y = \alpha X^{\beta} E(z)^{\gamma}, \tag{11.31}$$

Which in logarithmic space, changes to :

$$y = 10^{\alpha} + \beta x + \gamma e(z), \tag{11.32}$$

Where :

Subscript `0` refer to units of the estimated parameters

$$y = \log_{10}\left(Y/Y_0\right), \tag{11.33}$$
$$x = \log_{10}\left(X/X_0\right), \tag{11.34}$$
$$e(z) = \log_{10}\left(E(z)\right). \tag{11.35}$$

The slope and evolution with redshift of the scaling relations predicted by the the self-similar theory are listed in Table 11.1. For what follows, we will fix the value of γ to the self-similar values listed in Table 11.1.

Table 11.1: The self similar values for scaling relations in the form of $Y \propto \alpha X^{\beta} E(z)^{\gamma}$.

(Y, X)	γ_{ss}	β_{ss}
T_X–M	1	3/2
L_X–M	7/3	4/3
L_X–T	1	2
Y–M	2/3	5/3

We defer the study of the possible evolution of the scaling relations with redshift to future work.
Here, we only look for estimating α and β by minimizing, for the n data points (x_i, y_i) that we have, the (sum of squared) residuals $\varepsilon_i = y_i - 10^{\alpha} - \beta x_i - \gamma_{ss} e(z)$. We perform this ordinary least squares regression using scipy's `optimize.least_squares` function. We opt for a robust fit using a Cauchy loss function and a soft margin of 10% between inlier and outlier residuals.
The use of the Cauchy loss function allows us to severely weaken the outliers influence, unlike the linear least square fit.

To sample the same redshift range as the reference observations that will be presented later, we will only fit data points with $z \lesssim 1.5$. We show, in Chapter B, for completeness the slopes inferred on wider and smaller redshift bins.
However, the slopes and intersects are consistent in all redshift ranges.

11.3.2 Gas fractions vs Mass

We show in Figure 11.14 the X-ray emitting gas fractions of all Rhapsody-G halos as a function of their total mass enclosing 500 times the critical density. We do not make any distinction on the type of simulation yet. This X-ray emitting gas $f_{\mathrm{gas,X,500}}$ is simply the ratio of the mass of the hot gas , i.e. with $T_{\mathrm{gas}} > 0.5\,\mathrm{keV}$, to the total mass inside R_{500}.

We notice that $f_{\mathrm{gas,X,500}}$ typically scatters between 0.12 and 0.16 for all halos. These values corresponds respectively to 0.76 and 1.00 times the universal baryon fraction.[28]

28: We recall that our simulations use the cosmology of Planck Collaboration *et al.* [241] with $\Omega_{\mathrm{m}} = 0.309$ and $\Omega_{\mathrm{b}} = 0.049$.

We compare our data with the hydrostatic gas fractions and total masses corrected for non-thermal pressure of the X-COP sample

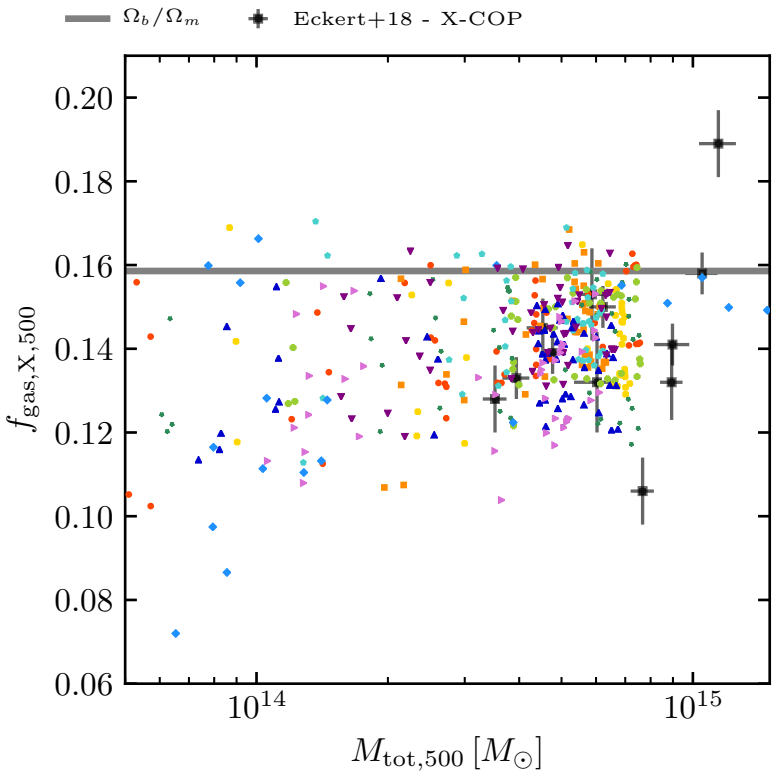

Figure 11.14: Fractions of X-ray emitting gas (i.e. with temperature above 0.5 keV) as a function of the total mass M_{500}.

(values are taken from Table 2 of Eckert *et al.* [50]). Hydrostatic gas fractions should be biased high compared to the true gas fraction as the total cluster mass should be biased low[29] . In spite of that, our fractions of X-ray emitting gas at the high mass end are in agreement with the results of Eckert *et al.* [50].

We will now look in more detail at the gas fractions in our different types of simulations. We plot in Figure 11.15, the same results shown in the Figure 11.14 but where we use a different color-coding for each different type of simulations. Consistently, and throughout this thesis, we show the simulations using the mass-weighted (`MW`) AGN feedback model in blue while the volume-weighted (`VW`) model is shown in red. Purple will stands for simulation using a MW AGN feedback model with anisotropic thermal conduction (`MC`) and black for non-radiative (`NR`) runs.

In Figure 11.15 we see that our halos in each type of simulation occupy a different place in the $f_{\rm gas,X,500} - M_{500}$ plane. The NR simulations systematically show the largest gas fractions. Full-physics runs reveal that gas fraction is lower in lower mass halos while such trends are not observed for the adiabatic runs.

The `MW` runs shows the steeper increase with mass to reach slightly

29: From X-ray/SZ observations of the ICM, hydrostatic masses are inferred using the hydrostatic equilibrium defined in Equation 11.13. Therefore this mass estimate disregards non-thermal contributions to the total ICM pressure. Consequently, the hydrostatic pressure underestimate the total ICM pressure hence the derived hydrostatic mass is lower than the true mass. Thus, gas fractions derived from hydrostatic mass estimates are biased high as $f_{\rm gas} \propto M_{\rm tot}^{-1}$.

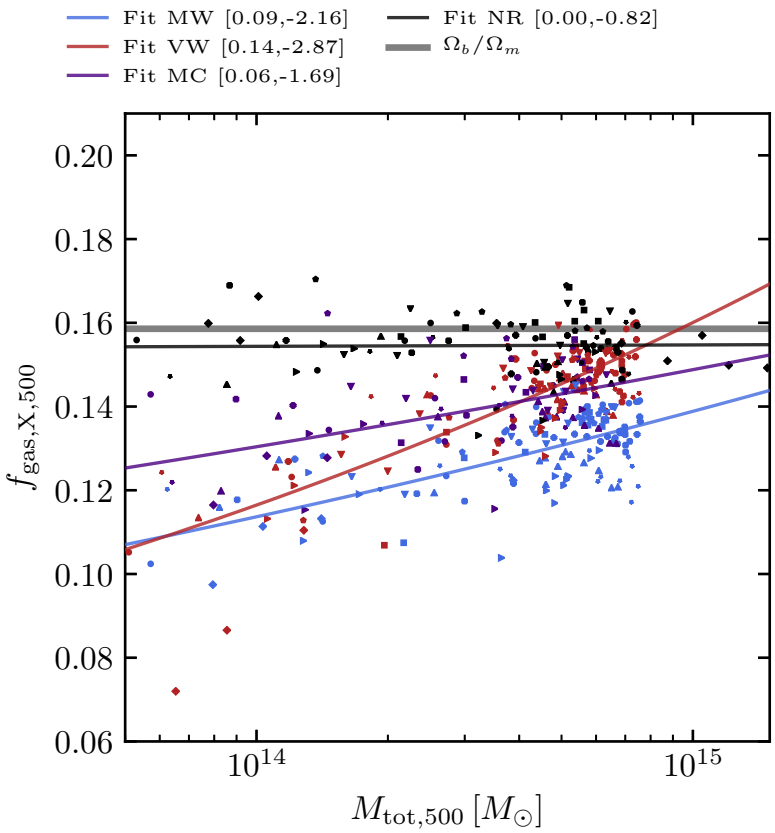

Figure 11.15: Fractions of X-ray emitting gas (i.e. with temperature above 0.5 keV) as a function of the total mass M_{500}.

lower gas fraction compared to `NR` halos. `MC` and `VW` simulations indicate also a positive slope (although shallower than the MW) with increasing mass to reach different gas fractions at the highest halo masses, with the VW ones being the lowest.

To understand the cause of these trends, let us look in more detail at various ratios :

$$f_{\mathrm{gas},500} = \frac{M_{\mathrm{gas}}(< R_{500})}{M_{500}}, \tag{11.36}$$

$$f_{*,500} = \frac{M_{*}(< R_{500})}{M_{500}}, \tag{11.37}$$

$$f_{\mathrm{b},500} = \frac{M_{\mathrm{gas}}(< R_{500}) + M_{*}(< R_{500})}{M_{500}}, \tag{11.38}$$

being respectively the total gas, the stellar and the baryon fractions.

In the left panel of Figure 11.16, we can see that in the case of the non-radiative run (shown in black), the gas fraction is close to universal at all masses (or redshifts).
On the other hand, for the mass-weighted AGN model (shown in blue), we see that the gas fraction is $\sim 10\%$ lower compared to the non-radiative run. However, we see in the middle panel that stars make up 2.5% of the total mass inside R_{500}. This indicates that the

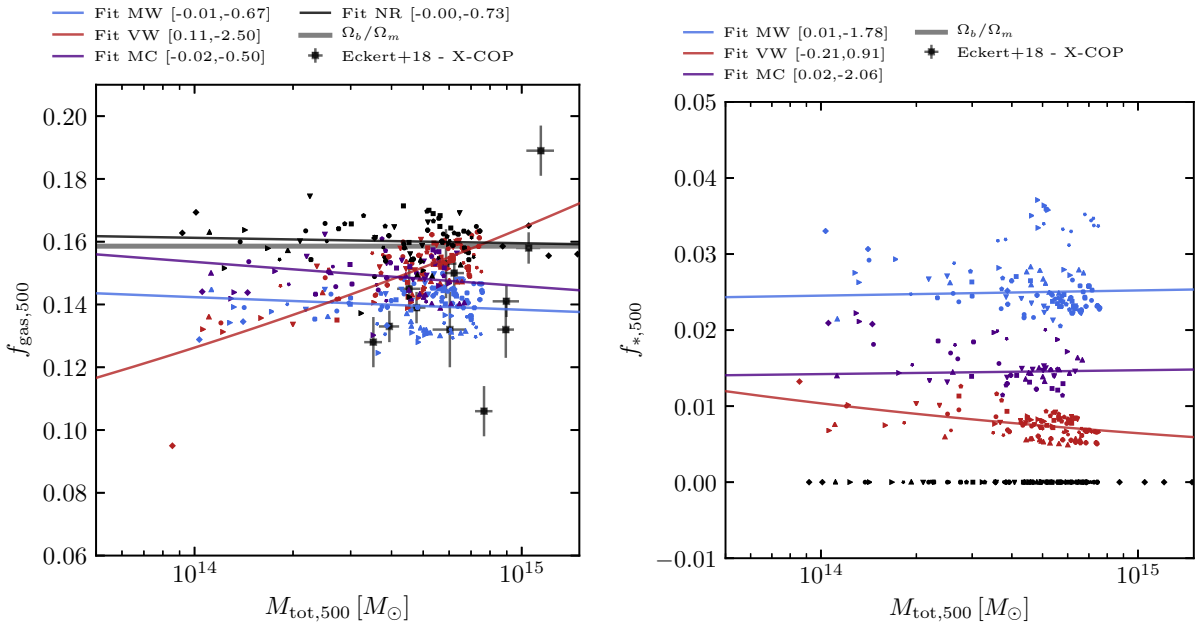

Figure 11.16: Fractions of gas (*left*) and stars (*left*) as function of the total cluster mass M_{500} inside R_{500}, the radius enclosing 500 times the critical density.

"missing" gas was in fact converted into stars.
In the right panel, we see that black and blue symbols are scattered around the universal baryon fraction, as well as the purple symbols that stand for the run with mass-weighted AGN model and anisotropic thermal conduction.

From these three plots, we see can already see that the effect of anisotropic thermal conduction is to reduce the amount of stars by a factor of two[30] compared to the `MW` simulations without thermal conduction. Clusters in the `MW` and `MC` simulations evolved in parallel in the three plots, with `MC` runs have lower stellar mass and higher gas fractions.

For the volume-weighted AGN model run, we know already from Section 9.3, that this is the most efficient model in heating the intra-cluster medium, hence quenching the star formation. We thus understand easily why stellar fractions observed in the right panel of Figure 11.16 are the lowest. The gas fraction is increasing with M_{500}, while the stellar fraction shows an opposite trend.
The strong heating happening at high redshifts when M_{500} is roughly lower than $10^{14}\mathrm{M}_\odot$ helps to prevent the build-up of cold gas hence the formation of new stars. While this relatively hot ICM is slowly radiatively cooling, cold gas will fall to the cluster centre without forming any more stars.
As the result, the fraction of stars contributing to M_{500} decreases as the cluster centres get more gas-rich. This contraction following

30: as we already shown in $M_* - M_h$ plot or cumulative stellar mass profiles in Chapter 10

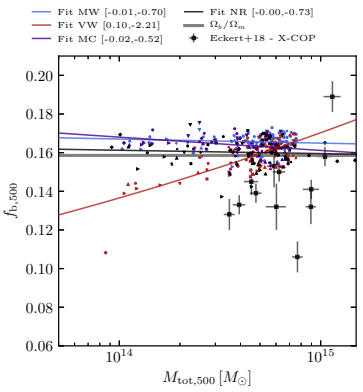

Figure 11.17: Fraction of baryons as function of the total cluster mass M_{500} enclosing 500 times the critical density.

the gas enrichment in the VW case can be seen in the Figure 11.16 where the relative amount of gas inside R_{500} is increasing with mass.

In (almost) a nutshell :

- During the proto-cluster formation, the gas is collapsing and inhomogeneities will form the first halo sub-structures. in In these clumps, the gas cool radiatively at a higher rate. Hence, they will condensate even more, to eventually form stars if local density allows. The cluster galaxies, depending on their total amount of stars, will preheat the ICM thanks to feedback from supernovae. As galaxies grow, their core will get dense enough to form a black hole. Sufficient gas accretion onto the central black hole will trigger an AGN activity.
  From this point, different stories can be told.

- In the MW AGN injection, feedback energy is deposited in the dense regions surrounding the black hole. Apart from preventing cold gas accretion that quenches further the AGN activity, the energy will stay confined near the BH and gets quickly thermalised by the cold and dense environnement. Hence, this AGN energy cannot heat the ICM outside the core. The cluster gas is left free to cool at increasing rates and galaxies can freely grow in mass.

- When, the AGN energy is on the other hand injected rather in a VW way, we noticed a dramatic change. More energy is deposited in less dense regions and can escape the cluster core to reach large radii. In the meanwhile, cold gas accretion onto the BH can persist. As a result, the AGN feedback energy permeates the intra cluster gas on large distances and prevent further gas cooling that quenches dramatically star formation. This reduced stellar component will also result in a lower SN heating at lower redshift. Therefore at $z \leqslant 1$, when AGN activity decreases, the lack of heating sources cannot offset the radiative losses in the ICM. As a result, the cooling gas falls to the cluster centre without forming any more stars. We found a similar build-up of cold gas in the cluster centre to the MW case, but the star formation and thermal histories are unalike.

- If we go back to the scenario with the MW AGN model, but we incorporate anisotropic thermal conduction, we have a third story. In these MC simulations, thermal conduction act in the purpose of flattening any temperature gradients by behaving like a cooling or heating source (as already discussed in Section 8.3). The resulting smoother ICM is less prone to gas

fragmentation that should give birth to stars. This reduced cluster stellar content will not be as efficient as in the sister `MW` simulation in heating the ICM via SN feedback. Thermal conduction seems not to enhanced AGN activity, but quite the contrary. As it participates to smooth the gas, dense cold gas accretion onto the BH is reduced. It does not show to play a significant role at transporting the AGN energy outwards. As the result, the ICM is cooling even more, in combination to the lack of SN heating. Thermal conduction is not improving any AGN heating, but seems to only delay the cooling catastrophe.

11.3.3 X-ray temperature vs Mass

Our results show good agreement with previously published scaling relations. However, we will investigate in more details how our cluster sample compares to other works. In Figure 11.18, we show as solid lines studies that use "unbiased" mass measurements, and as dash-dotted line, the ones using hydrostatic mass estimates. We can clearly see on this figure that for a given X-ray temperature, studies using biased hydrostatic mass estimates, shown as dashed dotted lines, indicate for a lower halo mass compared to true (in the case of simulation works) or weak lensing masses shown as solid lines (which are bot derived through the hydrostatic assumption).

The temperature estimates that we use were derived from the spectral fitting, and, we use the total cluster true mass directly measured from the simulation summing the dark matter, stellar and gaseous components.
We plot results for all our snapshots without differencing yet the type of simulations (`MW`, `VW`, `MC` or `NR`). We use the same color for the "same" halo (e.g. `Halo 211` shown in red). So we see on this in the T-M plane, the evolution track of our clusters as they grow in mass.

By looking at the temperature mass scaling relation in Figure 11.18, our simulations seems to indicate a steeper slope than most of the studies shown in this figure, with the exception of Bulbul *et al.* [404]. In the higher mass range our result agrees well with studies using unbiased mass measurements.

Simulations results such as those discussed by Biffi *et al.* [405], Cui *et al.* [166] and Henden *et al.* [406] directly measure the total cluster mass, while Lieu *et al.* [407] uses weak lensing masses and (core-included) galaxy clusters X-ray temperatures from the XXL survey.[31] The core inclusion in the temperature measurements of

31: In fact, masses inferred via the weak lensing effect also suffer from some bias. But, for simplification here we assume weak lensing mass estimates to be rather "unbiased" compared to hydrostatic mass measurements

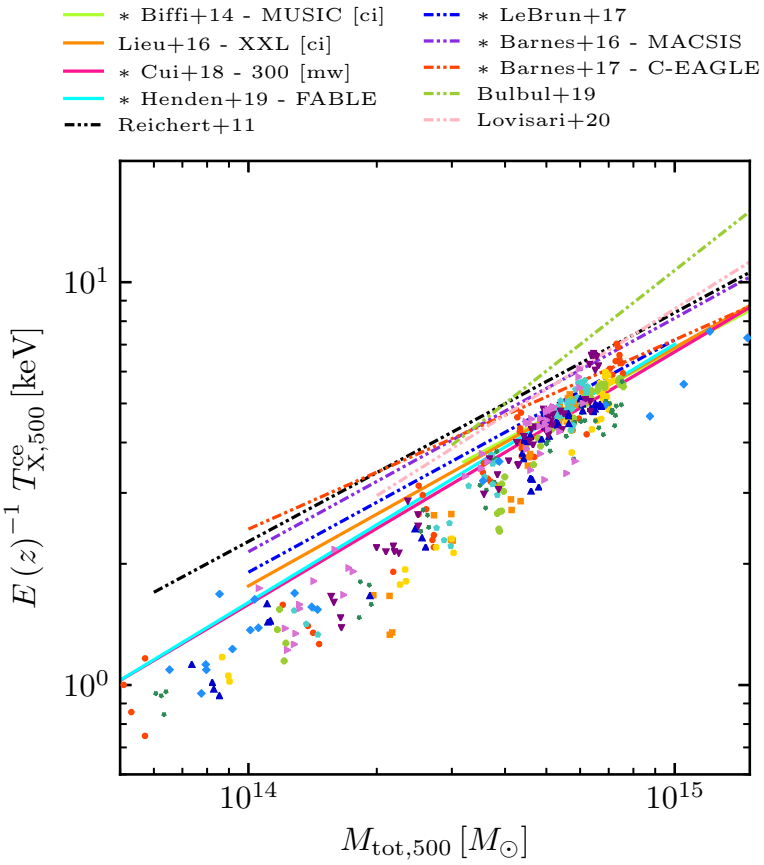

Figure 11.18: Core excluded X-ray temperature - mass scaling relation. Our data in shows by the colored symbols and we do not distinct between the different set of simulations (`MW`, `VW`, `MW` and `NR`). Colors and symbols corresponds to one halo following the same coloring as before. Other published works are reported as dashed and solid lines for respectively studies using biased or unbiased mass estimates. Simulation works are indicated by the asterisks in the legend.

Lieu *et al.* [407] can explain why their scaling relation is offset to higher temperatures compared to our results but also other simulation works. We showed in Section 11.2.2 that the core inclusion can significantly bias high the X-ray luminosity. Nevertheless, it seems to agree rather well with our data within scatter. Biffi *et al.* [405] also used core-included temperature measurements and show the same of offset as Lieu *et al.* [407] and show a slightly shallower slope compared to our data too.

We recall that, at higher redshifts, our spectroscopic fit tend to slightly underestimate the X-ray temperature induced by the abundance of low temperature gas.[32] As the result, at lower masses we should be measuring higher temperatures. Hence, we should find shallower slopes.
However, when we fit the slope in different redshift ranges we notice in that the obtained slopes do not significantly differ. We give in Chapter B the scaling relations fitted in different redshift ranges in Figure B.1.

32: see in Figure 11.10

We now make the distinction, in Figure 11.19, between the different types of simulations.

Surprisingly, we see in Figure 11.19 that the scaling relations inferred

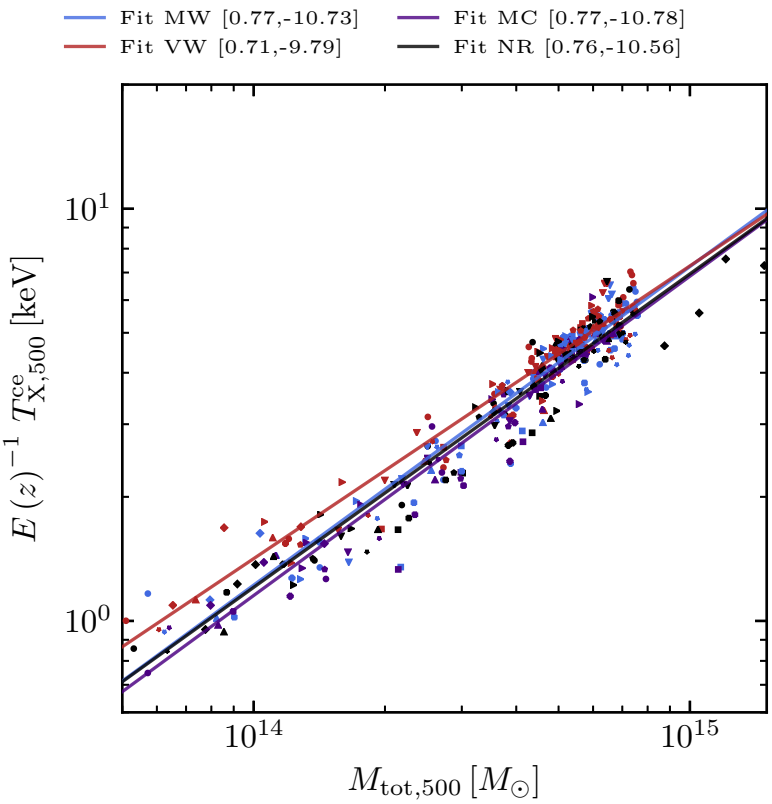

Figure 11.19: Same as Figure 11.10 but we color-coded symbols by the type of simulations. Simulations with a MW AGN models are shown in blue, while VW in red. Simulations with anisotropic thermal conduction and a MW AGN model are plotted in purple. Finally, the NR simulations are shown in black. We plot their respective best fit scaling relation using the same colors. In the legend , we note next in brackets and next to their labels, the slopes and normalisations parameters.

for the MW, MC and NR are very similar in slope and normalisation. It means that in our MW simulation the anisotropic thermal conduction does not significantly impact the ICM temperature outside the core. The VW simulations show a shallower slope but converge to the same temperatures in the high mass range. It illustrates the efficient AGN heating in lower mass halos, where the hot gas can escape more easily because of shallower potential well.
However, all simulations converge to the same temperatures with similar scatter for masses above $5 \times 10^{14}\,M_\odot$. They all agree with slopes $\sim 15\%$ steeper than the self-similar expectation.

It indicates that, in our simulations, at the high mass or low redshifts we do not observe any significant differences.
We surprisingly see that the NR simulations are able to reproduce the same core-excised temperatures than the full-physics simulations. It indicates that non-gravitational processes mostly affect the core. We see that in the radial range $0.15 \lesssim r/R_{500} \lesssim 1$, radiative cooling, thermal conduction, AGN and SF feedback do not play a major role on the ICM temperature. We note however that the very effective VW AGN feedback is able to heat the gas at these radii, in the lower mass regime, where the potential well is the shallowest. It indicates that the radiative cooling low entropy gas will be turn into stars or sink towards the core to fuel AGN activity. The resulting AGN

energy will not be able to produce a noticeable effect on the global ICM temperature in $[0.15R_{500}, 1R_{500}]$.

(Y, X)		α	β
$T^{ce}_{X,500}$–M_{500}	MW	−10.73	0.77
	VW	−9.79	0.71
2/3	MC	−10.78	0.77
	NR	−10.56	0.76
∗ Biffi *et al.* [405]		0.56 ± 0.03	
Lieu *et al.* [407]		0.56 ± 0.12	
∗ Cui *et al.* [166]		0.627 ± 0.007	
∗ Henden *et al.* [406]		0.64 ± 0.02	
Reichert *et al.* [408]		0.57 ± 0.03	
∗ Le Brun *et al.* [409]		0.577 ± 0.006	
∗ Barnes *et al.* [99]		0.58 ± 0.01	
∗ Barnes *et al.* [112]		0.47 ± 0.07	
Bulbul *et al.* [404]		0.83 ± 0.10	
Lovisari *et al.* [71]		0.66 ± 0.06	

Table 11.2: Fitted parameters using Cauchy robust fitting for halos with $z \lesssim 1.5$. We add in the lower part of the table, slope of the studies used in Figure 11.18. We note by an asterisk, as in the Figure 11.18, simulation studies. We see that our slopes are generally steeper than most of the published works.

To infer the slopes of our scalling relations, we use a robust fitting which allow to overlook outliers in the fitting process. As a result, we see that the inferred scaling relations fit well our data.

We see in Table 11.5 that all studies provides different slopes and normalisation.
Normalisation differences can be attributed to the method used to infer cluster masses (as discussed at the beginning of this section). Concerning the slopes, Sun *et al.* [410] and Lovisari *et al.* [411][33] showed that they remain consistent for low mass groups to massive cluster. Hence non-gravitational processes should not affect the T-M scaling relations even in a different mass (or temperature) range.
Bulbul *et al.* [404] actually found the steepest slope. They explain this apparent tension by the fact that they simultaneously fit the mass and redshift trend of the scaling relation in opposition to the assumed self-similar redshift evolution in other studies. Lovisari *et al.* [71] claim that it could also be explained if their SPT-SZ masses suffer from a mass-dependent bias (similar to the Planck mass estimates).
We see that our results agrees with Biffi *et al.* [405] that use of mass-weighted core included temperatures.

33: Not shown here for clarity.

Previously, we saw in Figure 11.10 that mass-weighted temperatures are a factor of ∼ 2 lower than the SF ones and that the inclusion or exclusion of the core only introduce a 5% difference at maximum.[34]
Assuming that a factor of 2 lower temperatures, the results of Biffi *et al.* [405] and Henden *et al.* [406] is in agreement with our data. On the other hand, it would shift the scaling relation of Cui *et al.*

34: In the mass range $\sim 3 - 20 \times 10^{14} M_\odot$.

[166] even to lower temperatures.

Noticeably, we observe a steeper slope than other simulation works. It implies that our simulations show higher ICM temperature in the high mass end than other simulation results[35] .

35: For instance, the AGN feedback of the FABLE [406] simulations is relatively ineffective at heating and expelling gas at larger radii which could explain the lower core-excluded temperatures they found compared to us.

11.3.4 X-ray luminosity vs Mass

The X-ray luminosity mass scaling relation is important as it can relate one of the "cheapest" X-ray observables to the total cluster mass. It will be of a great use for future X-ray surveys such as e-ROSITA that will collect too few photons to infer any spectra or construct any mass profiles.On the other hand, with secure redshift information, it will be possible to measure the X-ray luminosity with very shallow observations.
It is of great use to have a well calibrated $L_X - M$ scaling relation and accurate determination of its scatter. But, the X-ray luminosity measurement is very sensitive to the energy band from which it is derived as well as the flux extraction method. As the result, among all the X-ray scaling relations, it is the one that shows the largest scatter.
As we saw in Equation 11.18 the luminosity is proportional to the square of the gas density. Therefore a slight change in the gas fraction could lead to very different L_X estimates and a pronounced deviation from the self-similar expectation. A large number of previous studies (such as Reichert *et al.* [408]) showed that L_X can be strongly affected by non-gravitational processes, the ICM dynamical state and the presence of a cool-core. As most of the merging and cooling happens in the core, excluding it from the analysis allows to significantly reduce the observed scatter. As we saw in Section 11.2.2, excluding the core in our analysis allows to significantly reduce the scatter too.

Because the X-ray luminosity is highly sensitive to the ICM dynamical state, the presence of a cool core or non-gravitational processes, we can understand why we observe in Figure 11.20 a diversity of slopes and normalisations in the published scaling relations. Our results seems consistent with the simulation results of Barnes *et al.* [99] and Biffi *et al.* [405] as well as observational results of Lovisari *et al.* [71] when we account for $\sim$ 20% hydrostatic mass bias. On the other hand, accounting for this bias increases the offset from the results of Barnes *et al.* [99] and Bulbul *et al.* [404]. Indeed, they have lower luminosities/higher masses compared to our results and the previously mentioned studies.
Our data seems in agreement with the observational results of Mantz *et al.* [412] but with higher luminosities at fixed mass.

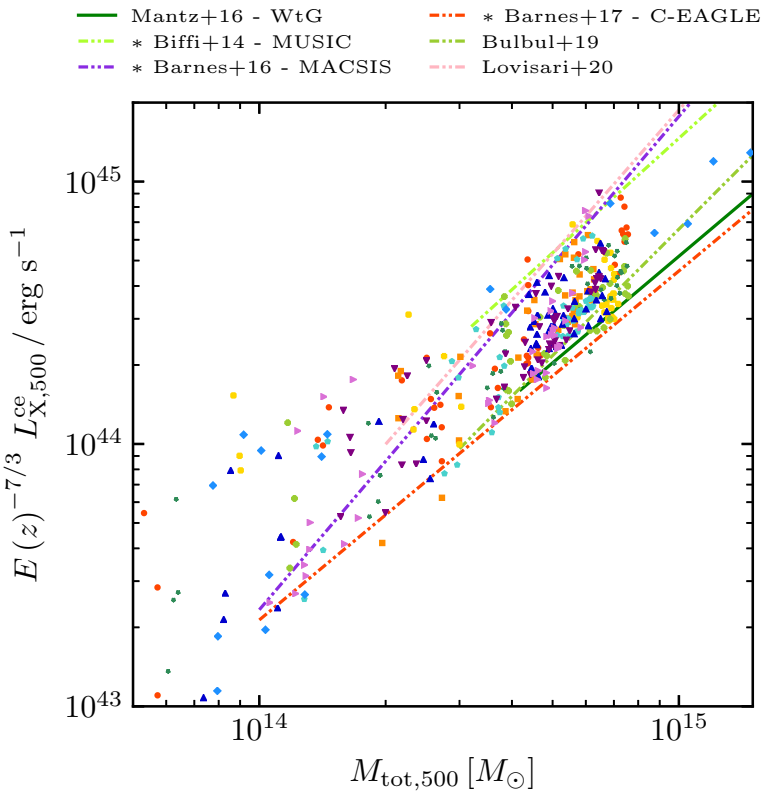

Figure 11.20: Same as Figure 11.18 but for the core excluded X-ray luminosity - mass scaling relation.

If we look in more detail at the X-ray luminosity mass scaling relation Figure 11.21, we see that slopes of the different simulation types shows the same trends as of the X-ray emitting gas fraction relations in Figure 11.15. We note that the steepest slope is observed for the VW run, followed by the MW and MC runs while NR exhibits the shallowest slope. The MW slope matches the self-similar expectation on average but with the greatest scatter.
The higher normalisation of the NR scaling relation is due to the fact that the NR halos are by definition more gas rich, hence more X-ray luminous[36] .

We observe a little normalisation offset between the MW and MC scaling relations showing the effect of the thermal conduction. By smoothing out thermal gradients in the ICM, thermal conduction is able to prevent some cold gas from fuelling star formation or from falling to the core to feed AGN feedback. This is observed in Figure 11.14 where the MC gas fractions are $\sim 25\%$ higher on average than MW. We draw the same conclusions as in Section 11.3.2, where thermal conduction allows to keep the ICM denser, by preventing its condensation. In the MC simulations, the larger amount of gas cools radiatively at a greater rate[37] than in MW simulation yielding a greater X-ray emission.

36: As the other simulations include star formation, that lowers the gas fraction to yield similar baryonic fractions

37: $\Lambda(T) \propto \rho^2\sqrt{T}$, mostly Bremsstrahlung emission

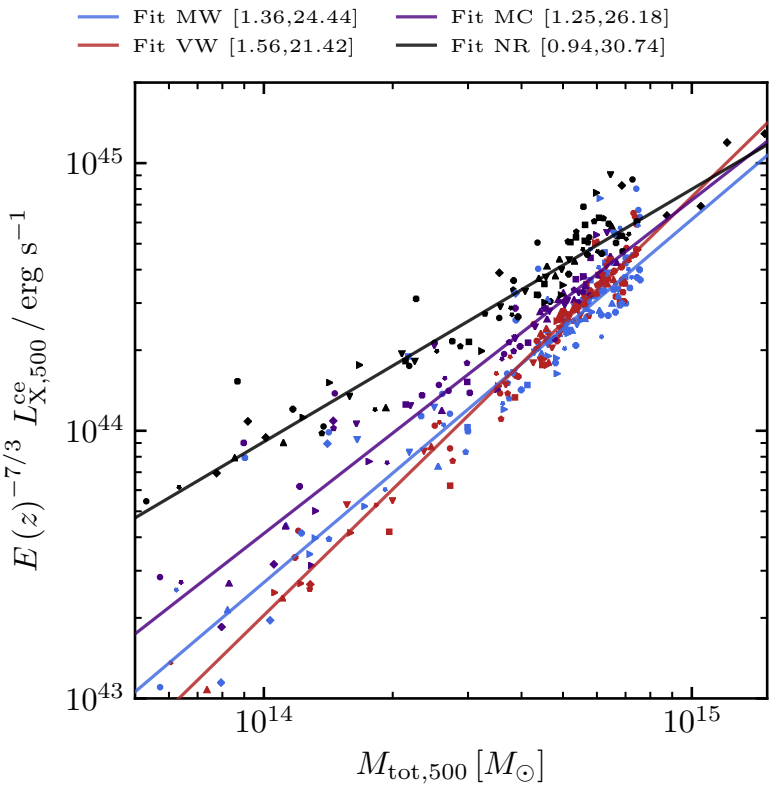

Figure 11.21: Same as Figure 11.18 but for the core excluded X-ray luminosity - mass scaling relation. We observe now a very distinct scaling relations with a wide range of slopes from ~ 0.9 to ~ 1.6 while the a value of ~ 1.3 is expected from the self-similar model.

The steep evolution of the VW simulation in the $L_X - M$ plane can be understood by the build-up of cold gas which we already discussed in Section 11.3.2. The strong VW AGN heating of the ICM to large radii can explain the dim luminosities at lower masses. But as the AGN activity decreases, the ICM cooling takes over to yield higher X-ray luminosities as we can see in Figure 11.21.

In Table 11.5, we collected the slopes from the litterature and our study shown in Figure 11.20 where we distinguish simulations works with asterisks.

MACSIS simulations of Barnes *et al.* [99] and observational results of Mantz *et al.* [412] agrees rather well with our MW simulations. On the other hand result of Bulbul *et al.* [404] agrees with our VW simulations. MUSIC clusters of Biffi *et al.* [405] are in between MW and VW simulations. And finally C-EAGLE simulations of Barnes *et al.* [112] and XMM observations of Lovisari *et al.* [71] shows the steepest slopes. The steepening of the $L_X - M$ scaling relation of the C-EAGLE can be attributed to their effective AGN feedback heating at low masses.

11.3.5 Integrated Compton Y vs Mass

We now look at the Sunyaev-Zel'dovich (SZ) scaling relation. The integrated Compton Y_{SZ} is a measure of the integrated ICM pres-

(Y, X)		α	β
$L^{ce}_{X,500}$–M_{500}	MW	24.44	1.36
	VW	21.42	1.56
4/3	MC	26.18	1.25
	NR	30.74	0.94
∗ Biffi *et al.* [405]		1.45 ± 0.05	
Mantz *et al.* [412]		1.65 ± 0.14	
∗ Barnes *et al.* [99]		1.88 ± 0.05	
∗ Barnes *et al.* [112]		1.33 ± 0.13	
Bulbul *et al.* [404]		1.60 ± 0.17	
Lovisari *et al.* [71]		1.82 ± 0.25	

Table 11.3: Fitted parameters using Cauchy robust fitting for halos with $z \lesssim 1.5$. We add in the lower part of the table, slope of the studies used in Figure 11.18. We see that our slopes are generally steeper than most of the previous studies.

sure along the line of sight.[38] .

From Figure 11.22, we see that the Y_{SZ} parameter is tightly connected to the cluster mass where we observe the lowest scatter compared to the X-ray scaling relations. Indeed, this parameter probe the mass-weighted temperature which is much less sensitive to clumpiness of the gas (as opposed to the emission measure weighted temperature of X-ray quantities).

38: see in Section 3.1.3

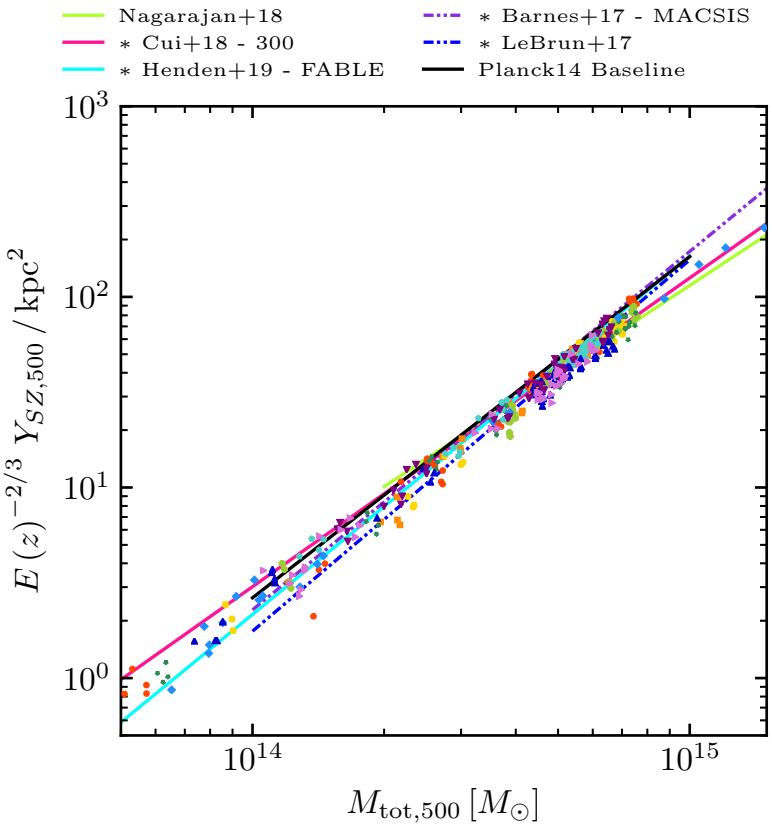

Figure 11.22: Same as Figure 11.18 but for the integrated Compton-Y parameter integrated within R_{500}. Less sactter is observed for the SZ scaling relations compared to the X-ray scalings. Our simulated halos are in good agreement with previous results both from simulations and observations.

Our results agree well with previously published results and our global slope agrees rather well with simulation results of Barnes

et al. [99], Cui *et al.* [166], and Le Brun *et al.* [409] and the Planck baseline relation [41] . We note that on the high mass end, we lie on the (shallower) observational scaling relation of Nagarajan *et al.* [413] and Cui *et al.* [166]. At lower masses, we find a good agreement with the relation of Henden *et al.* [406].

As Y_{SZ} is mass-dependant, it is less constrained at lower masses in observational studies. As a result, observational slopes can quite differ e.g. if we extrapolate Nagarajan *et al.* [413] and Planck baseline at lower masses.

We can see that all halos seem to lie on the same scaling but we differentiate the simulations based on the physical models used in Figure 11.23. We see that slight different slopes are found, with in

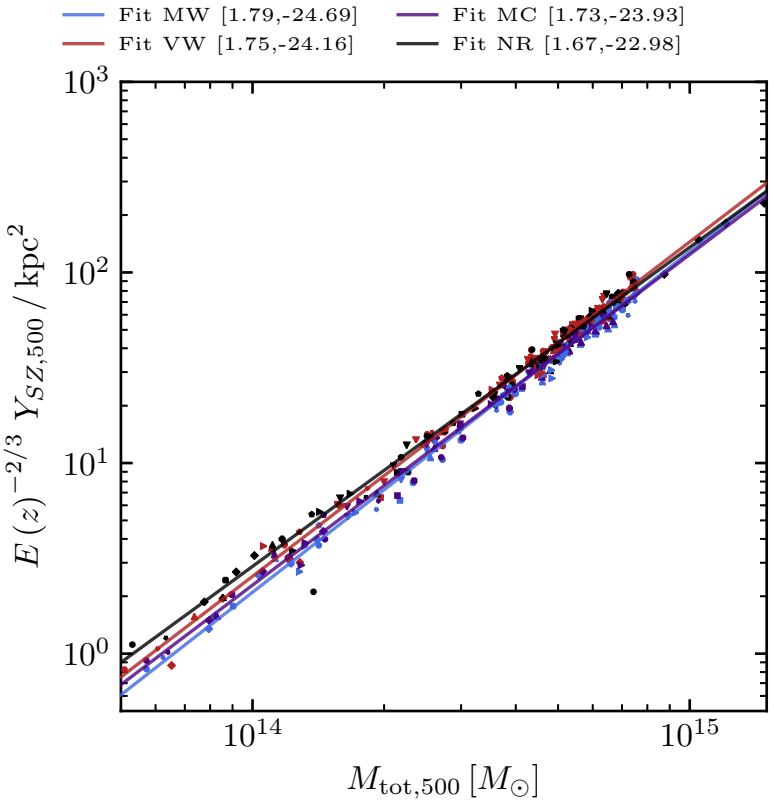

Figure 11.23: We differentiate the halos plotted in Figure 11.22 as a function of the models in the simulations. Again, blue line show the best fit scaling relation for simulations with the mass-weighted (MW) AGN injection model and blue line is for the volume-weighted (VW). Purple line show the best fit scaling for the simulations with anisotropic conduction in the MW AGN model. Finally black line is for non-radiative simulations.

ascending order : `NR`,`VW`, `MC` and `MW`.
We can understand the difference because `NR` simulations shows the highest gas pressure, and `VW` simulations produce higher ICM temperatures (hence higher pressures) at lower halo mass due to its efficient gas heating. Also, at lower masses, conduction acts non-negligibly to flatten out the ICM temperature gradients. Therefore `MW` simulations show greater gas cooling which translate into lower gas pressures.

(Y, X)		α	β
$Y_{SZ,500}$–M_{500}	MW	−24.69	1.79
	VW	−24.16	1.75
5/3	MC	−23.93	1.73
	NR	−22.98	1.67
Planck Collaboration *et al.* [41]		1.79 ± 0.065	
Nagarajan *et al.* [413]		1.51 ± 0.31	
∗ Cui *et al.* [166]		1.62 ± 0.31	
∗ Henden *et al.* [406]		1.88 ± 0.05	
∗ Barnes *et al.* [112]		1.69 ± 0.07	
∗Le Brun *et al.* [409]		1.948 ± 0.018	

Table 11.4: Fitted parameters using Cauchy robust fitting for halos with $z \lesssim 1.5$. We add in the lower part of the table, slope of the studies used in Figure 11.22.

We measure the X-ray analogue of Y_{SZ} by taking the product of mass of the X-ray emitting gas ($M_{gas,X}$) and the X-ray temperature from our spectral fit (T_X).

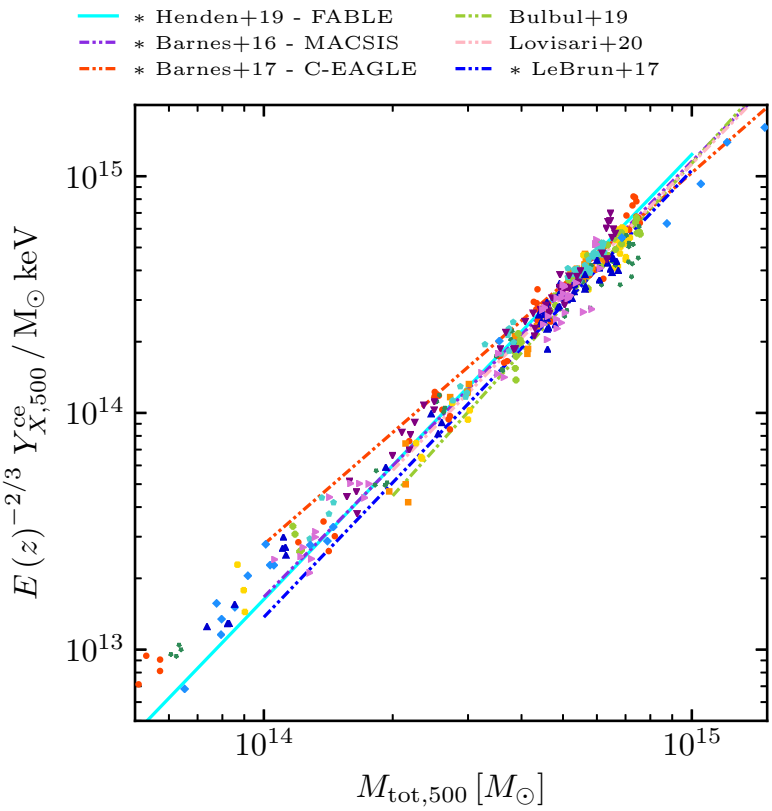

Figure 11.24: Same as Figure 11.22 but for the X-ray analogue Y_X

We observe a greater scatter than from the SZ scaling relation in Figure 11.24, as this Y_X parameter is more sensitive to the internal structure of the gas. The clumpiness of the ICM will boost the value of the Y_X compared to the Y_{SZ}. On the other hand, a completely smooth ICM will give equality between Y_X and Y_{XSZ} as in this case we have $\langle n^2 \rangle = \langle n \rangle^2$ (which shows the respective dependance of the Y_X and Y_{SZ} on the gas number density).

Our data are generally consistent with results of the studies plotted in Figure 11.24 and seem to indicate for a shallower slope with the exception of the C-EAGLE simulations of Barnes *et al.* [112] which indicate somehow for higher values of Y_X.

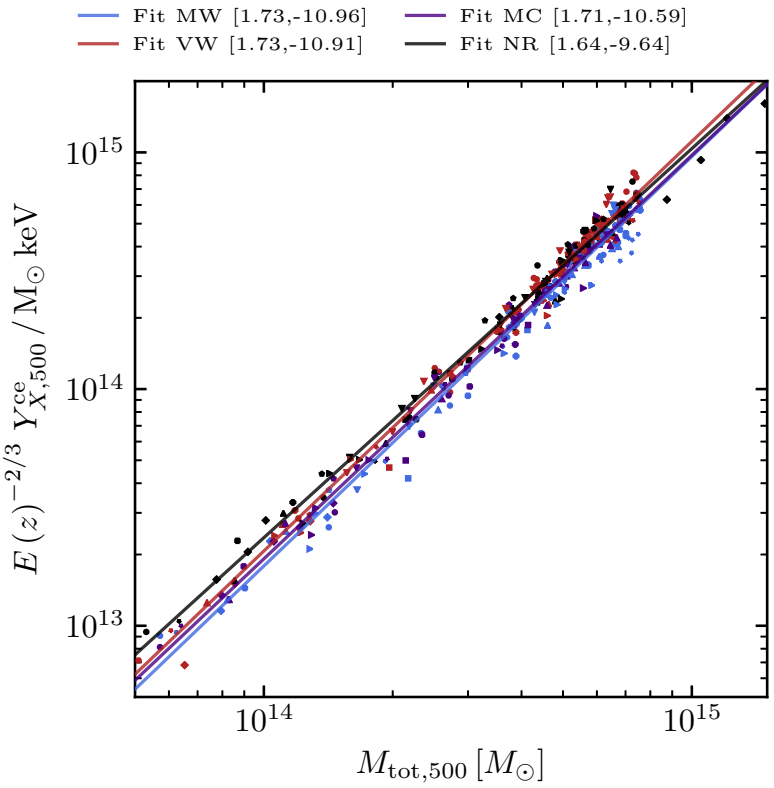

Figure 11.25: Comparison of the slope for the different simulations for the Y_X–M scaling relation. We observe

If we look independently the results of each type of simulations in Figure 11.25, we observe a similar trend as in Figure 11.23. Indeed we see for the `MW`, `MC`, `VW` and `NR` simulations respectively, an increased offset. With the `NR` runs having on average higher values compared to the `MW` simulations.

Our results shows that the Y_X–M shows the lowest scatter among the X-ray scaling relations that we studied. Therefore, Y_X is a low scatter proxy that can be used for cosmology compared to the X-ray temperature or luminosity that are very sensitive to the dynamical state of the ICM.
We also see that our slopes for the full-physics simulations and normalisations are very similar. It indicates that physical processes do not contribute much to the offset of the Y_{SZ} or Y_X observables.

(Y, X)		α	β
$Y_{X,500}$–M_{500}	MW	−10.964	1.730
	VW	−10.911	1.731
5/3	MC	−10.593	1.705
	NR	−9.641	1.644
∗ Barnes *et al.* [99]		1.84 ± 0.05	
∗ Barnes *et al.* [112]		1.57 ± 0.07	
∗Le Brun *et al.* [409]		1.948 ± 0.018	
∗ Henden *et al.* [406]		1.88 ± 0.05	
Bulbul *et al.* [404]		2.01 ± 0.20	
Lovisari *et al.* [71]		1.85 ± 0.10	

Table 11.5: Fitted parameters using Cauchy robust fitting for halos with $z \lesssim 1.5$. We add in the lower part of the table, slope of the studies used in Figure 11.24.

11.4 Summary

In this chapter we presented the Kaiser's model which predicts a self-similar evolution of galaxy clusters based on various assumptions such as spherical symmetry, hydrostatic equilibrium for instance and do not consider non-gravitational processes.
Despite the crude assumptions, this model provides useful scaling relations between easily observed ICM properties to the cluster total mass. Indeed, precise cluster mass estimates are of paramount importance for cluster cosmology and in particular for galaxy cluster counts.

However, non-gravitational processes such as galactic feedback or physical processes within the ICM should participate to deviate cluster observables for the self-similar expectations. The level to which these process participate to the offset needs to be studied in order to provide robust calibrations of the cluster scaling relations.

We saw in Section 5.6, that scaling relation of the Rhapsody-G sample in Hahn *et al.* [111] showed some inconsistencies. Therefore, we developed new methods to derive cluster observables in order to approach to observers' methodology as close as possible.
We now simulate ICM spectra which we fit to a single temperature plasma model. Thus, we are able to derive a spectroscopic temperature which is found to be more suited than common weighted averaged temperatures. We are thus able to compute the X-ray luminosity by integrating the derived spectrum over a given energy band.
With these improved methods, the scaling relations presented in this chapter are found to be in agreement with various observational and numerical studies.

In our scaling relations, the inclusion of various sub-grid models

do not significantly impact the scaling relations in the high mass range with respect to non-radiative simulations. Therefore, non gravitational processes do not affect the ICM observables outside the core.
This is a good new as our findings indicate that cluster observables seems to be robust regardless the dynamical state of the cluster or sub-grid models employed in numerical simulations.

Summary

Conclusions 12

In this chapter, we will sum up the main results presented in this thesis and show some future prospects.

12.1 Conclusions

Clusters of galaxies are the endpoints of the process of structure formation. As such, they optimally trace the growth of structures and can be used to put constraints on our cosmology. Additionally, their dense environments offer an interesting astrophysical laboratory to test our current theories of galaxy evolution.

From the cosmic microwave background to the large scale structures, the ΛCDM cosmological model remains a successful framework but the picture of our Universe is still incomplete and faces many challenges (e.g. the nature of dark energy and dark matter). With continuously improved measurements and new galaxy survey catalogs that allow us to measure the model parameters with high accuracy, we entered in the "era of precision cosmology". While precise measurements converge toward the ΛCDM model, independent probes exposed tensions in our current paradigm such as in the determination of the Hubble parameter (4.4σ) [11, 414, 415] or the present root-mean-square matter fluctuation averaged over a sphere of radius $8\,h^{-1}$Mpc (1.5σ) [41, 51].
Is it due to new physics, to experimental systematics or does it represent real cracks in the building of the the ΛCDM model ?
It remains to be assessed whether these discrepancies are structural and thus hint towards a major revision of our vision of the cosmological Universe, or can they be cured with minor modifications at different scales or accurately modelled systematics.

Especially, the so-called "mass bias" was suspected to be the root of the σ_8 tension between the CMB anisotropies (early Universe probe) and cluster counts (late Universe probe) both investigated by the Planck satellite. Indeed, supported by recent observational evidences, cluster masses estimated under the hydrostatic equilibrium assumption (such as in Planck or X-ray analyses) are underestimated with respect to the mass measured with other methods (e.g. weak lensing) [8, 416]. It is therefore crucial to refine the estimate of the total cluster gravitating mass as precisely as possible by

constraining in great detail the sources of bias or by providing reliable corrections.

In this context, cosmological hydrodynamical simulations are insightful tools for understanding the nature and origin of the hydrostatic mass bias.
Indeed, numerical simulations play an important role in cosmology by allowing us to connect theoretical models to observations, which in turn allows us to constrain parameters and to refine or reject models. They can closely follow the non-linear processes and study the physical processes related to the formation and evolution of cluster of galaxies. Therefore, advanced numerical models providing realistic populations of simulated clusters can provide precise quantifications of the energy budget of clusters and thus, the underestimation of the total mass.

The work presented in this thesis aims at refining the models of galaxy formation with the inclusion of more physics needed to reproduce realistic clusters. Indeed, while simulations of small cosmic volumes of Milky-Way size halo are making substantial progress, realising the cluster galaxy population and the correct structure of the intra-cluster medium (notably in cool-core systems) remains a formidable challenge.
From a suite of multi-physics cosmological simulations of 10 high-mass halos at high spatial resolution ($\sim 2\,h^{-1}$kpc) with the adaptative mesh Eulerian code Ramses, we studied the impact of baryonic physics on the evolution of clusters.

In Chapter 7, we started to look at the magnetic field in clusters, needed for the transport of charged ICM particles. We found that no additional magnetic amplification above the pure compression amplification is found in our simulations. As a result, we do not reach the observed μG values of the magnetic fields in our simulated clusters. However, we showed that the initial seed magnetic field topology has an impact of the final magnetic amplified strengths. The more coherent the seed field is on large scale, the greater is the amplification.

The presence of magnetic fields inhibit the transport of charged particles in the ICM, hence transport processes such as heat diffusion become highly anisotropic. We thus studied in Chapter 8 the effect of anisotropic thermal conduction on the intra-cluster gas. We found that conduction can act as a cooling and heating source depending on the local temperature gradient and is effective at flattening out gas substructures in the ICM.

In Chapter 9 we presented the improvements compared to the original Rhapsody-G simulations especially in the treatment of supermassive black holes. We found the star formation in proto-clusters can be controlled by the seeding of SMBHs and by "tidally" decaying their orbits. Precisely, the latter drastically boost the gas accretion onto SMBHs.

Different AGN feedback models were studied in Chapter 9 and 10 with also the effect thermal conduction. We found that the slight change of the AGN energy deposition can have a drastic effect on the ICM and cluster galaxy populations.
A mass-weighted AGN energy deposition injects the feedback energy preferentially in gas-rich regions around the SMBH. Surrounded by both dense and cold gas, the AGN energy cannot escape the SMBH accretion which leave the intra-cluster gas at larger radii free to cool. As the result, star formation rates in the ICM are high which produce overly massive galaxies and the ICM exhibits a cool core.
With a volume-weighted AGN energy, the deposition is homogeneous around the SMBH (i.e. a volume-weighted injection), more energy is deposited in less dense regions and can escape to efficiently heat the ICM on large distances. Therefore, star formation is remarkably quenched and the ICM now exhibits a non-cool core structure.
Anisotropic thermal conduction flattens out temperatures inhomogeneities in the proto-clusters, hence participates at preventing the formation of cold gas clumps where stars form. As a result, the stellar content of halos is reduced by a factor 2. However, the drawback of a smooth ICM is that the cold gas accretion on the SMBHs is lowered which therefore decrease the AGN efficiency. As the result, a more gas-rich ICM cools at faster rates and produces stronger cooling flow clusters than in simulations without thermal conduction.

Finally in Chapter 11, we described our new derivation of cluster observables being more similar to observers' methodology. We have shown in Chapter 10 that clusters of our Rhapsody-G sample compare relatively well to observed radial profiles but still show discrepancies. The various cluster scaling relations are found to be in good agreement with various observational and numerical studies. While the different AGN models tested in this work as well as thermal conduction reproduce different ICM structures, our cluster scaling relations appear to be rather insensitive to sub-grid model changes especially at the high-mass end.

To conclude we saw that reproducing realistic galaxy clusters in

numerical simulations is challenging. Slight changes in the AGN sub-grid models or the inclusion of thermal conduction in our high resolution simulations of galaxy clusters can yields very different results. While we can reproduce to some extend cluster properties in agreement with observational results, more refined sub-grid physical models and additional physics (such as kinetic AGN feedback, cosmic rays e.g.) are needed in our simulations to better match observational constraints and understand the physical processes at play within the ICM. More effort is required to estimate the energy budget of galaxy clusters and the amount of non-thermal support in the ICM provided by merger activity, shocks, ICM turbulence, magnetic fields and cosmic ray. Indeed, a precise quantification of their contribution to the cluster energy budget is mandatory to put constraints on the underestimation of the total cluster mass in hydrostatic mass estimates. Therefore, it will enable to fully exploit the predictive power of numerical simulations to calibrate cluster scaling relations used for cosmology.

12.2 Perspectives

Thanks to their rich nature, galaxy clusters are unique astrophysical laboratories to study the interaction of supermassive black holes with the surrounding intra-cluster medium, the complex effects of the cluster environment on galaxies, as well as a wide range of non-thermal processes like magnetic field amplification and cosmic ray acceleration. The variety of involved physical processes and the results obtained during this PhD offer many interesting and promising possibilities for future scientific studies.

We saw in Chapter 7, the interesting coupling between the magnetic seed field topology and the amplification. The field at $z = 0$ seems to have totally lost the information of its initial topology. However a detailed characterisation of its distribution still needs to be done. It could be interesting to pinpoint astrophysical processes able to bend and reorient magnetic fields in the ICM. Indeed, the orientation of the field is crucial for the transport of ICM particles and cosmic rays and could provide informations on the actual efficiency of thermal conduction.
From our simulations, thermal conduction does not play a significant role at transporting the AGN feedback energy on large distances, at odds with the findings of Kannan *et al.* [114]. Therefore, investigating wether magnetic fields tend to be more tangential or radial should provide insightful answers on the efficiency of thermal conduction in the ICM and on its (an)isotropic nature.
Moreover, connecting turbulent velocities and magnetic fields in galaxy clusters by studying magnetic fields and velocity structure

functions could help to understand the magnetic (non-)amplification.

The implementation of thermal conduction of Dubois & Commerçon [179] in Ramses includes a separate treatment of electrons and ions. Although our simulations already have this information, we did not yet exploit this asset but we are able to resolve differences in the distribution and energetics of electrons and ions in the ICM.
Moreover, we can also incorporate cosmic rays in our galaxy cluster simulations. As such, we would be able to generate synthetic radio emission maps of our cluster sample to study the connection between the location and morphology of radio emission with astrophysical processes (shocks, AGN, mergers or ICM turbulence). We could also follow the evolution of the spectral energy distribution of CRs as a function of time and space to comprehend the acceleration and diffusion of CRs in the ICM.

We saw that the AGN thermal feedback models tested in this work were not able to a reproduce realistic ICM. Both the volume- and mass-weighted thermal AGN models depend on the energy accumulation threshold that induce episodic and relatively violent AGN feedback events. At odds with the findings of Le Brun *et al.* [162], changing this energy threshold or even allowing a continuous and immediate thermal energy injection did not provide any satisfactory ICM structures.
Ideally, the energy injection should depend on the SMBH gas accretion in a way that, in low accretion regime, kinetic feedback would be triggered (radio mode) and in the high accretion regime, thermal feedback (quasar mode). In a preliminary study (not shown here), we found that when a constant fraction of the AGN feedback (20%) is returned as a kinetic jet, the AGN is able to prevent some cold gas accumulation from a cooling catastrophe similarly to teh results of Meece *et al.* [223].
However, it is not clear how both kinetic and thermal AGN feedback energy should by deposited near the SMBH.
While radio mode feedback is associated to highly collimated jets, quasar mode should be more isotropic because of the radiation pressure-driven outflows from the dense accretion regions.
We saw in this work that the injection of the AGN energy can dramatically change the ICM structure. It would be interesting to test in galaxy cluster simulations, refined sub-grid AGN feedback models that incorporate e.g. a mixed mass- and volume-weighted thermal feedback and kinetic AGN feedback which depends on SMBH accretion rate. Certainly, further improvements to our sub-grid AGN feedback models are necessary to reproduce both a realistic cluster galaxy population and the internal structure of

observed ICM.

With the improvements in our SMBH modelling and the study of different AGN feedback models, the ICM structure of our halos substantially changed from the previous Rhapsody-G simulations. Is the CC/NCC dichotomy found by Hahn *et al.* [111] also present in our new simulations ? If so, what are the mean thermodynamic radial profiles and scaling relations for both the CC and NCC populations ?

Regarding cluster scaling relations, we only studied the slope and normalisation of best fit scaling relations of our Rhapsody-G sample in Chapter 11. However, if we look at the time evolution of individual halos about the best-fitting relation, we could quantify the intrinsic scatter and identify its origin. Indeed, astrophysical processes, such as AGN feedback events or mergers, participate to the offset of cluster properties from the best fit scaling relations (e.g. by increasing the ICM temperature or X-ray luminosity as we can see in Figure B.4).
Additionally, thanks to the variety of halos in our Rhapsody-G sample, we could investigate in more detail and at cosmic variance, wether cluster scaling relations (slope, normalisation and intrinsic scatter) evolve with redshift or not. Thus, we could verify wether the assumption of a redshift-independent slope in observational studies is valid.

We saw in Chapter 11 especially for the $L_X - M$ and $T_X - M$ scaling relations, that accounting for a mass bias of $\sim 20\%$ could bring our data and studies based on hydrostatic mass estimates to an agreement. Having access to the true thermal pressure of the cluster, we could also directly derive the hydrostatic mass of our clusters and compare it to the true mass to infer a true bias value. We could additionally use our spectroscopic fit to extract X-ray temperatures and electron densities in concentric shells (either 2D projected or 3D) and retrieve the hydrostatic mass profiles similarly to observational studies.
The pressure profile could also be recover from synthetic X-ray or SZ surface brightness maps that accounts for instruments' response functions and angular resolutions. Characterising the value and any mass dependance of the hydrostatic mass bias is of paramount importance for cluster counts cosmology.

To conclude, improvements of our sub-grid models and more detailed investigations of our present (and future) cosmological simulations of galaxy clusters would allow to better understand

processes continually shaping the cluster's baryonic components. Because cluster properties are a complex interplay of both cosmology and astrophysics, a detailed understanding of both the internal structure of clusters and how it affects their observational signatures, is critical to unshackle the large leverage of galaxy clusters as cosmological probes.

Appendix

Additional material on ICM radial profiles

A

A.1 Radial profiles of the Rhapsody-G sample at $z \leqslant 0.5$

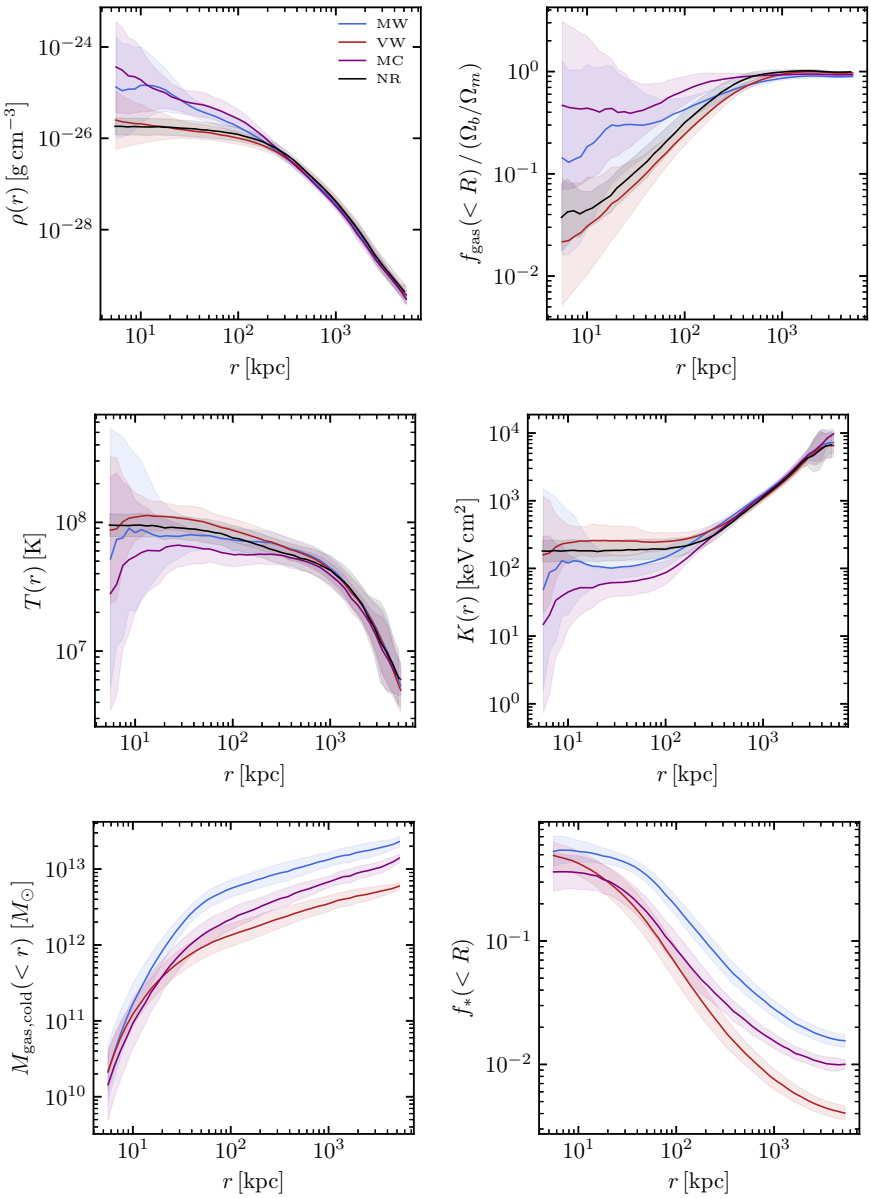

Figure A.1: Similar to Figure 10.8 and Figure 10.9, we show the mean radial profiles of ICM thermodynamic quantities but not rescaled by the self-similar values at R_{500} for our Rhapsody-G sample at $z \leqslant 0.5$.

Additional material on scaling relations

B

B.1 Scaling relations in different redshift ranges

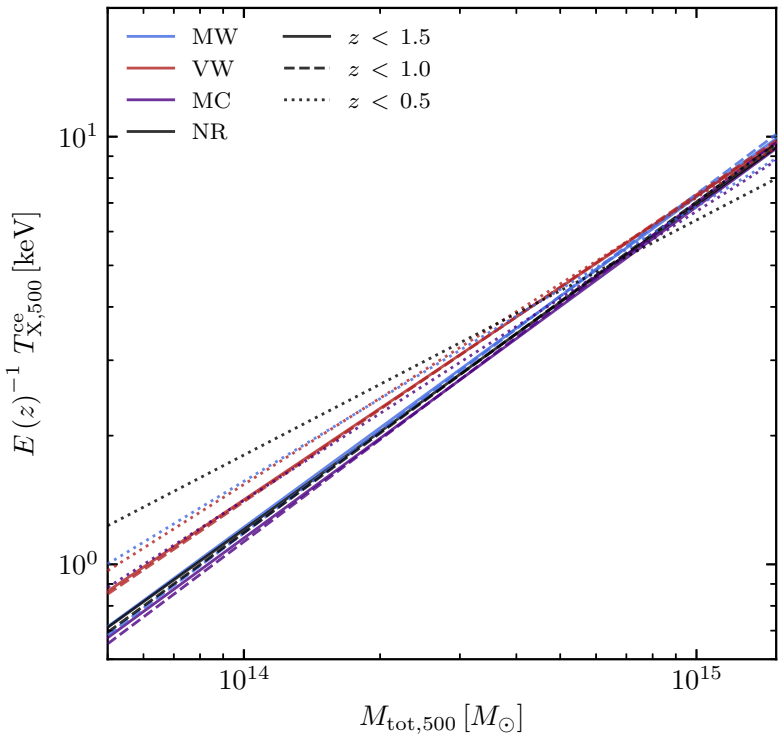

Figure B.1: We plot here the temperature-mass scaling relations similarly to Figure 11.19. The solid line show the scaling relation fitted in the redshift range $0 \leqslant z \leqslant 1.5$ which is the same one shown in Figure 11.18. We add as dashed and dotted lines, fits performed in respectively $z \leqslant 1.0$ and $z \leqslant 0.5$

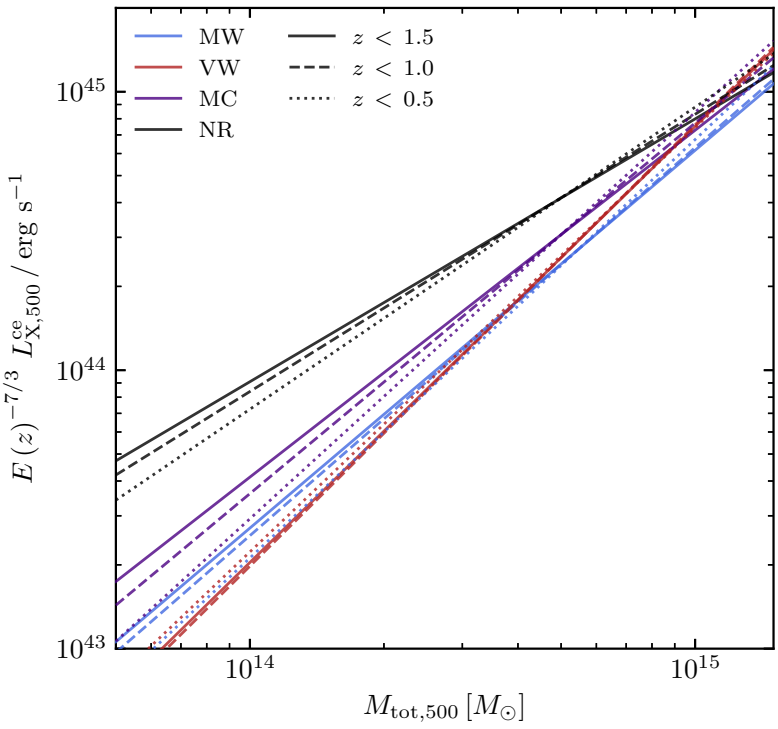

Figure B.2: Same as Figure B.1 but for the X-ray luminosity. See Figure 11.21 for the $z \leqslant 1.5$ scaling relation with data points.

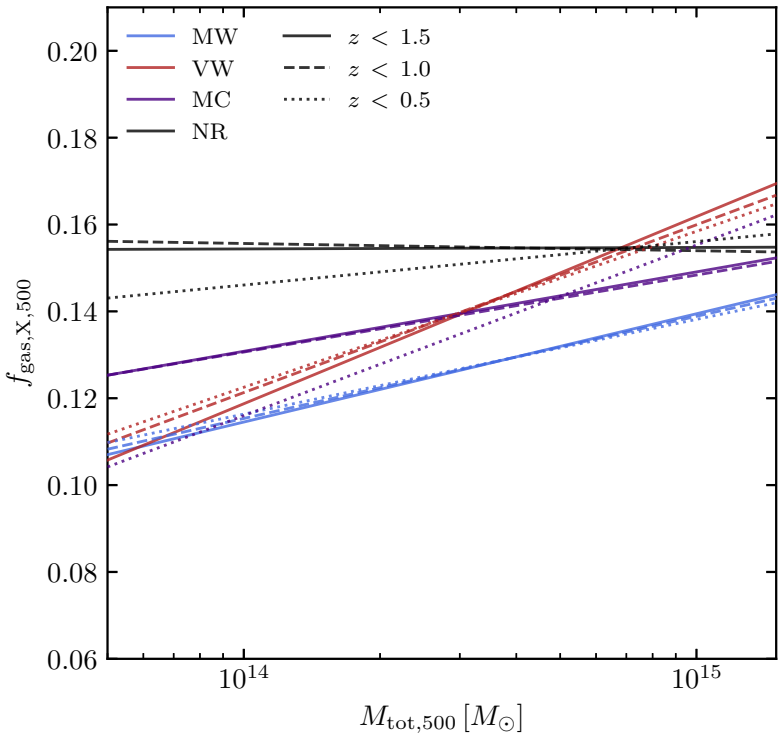

Figure B.3: Same as before but for the gas fraction, see Figure 11.15 for the relations at $z \leqslant 1.5$ with actual data

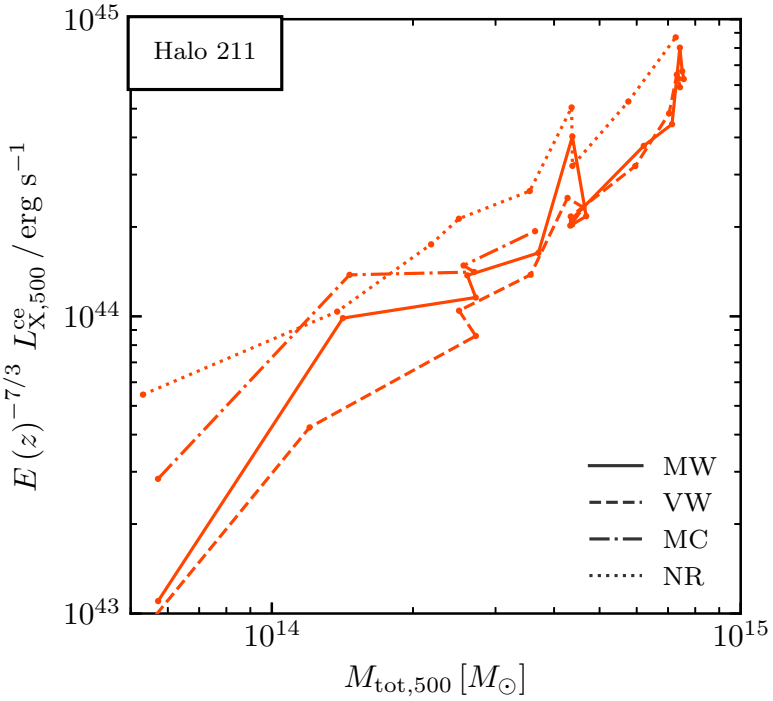

Figure B.4: Core excluded X-ray luminosity as a function of the total mass for `Halo 211`. We show the evolution of the halo in the `MW` (solid), `VW` (dashed), `MC` (dash-dotted) and `NR` (dotted) simulation. We can see for instance see the influence of a major merger on the X-ray luminosity at $M_{500} \sim 4 \times 10^{14} \mathrm{M}_\odot$.

Bibliography

Here are the references in citation order.

1. Messier, C. *Catalogue des Nébuleuses et des Amas d'Étoiles (Catalog of Nebulae and Star Clusters)* Connoissance des Temps ou des Mouvements Célestes. Jan. 1781 (cited on page 3).
2. Herschel, W. On the Construction of the Heavens. *Philosophical Transactions of the Royal Society of London Series I* **75,** 213–266 (Jan. 1785) (cited on page 3).
3. Biviano, A. *From Messier to Abell: 200 Years of Science with Galaxy Clusters* in *Constructing the Universe with Clusters of Galaxies* (eds Durret, F. & Gerbal, D.) (Jan. 2000), 1 (cited on page 3).
4. Hubble, E. P. *Realm of the Nebulae* (1936) (cited on page 3).
5. Abell, G. O. The Distribution of Rich Clusters of Galaxies. ApJS **3,** 211 (May 1958) (cited on page 3).
6. de Vaucouleurs, G. in *Galaxies and the Universe* (eds Sandage, A., Sandage, M. & Kristian, J.) 557 (1975) (cited on page 3).
7. Peebles, P. J. E. *The large-scale structure of the universe* (1980) (cited on page 3).
8. Pratt, G. W. *et al.* The Galaxy Cluster Mass Scale and Its Impact on Cosmological Constraints from the Cluster Population. Space Sci. Rev. **215,** 25 (Feb. 2019) (cited on pages 4, 26, 220).
9. Borgani, S. & Kravtsov, A. Cosmological Simulations of Galaxy Clusters. *Advanced Science Letters* **4,** 204–227 (Feb. 2011) (cited on pages 5, 185, 186).
10. Allen, S. W., Evrard, A. E. & Mantz, A. B. Cosmological Parameters from Observations of Galaxy Clusters. ARA&A **49,** 409–470 (Sept. 2011) (cited on pages 5, 21, 22).
11. Planck Collaboration *et al.* Planck 2018 results. VI. Cosmological parameters. A&A **641,** A6 (Sept. 2020) (cited on pages 12, 24, 81, 220).
12. Mo, H., van den Bosch, F. C. & White, S. *Galaxy Formation and Evolution* (2010) (cited on pages 14, 20, 99).
13. Gunn, J. E. & Gott J. Richard, I. On the Infall of Matter Into Clusters of Galaxies and Some Effects on Their Evolution. ApJ **176,** 1 (Aug. 1972) (cited on page 16).
14. Lynden-Bell, D. Statistical mechanics of violent relaxation in stellar systems. MNRAS **136,** 101 (Jan. 1967) (cited on page 18).
15. Press, W. H. & Schechter, P. Formation of Galaxies and Clusters of Galaxies by Self-Similar Gravitational Condensation. ApJ **187,** 425–438 (Feb. 1974) (cited on pages 19, 47).
16. Bond, J. R., Cole, S., Efstathiou, G. & Kaiser, N. Excursion Set Mass Functions for Hierarchical Gaussian Fluctuations. ApJ **379,** 440 (Oct. 1991) (cited on page 20).
17. Jenkins, A. *et al.* The mass function of dark matter haloes. MNRAS **321,** 372–384 (Feb. 2001) (cited on page 20).

18. Tinker, J. *et al.* Toward a Halo Mass Function for Precision Cosmology: The Limits of Universality. ApJ **688,** 709–728 (Dec. 2008) (cited on page 20).
19. Eke, V. R., Cole, S. & Frenk, C. S. Cluster evolution as a diagnostic for Omega. MNRAS **282,** 263–280 (Sept. 1996) (cited on page 21).
20. Zwicky, F. Die Rotverschiebung von extragalaktischen Nebeln. *Helvetica Physica Acta* **6,** 110–127 (Jan. 1933) (cited on page 22).
21. Hoessel, J. G., Gunn, J. E. & Thuan, T. X. The photometry properties of brightest cluster galaxies. I. Absolute magnitudes in 116 nearby Abell clusters. ApJ **241,** 486–492 (Oct. 1980) (cited on page 22).
22. Bahcall, N. A. & Soneira, R. M. The spatial correlation function of rich clusters of galaxies. ApJ **270,** 20–38 (July 1983) (cited on page 22).
23. Fabian, A. C. On the baryon content of the Shapley supercluster. MNRAS **253,** 29P (Dec. 1991) (cited on page 22).
24. Briel, U. G., Henry, J. P. & Boehringer, H. Observation of the Coma cluster of galaxies with ROSAT during the all-sky-survey. A&A **259,** L31–L34 (June 1992) (cited on page 22).
25. White, S. D. M., Navarro, J. F., Evrard, A. E. & Frenk, C. S. The baryon content of galaxy clusters: a challenge to cosmological orthodoxy. Nature **366,** 429–433 (Dec. 1993) (cited on page 22).
26. Borgani, S. *et al.* Measuring Ω_m with the ROSAT Deep Cluster Survey. ApJ **561,** 13–21 (Nov. 2001) (cited on page 22).
27. Reiprich, T. H. & Böhringer, H. The Mass Function of an X-Ray Flux-limited Sample of Galaxy Clusters. ApJ **567,** 716–740 (Mar. 2002) (cited on page 22).
28. Seljak, U. Cluster number density normalization from the observed mass-temperature relation. MNRAS **337,** 769–773 (Dec. 2002) (cited on page 22).
29. Allen, S. W., Schmidt, R. W., Fabian, A. C. & Ebeling, H. Cosmological constraints from the local X-ray luminosity function of the most X-ray-luminous galaxy clusters. MNRAS **342,** 287–298 (June 2003) (cited on page 22).
30. Schuecker, P., Böhringer, H., Collins, C. A. & Guzzo, L. The REFLEX galaxy cluster survey. VII. Omega$_m$ and sigma$_8$ from cluster abundance and large-scale clustering. A&A **398,** 867–877 (Feb. 2003) (cited on page 22).
31. Henry, J. P., Evrard, A. E., Hoekstra, H., Babul, A. & Mahdavi, A. The X-Ray Cluster Normalization of the Matter Power Spectrum. ApJ **691,** 1307–1321 (Feb. 2009) (cited on page 22).
32. Markevitch, M. *et al.* Direct Constraints on the Dark Matter Self-Interaction Cross Section from the Merging Galaxy Cluster 1E 0657-56. ApJ **606,** 819–824 (May 2004) (cited on pages 22, 23).
33. Randall, S. W., Markevitch, M., Clowe, D., Gonzalez, A. H. & Bradač, M. Constraints on the Self-Interaction Cross Section of Dark Matter from Numerical Simulations of the Merging Galaxy Cluster 1E 0657-56. ApJ **679,** 1173–1180 (June 2008) (cited on page 23).
34. Menanteau, F. *et al.* The Atacama Cosmology Telescope: ACT-CL J0102-4915 "El Gordo," a Massive Merging Cluster at Redshift 0.87. ApJ **748,** 7 (Mar. 2012) (cited on pages 23, 35).

35. Cucciati, O. *et al.* The progeny of a cosmic titan: a massive multi-component proto-supercluster in formation at z = 2.45 in VUDS. A&A **619,** A49 (Nov. 2018) (cited on page 23).
36. Hayashi, M. *et al.* The whole picture of the large-scale structure of the CL1604 supercluster at z ~ 0.9. PASJ **71,** 112 (Dec. 2019) (cited on page 23).
37. Keenan, R. C., Barger, A. J. & Cowie, L. L. Evidence for a ~300 Megaparsec Scale Under-density in the Local Galaxy Distribution. ApJ **775,** 62 (Sept. 2013) (cited on page 24).
38. Haslbauer, M., Banik, I. & Kroupa, P. The KBC void and Hubble tension contradict ΛCDM on a Gpc scale - Milgromian dynamics as a possible solution. MNRAS **499,** 2845–2883 (Dec. 2020) (cited on page 24).
39. Aiola, S. *et al.* The Atacama Cosmology Telescope: DR4 maps and cosmological parameters. J. Cosmology Astropart. Phys. **2020,** 047 (Dec. 2020) (cited on page 24).
40. Riess, A. G. The expansion of the Universe is faster than expected. *Nature Reviews Physics* **2,** 10–12 (Jan. 2020) (cited on page 24).
41. Planck Collaboration *et al.* Planck 2013 results. XX. Cosmology from Sunyaev-Zeldovich cluster counts. A&A **571,** A20 (Nov. 2014) (cited on pages 24, 25, 89, 214, 215, 220).
42. Planck Collaboration *et al.* Planck 2013 results. XXIX. The Planck catalogue of Sunyaev-Zeldovich sources. A&A **571,** A29 (Nov. 2014) (cited on page 24).
43. Biffi, V. *et al.* On the Nature of Hydrostatic Equilibrium in Galaxy Clusters. ApJ **827,** 112 (Aug. 2016) (cited on page 24).
44. Angelinelli, M. *et al.* Turbulent pressure support and hydrostatic mass bias in the intracluster medium. MNRAS **495,** 864–885 (June 2020) (cited on page 24).
45. Ansarifard, S. *et al.* The Three Hundred Project: Correcting for the hydrostatic-equilibrium mass bias in X-ray and SZ surveys. A&A **634,** A113 (Feb. 2020) (cited on page 24).
46. Barnes, D. J. *et al.* Characterizing hydrostatic mass bias with MOCK-X. MNRAS (May 2021) (cited on page 24).
47. Smith, G. P. *et al.* LoCuSS: Testing hydrostatic equilibrium in galaxy clusters. MNRAS **456,** L74–L78 (Feb. 2016) (cited on page 24).
48. Hoekstra, H. *et al.* The Canadian Cluster Comparison Project: detailed study of systematics and updated weak lensing masses. MNRAS **449,** 685–714 (May 2015) (cited on page 24).
49. Ettori, S. *et al.* Hydrostatic mass profiles in X-COP galaxy clusters. A&A **621,** A39 (Jan. 2019) (cited on page 24).
50. Eckert, D. *et al.* Non-thermal pressure support in X-COP galaxy clusters. A&A **621,** A40 (Jan. 2019) (cited on pages 24, 202).
51. Salvati, L., Douspis, M. & Aghanim, N. Constraints from thermal Sunyaev-Zel'dovich cluster counts and power spectrum combined with CMB. A&A **614,** A13 (June 2018) (cited on pages 24, 220).
52. Morishita, T. *et al.* Characterizing Intracluster Light in the Hubble Frontier Fields. ApJ **846,** 139 (Sept. 2017) (cited on page 26).
53. Girardi, M., Biviano, A., Giuricin, G., Mardirossian, F. & Mezzetti, M. Velocity Dispersions in Galaxy Clusters. ApJ **404,** 38 (Feb. 1993) (cited on page 26).

54. Amodeo, S. *et al.* Spectroscopic Confirmation and Velocity Dispersions for 20 Planck Galaxy Clusters at 0.16 < z < 0.78. ApJ **853,** 36 (Jan. 2018) (cited on page 26).
55. Hopkins, A. M. The Dawes Review 8: Measuring the Stellar Initial Mass Function. PASA **35,** e039 (Nov. 2018) (cited on page 27).
56. Lynds, R. & Petrosian, V. *Giant Luminous Arcs in Galaxy Clusters* in *Bulletin of the American Astronomical Society* **18** (Sept. 1986), 1014 (cited on page 27).
57. Fort, B., Mellier, Y., Picat, J. P., Rio, Y. & Lelievre, G. *Multiaperture spectroscopy with rapid mask fabrication and installation.* in *Instrumentation in astronomy VI* (ed Crawford, D. L.) **627** (Jan. 1986), 321–327 (cited on page 27).
58. Tyson, J. A., Valdes, F. & Wenk, R. A. Detection of Systematic Gravitational Lens Galaxy Image Alignments: Mapping Dark Matter in Galaxy Clusters. ApJ **349,** L1 (Jan. 1990) (cited on page 27).
59. Narayan, R. & Bartelmann, M. Lectures on Gravitational Lensing. *arXiv e-prints,* astro–ph/9606001 (June 1996) (cited on page 28).
60. Okabe, N. *et al.* LoCuSS: Calibrating Mass-observable Scaling Relations for Cluster Cosmology with Subaru Weak-lensing Observations. ApJ **721,** 875–885 (Sept. 2010) (cited on page 28).
61. Hoekstra, H., Mahdavi, A., Babul, A. & Bildfell, C. The Canadian Cluster Comparison Project: weak lensing masses and SZ scaling relations. MNRAS **427,** 1298–1311 (Dec. 2012) (cited on page 28).
62. Umetsu, K. *et al.* CLASH: Weak-lensing Shear-and-magnification Analysis of 20 Galaxy Clusters. ApJ **795,** 163 (Nov. 2014) (cited on page 28).
63. von der Linden, A. *et al.* Weighing the Giants - I. Weak-lensing masses for 51 massive galaxy clusters: project overview, data analysis methods and cluster images. MNRAS **439,** 2–27 (Mar. 2014) (cited on page 28).
64. Kellogg, E., Gursky, H., Murray, S., Tananbaum, H. & Giacconi, R. X-Ray Sources Near the Galactic Center Observed by UHURU. ApJ **169,** L99 (Nov. 1971) (cited on page 28).
65. Gursky, H. *et al.* X-Ray Emission from Rich Clusters of Galaxies. ApJ **173,** L99 (May 1972) (cited on page 28).
66. Sarazin, C. L. X-ray emission from clusters of galaxies. *Reviews of Modern Physics* **58,** 1–115 (Jan. 1986) (cited on page 28).
67. Irwin, J. A. *et al.* The Cheshire Cat Gravitational Lens: The Formation of a Massive Fossil Group. ApJ **806,** 268 (June 2015) (cited on page 29).
68. Arnaud, M. *X-ray observations of clusters of galaxies* in *Background Microwave Radiation and Intracluster Cosmology* (eds Melchiorri, F. & Rephaeli, Y.) (Jan. 2005), 77 (cited on page 30).
69. Ghisellini, G. *Radiative Processes in High Energy Astrophysics* (2013) (cited on page 30).
70. Ghirardini, V. *et al.* Universal thermodynamic properties of the intracluster medium over two decades in radius in the X-COP sample. A&A **621,** A41 (Jan. 2019) (cited on pages 31, 39, 176, 178–180).
71. Lovisari, L. *et al.* X-Ray Scaling Relations for a Representative Sample of Planck-selected Clusters Observed with XMM-Newton. ApJ **892,** 102 (Apr. 2020) (cited on pages 31, 209, 210, 212, 213, 217).

72. The CHEX-MATE Collaboration *et al.* The Cluster HEritage project with XMM-Newton: Mass Assembly and Thermodynamics at the Endpoint of structure formation. I. Programme overview. *arXiv e-prints,* arXiv:2010.11972 (Oct. 2020) (cited on page 31).
73. Vikhlinin, A. *et al.* Chandra Cluster Cosmology Project. II. Samples and X-Ray Data Reduction. ApJ **692,** 1033–1059 (Feb. 2009) (cited on page 31).
74. Arnaud, M. *et al.* The universal galaxy cluster pressure profile from a representative sample of nearby systems (REXCESS) and the Y_{SZ} - M_{500} relation. A&A **517,** A92 (July 2010) (cited on pages 31, 39, 40).
75. Yan, Z. *et al.* An analysis of galaxy cluster mis-centring using cosmological hydrodynamic simulations. MNRAS **493,** 1120–1129 (Mar. 2020) (cited on page 31).
76. Bourdin, H., Sauvageot, J. .-., Slezak, E., Bijaoui, A. & Teyssier, R. Temperature map computation for X-ray clusters of galaxies. A&A **414,** 429–443 (Feb. 2004) (cited on page 31).
77. Bourdin, H. & Mazzotta, P. Temperature structure of the intergalactic medium within seven nearby and bright clusters of galaxies observed with XMM-Newton. A&A **479,** 307–320 (Feb. 2008) (cited on page 31).
78. Macario, G. *et al.* A Shock Front in the Merging Galaxy Cluster A754: X-ray and Radio Observations. ApJ **728,** 82 (Feb. 2011) (cited on page 31).
79. Russell, H. R. *et al.* Chandra observation of two shock fronts in the merging galaxy cluster Abell 2146. MNRAS **406,** 1721–1733 (Aug. 2010) (cited on page 31).
80. Owers, M. S., Nulsen, P. E. J., Couch, W. J. & Markevitch, M. A High Fidelity Sample of Cold Front Clusters from the Chandra Archive. ApJ **704,** 1349–1370 (Oct. 2009) (cited on page 31).
81. Zhuravleva, I. *et al.* Turbulent heating in galaxy clusters brightest in X-rays. Nature **515,** 85–87 (Nov. 2014) (cited on page 32).
82. Sunyaev, R. A. & Zeldovich, Y. B. Small-Scale Fluctuations of Relic Radiation. Ap&SS **7,** 3–19 (Apr. 1970) (cited on page 31).
83. Sunyaev, R. A. & Zeldovich, Y. B. The Observations of Relic Radiation as a Test of the Nature of X-Ray Radiation from the Clusters of Galaxies. *Comments on Astrophysics and Space Physics* **4,** 173 (Nov. 1972) (cited on page 31).
84. Sunyaev, R. A. & Zeldovich, Y. B. The velocity of clusters of galaxies relative to the microwave background - The possibility of its measurement. MNRAS **190,** 413–420 (Feb. 1980) (cited on page 31).
85. Carlstrom, J. E., Holder, G. P. & Reese, E. D. Cosmology with the Sunyaev-Zel'dovich Effect. ARA&A **40,** 643–680 (Jan. 2002) (cited on pages 33, 35).
86. Birkinshaw, M. The Sunyaev-Zel'dovich effect. Phys. Rep. **310,** 97–195 (Mar. 1999) (cited on page 34).
87. Hand, N. *et al.* Evidence of Galaxy Cluster Motions with the Kinematic Sunyaev-Zel'dovich Effect. Phys. Rev. Lett. **109,** 041101 (July 2012) (cited on page 34).
88. Ferrari, C., Govoni, F., Schindler, S., Bykov, A. M. & Rephaeli, Y. Observations of Extended Radio Emission in Clusters. Space Sci. Rev. **134,** 93–118 (Feb. 2008) (cited on pages 36–38).

89. Pearce, C. J. J. *et al.* VLA Radio Observations of the HST Frontier Fields Cluster Abell 2744: The Discovery of New Radio Relics. ApJ **845,** 81 (Aug. 2017) (cited on page 36).
90. Feretti, L., Giovannini, G., Govoni, F. & Murgia, M. *Clusters of galaxies: observational properties of the diffuse radio emission* May 2012 (cited on page 36).
91. van Weeren, R. J. *et al. Diffuse Radio Emission from Galaxy Clusters* Feb. 2019 (cited on pages 36, 38).
92. Brunetti, G. & Jones, T. W. Cosmic Rays in Galaxy Clusters and Their Nonthermal Emission. *International Journal of Modern Physics D* **23,** 1430007–98 (Mar. 2014) (cited on pages 36, 102).
93. Govoni, F. & Feretti, L. Magnetic Fields in Clusters of Galaxies. *International Journal of Modern Physics D* **13,** 1549–1594 (Jan. 2004) (cited on pages 38, 98).
94. Van Eck, C. L. *et al.* Faraday tomography of the local interstellar medium with LOFAR: Galactic foregrounds towards IC 342. A&A **597,** A98 (Jan. 2017) (cited on page 38).
95. Govoni, F. *et al. Cosmic Magnetism Science in the SKA1 Era* Square Kilometre Array Organisation Science Working Group Assessment Workshop Summary. Mar. 2014 (cited on page 38).
96. McDonald, M. *et al.* The Remarkable Similarity of Massive Galaxy Clusters from z ~ 0 to z ~ 1.9. ApJ **843,** 28 (July 2017) (cited on pages 39, 176, 178, 180).
97. Mantz, A. B., Allen, S. W., Morris, R. G. & Schmidt, R. W. Cosmology and astrophysics from relaxed galaxy clusters - III. Thermodynamic profiles and scaling relations. MNRAS **456,** 4020–4039 (Mar. 2016) (cited on page 39).
98. Okabe, N. *et al.* Universal profiles of the intracluster medium from Suzaku X-ray and Subaru weak-lensing observations*. PASJ **66,** 99 (Oct. 2014) (cited on page 39).
99. Barnes, D. J. *et al.* The redshift evolution of massive galaxy clusters in the MACSIS simulations. MNRAS **465,** 213–233 (Feb. 2017) (cited on pages 39, 58, 209, 210, 212, 213, 217).
100. Fabian, A. C. Cooling Flows in Clusters of Galaxies. ARA&A **32,** 277–318 (Jan. 1994) (cited on page 39).
101. Fabian, A. C. Observational Evidence of Active Galactic Nuclei Feedback. ARA&A **50,** 455–489 (Sept. 2012) (cited on page 39).
102. Peterson, J. R. & Fabian, A. C. X-ray spectroscopy of cooling clusters. Phys. Rep. **427,** 1–39 (Apr. 2006) (cited on page 39).
103. McNamara, B. R. & Nulsen, P. E. J. Mechanical feedback from active galactic nuclei in galaxies, groups and clusters. *New Journal of Physics* **14,** 055023 (May 2012) (cited on page 39).
104. Kaastra, J. S. *et al.* XMM-Newton observations of the cluster of galaxies Sérsic 159-03. A&A **365,** L99–L103 (Jan. 2001) (cited on page 40).
105. Peterson, J. R. *et al.* X-ray imaging-spectroscopy of Abell 1835. A&A **365,** L104–L109 (Jan. 2001) (cited on page 40).
106. Peterson, J. R. *et al.* High-Resolution X-Ray Spectroscopic Constraints on Cooling-Flow Models for Clusters of Galaxies. ApJ **590,** 207–224 (June 2003) (cited on page 40).
107. Kravtsov, A. V. & Borgani, S. Formation of Galaxy Clusters. ARA&A **50,** 353–409 (Sept. 2012) (cited on page 40).

108. Dubois, Y. *et al.* Dancing in the dark: galactic properties trace spin swings along the cosmic web. MNRAS **444,** 1453–1468 (Oct. 2014) (cited on pages 41, 53, 58, 85, 143).
109. Schaye, J. *et al.* The EAGLE project: simulating the evolution and assembly of galaxies and their environments. MNRAS **446,** 521–554 (Jan. 2015) (cited on page 41).
110. Springel, V. *et al.* First results from the IllustrisTNG simulations: matter and galaxy clustering. MNRAS **475,** 676–698 (Mar. 2018) (cited on pages 41, 54, 58).
111. Hahn, O. *et al.* Rhapsody-G simulations - I. The cool cores, hot gas and stellar content of massive galaxy clusters. MNRAS **470,** 166–186 (Sept. 2017) (cited on pages 41, 55, 80, 83–88, 92, 143, 162, 179, 217, 225).
112. Barnes, D. J. *et al.* The Cluster-EAGLE project: global properties of simulated clusters with resolved galaxies. MNRAS **471,** 1088–1106 (Oct. 2017) (cited on pages 41, 58, 209, 212, 213, 215–217).
113. Barnes, D. J. *et al.* A census of cool-core galaxy clusters in IllustrisTNG. MNRAS **481,** 1809–1831 (Dec. 2018) (cited on pages 41, 55).
114. Kannan, R. *et al.* Increasing Black Hole Feedback-induced Quenching with Anisotropic Thermal Conduction. ApJ **837,** L18 (Mar. 2017) (cited on pages 41, 134, 160, 161, 223).
115. Michaux, M., Hahn, O., Rampf, C. & Angulo, R. E. Accurate initial conditions for cosmological N-body simulations: minimizing truncation and discreteness errors. MNRAS **500,** 663–683 (Jan. 2021) (cited on page 43).
116. Lewis, A., Challinor, A. & Lasenby, A. Efficient Computation of Cosmic Microwave Background Anisotropies in Closed Friedmann-Robertson-Walker Models. *The Astrophysical Journal* **538,** 473–476 (Aug. 2000) (cited on page 43).
117. Blas, D., Lesgourgues, J. & Tram, T. The Cosmic Linear Anisotropy Solving System (CLASS). Part II: Approximation schemes. *Journal of Cosmology and Astroparticle Physics* **2011,** 034–034 (July 2011) (cited on page 43).
118. Bardeen, J. M., Bond, J. R., Kaiser, N. & Szalay, A. S. The Statistics of Peaks of Gaussian Random Fields. ApJ **304,** 15 (May 1986) (cited on page 43).
119. Eisenstein, D. J. & Hu, W. Baryonic Features in the Matter Transfer Function. ApJ **496,** 605–614 (Mar. 1998) (cited on page 43).
120. Hahn, O. & Abel, T. Multi-scale initial conditions for cosmological simulations. MNRAS **415,** 2101–2121 (Aug. 2011) (cited on pages 44, 80, 81, 92).
121. Barnes, J. & Hut, P. A hierarchical O(N log N) force-calculation algorithm. Nature **324,** 446–449 (Dec. 1986) (cited on page 46).
122. Springel, V., Yoshida, N. & White, S. D. M. GADGET: a code for collisionless and gasdynamical cosmological simulations. New A **6,** 79–117 (Apr. 2001) (cited on page 46).
123. Wang, J. *et al.* Universal structure of dark matter haloes over a mass range of 20 orders of magnitude. Nature **585,** 39–42 (Sept. 2020) (cited on page 47).
124. Sheth, R. K., Mo, H. J. & Tormen, G. Ellipsoidal collapse and an improved model for the number and spatial distribution of dark matter haloes. MNRAS **323,** 1–12 (May 2001) (cited on page 47).

125. Navarro, J. F., Frenk, C. S. & White, S. D. M. The Structure of Cold Dark Matter Halos. ApJ **462,** 563 (May 1996) (cited on pages 47, 81).
126. Navarro, J. F., Frenk, C. S. & White, S. D. M. A Universal Density Profile from Hierarchical Clustering. ApJ **490,** 493–508 (Dec. 1997) (cited on page 47).
127. Navarro, J. F. *et al.* The inner structure of ΛCDM haloes - III. Universality and asymptotic slopes. MNRAS **349,** 1039–1051 (Apr. 2004) (cited on page 48).
128. Wiersma, R. P. C., Schaye, J., Theuns, T., Dalla Vecchia, C. & Tornatore, L. Chemical enrichment in cosmological, smoothed particle hydrodynamics simulations. MNRAS **399,** 574–600 (Oct. 2009) (cited on page 51).
129. Dolag, K., Borgani, S., Schindler, S., Diaferio, A. & Bykov, A. M. Simulation Techniques for Cosmological Simulations. Space Sci. Rev. **134,** 229–268 (Feb. 2008) (cited on page 51).
130. Maio, U., Dolag, K., Ciardi, B. & Tornatore, L. Metal and molecule cooling in simulations of structure formation. MNRAS **379,** 963–973 (Aug. 2007) (cited on page 51).
131. Krumholz, M. R., Dekel, A. & McKee, C. F. A Universal, Local Star Formation Law in Galactic Clouds, nearby Galaxies, High-redshift Disks, and Starbursts. ApJ **745,** 69 (Jan. 2012) (cited on pages 52, 53).
132. Schmidt, M. The Rate of Star Formation. ApJ **129,** 243 (Mar. 1959) (cited on page 52).
133. Kennicutt Robert C., J. The Star Formation Law in Galactic Disks. ApJ **344,** 685 (Sept. 1989) (cited on page 52).
134. Schaye, J. & Dalla Vecchia, C. On the relation between the Schmidt and Kennicutt-Schmidt star formation laws and its implications for numerical simulations. MNRAS **383,** 1210–1222 (Jan. 2008) (cited on page 52).
135. Springel, V., Di Matteo, T. & Hernquist, L. Modelling feedback from stars and black holes in galaxy mergers. MNRAS **361,** 776–794 (Aug. 2005) (cited on pages 52, 53, 75, 79).
136. Kim, C.-G. & Ostriker, E. C. Momentum Injection by Supernovae in the Interstellar Medium. ApJ **802,** 99 (Apr. 2015) (cited on page 53).
137. Smith, M. C., Sijacki, D. & Shen, S. Supernova feedback in numerical simulations of galaxy formation: separating physics from numerics. MNRAS **478,** 302–331 (July 2018) (cited on page 53).
138. Stinson, G. *et al.* Star formation and feedback in smoothed particle hydrodynamic simulations - I. Isolated galaxies. MNRAS **373,** 1074–1090 (Dec. 2006) (cited on pages 53, 73).
139. Teyssier, R., Pontzen, A., Dubois, Y. & Read, J. I. Cusp-core transformations in dwarf galaxies: observational predictions. MNRAS **429,** 3068–3078 (Mar. 2013) (cited on pages 53, 72).
140. Bigiel, F. *et al.* A Constant Molecular Gas Depletion Time in Nearby Disk Galaxies. ApJ **730,** L13 (Apr. 2011) (cited on page 53).
141. Volonteri, M. Formation of supermassive black holes. A&A Rev. **18,** 279–315 (July 2010) (cited on page 53).
142. Rosas-Guevara, Y. M. *et al.* The impact of angular momentum on black hole accretion rates in simulations of galaxy formation. MNRAS **454,** 1038–1057 (Nov. 2015) (cited on pages 53, 76).

143. Weinberger, R. *et al.* Simulating galaxy formation with black hole driven thermal and kinetic feedback. MNRAS **465,** 3291–3308 (Mar. 2017) (cited on pages 53, 77).
144. Booth, C. M. & Schaye, J. Cosmological simulations of the growth of supermassive black holes and feedback from active galactic nuclei: method and tests. MNRAS **398,** 53–74 (Sept. 2009) (cited on pages 53, 75, 79, 95, 153, 162).
145. Marinacci, F., Vogelsberger, M., Mocz, P. & Pakmor, R. The large-scale properties of simulated cosmological magnetic fields. MNRAS **453,** 3999–4019 (Nov. 2015) (cited on pages 54, 58, 107, 111, 114, 117, 119, 120, 123, 124).
146. Nelson, D. *et al.* First results from the IllustrisTNG simulations: the galaxy colour bimodality. MNRAS **475,** 624–647 (Mar. 2018) (cited on pages 54, 58).
147. Naiman, J. P. *et al.* First results from the IllustrisTNG simulations: a tale of two elements - chemical evolution of magnesium and europium. MNRAS **477,** 1206–1224 (June 2018) (cited on pages 54, 58).
148. Pillepich, A. *et al.* Simulating galaxy formation with the IllustrisTNG model. MNRAS **473,** 4077–4106 (Jan. 2018) (cited on pages 54, 55, 58).
149. Zjupa, J., Schäfer, B. M. & Hahn, O. Intrinsic Alignments in IllustrisTNG and their implications for weak lensing: Tidal shearing and tidal torquing mechanisms put to the test. *arXiv e-prints,* arXiv:2010.07951 (Oct. 2020) (cited on page 55).
150. Schaye, J. *et al.* The EAGLE project: simulating the evolution and assembly of galaxies and their environments. MNRAS **446,** 521–554 (Jan. 2015) (cited on pages 55, 58).
151. Vogelsberger, M., Marinacci, F., Torrey, P. & Puchwein, E. Cosmological simulations of galaxy formation. *Nature Reviews Physics* **2,** 42–66 (Jan. 2020) (cited on pages 56, 57).
152. Naab, T. & Ostriker, J. P. *Theoretical Challenges in Galaxy Formation* Aug. 2017 (cited on pages 56, 57).
153. Rasia, E. *et al.* Cool Core Clusters from Cosmological Simulations. ApJ **813,** L17 (Nov. 2015) (cited on pages 55, 134).
154. Teyssier, R. Cosmological hydrodynamics with adaptive mesh refinement. A new high resolution code called RAMSES. A&A **385,** 337–364 (Apr. 2002) (cited on pages 57, 61).
155. Bryan, G. L. *et al.* ENZO: An Adaptive Mesh Refinement Code for Astrophysics. ApJS **211,** 19 (Apr. 2014) (cited on page 57).
156. Springel, V. The cosmological simulation code GADGET-2. MNRAS **364,** 1105–1134 (Dec. 2005) (cited on page 57).
157. Springel, V. E pur si muove: Galilean-invariant cosmological hydrodynamical simulations on a moving mesh. MNRAS **401,** 791–851 (Jan. 2010) (cited on page 57).
158. Menon, H. *et al.* Adaptive techniques for clustered N-body cosmological simulations. *Computational Astrophysics and Cosmology* **2,** 1 (Mar. 2015) (cited on page 57).
159. Vogelsberger, M. *et al.* Introducing the Illustris Project: simulating the coevolution of dark and visible matter in the Universe. MNRAS **444,** 1518–1547 (Oct. 2014) (cited on page 58).

160. Nelson, D. *et al.* First results from the TNG50 simulation: galactic outflows driven by supernovae and black hole feedback. MNRAS **490,** 3234–3261 (Dec. 2019) (cited on page 58).
161. Pillepich, A. *et al.* First results from the TNG50 simulation: the evolution of stellar and gaseous discs across cosmic time. MNRAS **490,** 3196–3233 (Dec. 2019) (cited on page 58).
162. Le Brun, A. M. C., McCarthy, I. G., Schaye, J. & Ponman, T. J. Towards a realistic population of simulated galaxy groups and clusters. MNRAS **441,** 1270–1290 (June 2014) (cited on pages 58, 96, 224).
163. McCarthy, I. G., Schaye, J., Bird, S. & Le Brun, A. M. C. The BAHAMAS project: calibrated hydrodynamical simulations for large-scale structure cosmology. MNRAS **465,** 2936–2965 (Mar. 2017) (cited on page 58).
164. Wu, H.-Y. *et al.* RHAPSODY-G simulations: galaxy clusters as baryonic closed boxes and the covariance between hot gas and galaxies. MNRAS **452,** 1982–1991 (Sept. 2015) (cited on pages 58, 80, 92).
165. Henden, N. A., Puchwein, E., Shen, S. & Sijacki, D. The FABLE simulations: a feedback model for galaxies, groups, and clusters. MNRAS **479,** 5385–5412 (Oct. 2018) (cited on page 58).
166. Cui, W. *et al.* The Three Hundred project: a large catalogue of theoretically modelled galaxy clusters for cosmological and astrophysical applications. MNRAS **480,** 2898–2915 (Nov. 2018) (cited on pages 58, 206, 209, 213–215).
167. Tremmel, M. *et al.* Introducing ROMULUSC: a cosmological simulation of a galaxy cluster with an unprecedented resolution. MNRAS **483,** 3336–3362 (Mar. 2019) (cited on page 58).
168. Frenk, C. S. *et al.* The Santa Barbara Cluster Comparison Project: A Comparison of Cosmological Hydrodynamics Solutions. ApJ **525,** 554–582 (Nov. 1999) (cited on page 58).
169. Sembolini, F. *et al.* nIFTy galaxy cluster simulations - I. Dark matter and non-radiative models. MNRAS **457,** 4063–4080 (Apr. 2016) (cited on pages 58, 59).
170. Sembolini, F. *et al.* nIFTy galaxy cluster simulations - II. Radiative models. MNRAS **459,** 2973–2991 (July 2016) (cited on pages 58, 59).
171. Elahi, P. J. *et al.* nIFTY galaxy cluster simulations - III. The similarity and diversity of galaxies and subhaloes. MNRAS **458,** 1096–1116 (May 2016) (cited on pages 58–60).
172. Cui, W. *et al.* nIFTy galaxy cluster simulations - IV. Quantifying the influence of baryons on halo properties. MNRAS **458,** 4052–4073 (June 2016) (cited on page 58).
173. Truelove, J. K. *et al.* The Jeans Condition: A New Constraint on Spatial Resolution in Simulations of Isothermal Self-gravitational Hydrodynamics. ApJ **489,** L179–L183 (Nov. 1997) (cited on pages 62, 71).
174. Martel, H. & Shapiro, P. R. A convenient set of comoving cosmological variables and their application. MNRAS **297,** 467–485 (June 1998) (cited on page 64).
175. Ryu, D., Ostriker, J. P., Kang, H. & Cen, R. A Cosmological Hydrodynamic Code Based on the Total Variation Diminishing Scheme. ApJ **414,** 1 (Sept. 1993) (cited on page 64).

176. Doumler, T. & Knebe, A. Investigating the influence of magnetic fields upon structure formation with AMIGA - a C code for cosmological magnetohydrodynamics. MNRAS **403,** 453–473 (Mar. 2010) (cited on page 65).
177. Fromang, S., Hennebelle, P. & Teyssier, R. A high order Godunov scheme with constrained transport and adaptive mesh refinement for astrophysical magnetohydrodynamics. A&A **457,** 371–384 (Oct. 2006) (cited on pages 66, 67, 112, 120).
178. Evans, C. R. & Hawley, J. F. Simulation of Magnetohydrodynamic Flows: A Constrained Transport Model. ApJ **332,** 659 (Sept. 1988) (cited on pages 66, 112).
179. Dubois, Y. & Commerçon, B. An implicit scheme for solving the anisotropic diffusion of heat and cosmic rays in the RAMSES code. A&A **585,** A138 (Jan. 2016) (cited on pages 66–68, 134, 224).
180. Commerçon, B., Teyssier, R., Audit, E., Hennebelle, P. & Chabrier, G. Radiation hydrodynamics with adaptive mesh refinement and application to prestellar core collapse. I. Methods. A&A **529,** A35 (May 2011) (cited on page 67).
181. Katz, N., Weinberg, D. H. & Hernquist, L. Cosmological Simulations with TreeSPH. ApJS **105,** 19 (July 1996) (cited on page 68).
182. Sutherland, R. S. & Dopita, M. A. Cooling Functions for Low-Density Astrophysical Plasmas. ApJS **88,** 253 (Sept. 1993) (cited on pages 68, 94).
183. Rosen, A. & Bregman, J. N. Global Models of the Interstellar Medium in Disk Galaxies. ApJ **440,** 634 (Feb. 1995) (cited on page 68).
184. Haardt, F. & Madau, P. Radiative Transfer in a Clumpy Universe. II. The Ultraviolet Extragalactic Background. ApJ **461,** 20 (Apr. 1996) (cited on pages 69, 94).
185. Cavagnolo, K. W., Donahue, M., Voit, G. M. & Sun, M. Intracluster Medium Entropy Profiles for a Chandra Archival Sample of Galaxy Clusters. ApJS **182,** 12–32 (May 2009) (cited on pages 69, 177, 180).
186. Springel, V. & Hernquist, L. Cosmological smoothed particle hydrodynamics simulations: a hybrid multiphase model for star formation. MNRAS **339,** 289–311 (Feb. 2003) (cited on page 70).
187. Kennicutt Robert C., J. The Global Schmidt Law in Star-forming Galaxies. ApJ **498,** 541–552 (May 1998) (cited on page 71).
188. Krumholz, M. R. & Tan, J. C. Slow Star Formation in Dense Gas: Evidence and Implications. ApJ **654,** 304–315 (Jan. 2007) (cited on page 71).
189. Salpeter, E. E. The Luminosity Function and Stellar Evolution. ApJ **121,** 161 (Jan. 1955) (cited on pages 71, 85, 143).
190. Minkowski, R. Spectra of the Supernova in NGC 4725. PASP **52,** 206 (June 1940) (cited on page 72).
191. Wheeler, J. C. & Harkness, R. P. Type I supernovae. *Reports on Progress in Physics* **53,** 1467–1557 (Dec. 1990) (cited on page 72).
192. Schneider, P. *Extragalactic Astronomy and Cosmology: An Introduction* (2015) (cited on page 72).
193. Sedov, L. I. *Similarity and Dimensional Methods in Mechanics* (1959) (cited on page 72).

194. Taylor, G. The Formation of a Blast Wave by a Very Intense Explosion. I. Theoretical Discussion. *Proceedings of the Royal Society of London Series A* **201,** 159–174 (Mar. 1950) (cited on page 72).
195. Dubois, Y. & Teyssier, R. On the onset of galactic winds in quiescent star forming galaxies. A&A **477,** 79–94 (Jan. 2008) (cited on page 72).
196. Dubois, Y. *et al.* Black hole evolution - I. Supernova-regulated black hole growth. MNRAS **452,** 1502–1518 (Sept. 2015) (cited on pages 72, 73).
197. Bleuler, A. & Teyssier, R. Towards a more realistic sink particle algorithm for the RAMSES CODE. MNRAS **445,** 4015–4036 (Dec. 2014) (cited on pages 73, 74, 77).
198. Jappsen, A. .-., Klessen, R. S., Larson, R. B., Li, Y. & Mac Low, M. .-. The stellar mass spectrum from non-isothermal gravoturbulent fragmentation. A&A **435,** 611–623 (May 2005) (cited on page 73).
199. Shen, S. & Wadsley, J. Proto-Brown Dwarf Disks as Products of Protostellar Disk Encounters. ApJ **651,** L145–L148 (Nov. 2006) (cited on page 73).
200. Wang, P., Li, Z.-Y., Abel, T. & Nakamura, F. Outflow Feedback Regulated Massive Star Formation in Parsec-Scale Cluster-Forming Clumps. ApJ **709,** 27–41 (Jan. 2010) (cited on page 73).
201. Federrath, C., Banerjee, R., Clark, P. C. & Klessen, R. S. Modeling Collapse and Accretion in Turbulent Gas Clouds: Implementation and Comparison of Sink Particles in AMR and SPH. ApJ **713,** 269–290 (Apr. 2010) (cited on page 73).
202. Gong, H. & Ostriker, E. C. Implementation of Sink Particles in the Athena Code. ApJS **204,** 8 (Jan. 2013) (cited on page 73).
203. Bleuler, A., Teyssier, R., Carassou, S. & Martizzi, D. PHEW: a parallel segmentation algorithm for three-dimensional AMR datasets. Application to structure detection in self-gravitating flows. *Computational Astrophysics and Cosmology* **2,** 5 (June 2015) (cited on pages 74, 95).
204. Biernacki, P., Teyssier, R. & Bleuler, A. On the dynamics of supermassive black holes in gas-rich, star-forming galaxies: the case for nuclear star cluster co-evolution. MNRAS **469,** 295–313 (July 2017) (cited on pages 75, 77–80, 148).
205. Begelman, M. C., Volonteri, M. & Rees, M. J. Formation of supermassive black holes by direct collapse in pre-galactic haloes. MNRAS **370,** 289–298 (July 2006) (cited on page 75).
206. Hoyle, F. & Lyttleton, R. A. The effect of interstellar matter on climatic variation. *Proceedings of the Cambridge Philosophical Society* **35,** 405 (Jan. 1939) (cited on page 75).
207. Bondi, H. & Hoyle, F. On the mechanism of accretion by stars. MNRAS **104,** 273 (Jan. 1944) (cited on page 75).
208. Bondi, H. On spherically symmetrical accretion. MNRAS **112,** 195 (Jan. 1952) (cited on page 75).
209. Edgar, R. A review of Bondi-Hoyle-Lyttleton accretion. New A Rev. **48,** 843–859 (Sept. 2004) (cited on page 75).
210. Shakura, N. I. & Sunyaev, R. A. Reprint of 1973A&A....24..337S. Black holes in binary systems. Observational appearance. A&A **500,** 33–51 (June 1973) (cited on page 76).

211. Negri, A. & Volonteri, M. Black hole feeding and feedback: the physics inside the 'sub-grid'. MNRAS **467,** 3475–3492 (May 2017) (cited on page 76).
212. Sijacki, D., Springel, V., Di Matteo, T. & Hernquist, L. A unified model for AGN feedback in cosmological simulations of structure formation. MNRAS **380,** 877–900 (Sept. 2007) (cited on page 77).
213. Gabor, J. M. & Bournaud, F. Simulations of supermassive black hole growth in high-redshift disc galaxies. MNRAS **434,** 606–620 (Sept. 2013) (cited on pages 77, 79).
214. Wurster, J. & Thacker, R. J. A comparative study of AGN feedback algorithms. MNRAS **431,** 2513–2534 (May 2013) (cited on page 77).
215. Hirschmann, M. *et al.* Cosmological simulations of black hole growth: AGN luminosities and downsizing. MNRAS **442,** 2304–2324 (Aug. 2014) (cited on page 77).
216. Costa, T., Sijacki, D. & Haehnelt, M. G. Feedback from active galactic nuclei: energy- versus momentum-driving. MNRAS **444,** 2355–2376 (Nov. 2014) (cited on page 77).
217. Volonteri, M., Dubois, Y., Pichon, C. & Devriendt, J. The cosmic evolution of massive black holes in the Horizon-AGN simulation. MNRAS **460,** 2979–2996 (Aug. 2016) (cited on page 77).
218. Shen, Y., Hwang, H.-C., Zakamska, N. & Liu, X. Varstrometry for Off-nucleus and Dual Sub-Kpc AGN (VODKA): How Well Centered Are Low-z AGN? ApJ **885,** L4 (Nov. 2019) (cited on page 78).
219. Reines, A. E., Condon, J. J., Darling, J. & Greene, J. E. A New Sample of (Wandering) Massive Black Holes in Dwarf Galaxies from High-resolution Radio Observations. ApJ **888,** 36 (Jan. 2020) (cited on page 78).
220. Pfister, H., Volonteri, M., Dubois, Y., Dotti, M. & Colpi, M. The erratic dynamical life of black hole seeds in high-redshift galaxies. MNRAS **486,** 101–111 (June 2019) (cited on page 78).
221. Boldrini, P., Mohayaee, R. & Silk, J. Subhalo sinking and off-centre massive black holes in dwarf galaxies. MNRAS **495,** L12–L16 (June 2020) (cited on page 78).
222. Dubois, Y., Devriendt, J., Slyz, A. & Teyssier, R. Self-regulated growth of supermassive black holes by a dual jet-heating active galactic nucleus feedback mechanism: methods, tests and implications for cosmological simulations. MNRAS **420,** 2662–2683 (Mar. 2012) (cited on pages 79, 83).
223. Meece, G. R., Voit, G. M. & O'Shea, B. W. Triggering and Delivery Algorithms for AGN Feedback. ApJ **841,** 133 (June 2017) (cited on pages 79, 224).
224. Teyssier, R., Moore, B., Martizzi, D., Dubois, Y. & Mayer, L. Mass distribution in galaxy clusters: the role of Active Galactic Nuclei feedback. MNRAS **414,** 195–208 (June 2011) (cited on page 79).
225. Martizzi, D. *et al.* RHAPSODY-G simulations - II. Baryonic growth and metal enrichment in massive galaxy clusters. MNRAS **459,** 4408–4427 (July 2016) (cited on pages 80, 84, 85, 92).
226. Wu, H.-Y., Hahn, O., Wechsler, R. H., Mao, Y.-Y. & Behroozi, P. S. Rhapsody. I. Structural Properties and Formation History from a Statistical Sample of Re-simulated Cluster-size Halos. ApJ **763,** 70 (Feb. 2013) (cited on pages 80, 82, 83, 92).

227. Wu, H.-Y., Hahn, O., Wechsler, R. H., Behroozi, P. S. & Mao, Y.-Y. Rhapsody. II. Subhalo Properties and the Impact of Tidal Stripping From a Statistical Sample of Cluster-size Halos. ApJ **767,** 23 (Apr. 2013) (cited on pages 80, 92).
228. Behroozi, P. S., Wechsler, R. H. & Wu, H.-Y. The ROCKSTAR Phase-space Temporal Halo Finder and the Velocity Offsets of Cluster Cores. ApJ **762,** 109 (Jan. 2013) (cited on pages 81, 83).
229. Behroozi, P. S. *et al.* Gravitationally Consistent Halo Catalogs and Merger Trees for Precision Cosmology. ApJ **763,** 18 (Jan. 2013) (cited on page 81).
230. Crocce, M., Pueblas, S. & Scoccimarro, R. Transients from initial conditions in cosmological simulations. MNRAS **373,** 369–381 (Nov. 2006) (cited on page 81).
231. Kravtsov, A. V., Vikhlinin, A. A. & Meshcheryakov, A. V. Stellar Mass—Halo Mass Relation and Star Formation Efficiency in High-Mass Halos. *Astronomy Letters* **44,** 8–34 (Jan. 2018) (cited on pages 83, 143).
232. Behroozi, P. S., Wechsler, R. H. & Conroy, C. The Average Star Formation Histories of Galaxies in Dark Matter Halos from z = 0-8. ApJ **770,** 57 (June 2013) (cited on page 83).
233. Martizzi, D., Teyssier, R. & Moore, B. The formation of the brightest cluster galaxies in cosmological simulations: the case for active galactic nucleus feedback. MNRAS **420,** 2859–2873 (Mar. 2012) (cited on page 84).
234. Woo, J. *et al.* Dependence of galaxy quenching on halo mass and distance from its centre. MNRAS **428,** 3306–3326 (Feb. 2013) (cited on pages 83, 84, 168, 169).
235. Liu, F. S., Mao, S. & Meng, X. M. Star formation activities in early-type brightest cluster galaxies. MNRAS **423,** 422–436 (June 2012) (cited on pages 84, 168, 169).
236. McDonald, M. *et al.* Deep Chandra, HST-COS, and Megacam Observations of the Phoenix Cluster: Extreme Star Formation and AGN Feedback on Hundred Kiloparsec Scales. ApJ **811,** 111 (Oct. 2015) (cited on page 84).
237. Oliva-Altamirano, P. *et al.* The accretion histories of brightest cluster galaxies from their stellar population gradients. MNRAS **449,** 3347–3359 (June 2015) (cited on page 85).
238. Gallazzi, A., Charlot, S., Brinchmann, J., White, S. D. M. & Tremonti, C. A. The ages and metallicities of galaxies in the local universe. MNRAS **362,** 41–58 (Sept. 2005) (cited on page 85).
239. Mantz, A. B. *et al.* Cosmology and astrophysics from relaxed galaxy clusters - II. Cosmological constraints. MNRAS **440,** 2077–2098 (May 2014) (cited on pages 85, 86).
240. Mazzotta, P., Rasia, E., Moscardini, L. & Tormen, G. Comparing the temperatures of galaxy clusters from hydrodynamical N-body simulations to Chandra and XMM-Newton observations. MNRAS **354,** 10–24 (Oct. 2004) (cited on pages 88, 189, 196).
241. Planck Collaboration *et al.* Planck 2015 results. XIII. Cosmological parameters. A&A **594,** A13 (Sept. 2016) (cited on pages 92, 97, 179, 201).
242. Buehlmann, M. & Hahn, O. The cosmIC database. *tbd* (in prep, 2021) (cited on page 92).

243. Angulo, R. E., Hahn, O. & Abel, T. How closely do baryons follow dark matter on large scales? MNRAS **434,** 1756–1764 (Sept. 2013) (cited on page 93).
244. Hahn, O., Rampf, C. & Uhlemann, C. Higher order initial conditions for mixed baryon-CDM simulations. MNRAS **503,** 426–445 (May 2021) (cited on page 93).
245. Khoraminezhad, H., Lazeyras, T., Angulo, R. E., Hahn, O. & Viel, M. Quantifying the impact of baryon-CDM perturbations on halo clustering and baryon fraction. J. Cosmology Astropart. Phys. **2021,** 023 (Mar. 2021) (cited on page 93).
246. Neronov, A. & Vovk, I. Evidence for Strong Extragalactic Magnetic Fields from Fermi Observations of TeV Blazars. *Science* **328,** 73 (Apr. 2010) (cited on page 98).
247. Ryu, D., Schleicher, D. R. G., Treumann, R. A., Tsagas, C. G. & Widrow, L. M. *Magnetic Fields in the Large-Scale Structure of the Universe* May 2012 (cited on page 98).
248. Willson, M. A. G. Radio observations of the cluster of galaxies in Coma Berenices - the 5C4 survey. MNRAS **151,** 1 (Jan. 1970) (cited on page 98).
249. Kim, K. .-., Kronberg, P. P., Dewdney, P. E. & Landecker, T. L. The Halo and Magnetic Field of the Coma Cluster of Galaxies. ApJ **355,** 29 (May 1990) (cited on page 98).
250. Schekochihin, A. A. & Cowley, S. C. in *Magnetohydrodynamics: Historical Evolution and Trends* (eds Molokov, S., Moreau, R. & Moffatt, H. K.) 85 (2007) (cited on pages 98, 99).
251. Govoni, F. *et al.* The intracluster magnetic field power spectrum in Abell 2255. A&A **460,** 425–438 (Dec. 2006) (cited on page 98).
252. Bonafede, A. *et al. Unravelling the origin of large-scale magnetic fields in galaxy clusters and beyond through Faraday Rotation Measures with the SKA* in *Advancing Astrophysics with the Square Kilometre Array (AASKA14)* (Apr. 2015), 95 (cited on page 99).
253. Govoni, F. *et al. Cluster magnetic fields through the study of polarized radio halos in the SKA era* in *Advancing Astrophysics with the Square Kilometre Array (AASKA14)* (Apr. 2015), 105 (cited on page 99).
254. Ferrari, C. *et al. Non-thermal emission from galaxy clusters: feasibility study with SKA* in *Advancing Astrophysics with the Square Kilometre Array (AASKA14)* (Apr. 2015), 75 (cited on page 100).
255. Vazza, F. *et al. Filaments of the radio cosmic web: opportunities and challenges for SKA* in *Advancing Astrophysics with the Square Kilometre Array (AASKA14)* (Apr. 2015), 97 (cited on page 100).
256. Botteon, A. *et al.* A giant radio bridge connecting two galaxy clusters in Abell 1758. MNRAS **499,** L11–L15 (Dec. 2020) (cited on page 100).
257. Govoni, F. *et al.* A radio ridge connecting two galaxy clusters in a filament of the cosmic web. *Science* **364,** 981–984 (June 2019) (cited on page 100).
258. Trivedi, P., Subramanian, K. & Seshadri, T. R. Primordial magnetic field limits from the CMB trispectrum: Scalar modes and Planck constraints. Phys. Rev. D **89,** 043523 (Feb. 2014) (cited on page 100).
259. Planck Collaboration *et al.* Planck 2015 results. XIX. Constraints on primordial magnetic fields. A&A **594,** A19 (Sept. 2016) (cited on page 100).

260. Subramanian, K. The origin, evolution and signatures of primordial magnetic fields. *Reports on Progress in Physics* **79,** 076901 (July 2016) (cited on pages 101, 106).
261. Donnert, J., Vazza, F., Brüggen, M. & ZuHone, J. *Magnetic Field Amplification in Galaxy Clusters and Its Simulation* Dec. 2018 (cited on pages 101, 103, 107, 108).
262. Biermann, L. Über den Ursprung der Magnetfelder auf Sternen und im interstellaren Raum (miteinem Anhang von A. Schlüter). *Zeitschrift Naturforschung Teil A* **5,** 65 (Jan. 1950) (cited on page 101).
263. Lazar, M., Smolyakov, A., Schlickeiser, R. & Shukla, P. K. A comparative study of the filamentation and Weibel instabilities and their cumulative effect. I. Non-relativistic theory. *Journal of Plasma Physics* **75,** 19–33 (Feb. 2009) (cited on page 101).
264. Brandenburg, A. & Subramanian, K. Astrophysical magnetic fields and nonlinear dynamo theory. Phys. Rep. **417,** 1–209 (Oct. 2005) (cited on page 101).
265. Bertone, S., Vogt, C. & Enßlin, T. Magnetic field seeding by galactic winds. MNRAS **370,** 319–330 (July 2006) (cited on page 101).
266. Donnert, J. & Brunetti, G. An efficient Fokker-Planck solver and its application to stochastic particle acceleration in galaxy clusters. MNRAS **443,** 3564–3577 (Oct. 2014) (cited on page 102).
267. Schekochihin, A. A., Maron, J. L., Cowley, S. C. & McWilliams, J. C. The Small-Scale Structure of Magnetohydrodynamic Turbulence with Large Magnetic Prandtl Numbers. ApJ **576,** 806–813 (Sept. 2002) (cited on page 103).
268. Bell, A. R. Turbulent amplification of magnetic field and diffusive shock acceleration of cosmic rays. MNRAS **353,** 550–558 (Sept. 2004) (cited on page 103).
269. Riquelme, M. A. & Spitkovsky, A. Magnetic Amplification by Magnetized Cosmic Rays in Supernova Remnant Shocks. ApJ **717,** 1054–1066 (July 2010) (cited on page 103).
270. Marcowith, A. *et al.* The microphysics of collisionless shock waves. *Reports on Progress in Physics* **79,** 046901 (Apr. 2016) (cited on page 103).
271. Brüggen, M., Bykov, A., Ryu, D. & Röttgering, H. Magnetic Fields, Relativistic Particles, and Shock Waves in Cluster Outskirts. Space Sci. Rev. **166,** 187–213 (May 2012) (cited on page 104).
272. Inoue, T., Yamazaki, R. & Inutsuka, S.-i. Turbulence and Magnetic Field Amplification in Supernova Remnants: Interactions Between a Strong Shock Wave and Multiphase Interstellar Medium. ApJ **695,** 825–833 (Apr. 2009) (cited on page 104).
273. Iapichino, L. & Brüggen, M. Magnetic field amplification by shocks in galaxy clusters: application to radio relics. MNRAS **423,** 2781–2788 (July 2012) (cited on page 104).
274. Stroe, A. *et al.* Discovery of spectral curvature in the shock downstream region: CIZA J2242.8+5301. A&A **555,** A110 (July 2013) (cited on page 104).
275. Zuhone, J. A. & Roediger, E. Cold fronts: probes of plasma astrophysics in galaxy clusters. *Journal of Plasma Physics* **82,** 535820301 (June 2016) (cited on page 104).
276. Walker, S. A., ZuHone, J., Fabian, A. & Sanders, J. The split in the ancient cold front in the Perseus cluster. *Nature Astronomy* **2,** 292–296 (Feb. 2018) (cited on page 104).

277. Zinger, E. *et al.* Cold fronts and shocks formed by gas streams in galaxy clusters. MNRAS **476,** 56–70 (May 2018) (cited on page 104).
278. Lyutikov, M. Magnetic draping of merging cores and radio bubbles in clusters of galaxies. MNRAS **373,** 73–78 (Nov. 2006) (cited on page 104).
279. Mazzotta, P. & Giacintucci, S. Do Radio Core-Halos and Cold Fronts in Non-Major-Merging Clusters Originate from the Same Gas Sloshing? ApJ **675,** L9 (Mar. 2008) (cited on page 104).
280. ZuHone, J. A., Markevitch, M., Brunetti, G. & Giacintucci, S. Turbulence and Radio Mini-halos in the Sloshing Cores of Galaxy Clusters. ApJ **762,** 78 (Jan. 2013) (cited on page 105).
281. Dubois, Y. & Teyssier, R. Cosmological MHD simulation of a cooling flow cluster. A&A **482,** L13–L16 (May 2008) (cited on pages 107, 114, 117, 123, 124).
282. Dolag, K., Bykov, A. M. & Diaferio, A. Non-Thermal Processes in Cosmological Simulations. Space Sci. Rev. **134,** 311–335 (Feb. 2008) (cited on page 108).
283. Dolag, K., Grasso, D., Springel, V. & Tkachev, I. Constrained simulations of the magnetic field in the local Universe and the propagation of ultrahigh energy cosmic rays. J. Cosmology Astropart. Phys. **2005,** 009 (Jan. 2005) (cited on page 108).
284. Kolmogorov, A. The Local Structure of Turbulence in Incompressible Viscous Fluid for Very Large Reynolds' Numbers. *Akademiia Nauk SSSR Doklady* **30,** 301–305 (Jan. 1941) (cited on page 108).
285. Vazza, F., Tormen, G., Cassano, R., Brunetti, G. & Dolag, K. Turbulent velocity fields in smoothed particle hydrodymanics simulated galaxy clusters: scaling laws for the turbulent energy. MNRAS **369,** L14–L18 (June 2006) (cited on page 108).
286. Ryu, D., Kang, H., Cho, J. & Das, S. Turbulence and Magnetic Fields in the Large-Scale Structure of the Universe. *Science* **320,** 909 (May 2008) (cited on page 108).
287. Nagai, D., Kravtsov, A. V. & Vikhlinin, A. Effects of Galaxy Formation on Thermodynamics of the Intracluster Medium. ApJ **668,** 1–14 (Oct. 2007) (cited on pages 109, 156, 173).
288. Battaglia, N., Bond, J. R., Pfrommer, C. & Sievers, J. L. On the Cluster Physics of Sunyaev-Zel'dovich and X-Ray Surveys. II. Deconstructing the Thermal SZ Power Spectrum. ApJ **758,** 75 (Oct. 2012) (cited on page 109).
289. Nelson, K., Lau, E. T. & Nagai, D. Hydrodynamic Simulation of Non-thermal Pressure Profiles of Galaxy Clusters. ApJ **792,** 25 (Sept. 2014) (cited on page 109).
290. Schmidt, W., Byrohl, C., Engels, J. F., Behrens, C. & Niemeyer, J. C. Viscosity, pressure and support of the gas in simulations of merging cool-core clusters. MNRAS **470,** 142–156 (Sept. 2017) (cited on page 109).
291. Xu, H., Li, H., Collins, D. C., Li, S. & Norman, M. L. Turbulence and Dynamo in Galaxy Cluster Medium: Implications on the Origin of Cluster Magnetic Fields. ApJ **698,** L14–L17 (June 2009) (cited on pages 109, 110, 114, 123).
292. Vazza, F. *et al.* Turbulent motions and shocks waves in galaxy clusters simulated with adaptive mesh refinement. A&A **504,** 33–43 (Sept. 2009) (cited on page 109).

293. Vazza, F., Brunetti, G., Gheller, C., Brunino, R. & Brüggen, M. Massive and refined. II. The statistical properties of turbulent motions in massive galaxy clusters with high spatial resolution. A&A **529,** A17 (May 2011) (cited on page 109).
294. Iapichino, L., Schmidt, W., Niemeyer, J. C. & Merklein, J. Turbulence production and turbulent pressure support in the intergalactic medium. MNRAS **414,** 2297–2308 (July 2011) (cited on page 109).
295. Ruszkowski, M., Lee, D., Brüggen, M., Parrish, I. & Oh, S. P. Cosmological Magnetohydrodynamic Simulations of Cluster Formation with Anisotropic Thermal Conduction. ApJ **740,** 81 (Oct. 2011) (cited on pages 109, 110, 133, 134, 158).
296. Vazza, F., Roediger, E. & Brüggen, M. Turbulence in the ICM from mergers, cool-core sloshing, and jets: results from a new multi-scale filtering approach. A&A **544,** A103 (Aug. 2012) (cited on page 109).
297. Miniati, F. The Matryoshka Run: A Eulerian Refinement Strategy to Study the Statistics of Turbulence in Virialized Cosmic Structures. ApJ **782,** 21 (Feb. 2014) (cited on pages 109, 110).
298. Miniati, F. The Matryoshka Run. II. Time-dependent Turbulence Statistics, Stochastic Particle Acceleration, and Microphysics Impact in a Massive Galaxy Cluster. ApJ **800,** 60 (Feb. 2015) (cited on pages 109, 110).
299. Burgers, J. M. in *Selected Papers of J. M. Burgers* (eds Nieuwstadt, F. T. M. & Steketee, J. A.) 335–389 (Springer Netherlands, Dordrecht, 1995) (cited on page 110).
300. Dolag, K., Bartelmann, M. & Lesch, H. SPH simulations of magnetic fields in galaxy clusters. A&A **348,** 351–363 (Aug. 1999) (cited on page 110).
301. Dolag, K., Bartelmann, M. & Lesch, H. Evolution and structure of magnetic fields in simulated galaxy clusters. A&A **387,** 383–395 (May 2002) (cited on page 110).
302. Dolag, K. & Enßlin, T. A. Radio halos of galaxy clusters from hadronic secondary electron injection in realistic magnetic field configurations. A&A **362,** 151–157 (Oct. 2000) (cited on page 110).
303. Dolag, K. & Schindler, S. The effect of magnetic fields on the mass determination of clusters of galaxies. A&A **364,** 491–496 (Dec. 2000) (cited on page 110).
304. Dolag, K., Evrard, A. & Bartelmann, M. The temperature-mass relation in magnetized galaxy clusters. A&A **369,** 36–41 (Apr. 2001) (cited on page 110).
305. Dolag, K., Grasso, D., Springel, V. & Tkachev, I. Constrained simulations of the magnetic field in the local Universe and the propagation of ultrahigh energy cosmic rays. J. Cosmology Astropart. Phys. **2005,** 009 (Jan. 2005) (cited on page 110).
306. Dolag, K., Gaensler, B. M., Beck, A. M. & Beck, M. C. Constraints on the distribution and energetics of fast radio bursts using cosmological hydrodynamic simulations. MNRAS **451,** 4277–4289 (Aug. 2015) (cited on page 110).
307. Donnert, J., Dolag, K., Lesch, H. & Müller, E. Cluster magnetic fields from galactic outflows. MNRAS **392,** 1008–1021 (Jan. 2009) (cited on page 110).

308. Beck, A. M., Dolag, K., Lesch, H. & Kronberg, P. P. Strong magnetic fields and large rotation measures in protogalaxies from supernova seeding. MNRAS **435,** 3575–3586 (Nov. 2013) (cited on page 110).
309. Xu, H., Li, H., Collins, D. C., Li, S. & Norman, M. L. Evolution and Distribution of Magnetic Fields from Active Galactic Nuclei in Galaxy Clusters. II. The Effects of Cluster Size and Dynamical State. ApJ **739,** 77 (Oct. 2011) (cited on page 110).
310. Vazza, F., Brunetti, G., Brüggen, M. & Bonafede, A. Resolved magnetic dynamo action in the simulated intracluster medium. MNRAS **474,** 1672–1687 (Feb. 2018) (cited on pages 111, 117).
311. Domínguez-Fernández, P., Vazza, F., Brüggen, M. & Brunetti, G. Dynamical evolution of magnetic fields in the intracluster medium. MNRAS **486,** 623–638 (June 2019) (cited on pages 111, 114, 123).
312. Mocz, P. *et al.* A moving mesh unstaggered constrained transport scheme for magnetohydrodynamics. MNRAS **463,** 477–488 (Nov. 2016) (cited on pages 111, 113, 120, 123, 124).
313. Price, D. J. Resolving high Reynolds numbers in smoothed particle hydrodynamics simulations of subsonic turbulence. MNRAS **420,** L33–L37 (Feb. 2012) (cited on page 111).
314. Kritsuk, A. G. *et al.* Comparing Numerical Methods for Isothermal Magnetized Supersonic Turbulence. ApJ **737,** 13 (Aug. 2011) (cited on page 111).
315. Rieder, M. & Teyssier, R. A small-scale dynamo in feedback-dominated galaxies as the origin of cosmic magnetic fields - I. The kinematic phase. MNRAS **457,** 1722–1738 (Apr. 2016) (cited on page 111).
316. Hopkins, P. F. A new class of accurate, mesh-free hydrodynamic simulation methods. MNRAS **450,** 53–110 (June 2015) (cited on page 111).
317. Bauer, A. *et al.* Simulating Turbulence Using the Astrophysical Discontinuous Galerkin Code TENET. *arXiv e-prints,* arXiv:1602.09079 (Feb. 2016) (cited on pages 111, 112).
318. Stasyszyn, F. A. & Elstner, D. A vector potential implementation for smoothed particle magnetohydrodynamics. *Journal of Computational Physics* **282,** 148–156 (Feb. 2015) (cited on page 111).
319. Dobbs, C. L., Price, D. J., Pettitt, A. R., Bate, M. R. & Tricco, T. S. Magnetic field evolution and reversals in spiral galaxies. MNRAS **461,** 4482–4495 (Oct. 2016) (cited on page 111).
320. Powell, K. G., Roe, P. L., Linde, T. J., Gombosi, T. I. & De Zeeuw, D. L. A Solution-Adaptive Upwind Scheme for Ideal Magnetohydrodynamics. *Journal of Computational Physics* **154,** 284–309 (Sept. 1999) (cited on pages 112, 119).
321. Dedner, A. *et al.* Hyperbolic Divergence Cleaning for the MHD Equations. *Journal of Computational Physics* **175,** 645–673 (Jan. 2002) (cited on pages 112, 113).
322. Marder, B. A Method for Incorporating Gauss' Law into Electromagnetic PIC Codes. *Journal of Computational Physics* **68,** 48–55 (Jan. 1987) (cited on pages 112, 113).
323. Teyssier, R., Fromang, S. & Dormy, E. Kinematic dynamos using constrained transport with high order Godunov schemes and

adaptive mesh refinement. *Journal of Computational Physics* **218,** 44–67 (Oct. 2006) (cited on page 112).

324. Stone, J. M., Gardiner, T. A., Teuben, P., Hawley, J. F. & Simon, J. B. Athena: A New Code for Astrophysical MHD. ApJS **178,** 137–177 (Sept. 2008) (cited on page 113).
325. Hopkins, P. F. A constrained-gradient method to control divergence errors in numerical MHD. MNRAS **462,** 576–587 (Oct. 2016) (cited on page 113).
326. Pakmor, R. & Springel, V. Simulations of magnetic fields in isolated disc galaxies. MNRAS **432,** 176–193 (June 2013) (cited on pages 113, 119).
327. Dolag, K. & Stasyszyn, F. An MHD GADGET for cosmological simulations. MNRAS **398,** 1678–1697 (Oct. 2009) (cited on page 113).
328. Price, D. J. *et al.* Phantom: A Smoothed Particle Hydrodynamics and Magnetohydrodynamics Code for Astrophysics. PASA **35,** e031 (Sept. 2018) (cited on page 113).
329. Quilis, V., Martí, J.-M. & Planelles, S. Cosmic magnetic fields with masclet: an application to galaxy clusters. MNRAS **494,** 2706–2717 (May 2020) (cited on pages 113, 114, 123).
330. Waagan, K., Federrath, C. & Klingenberg, C. A robust numerical scheme for highly compressible magnetohydrodynamics: Nonlinear stability, implementation and tests. *Journal of Computational Physics* **230,** 3331–3351 (May 2011) (cited on page 113).
331. Collins, D. C., Xu, H., Norman, M. L., Li, H. & Li, S. Cosmological Adaptive Mesh Refinement Magnetohydrodynamics with Enzo. ApJS **186,** 308–333 (Feb. 2010) (cited on page 113).
332. Wang, P. & Abel, T. Magnetohydrodynamic Simulations of Disk Galaxy Formation: The Magnetization of the Cold and Warm Medium. ApJ **696,** 96–109 (May 2009) (cited on page 113).
333. Tricco, T. S. & Price, D. J. Constrained hyperbolic divergence cleaning for smoothed particle magnetohydrodynamics. *Journal of Computational Physics* **231,** 7214–7236 (Aug. 2012) (cited on page 113).
334. Mocz, P., Burkhart, B., Hernquist, L., McKee, C. F. & Springel, V. Moving-mesh Simulations of Star-forming Cores in Magneto-gravo-turbulence. ApJ **838,** 40 (Mar. 2017) (cited on page 113).
335. Mocz, P. & Burkhart, B. Star formation from dense shocked regions in supersonic isothermal magnetoturbulence. MNRAS **480,** 3916–3927 (Nov. 2018) (cited on page 113).
336. Hopkins, P. F. & Raives, M. J. Accurate, meshless methods for magnetohydrodynamics. MNRAS **455,** 51–88 (Jan. 2016) (cited on page 113).
337. Vazza, F., Brüggen, M., Gheller, C. & Wang, P. On the amplification of magnetic fields in cosmic filaments and galaxy clusters. MNRAS **445,** 3706–3722 (Dec. 2014) (cited on pages 114, 117, 123).
338. Vogelsberger, M. *et al.* A model for cosmological simulations of galaxy formation physics. MNRAS **436,** 3031–3067 (Dec. 2013) (cited on page 119).
339. Zakamska, N. L. & Narayan, R. Models of Galaxy Clusters with Thermal Conduction. ApJ **582,** 162–169 (Jan. 2003) (cited on page 126).

340. Voit, G. M. & Donahue, M. Cooling Time, Freefall Time, and Precipitation in the Cores of ACCEPT Galaxy Clusters. ApJ **799,** L1 (Jan. 2015) (cited on pages 126, 134).
341. Rutherford, E. The scattering of α and β particles by matter and the structure of the atom. *The London, Edinburgh, and Dublin Philosophical Magazine and Journal of Science* **21,** 669–688 (1911) (cited on page 127).
342. Fitzpatrick, R. *Plasma Physics: An Introduction* (CRC Press, 2014) (cited on page 127).
343. Spitzer, L. *Physics of Fully Ionized Gases* (1962) (cited on page 128).
344. Qiu, Y., Bogdanović, T., Li, Y., McDonald, M. & McNamara, B. R. The formation of dusty cold gas filaments from galaxy cluster simulations. *Nature Astronomy* **4,** 900–906 (May 2020) (cited on page 129).
345. Spitzer, L. & Härm, R. Transport Phenomena in a Completely Ionized Gas. *Physical Review* **89,** 977–981 (Mar. 1953) (cited on page 129).
346. Cowie, L. L. & McKee, C. F. The evaporation of spherical clouds in a hot gas. I. Classical and saturated mass loss rates. ApJ **211,** 135–146 (Jan. 1977) (cited on page 130).
347. Sarazin, C. L. *X-ray emission from clusters of galaxies* (1988) (cited on page 130).
348. Arth, A., Dolag, K., Beck, A. M., Petkova, M. & Lesch, H. Anisotropic thermal conduction in galaxy clusters with MHD in Gadget. *arXiv e-prints,* arXiv:1412.6533 (Dec. 2014) (cited on pages 130, 134).
349. Braginskii, S. I. Transport Processes in a Plasma. *Reviews of Plasma Physics* **1,** 205 (Jan. 1965) (cited on page 130).
350. Chandran, B. D. G. & Cowley, S. C. Thermal Conduction in a Tangled Magnetic Field. Phys. Rev. Lett. **80,** 3077–3080 (Apr. 1998) (cited on pages 131, 132).
351. Krommes, J. A., Oberman, C. & Kleva, R. G. Plasma transport in stochastic magnetic fields. Part 3. Kinetics of test particle diffusion. *Journal of Plasma Physics* **30,** 11–56 (Aug. 1983) (cited on page 131).
352. Rechester, A. B. & Rosenbluth, M. N. Electron heat transport in a tokamak with destroyed magnetic surfaces. Phys. Rev. Lett. **40,** 38–41 (Jan. 1978) (cited on page 132).
353. Narayan, R. & Medvedev, M. V. Thermal Conduction in Clusters of Galaxies. ApJ **562,** L129–L132 (Dec. 2001) (cited on page 132).
354. Shalchi, A. Perpendicular Transport of Energetic Particles in Magnetic Turbulence. Space Sci. Rev. **216,** 23 (Feb. 2020) (cited on page 132).
355. Gary, S. P. *Theory of Space Plasma Microinstabilities* (1993) (cited on page 132).
356. Komarov, S. V., Churazov, E. M., Kunz, M. W. & Schekochihin, A. A. Thermal conduction in a mirror-unstable plasma. MNRAS **460,** 467–477 (July 2016) (cited on page 132).
357. Komarov, S., Schekochihin, A. A., Churazov, E. & Spitkovsky, A. Self-inhibiting thermal conduction in a high- , whistler-unstable plasma. *Journal of Plasma Physics* **84,** 905840305 (June 2018) (cited on page 132).
358. Balbus, S. A. Stability, Instability, and "Backward" Transport in Stratified Fluids. ApJ **534,** 420–427 (May 2000) (cited on page 133).

359. Quataert, E. Buoyancy Instabilities in Weakly Magnetized Low-Collisionality Plasmas. ApJ **673,** 758–762 (Feb. 2008) (cited on page 133).
360. Parrish, I. J. & Stone, J. M. Nonlinear Evolution of the Magnetothermal Instability in Two Dimensions. ApJ **633,** 334–348 (Nov. 2005) (cited on page 133).
361. Bogdanović, T., Reynolds, C. S., Balbus, S. A. & Parrish, I. J. Simulations of Magnetohydrodynamics Instabilities in Intracluster Medium Including Anisotropic Thermal Conduction. ApJ **704,** 211–225 (Oct. 2009) (cited on page 133).
362. Avara, M. J., Reynolds, C. S. & Bogdanović, T. Role of Magnetic Field Strength and Numerical Resolution in Simulations of the Heat-flux-driven Buoyancy Instability. ApJ **773,** 171 (Aug. 2013) (cited on page 133).
363. Berlok, T., Quataert, E., Pessah, M. E. & Pfrommer, C. Suppressed heat conductivity in the intracluster medium: implications for the magneto-thermal instability. MNRAS **504,** 3435–3454 (July 2021) (cited on page 133).
364. Dolag, K., Jubelgas, M., Springel, V., Borgani, S. & Rasia, E. Thermal Conduction in Simulated Galaxy Clusters. ApJ **606,** L97–L100 (May 2004) (cited on page 134).
365. Kannan, R., Springel, V., Pakmor, R., Marinacci, F. & Vogelsberger, M. Accurately simulating anisotropic thermal conduction on a moving mesh. MNRAS **458,** 410–424 (May 2016) (cited on page 134).
366. Barnes, D. J. *et al.* Enhancing AGN efficiency and cool-core formation with anisotropic thermal conduction. MNRAS **488,** 3003–3013 (Sept. 2019) (cited on page 134).
367. Smith, B., O'Shea, B. W., Voit, G. M., Ventimiglia, D. & Skillman, S. W. Cosmological Simulations of Isotropic Conduction in Galaxy Clusters. ApJ **778,** 152 (Dec. 2013) (cited on page 134).
368. Yang, H. .-. K. & Reynolds, C. S. Interplay Among Cooling, AGN Feedback, and Anisotropic Conduction in the Cool Cores of Galaxy Clusters. ApJ **818,** 181 (Feb. 2016) (cited on page 134).
369. Sharma, P., Chandran, B. D. G., Quataert, E. & Parrish, I. J. Buoyancy Instabilities in Galaxy Clusters: Convection Due to Adiabatic Cosmic Rays and Anisotropic Thermal Conduction. ApJ **699,** 348–361 (July 2009) (cited on page 134).
370. Banerjee, N. & Sharma, P. Turbulence and cooling in galaxy cluster cores. MNRAS **443,** 687–697 (Sept. 2014) (cited on page 134).
371. Chabrier, G. Galactic Stellar and Substellar Initial Mass Function. PASP **115,** 763–795 (July 2003) (cited on page 143).
372. Behroozi, P. *et al.* The Universe at z > 10: predictions for JWST from the UNIVERSEMACHINE DR1. MNRAS **499,** 5702–5718 (Dec. 2020) (cited on pages 143, 144, 147, 155, 168, 169).
373. Dekel, A. & Silk, J. The Origin of Dwarf Galaxies, Cold Dark Matter, and Biased Galaxy Formation. ApJ **303,** 39 (Apr. 1986) (cited on page 143).
374. Silk, J. & Rees, M. J. Quasars and galaxy formation. A&A **331,** L1–L4 (Mar. 1998) (cited on page 143).
375. Silk, J. & Mamon, G. A. The current status of galaxy formation. *Research in Astronomy and Astrophysics* **12,** 917–946 (Aug. 2012) (cited on pages 143, 144).

376. McNamara, B. R. & Nulsen, P. E. J. Heating Hot Atmospheres with Active Galactic Nuclei. ARA&A **45,** 117–175 (Sept. 2007) (cited on page 143).
377. Legrand, L. *et al.* The COSMOS-UltraVISTA stellar-to-halo mass relationship: new insights on galaxy formation efficiency out to z ~ 5. MNRAS **486,** 5468–5481 (July 2019) (cited on pages 143, 144, 147, 155, 168, 169).
378. Ma, L. *et al.* Seeds Don't Sink: Even Massive Black Hole "Seeds" Cannot Migrate to Galaxy Centers Efficiently. *arXiv e-prints,* arXiv:2101.02727 (Jan. 2021) (cited on page 148).
379. Ogiya, G., Hahn, O., Mingarelli, C. M. F. & Volonteri, M. Accelerated orbital decay of supermassive black hole binaries in merging nuclear star clusters. MNRAS **493,** 3676–3689 (Apr. 2020) (cited on page 148).
380. Barzilai, J. & Borwein, J. M. Two-Point Step Size Gradient Methods. *IMA Journal of Numerical Analysis* **8,** 141–148 (Jan. 1988) (cited on pages 148–150).
381. Fletcher, R. *On the Barzilai-Borwein Method* in *Optimization and Control with Applications* (eds Qi, L., Teo, K. & Yang, X.) (Springer US, Boston, MA, 2005), 235–256 (cited on page 149).
382. Cauchy, A. Methode générale pour la résolution des systemes d'équations simultanées. *Comptes Rendus de l'Academie des Science* **25,** 536–538 (1847) (cited on page 149).
383. Noeske, K. G. *et al.* Star Formation in AEGIS Field Galaxies since z=1.1: The Dominance of Gradually Declining Star Formation, and the Main Sequence of Star-forming Galaxies. ApJ **660,** L43–L46 (May 2007) (cited on pages 168–170).
384. Kormendy, J. & Ho, L. C. Coevolution (Or Not) of Supermassive Black Holes and Host Galaxies. ARA&A **51,** 511–653 (Aug. 2013) (cited on page 170).
385. Gebhardt, K. *et al.* Axisymmetric Dynamical Models of the Central Regions of Galaxies. ApJ **583,** 92–115 (Jan. 2003) (cited on page 170).
386. Beifiori, A., Courteau, S., Corsini, E. M. & Zhu, Y. On the correlations between galaxy properties and supermassive black hole mass. MNRAS **419,** 2497–2528 (Jan. 2012) (cited on page 170).
387. van den Bosch, R. C. E. Unification of the fundamental plane and Super Massive Black Hole Masses. ApJ **831,** 134 (Nov. 2016) (cited on pages 170, 171).
388. Kaiser, N. Evolution and clustering of rich clusters. MNRAS **222,** 323–345 (Sept. 1986) (cited on pages 173, 182, 183).
389. Voit, G. M., Kay, S. T. & Bryan, G. L. The baseline intracluster entropy profile from gravitational structure formation. MNRAS **364,** 909–916 (Dec. 2005) (cited on pages 173, 176, 179, 180).
390. Nagai, D., Kravtsov, A. V. & Vikhlinin, A. Effects of Galaxy Formation on Thermodynamics of the Intracluster Medium. ApJ **668,** 1–14 (Oct. 2007) (cited on page 173).
391. Pratt, G. W., Croston, J. H., Arnaud, M. & Böhringer, H. Galaxy cluster X-ray luminosity scaling relations from a representative local sample (REXCESS). A&A **498,** 361–378 (May 2009) (cited on pages 176, 179, 180, 199).
392. Planck Collaboration *et al.* Planck intermediate results. V. Pressure profiles of galaxy clusters from the Sunyaev-Zeldovich effect. A&A **550,** A131 (Feb. 2013) (cited on pages 176, 178, 180).

393. Gianfagna, G. *et al.* Exploring the hydrostatic mass bias in MUSIC clusters: application to the NIKA2 mock sample. MNRAS **502,** 5115–5133 (Apr. 2021) (cited on pages 177, 178, 180).
394. Piffaretti, R., Arnaud, M., Pratt, G. W., Pointecouteau, E. & Melin, J. .-. The MCXC: a meta-catalogue of x-ray detected clusters of galaxies. A&A **534,** A109 (Oct. 2011) (cited on pages 177, 180).
395. Mandelbrot, B. How Long Is the Coast of Britain? Statistical Self-Similarity and Fractional Dimension. *Science* **156,** 636–638 (May 1967) (cited on page 182).
396. Navarro, J. F., Frenk, C. S. & White, S. D. M. Simulations of X-ray clusters. MNRAS **275,** 720–740 (Aug. 1995) (cited on page 184).
397. Kravtsov, A. V., Vikhlinin, A. & Nagai, D. A New Robust Low-Scatter X-Ray Mass Indicator for Clusters of Galaxies. ApJ **650,** 128–136 (Oct. 2006) (cited on page 186).
398. Codis, S., Pogosyan, D. & Pichon, C. On the connectivity of the cosmic web: theory and implications for cosmology and galaxy formation. *Monthly Notices of the Royal Astronomical Society* **479,** 973–993 (June 2018) (cited on page 187).
399. Gouin, C., Bonnaire, T. & Aghanim, N. *Shape and connectivity of groups and clusters: Impact of dynamical state and accretion history* 2021 (cited on page 187).
400. Malavasi, N., Aghanim, N., Tanimura, H., Bonjean, V. & Douspis, M. Like a spider in its web: a study of the large-scale structure around the Coma cluster. A&A **634,** A30 (Feb. 2020) (cited on page 187).
401. Anders, E. & Grevesse, N. Abundances of the elements: Meteoritic and solar. Geochim. Cosmochim. Acta **53,** 197–214 (Jan. 1989) (cited on page 189).
402. Foreman-Mackey, D. *et al.* emcee: The MCMC Hammer, ascl:1303.002 (Mar. 2013) (cited on page 190).
403. Mantz, A. B., Allen, S. W., Morris, R. G. & von der Linden, A. Centre-excised X-ray luminosity as an efficient mass proxy for future galaxy cluster surveys. MNRAS **473,** 3072–3079 (Jan. 2018) (cited on page 199).
404. Bulbul, E. *et al.* X-Ray Properties of SPT-selected Galaxy Clusters at 0.2 < z < 1.5 Observed with XMM-Newton. ApJ **871,** 50 (Jan. 2019) (cited on pages 206, 209, 210, 212, 213, 217).
405. Biffi, V. *et al.* The MUSIC of galaxy clusters - II. X-ray global properties and scaling relations. MNRAS **439,** 588–603 (Mar. 2014) (cited on pages 206, 207, 209, 210, 212, 213).
406. Henden, N. A., Puchwein, E. & Sijacki, D. The redshift evolution of X-ray and Sunyaev-Zel'dovich scaling relations in the FABLE simulations. MNRAS **489,** 2439–2470 (Oct. 2019) (cited on pages 206, 209, 210, 214, 215, 217).
407. Lieu, M. *et al.* The XXL Survey . IV. Mass-temperature relation of the bright cluster sample. A&A **592,** A4 (June 2016) (cited on pages 206, 207, 209).
408. Reichert, A., Böhringer, H., Fassbender, R. & Mühlegger, M. Observational constraints on the redshift evolution of X-ray scaling relations of galaxy clusters out to z ∼1.5. A&A **535,** A4 (Nov. 2011) (cited on pages 209, 210).
409. Le Brun, A. M. C., McCarthy, I. G., Schaye, J. & Ponman, T. J. The scatter and evolution of the global hot gas properties of simulated

galaxy cluster populations. MNRAS **466,** 4442–4469 (Apr. 2017) (cited on pages 209, 213–215, 217).

410. Sun, M. *et al.* Chandra Studies of the X-Ray Gas Properties of Galaxy Groups. ApJ **693,** 1142–1172 (Mar. 2009) (cited on page 209).
411. Lovisari, L., Reiprich, T. H. & Schellenberger, G. Scaling properties of a complete X-ray selected galaxy group sample. A&A **573,** A118 (Jan. 2015) (cited on page 209).
412. Mantz, A. B. *et al.* Weighing the giants- V. Galaxy cluster scaling relations. MNRAS **463,** 3582–3603 (Dec. 2016) (cited on pages 210, 212, 213).
413. Nagarajan, A. *et al.* Weak-lensing mass calibration of the Sunyaev-Zel'dovich effect using APEX-SZ galaxy clusters. MNRAS **488,** 1728–1759 (Sept. 2019) (cited on pages 214, 215).
414. Riess, A. G. *et al.* Milky Way Cepheid Standards for Measuring Cosmic Distances and Application to Gaia DR2: Implications for the Hubble Constant. ApJ **861,** 126 (July 2018) (cited on page 220).
415. Riess, A. G., Casertano, S., Yuan, W., Macri, L. M. & Scolnic, D. Large Magellanic Cloud Cepheid Standards Provide a 1% Foundation for the Determination of the Hubble Constant and Stronger Evidence for Physics beyond ΛCDM. ApJ **876,** 85 (May 2019) (cited on page 220).
416. Ettori, S. *et al.* Mass Profiles of Galaxy Clusters from X-ray Analysis. Space Sci. Rev. **177,** 119–154 (Aug. 2013) (cited on page 220).